Doctoral Dissertation
Doctoral Program in Science Material (38th Cycle)

Advanced Polymer Electrolytes for Solid-State Li-Metal Batteries: A Rational Design Strategy from Materials to Scalable Processing

Francesco Gambino

Supervisor

Prof. Claudio Gerbaldi

Co-Supervisor

Dott. Matteo Destro

Politecnico di Torino

2026

I hereby declare that the contents and organisation of this dissertation constitute my own original work and do not compromise in any way the rights of third parties, including those relating to the security of personal data.

Francesco Gambino

Turin, 2026

Acknowledgments

I would like to thank my supervisor, Prof. Claudio Gerbaldi, and all the former and current members of the GAME Lab research group for these fruitful years. I would also like to thank Prof. Alexander S. Shaplov for welcoming me into the research group during my secondment at Luxembourg Institute of Science and Technology. I am especially grateful to Martina, for the support during these years.

My last thank goes to all my friends from DISAT, who were able to brighten these years and make them a little more joy

Preface

The endless pursuit for efficient and reliable energy sources has been amongst the main drivers of human progress. Indeed, energy underpins every aspect of modern society, from industrial production and transportation to communication technologies and digital infrastructures. Over the centuries, the way humanity has produced, stored, and used energy has shaped economic development, social organization, and technological innovation. The Industrial Revolution marked a major turning point when the large-scale exploitation of coal and the development of the steam engine, drastically transformed manufacturing and urban everyday life. Later, the discovery of electricity and the invention of electrochemical energy-storage enabled electrification on a global scale, opening the way to new industrial processes, communication systems, and consumer technologies. In the late 19th and early 20th centuries, the rise of internal combustion engines established petroleum as a strategic resource, deeply influencing both industrial growth and global geopolitics.

Today, society is facing a new energy transition, driven by the urgent need to reduce greenhouse-gas emissions, limit dependence on fossil fuels, and promote a more sustainable and resilient energy system. In this scenario, renewable energy sources such as solar, wind, and hydroelectric power are playing an increasingly pivotal role. However, their intrinsic intermittent nature makes efficient energy-storage technologies indispensable for balancing supply and demand, stabilizing electrical grids, and enabling the widespread electrification of transport and other sectors.

Among the available storage technologies, electrochemical energy-storage systems, particularly secondary batteries, have emerged as key enablers of this transition. At present, their relevance extends from portable electronics to electric vehicles and stationary grid storage. In this context, the development of safer, higher-energy, and longer-lasting batteries is one of the central challenges of

contemporary materials science and electrochemistry. Lithium-metal batteries, especially in all-solid-state configurations, are widely regarded as promising next-generation systems because of their potential to deliver high energy density while improving safety compared with conventional liquid electrolyte-based systems.

A key, critical component in these devices is the electrolyte. Solid polymer electrolytes (SPEs) are particularly attractive because they combine the advantages of solid-state operation with the processability, flexibility, and tunability typical of polymeric materials. Nevertheless, their practical implementation still requires significant advances in ionic conductivity, lithium-ion transport, interfacial compatibility with lithium metal, mechanical stability, and resistance to anodic oxidation, especially for operation in high-energy devices where compatibility with high-voltage cathodes is required.

Within this scenario, the aim of the work carried out during the three years of PhD and presented in this thesis was devoted to the development of novel SPEs for next-generation, advanced lithium-metal batteries. The research followed a progressive and rational optimization pathway, moving from the formulation of physically blended polymer electrolytes processed through scalable and industrially relevant solvent-free approaches, to the refinement of their properties by crosslinking strategies, plasticizing additives, and, finally, the molecular design of new lithium salts and single-ion conducting polymer architectures. At each stage, the materials were developed with the dual objective of improving the key performance indicators required for practical application, namely ionic conductivity, lithium-ion transport, interfacial compatibility with lithium metal, mechanical and thermal stability, and resistance to anodic oxidation, while also preserving processability and favouring manufacturing routes compatible with large-scale production. As a result, the thesis describes not only the development of increasingly optimized SPE formulations, but also the construction of a coherent materials-design strategy in which each successive step builds on the limitations and insights emerging from the previous one, ultimately contributing to the

advancement of safer, higher-energy, and more industrially viable solid-state battery technologies, including operation with high-energy 4V-class cathodes.

The outcome of the manuscript is organized into 8 chapters, with the introductory chapters 1-3 providing the general background, scientific context, and experimental framework, while the following chapters 4-8 present and discuss the main original results of the three years' work; concluding remarks at the end of the manuscript summarise the most impactful results, emphasizing the key takeaway messages while also reinforcing their importance in the broader context. ;

Chapter 1 introduces the basic concepts for electrochemical energy storage systems, describing their main characteristics and working principles. It also includes a brief overview of the most common electrochemical characterization techniques, along with a concise discussion of the evolution of secondary batteries and electrochemical double-layer capacitors (EDLCs).

In **Chapter 2** focuses on solid polymer electrolytes, highlighting their key features and discussing the main strategies currently adopted to achieve enhanced performances in all-solid-state lithium metal batteries (ASSLMBs).

Chapter 3 provides an overview of the materials used and details the experimental methods used for the preparation and characterization of SPEs, as well as the protocols followed for cathode fabrication and laboratory-scale electrochemical battery cell assembly.

Chapter 4 presents the preparation and comprehensive characterization of blend poly(ethylene oxide) (PEO) - polycarbonates (PCs) SPEs, produced through a sustainable, solvent-free, and readily scalable extrusion process. Effects of the nature of the PC component and of the PEO/PC ratio on the mechanical, morphological, and electrochemical properties of the resulting SPEs are systematically investigated with a view toward their application in ASSLMBs.

Chapter 5 builds upon the SPE systems developed in the previous chapter, and investigates the optimization of the most promising PEO/PEC formulation through a UV-induced crosslinking approach. The resulting electrolytes are flexible and self-standing, and display remarkable thermal and mechanical stabilities, non-

flammability, and structural integrity. Lithium-metal polymer cells assembled with a $LiFePO_4$-based composite catholyte (using the same SPE formulation as active binder) provide near-theoretical specific capacity up to medium current regimes and excellent rate capability at 70 °C.

In order to achieve enhanced cycling performance at lower temperatures, **Chapter 6** presents a novel SPE obtained by the same process used for developing the optimized electrolyte in Chapter 5, combined with the addition of a solid plastic crystal, namely succinonitrile (SN). Plasticization aims at concurrently enhancing bulk ion transport and electrochemical stability. Variation of the PEO/PEC ratio reveals that a PEO-rich composition (PEO-PEC 7:3) provides the optimal balance between plasticization and interfacial stability. Symmetrical Li‖Li cells employing this electrolyte exhibit stable and reversible lithium plating/stripping over 1400 hours, with moderate and stable overpotentials. In addition, laboratory-scale truly solid-state Li-metal cells both with LFP and NMC show remarkable galvanostatic charge/discharge performance, delivering nearly full practical specific capacity even at 40 °C.

Chapter 7 addresses another key aspect in SPE development, namely the design of novel, stable, and high-performing lithium salts. To the purpose, two asymmetric, low-melting thioether-TFSI lithium salts were synthesized via a modular thiolene strategy and incorporated into PEO-based SPEs. Their pronounced plasticizing effect efficiently suppresses PEO crystallinity while preserving ionic conductivity, Li^+ ion transference number, and electrochemical stability. In addition, both systems mitigate aluminum current-collector corrosion through the formation of a stable passivation layer, thus overcoming a major limitation of conventional LiTFSI-based electrolytes. As a result, the corresponding SPEs show improved compatibility with lithium metal and enable stable cycling in laboratory-scale Li‖$LiFePO_4$ battery cells.

The experimental work concludes with **Chapter 8,** which explores a new family of single-ion conducting polymers (SICPs), developed through the design and synthesis of advanced ionic-liquid-like monomers (ILMs) featuring a thioether

bridge between the methacrylic group and the (trifluoromethane)sulfonylimide (TFSI) anion. Their random copolymers with poly(ethylene glycol)methyl ethermethacrylate (PEGM) combine practically relevant ionic conductivity with markedly high transference number. When assembled in lab-scale, truly solid-state Li‖LFP battery cells, these advanced SICP electrolytes enable highly reversible cycling with high specific discharge capacity up to C/5. Rate-dependent voltage profiles reveal limited polarization even at higher current regimes, confirming effective Li^+ transport within the solid electrolyte architecture. Long-term cycling at C/15 demonstrates outstanding stability, upon long-term, reversible galvanostatic cycling with nearly overlapping voltage curves throughout whole operation.

Overall, this PhD thesis contributes to the development of advanced polymer-electrolyte materials for next-generation, solid-state electrochemical energy-storage systems. By combining materials design, scalable processing, and electrochemical validation, the work provides new insights into the relationships between composition, structure, and performance in solid polymer electrolytes. These findings contribute to the broader effort toward safer, higher-energy, and more sustainable battery technologies for an increasingly electrified society.

Contents

List of Tables

List of Figures

Chapter 1

Introduction

1.1 Energy Storage Systems

The availability of reliable and sustainable energy is one of the central challenges of modern society. Since the XIX century, the rapid increase of energy demand has been mainly covered through the use of fossil fuels. However, our dependence on these fuels is associated with some major issues such as their limited availability, their uneven geographical distribution, and the environmental concerns derived from the pollutants evolved by their combustion. According to recent international sources, global energy demand continues to rise, with growth in 2024 reaching 2.2%, almost twice the average rate observed over the previous decade. This increase has been accompanied by a marked acceleration in electricity demand, which rose by 4.3% in 2024, driven by electrification, digitalization, industrial growth, and the increasing energy requirements associated with cooling and data-intensive technologies [1]. Fossil fuels still play a dominant role in the global energy system (**Figure 1.1**), and energy-related CO_2 emissions reached a new record of 38.6 Gt CO_2 in 2024 [2]. These trends clearly illustrate the dual challenge faced by contemporary energy systems: meeting rising demand while drastically reducing greenhouse gas emissions.

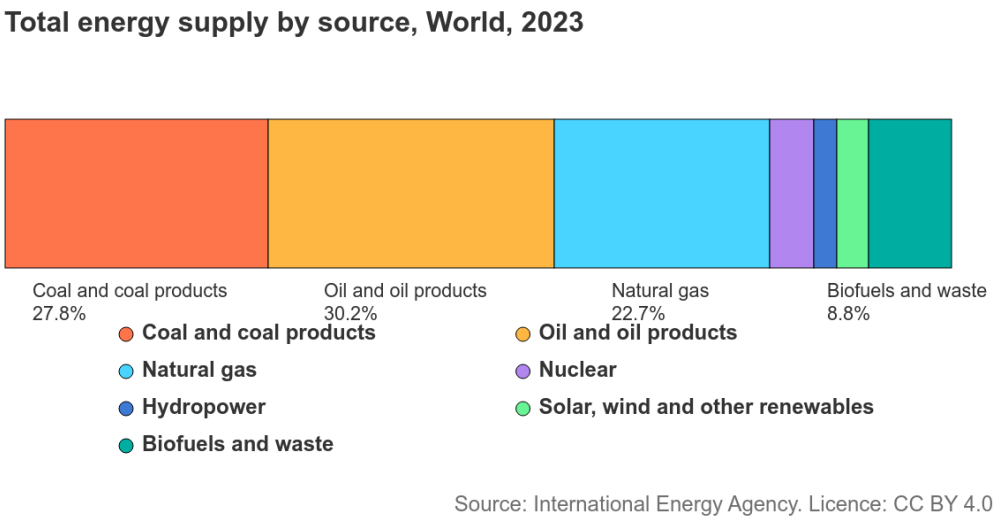

Figure 1.1 The breakdown of the World primary energy consumption in 2023. Source: data downloaded from IEA World Energy Statistics. Website visited on 2/4/26.

The transition toward a low-carbon, highly electrified society is critically dependent on the development of efficient, safe, and sustainable energy storage systems. Among the broad family of energy storage technologies, electrochemical energy storage (EES) systems, and particularly Lithium-ion batteries (LIBs), have assumed a central role because of their high energy density/efficiency, modularity, scalability, and compatibility with both portable (e.g., smartphone and laptop), and large-scale applications like electric vehicles (EVs). In this scenario, the development of efficient materials for EESs plays a crucial role on the replacement of conventional internal combustion engine (ICE) vehicles by electric vehicles, contributing to the reduction of greenhouse gases (GHG) emission and the pollution levels in big cities.

In such context, this chapter discusses how ESSs are classified and includes some basic concepts and details on general definitions.

1.1.1 Classification and Basic Concepts

EES devices involve the reversible transformation from electrical to chemical energy and viceversa. Systems storing and converting energy electrochemically chiefly include electrochemical capacitors (EC), batteries, and fuel cells.

Batteries are the most established and widely employed EES systems. The term battery commonly refers to a device where the energy is stored in the form of chemical energy, and it is released in the form of electric power upon a spontaneous faradaic (redox) process called discharge. Each electrochemical cell is formed by two electrodes, a cathode and an anode, and an electrolyte in between to physically separate them. During operation, oxidation takes place at the anode, generating electrons that flow through the external circuit, while reduction occurs at the cathode, where electrons are consumed. Simultaneously, ions migrate through the electrolyte to maintain charge neutrality within the cell. The electrical energy delivered by the battery is therefore the result of the difference in chemical potential between the two electrodes [3].

Generally, batteries can be divided into *primary* and *secondary* systems. A *primary battery* is a cell where the electrochemical reactions proceed irreversibly under normal operating conditions. Reactions proceed until the active materials are consumed, when the battery can no longer deliver energy and must be discarded. Primary batteries are assembled in the charged state and are discharged upon use. A *galvanic cell* is an example of a primary battery. In this type of cell, the *anode* is the negative electrode associated with oxidation reactions through which electrons are released into the external circuit and form positive ions in the electrolyte medium. The *cathode* is the positive electrode associated with reduction reactions induced by electrons flow from the external circuit. In a galvanic cell, the spontaneous process (discharge) is the migration of ions and electrons from the anode to the cathode (**Figure 1.2a**) and its driving force is the difference in electrochemical potential between the two electrodes at the open circuit potential (i.e. when no external current flows in the system), called electromotive force (e.m.f.) [4]. *Secondary* batteries, also referred to as rechargeable batteries, are based on electrochemical reactions that can be reversed by applying an external potential. This means that after the spontaneous discharge process , the cell may be recharged by using an external energy source that imposes a voltage greater than the cell voltage registered at open circuit potential (OCV) conditions, enabling the electrons to flow in the opposite direction and promoting the non-spontaneous process (charge) of the electrochemical system. During charge, the battery works as an *electrolytic cell* (**Figure 1.2b**). This reversibility makes secondary batteries particularly attractive for applications requiring repeated energy storage and

release, such as consumer electronics, electric mobility, and renewable energy storage.

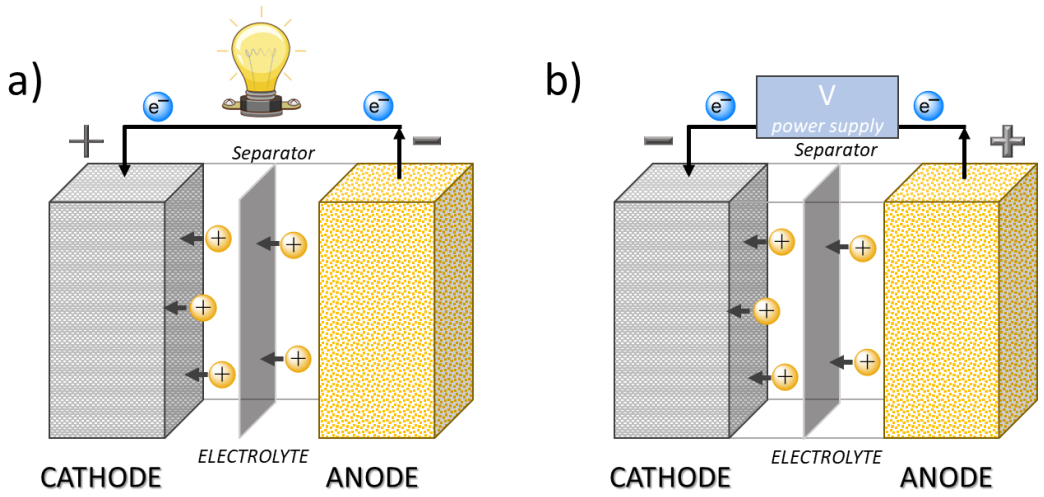

Figure 1.2. Schematic representation of a secondary battery working as a) a galvanic cell (discharge) and as b) an electrolytic cell (charge).

1.1.2 Electrochemical parameters and performance metrics

Capacity (Q)

The total amount of electric charge that can be supplied or accumulated by the system is defined as capacity and it is usually expressed in Coulomb (C) or Ampere-hour (Ah), where 1 Ah = 3600 Coulombs. In general, capacity is defined as the time integral of the current; under constant-current conditions, it can be calculated as the product of current and charge/discharge time as in **Equation 1**.

Equation 1

$$Q = i \cdot t$$

When the capacity delivered by a given active material is normalized per its mass (m) it is called *(gravimetric) specific capacity* (Q_{sp}) and expressed in Ah g^{-1}:

Equation 2

$$Q_{sp} = \frac{Q}{m}$$

Theoretical Specific Capacity

The theoretical (gravimetric) specific capacity (Ah g^{-1}) of an active electrode material can be estimated from Equation 3:

Equation 3

$$Q_{\text{th}} = \frac{nF}{3600 \cdot MM}$$

where n is the number of exchanged electrons, F is the Faraday's constant (96485 C mol^{-1}), and MM is the molar mass of the active material (g mol^{-1}).

Coulombic Efficiency (CE)

Coulombic efficiency (CE) is the ratio of the discharge capacity (Q_d) to the capacity stored during the preceding charge step (Q_c), expressed as a percentage:

Equation 4

$$CE = \frac{Q_d}{Q_c} \cdot 100$$

C-rate

The C-rate indicates how fast a battery is charged or discharged relative to its nominal capacity. It is expressed in fractions or multiples of C. A C-rate of 1C corresponds to the current required to fully discharge a battery in 1 hour, 0.5C or C/2 refers to the current to discharge in two hours and 2C to discharge in half an hour.

The *rate capability* describes the ability of a battery to retain its capacity when operated at increasingly higher current densities or C-rates. It is generally evaluated by comparing the discharge capacity measured at different rates with the value obtained at low current.

Energy (E)

The energy (E) supplied by an electrochemical power source is expressed in Joule (J) or more commonly in Watt hour (Wh), and it is related to the capacity as in **Equation** , where V is the cell voltage delivered by the system and I(t) the current as function of time:

Equation 5

$$E = \int V(t)I(t)dt$$

Following the concept of specific capacity, defined as capacity per unit mass, we can also define *specific energy*, which is thus defined as the energy output from

a battery per unit mass (Wh g^{-1}). On the other hand, considering energy per unit volume, *energy density* is defined (Wh L^{-1}).

Power (P)

The energy delivered by a material, or a power source, in a specific time. The instantaneous power is given by:

Equation 6

$$P(t) = \frac{\int I(t) \cdot V(t) dt}{\int dt}$$

Whereas the average power over a discharge process can be expressed as:

Equation 7

$$P = i \cdot V = \frac{Q \cdot V}{t} = \frac{E}{t}$$

The concepts of *specific energy* and *specific power* are essential to understand and compare the performances of different energy power sources.

1.2 Electrochemical methods of analysis

1.2.1 Electrochemical Impedance Spectroscopy

Electrochemical Impedance Spectroscopy (EIS) is a non-destructive electrochemical technique used to investigate the response of a system over a wide frequency range, providing information on charge transport and interfacial processes. The measured impedance describes the opposition to an alternating current (AC) and is expressed as a complex quantity with a real part, resistance, and an imaginary part, reactance [5].

In EIS, a small-amplitude AC voltage is applied to the electrochemical cell and the resulting current is recorded, generating spectra commonly represented by Nyquist or Bode plots. EIS is particularly useful for secondary Li-based batteries, where multiple resistive, capacitive, solid-liquid, and solid-solid interfacial contributions are present. Since these processes are characterized by different time

constants, EIS allows their separation over different frequency ranges and their interpretation through Nyquist plots and equivalent circuit models [6].

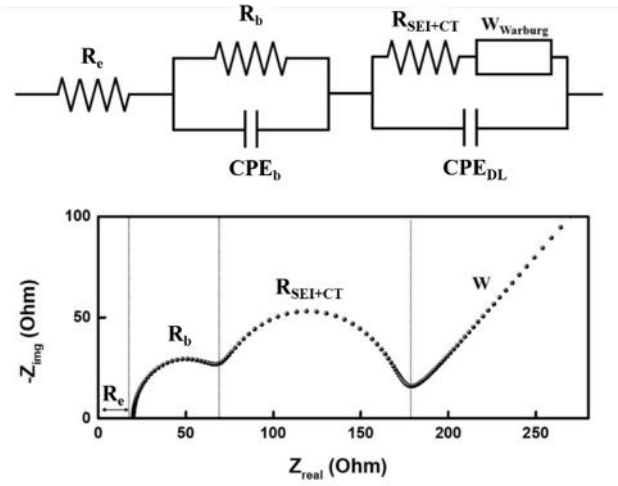

Figure 1.3 Each element in the Li battery half-cell equivalent circuit (top) corresponds to a section of the resulting EIS Nyquist plot (bottom).

As illustrated in **Figure 1.3**, for polymer electrolytes, the main impedance contributions are:

• Series resistance (R_e), or internal resistance, includes the electronic resistance of electrode materials, current collectors, and internal cell connections.

• Bulk resistance (R_b) reflects ionic conduction through the polymer matrix and depends on ionic conductivity, electrolyte composition, temperature, and polymer morphology. Its intercept with the real axis is commonly used to calculate electrolyte ionic conductivity.

• The intermediate-frequency semicircle is associated with electrode-electrolyte interfacial processes, including SEI resistance (R_{SEI}), related to ion transport through the passivation layer, and charge-transfer resistance (R_{CT}), which represents the kinetic barrier for electrochemical reactions. R_{CT} and the double-layer constant phase element are influenced by surface coating, phase transitions, electronic structure, and particle size.

• Warburg impedance ($W_{Warburg}$) is related to ion diffusion within electrode materials and appears as an inclined line in the low-frequency region of the Nyquist plot.

1.2.2 Galvanostatic measurements

Galvanostatic measurements involve applying a constant current to an electrochemical cell and monitoring the resulting voltage response over time. Indeed, it is possible to evaluate a device's ability to store and deliver energy [7]. Depending on the sign of the current, the battery can be charged or discharged. Each current step can be held for a given time, or until the voltage reaches a cut-off limit. From this test, fundamental battery performance data can be extracted, which include Coulombic efficiency, specific capacity, energy and power densities, given the geometry and weight involved. Moreover, the effect of varying the current or perform prolonged cycling allows to evaluate key parameters, such as rate capability, and cycling life, which are essential for practical battery applications.

Galvanostatic charge and discharge involve electrochemical reactions at the electrodes. The voltage response reflects the energy stored in the chemical bonds during charging and the release of this energy during discharge. As shown in **Figure 1.4**, voltage profiles of battery systems display a curve which can possess different shapes depending on the phenomena, and thus materials involved in the process.

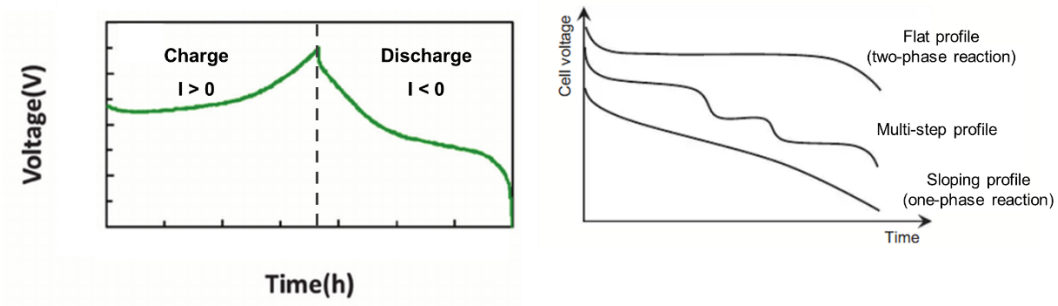

Figure 1.4 Typical galvanostatic charge/discharge profiles for an electrochemical cell and related characteristics of the different most common profiles depending on the electrochemical process.

Voltage profiles of battery systems display a curve which can possess different shapes depending on the electrochemical reaction(s) and, thus, corresponding materials involved in the process (**Figure 1.4**). A plateau is generally observed in the voltage curve when there is a two-phase reaction in the active material. A multi-step curve, showing more than one plateau region, is characteristic of electrochemical systems in which multiple two-phase reactions occur. A sloping profile is typical of a one-phase reaction.

Nevertheless, in a real system, the voltage measured during discharge is always lower than the open circuit voltage (V_{OC}) due to internal resistance of the cell and

polarization effects at both electrodes. Different types of polarizations can cause these losses and are generally described to be of activation, ohmic and concentration (**Figure 1.5**) [4].

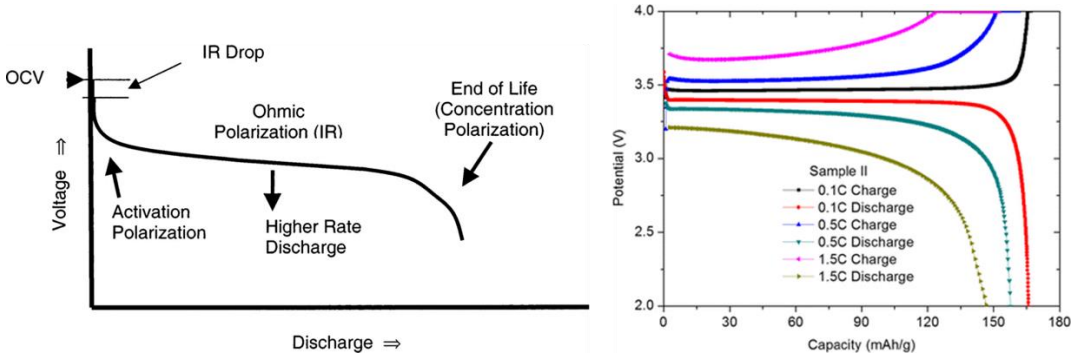

Figure 1.5 Characteristic discharge curves of a battery, showing various types of polarization(s). Reproduced and readapted with permission from ref. [4,10].

The voltage of the cell can be approximated by:

Equation 7

$$V = V_{OC} - IR$$

where V_{OC} is the potential recorded when no current is flowing. The discharge curve initially deviates from the V_{OC} through an instantaneous IR drop, which arises from the internal ohmic resistance of the cell, including the electrolyte, electrodes, separator, and electrical contacts. Following this initial step, the voltage is further lowered by activation polarization, related to the finite kinetics of the charge-transfer reactions at the electrode/electrolyte interfaces. During continued discharge, ohmic polarization and mass transport limitations contribute to a gradual voltage decrease. At high states of discharge, the development of concentration gradients within the electrolyte and electrode phases gives rise to concentration polarization, which becomes predominant near the end of discharge and leads to the abrupt voltage fall observed before the cut-off potential. This polarization contributions become increasingly pronounced as increasingly higher applied current(s). The most common tests conducted in galvanostatic set-up are long-term cycling, rate capability test, and plating deposition test (also called plating-stripping test). A representative example is provided by the $LiFePO_4$ charge/discharge profiles shown in **Figure 1.5**. Owing to the two-phase transition between $LiFePO_4$

and $FePO_4$, this material exhibits a characteristic flat plateau centered at approximately 3.45 V vs. Li^+/Li [8].

In addition to galvanostatic cycling in full cells, the interfacial stability and lithium-ion transport properties of a new electrolyte can be evaluated through lithium plating/stripping experiments performed in symmetric Li|electrolyte|Li cells. The *plating deposition test* is an important protocol used in the study of new electrolytes, salts or separators. This analysis implies the use of metal electrodes (*i.e.* lithium) on both sides, thus assembling a symmetric cell. Through the analysis of the cell overpotential, this technique allows to investigate the compatibility of the electrolyte/membrane/separator with the metal and its behavior upon reversible cations transfer and plating. Under galvanostatic conditions, the voltage profile obtained during repeated plating/stripping cycles provides direct information on the stability of lithium deposition, the interfacial resistance, and the ability of the electrolyte to sustain reversible lithium-ion transport. Ideally, the cell exhibits a low and stable polarization voltage over extended cycling, indicating homogeneous lithium deposition, efficient stripping, and the formation of a stable SEI. In contrast, a progressive increase in overpotential, large voltage fluctuations, or the sudden appearance of short-circuit behavior may indicate interfacial degradation, non-uniform lithium growth, or dendritic lithium penetration through the electrolyte [9].

1.3 Lithium-ion batteries: historical development and working principles

The development of lithium-ion batteries (LIBs) marks a turning point in the history of EES and represents one of the most important technological breakthroughs of the late twentieth century. Thanks to their high energy density, versatility, and light weight, LIBs currently lead the market, and their adoption and advancement are expected to increase rapidly to meet the demands of the sustainable transition towards a “green” or carbon-neutral society. The motivation for developing lithium-based rechargeable batteries lies in the intrinsic physicochemical properties of lithium. Lithium is the lightest metal in the periodic table and it exhibits the most negative standard reduction potential among all elements (−3.04 V vs. SHE). Owing to these characteristics, lithium is particularly attractive for the development of high-energy EES systems, as it enables realization

of batteries with both high specific capacity and high operating voltage. In particular, lithium metal provides a theoretical specific capacity of 3860 mAh g−1, making it the most desirable anode material from purely thermodynamic and gravimetric viewpoints [10]. Thus, earliest efforts toward developing rechargeable lithium-based batteries focused on the direct use of lithium metal as the negative electrode. During the ‘60s and ‘70s extensive research was devoted to non-aqueous electrolytes, since the high reactivity of lithium precluded the use of water-based systems. Several solvent–salt combinations were investigated to improve ionic conductivity and electrochemical stability, including combinations of cyclic and linear carbonates. A major conceptual breakthrough occurred in the 1970s with the development of intercalation cathodes. Rather than relying on conversion or dissolution reactions, these materials can reversibly host lithium ions within an open crystal structure, while preserving both structural integrity and redox reversibility. As a results, during the 1970s and 1980s Exxon and Moli, based on the invention by Whittingham, launched the first rechargeable lithium-metal batteries (LMB) [11]. However, their commercial deployment was limited by a series of safety-related incidents, including fires and explosions, which ultimately prevented the market-scale diffusion of these devices [12]. These issues were associated with the use of lithium metal at the anode: due to its extremely high chemical reactivity, lithium readily reacts with the electrolyte [13]. Following the safety problems associated with rechargeable LMBs, the central challenge became how to preserve the high energy of lithium-based systems while eliminating metallic lithium from the cell.

In 1980, when Goodenough introduced layered $LiCoO_2$ as a high-voltage (~4–5 V vs. Li^+/Li) intercalation cathode, significantly increasing the energy density of the system. [14]. $LiCoO_2$ possesses a layered structure in which lithium ions can be reversibly de-intercalated and intercalated while the cobalt redox couple compensates the charge. Compared with TiS_2, $LiCoO_2$ offered a much higher operating voltage, close to 4 V vs. Li^+/Li, enabling a substantial increase in energy density [15]. The decisive step toward modern LIBs was then taken by Akira Yoshino, who replaced lithium metal with a carbonaceous anode capable of reversibly hosting lithium ions. [16]. Yoshino focused on carbon-based materials and demonstrated that, when combined with an optimized electrolyte and a $LiCoO_2$ cathode, they could provide reversible lithium insertion without the severe

degradation problems associated with lithium metal. In this new configuration, lithium is stored in both electrodes and the cell operates through the shuttling of Li^+ ions between two intercalation hosts, giving rise to the so-called rocking-chair concept that underlies present-day LIBs (**Figure 1.6**). After further optimization of electrode shaping and engineering, current collectors, separator materials, and electrolyte composition, the first commercial LIB was finally introduced in the market by Sony in 1991, followed by A&T Battery Corp. in 1992.

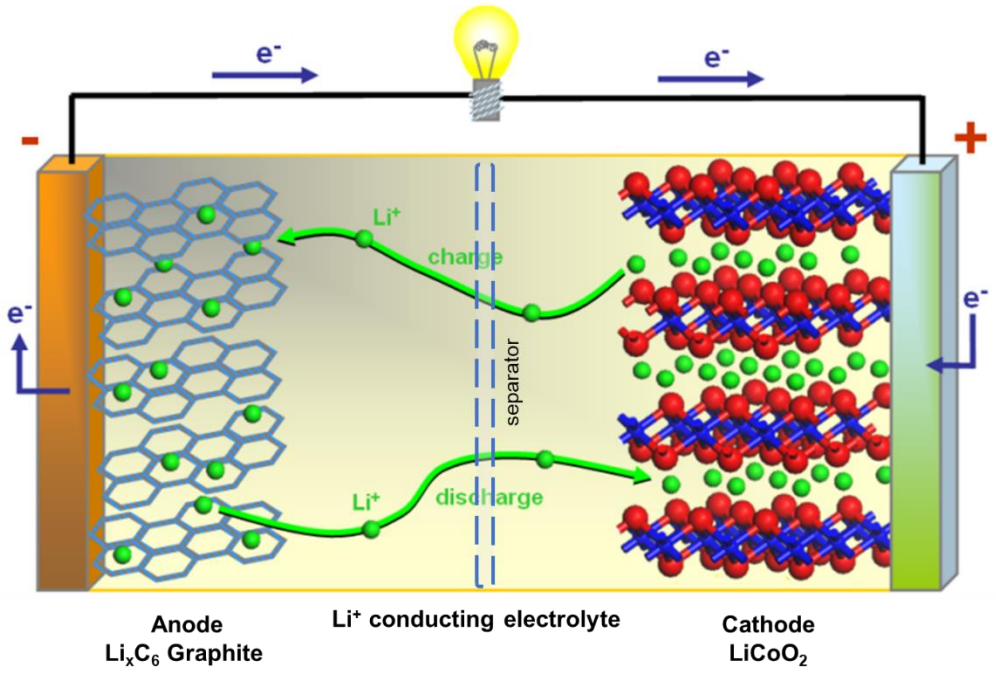

Figure 1.6 Schematic illustration of the first Li-ion battery ($LiCoO_2$/Liquid electrolyte/graphite). Reproduced and readapted with permission from ref. [17].

1.4 Materials in Li-based batteries

The performance of a secondary lithium-based battery is largely determined by the nature of its active and inactive materials, chiefly cathode, anode and electrolyte, which govern the energy density, operating voltage, rate capability, cycle life, safety, and long-term stability of the electrochemical cell. Since the earliest stages of their development, major research efforts have been directed toward the identification of new materials with enhanced performance.

1.4.1 Cathodes

The active materials used in commercial LIB cathodes generally belong to a few main families, including layered oxides, spinel oxides, and polyanionic compounds. These cathode materials can be broadly classified according to their crystal structure into layered oxides, spinels, and polyanionic compounds, the latter often adopting an olivine-type framework [18]. **Figure 1.7**, provides a qualitative comparison of the main characteristics of some of the most common cathode materials.

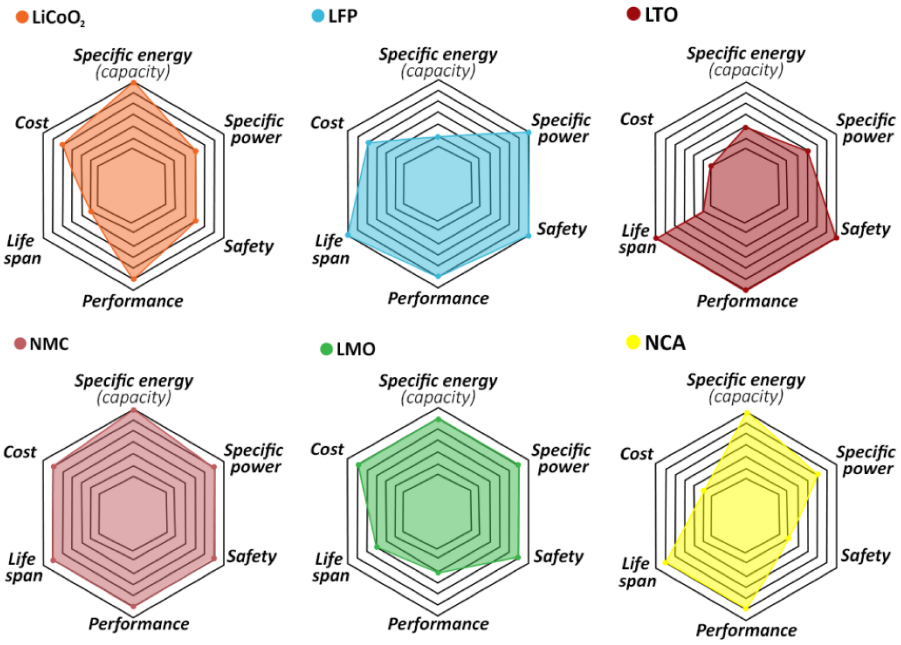

Figure 1.7 Comparison between different types of cathode materials for LIBs. Reproduced and readapted with permission from ref. [18].

The first commercially successful cathode material was lithium cobalt oxide ($LiCoO_2$, LCO), introduced in the early 1980s and later employed in the first commercial LIBs [19]. LCO is a single-phase intercalation material, which gives rise to a characteristic sloping voltage profile and a relatively high operating voltage of approximately 4.2 V vs. Li^+/Li. Although its theoretical capacity reaches 274 mAh g^{-1} under complete lithium extraction, full delithiation induces phase transitions accompanied by significant mechanical strain, hence the practical capacity is limited to about 150 mAh g^{-1}. To date, LCO is the most successful cathode material in LIBs for portable devices due to the high theoretical specific discharge capacity, good cycling and rate performances.

Although LCO dominated the early rechargeable LIB market, the limited availability and high cost of cobalt, together with concerns related to its toxicity and supply chain, rapidly highlighted the need for alternative cathode chemistries, particularly for heavy, large-scale applications such as hybrid electric vehicles (HEVs) and stationary energy storage [20]. To reduce or eliminate the use of costly and toxic cobalt, research efforts shifted toward lithium metal phosphates and $LiNi_xMn_yCo_zO_2$-based cathodes. These materials are now widely regarded as a new generation of cathode materials, offering the combination of safety, high power capability, and energy density required to meet the rapidly increasing demands of large-scale energy storage and transportation applications.

Among polyanionic materials, $LiFePO_4$ (LFP, lithium iron phosphate) stands because of its prominent advantages, including low cost, great thermal stability, negligible toxicity and enhanced safety [21,22]. These characteristics make it particularly attractive for applications where safety, reliability, and durability are prioritized over maximum energy density. LFP crystallizes in an olivine structure, in which lithium ions diffuse through one-dimensional channels, consisting of corner-shared FeO6 octahedra and edge-shared LiO_6 octahedra, linked together by PO_4 octahedra (**Figure 1.8a**). Its electrochemical reaction involves the Fe^{2+}/Fe^{3+} redox couple and produces a characteristic flat voltage plateau at approximately 3.4–3.5 V vs. Li^+/Li. The material shows a theoretical specific capacity of 170 mAh g^{-1} and its lithiation and delithiation proceed through a two-phase mechanism between $LiFePO_4$ and $FePO_4$, which share the same olivine framework. This feature assures its excellent reversibility and long cycle life [23]. However, this material has shown difficulties to reach the theoretical capacity under operation at room temperature, in addition the current densities to approach theoretical capacities need to be rather low, suggesting transport limitations of both ions and electrons. These limitations have been effectively mitigated through particle downsizing, carbon coating, and electrode architecture optimization [24].

In this context, layered transition metal oxides based on the structure of $LiCoO_2$ were developed. These layered oxides are often referred to as the '$LiMO_2$' structure, where a single transition metal or a mixture of several transition metals is employed (M = 3d transition metal, such as Ni, Co, Mn, Fe). Substitution of Co with the more abundant manganese led to preparation of $LiMnO_2$ (LMO). Despite a good

theoretical capacity of 285 mAh g^{-1} and a voltage range of 2.5 to 4.3 V, LMO showed rapid capacity fading, as the material transforms into a spinel structure upon cycling [25]. Due to the drawbacks of the individual layered materials (e.g., LCO, LMO), mixing of different transition metals has been proposed as a way to improve their performance as cathode materials. Reports on different binary layered oxide materials have shown that TM mixing is beneficial, and ternary oxides have shown further promise [26,27]. Ternary oxides combining Ni, Co, and Mn are usually commonly known as NMC ($LiNi_xMn_yCo_zO_2$) (**Figure 1.8b**). Layered NMC oxide materials can provide gravimetric capacities in the range 200−210 mAh g^{-1} in the voltage range of 3.0−4.3 V vs. Li^+/Li.

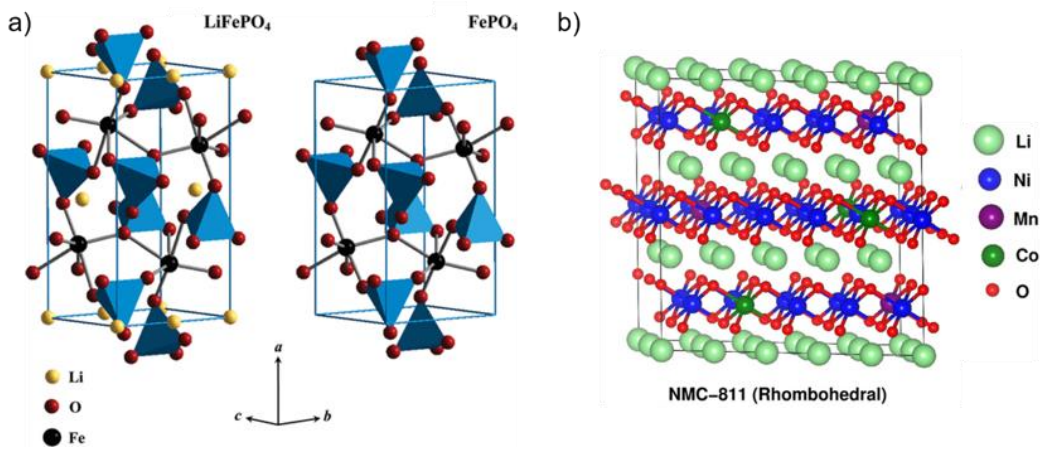

Figure 1.8 a) Crystal structures of $LiFePO_4$ and $FePO_4$. Reproduced and readapted with permission from ref. [28] b) Sketched illustration of the crystal structures of NMC811. Reproduced and readapted with permission from ref. [29].

The rationale behind combining Ni, Co, and Mn lies in the distinct and complementary properties contributed by each element: Ni mainly provides high capacity/energy through redox activity, Co improves electronic/ionic transport and suppresses Li/Ni cation mixing, and Mn provides structural and thermal stabilities during cycling, particularly by reducing reactivity with the electrophilic electrolyte solutions based on alkyl carbonate solvents. Nickel-rich NMC compositions, such as NMC622 or NMC811, offer improved capacity and are therefore particularly attractive at present for high-energy applications, especially electric vehicles. However, increasing the nickel content also tends to reduce thermal stability and can intensify surface degradation, transition metal dissolution, and interfacial

reactivity with the electrolyte [30]. As a consequence, the optimization of nickel-rich layered oxides requires careful control.

1.4.2 Anodes

The properties of the anode strongly affect battery capacity, coulombic efficiency, charge rate capability, and the overall stability of the cell. In LIBs, the anode is the electrode that hosts Li^+ ions during charging and releases them during discharge. Graphite is the most widely used anode material because of its low working potential, good reversibility, and long cycle life. Alternative carbonaceous materials are also explored, as well as composites with low percentages of alloying metals. However, alternative anodes such as silicon, tin, titanates, and conversion materials are also being investigated, as they can provide higher specific capacity or improved safety [31].

As previously mentioned, the most attractive anode remains lithium metall itself. Lithium metal does not require a host structure and therefore offers the highest possible specific capacity (3860 mAh^{-1} *vs.* ~372 mAh g^{-1} of the fully lithiated graphite) and the lowest possible anode potential [32]. For this reason, LMBs are often considered as the ultimate configuration for high-energy rechargeable lithium-based systems.

Before LMB becomes a viable technology, some challenges need to be overcome, the greatest of which are safety and cyclability. During charge, Li^+ ions are reduced and deposited on the lithium metal surface (plating), while during discharge lithium is removed (stripping). Repeated cycling often causes non-uniform deposition, leading to mossy or dendritic lithium growth. (**Figure 1.9**) [33]. These structures may form dead lithium or penetrate the separator, causing internal short circuits. Moreover, volume changes during plating can fracture the fragile SEI, exposing fresh lithium and promoting further uneven deposition.

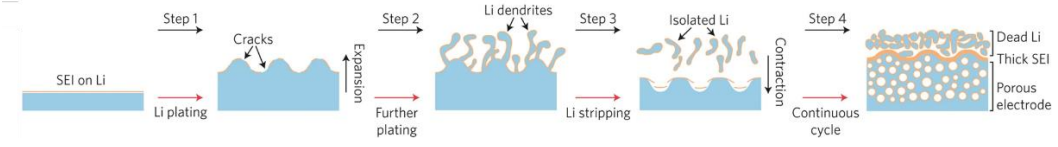

Figure 1.9 Schematics of the Li stripping/plating process with dendrite growth and related issues. Reproduced and readapted with permission from ref. [41].

These unwanted phenomena drastically decrease the performance of LMB, namely, the charge efficiency by which electrons are transferred in batteries decrease resulting in low Coulombic efficiency. For these reasons, although lithium metal is the most desirable anode from a theoretical standpoint, its safe and durable implementation requires the development of advanced electrolytes and interfaces capable of regulating lithium deposition and stabilizing the electrode/electrolyte contact [34]. This challenge has become one of the central research directions in modern battery science and has strongly contributed to the renewed interest in solid-state.

1.5 Electrolytes: is Solid the Key?

The remarkable progress achieved by LIBs over the last decades has been enabled not only by the development of high-performance electrode materials, but also by the optimization of the electrolyte. In commercial cells, the electrolyte is typically a liquid solution of a lithium salt dissolved in a mixture of aprotic organic solvents, such as carbonates, ethers, or esters, impregnated into a porous separator, offering excellent ionic conductivity at room temperature (RT). Although this configuration provides high ionic conductivity and good wetting of the electrodes, it also represents one of the most critical components from the perspectives of safety, durability, and cost. Indeed, after the cathode, the electrolyte is currently among the most expensive components of a LIB, and its composition strongly influences the electrochemical stability and long-term reliability of the cell. In addition, their high toxicity, flammability, and volatility pose safety hazards related to risk of leakage, high potential for gas production, in particular in combination with high energy density Li-metal negative electrodes [35,36]. These issues become even more critical in large-format batteries intended for electric vehicles and stationary storage, where the consequences of thermal failure can be tremendous.

The replacement of liquid electrolytes with solid-state electrolytes (SSEs) has emerged as one of the most promising strategies to address the safety and stability challenges of current lithium battery technology. In a solid-state battery, the electrolyte is no longer a flammable liquid but a solid ion-conducting medium, which can simultaneously act as ionic conductor and physical separator between the electrodes. This shift in electrolyte architecture is expected to provide several advantages, including enhanced safety, suppression of leakage, reduced

flammability, and the possibility of enabling lithium metal anodes, which are otherwise difficult to stabilize in conventional liquid systems..

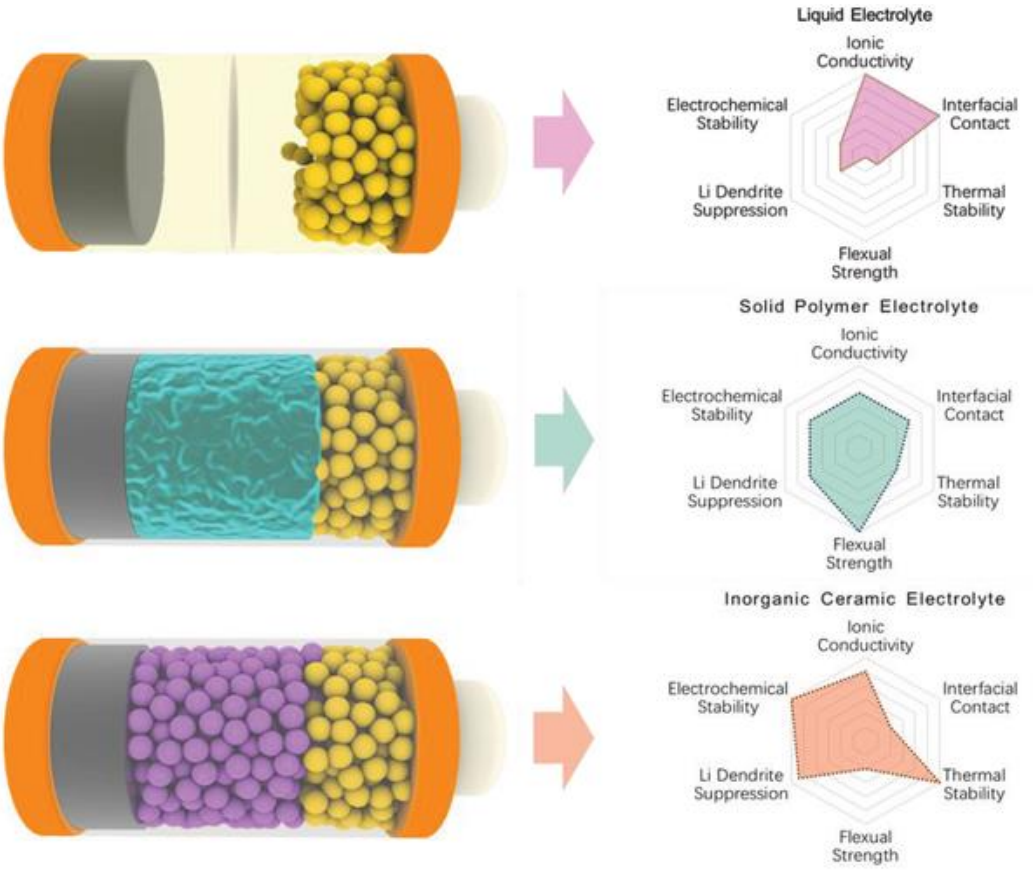

Figure 1.10 The performance comparisons of liquid electrolytes with SSEs, in particular solid polymer electrolytes and inorganic ceramic ones. Reproduced and readapted with permission from ref. [47]

Solid electrolytes can be broadly divided into two main classes: inorganic ceramic electrolytes (ICEs) and solid polymer electrolytes (SPEs) (**Figure 1.10**) [37,38].

In ICEs, lithium ions migrate by hopping between crystallographic sites within a rigid anionic or polyanionic framework. The accessible sites for lithium transport are typically vacancies or metastable interstitial positions, and the overall ionic conductivity depends on the energy required both to create these defects and to move lithium ions between them. In this case, the crystal structure plays a decisive role in defining the transport pathways and the associated activation barriers.

The most widely studied ceramic solid electrolytes include oxide-based and sulfide-based ion conductors. Oxide families comprise materials with perovskite,

NASICON, LISICON, and garnet-type structures, while sulfide-based conductors include thio-LISICON, LGPS, and argyrodite-type materials [39]. Many of the most conductive ceramic electrolytes are characterized by highly interconnected three-dimensional diffusion networks, often associated with body-centered cubic anionic frameworks, which facilitate rapid lithium transport. In these systems, the conductivity can be further tuned by elemental substitution, which affects the concentration of defects, the size and connectivity of migration channels, and the energy barrier for lithium hopping. These materials also present several important limitations. Their synthesis typically yields polycrystalline materials, in which individual crystallites are separated by grain boundaries. These interfaces can significantly hinder lithium transport, especially in oxide ceramics, where grain boundary resistance is often substantial. Furthermore, the dimensionality of the diffusion pathways is also crucial: three-dimensional conduction networks are generally preferred over one-dimensional pathways, which are more easily blocked by defects or impurities. Even when excellent conductivity is achieved in the bulk material, the practical implementation of ceramic electrolytes in practical battery cells remains challenging because of difficulties in electrode/electrolyte interfacial contact, mechanical brittleness, and the need for dense, defect-free processing.

A fundamentally different approach is represented by solid polymer electrolytes (SPEs), in which lithium-ion transport occurs through the dynamic coordination of cations with polar functional groups along the polymer backbone. In these materials, the dissolution of the lithium salt is driven by attractive ion–dipole interactions between the ions and the polymer host, which compete with the electrostatic attraction between cations and anions. The discovery of the first ion-conducting polymer systems in 1973 by Wright and co-workers marked the beginning of a major research field aimed at developing polymer electrolytes with ionic conductivity approaching that of liquid or aqueous systems [40].

The technological relevance of solid electrolytes is also reflected by their progressive translation from academic research to industrial development. A notable example is represented by the French company Blue Solutions, which has commercialized one of the first solid-state lithium batteries based on lithium metal polymer (LMP) technology. According to the company, these batteries employ a solid polymer electrolyte based on PEO and lithium salts, with no liquid or gel phase present, and use a lithium metal foil as the negative electrode together with a

$LiFePO_4$ positive electrode. This configuration is particularly attractive because it combines the intrinsic safety benefits of a solid electrolyte with the very high theoretical capacity of metallic lithium, thereby enabling a potentially higher energy density than conventional graphite-based lithium-ion cell. Indeed, Blue Solutions undertakes to create a sustainable value chain where over 80% of the cell metal components are re-used or recycled [41].

All-solid-state lithium metal batteries (SS-LMBs) are widely regarded as one of the most transformative directions in next-generation EES, with the potential to redefine the standards of safety, durability, and energy density. Their promise has sparked intense interest across both academia and industry, driving major efforts toward the design and optimization of solid-state electrolytes as the cornerstone of this technological breakthrough. Yet, despite their enormous potential, critical scientific and engineering challenges must still be overcome before SS-LMBs can rival, and ultimately surpass, conventional liquid-based battery systems.

References

[1] https://www.iea.org/reports/global-energy-review-2025/key-findings, (2026).

[2] H. Ritchie, M. Roser, https://ourworldindata.org/co2-emissions, (2026).

[3] H. Berg, Batteries for Electric Vehicles, Cambridge University Press, 2015.

[4] M. Winter, R.J. Brodd, What are batteries, fuel cells, and supercapacitors?, Chem. Rev. 104 (2004) 4245–4269. https://doi.org/10.1021/cr020730k.

[5] A.C. Lazanas, M.I. Prodromidis, Electrochemical Impedance Spectroscopy─A Tutorial, ACS Measurement Science Au 3 (2023) 162–193. https://doi.org/10.1021/acsmeasuresciau.2c00070.

[6] W. Hu, Y. Peng, Y. Wei, Y. Yang, Application of Electrochemical Impedance Spectroscopy to Degradation and Aging Research of Lithium-Ion Batteries, Journal of Physical Chemistry C 127 (2023) 4465–4495. https://doi.org/10.1021/acs.jpcc.3c00033.

[7] R. M. Dell, D. A. J. Rand, P. Connor, R. D. Bailey, Understanding Batteries, Royal Society of Chemistry, 2001.

[8] G. Cai, K.Y. Fung, K.M. Ng, K.L. Chu, K. Hui, L. Xue, Critical assessment of particle quality of commercial LiFePO4 cathode material using coin cells—a causal table for lithium-ion battery performance, Journal of Solid State Electrochemistry 20 (2016) 379–387. https://doi.org/10.1007/s10008-015-3032-3.

[9] J. Steiger, D. Kramer, R. Mönig, Microscopic observations of the formation, growth and shrinkage of lithium moss during electrodeposition and dissolution, Electrochim. Acta 136 (2014) 529–536. https://doi.org/10.1016/j.electacta.2014.05.120.

[10] J.-M. Tarascon, M. Armand, Issues and challenges facing rechargeable lithium batteries, Nature 414 (2001) 359–367. https://doi.org/https://doi.org/10.1038/35104644.

[11] M.S. Whittingham, Electrical energy storage and intercalation chemistry, Science (1979). 192 (1976) 1126–1127. https://doi.org/10.1126/science.192.4244.1126.

[12] B. Scrosati, J. Hassoun, Lithium batteries: current technologies and future trends, in: Woodhead Publishing Series in Energy, 2012.

[13] E. Peled, The Electrochemical Behavior of Alkali and Alkaline Earth Metals in Nonaqueous Battery Systems—The Solid Electrolyte Interphase Model, J. Electrochem. Soc. 126 (1979) 2047. https://doi.org/10.1149/1.2128859.

[14] K. Mizushima, P.C. Jones, P.J. Wiseman, J.B. Goodenough, LixCoO2 (0<x<-1): A new cathode material for batteries of high energy density, Mater. Res. Bull. 15 (1980) 783–789. https://doi.org/https://doi.org/10.1016/0025-5408(80)90012-4.

[15] P. Krivik, P. Baca, Electrochemical Energy Storage, Energy Storage - Technologies and Applications. InTech, 2013.

[16] A. Yoshino, The birth of the lithium-ion battery, Angew. Chem. Int. Ed. 51 (2012) 5798–5800. https://doi.org/10.1002/anie.201105006.

[17] H. Xia, Z. Luo, J. Xie, Nanostructured LiMn2O4 and their composites as high-performance cathodes for lithium-ion batteries, Progress in Natural Science: Materials International 22 (2012) 572–584. https://doi.org/10.1016/j.pnsc.2012.11.014.

[18] R.M. Salgado, F. Danzi, J.E. Oliveira, A. El-Azab, P.P. Camanho, M.H. Braga, The latest trends in electric vehicles batteries, Molecules 26 (2021). https://doi.org/10.3390/molecules26113188.

[19] S.D. Zhang, M.Y. Qi, S.J. Guo, Y.G. Sun, X.X. Tan, P.Z. Ma, J.Y. Li, R.Z. Yuan, A.M. Cao, L.J. Wan, Advancing to 4.6 V Review and Prospect in Developing High-Energy-Density LiCoO2 Cathode for Lithium-Ion Batteries, Small Methods 6 (2022). https://doi.org/10.1002/smtd.202200148.

[20] B.E. Murdock, K.E. Toghill, N. Tapia-Ruiz, A Perspective on the Sustainability of Cathode Materials used in Lithium-Ion Batteries, Adv. Energy Mater. 11 (2021). https://doi.org/10.1002/aenm.202102028.

[21] A.K. Padhi, J.B. Goodenough, Phospho-olivines as Positive-Electrode Materials for Rechargeable Lithium Batteries, J. Electrochem. Soc. 144 (1997) 1199–1194.

[22] H. Huang, T. Faulkner, J. Barker, M.Y. Saidi, Lithium metal phosphates, power and automotive applications, J. Power Sources 189 (2009) 748–751. https://doi.org/10.1016/j.jpowsour.2008.08.024.

[23] M. Armand, P. Axmann, D. Bresser, M. Copley, K. Edström, C. Ekberg, D. Guyomard, B. Lestriez, P. Novák, M. Petranikova, W. Porcher, S. Trabesinger, M. Wohlfahrt-Mehrens, H. Zhang, Lithium-ion batteries – Current state of the art and anticipated developments, J. Power Sources 479 (2020). https://doi.org/10.1016/j.jpowsour.2020.228708.

[24] S.P. Chen, D. Lv, J. Chen, Y.H. Zhang, F.N. Shi, Review on Defects and Modification Methods of LiFePO4Cathode Material for Lithium-Ion Batteries, Energy and Fuels 36 (2022) 1232–1251. https://doi.org/10.1021/acs.energyfuels.1c03757.

[25] J.W. Fergus, Recent developments in cathode materials for lithium ion batteries, J. Power Sources 195 (2010) 939–954. https://doi.org/10.1016/j.jpowsour.2009.08.089.

[26] E. Zhecheva, R. Stoyanova, Stabilization of the layered crystal structure of LiNi02 by Co-substitution, Solid State Ion. 66 (1993) 143–149. https://doi.org/https://doi.org/10.1016/0167-2738(93)90037-4.

[27] H.J. Noh, S. Youn, C.S. Yoon, Y.K. Sun, Comparison of the structural and electrochemical properties of layered Li[NixCoyMnz]O2 (x = 1/3, 0.5, 0.6, 0.7, 0.8 and 0.85) cathode material for lithium-ion batteries, J. Power Sources 233 (2013) 121–130. https://doi.org/10.1016/j.jpowsour.2013.01.063.

[28] L. Castro, R. Dedryvère, M. El Khalifi, P.E. Lippens, J. Bréger, C. Tessier, D. Gonbeau, The spin-polarized electronic structure of LiFePO4 and FePO 4 evidenced by in-lab XPS, Journal of Physical Chemistry C 114 (2010) 17995–18000. https://doi.org/10.1021/jp106631v.

[29] H. Banerjee, C.P. Grey, A.J. Morris, Stability and Redox Mechanisms of Ni-Rich NMC Cathodes: Insights from First-Principles Many-Body Calculations, Chemistry of Materials 36 (2024) 6575–6587. https://doi.org/10.1021/acs.chemmater.4c00928.

[30] T. Li, X.Z. Yuan, L. Zhang, D. Song, K. Shi, C. Bock, Degradation Mechanisms and Mitigation Strategies of Nickel-Rich NMC-Based Lithium-Ion Batteries, Electrochemical Energy Reviews 3 (2020) 43–80. https://doi.org/10.1007/s41918-019-00053-3.

[31] P.U. Nzereogu, A.D. Omah, F.I. Ezema, E.I. Iwuoha, A.C. Nwanya, Anode materials for lithium-ion batteries: A review, Applied Surface Science Advances 9 (2022). https://doi.org/10.1016/j.apsadv.2022.100233.

[32] B. Liu, J.G. Zhang, W. Xu, Advancing Lithium Metal Batteries, Joule 2 (2018) 833–845. https://doi.org/10.1016/j.joule.2018.03.008.

[33] D. Lin, Y. Liu, Y. Cui, Reviving the lithium metal anode for high-energy batteries, Nat. Nanotechnol. 12 (2017) 194–206. https://doi.org/10.1038/nnano.2017.16.

[34] W. Xu, J. Wang, F. Ding, X. Chen, E. Nasybulin, Y. Zhangad, J.-G. Zhang, Lithium metal anodes for rechargeable batteries, Energy Environ. Sci. 7 (2014) 513–537. https://doi.org/https://doi.org/10.1039/C3EE40795K.

[35] S. Chen, K. Wen, J. Fan, Y. Bando, D. Golberg, Progress and future prospects of high-voltage and high-safety electrolytes in advanced lithium batteries: From liquid to solid electrolytes, J. Mater. Chem. A Mater. 6 (2018) 11631–11663. https://doi.org/10.1039/c8ta03358g.

[36] J.B. Goodenough, Y. Kim, Challenges for rechargeable Li batteries, Chemistry of Materials 22 (2010) 587–603. https://doi.org/10.1021/cm901452z.

[37] Z. Zhang, Y. Shao, B. Lotsch, Y.S. Hu, H. Li, J. Janek, L.F. Nazar, C.W. Nan, J. Maier, M. Armand, L. Chen, New horizons for inorganic solid state ion conductors, Energy Environ. Sci. 11 (2018) 1945–1976. https://doi.org/10.1039/c8ee01053f.

[38] H. Li, Z. Xu, J. Yang, J. Wang, S.I. Hirano, Polymer electrolytes for rechargeable lithium metal batteries, Sustain. Energy Fuels 4 (2020) 5469–5487. https://doi.org/10.1039/d0se01065k.

[39] S. Li, S.Q. Zhang, L. Shen, Q. Liu, J. Bin Ma, W. Lv, Y.B. He, Q.H. Yang, Progress and Perspective of Ceramic/Polymer Composite Solid Electrolytes for Lithium Batteries, Advanced Science 7 (2020). https://doi.org/10.1002/advs.201903088.
[40] M. Armand, The history of polymer electrolytes, Solid State Ion. 69 (1994). https://doi.org/https://doi.org/10.1016/0167-2738(94)90419-7.
[41] https://www.blue-solutions.com/fr/produits/, (n.d.).

Chapter 2

Polymer-based Electrolytes for Lithium Metal Batteries

2.1 Polymer-based Electrolytes driving the liquid-to-solid transition

Considering the status of conventional LIBs, the non-solid component is the liquid electrolyte, being a combination of flammable solvents, such as ethers or carbonates, additives and alkali metal salt. The replacement of liquid electrolytes with solid state alternatives (ceramic, polymer or composite) is necessary for the development of fully solid-state batteries [1–3]. Solid polymer electrolytes, which are made of a polymeric matrix and lithium salts, have emerged as a promising candidate due to their intrinsic advantages, including improved safety, ease of synthesis, low cost, mechanical adaptability and suitability for manufacturing process at scale [4,5]. Thus, polymers such as polyethylene oxide (PEO) have gained significant attention as a polymer matrix since the 1970s, thanks to the oxygen in the polymeric chain, being able to coordinate Li^+, allowing the hopping mechanism to let the cation move through the system, while enhancing the solubility of the lithium salts [6]. Considering the main research topic of this PhD the development of advanced SPEs, following a brief discussion on key features for their electrochemical performance, a summary is given on the status of polymer matrixes commonly employed in LMBs. Finally, the main strategies to improve the properties of SPEs are presented. Main text and reported figures in this Chapter are reproduced and readapted from the review article submitted and under review at the time of writing of this manuscript: F. Gambino *et al.*, Shaping the “solid-state

lithium metal battery era" with polymer-based electrolytes, Electrochem. Energy Rev. (2026), under review.

2.2 Key features for electrochemical performance

Among numerous solid-state electrolyte systems that have been studied and proposed for applications in ASSBs, SPEs are the most promising candidates for enabling safe and practically up-scalable devices. Despite great potential offered by their mechanical properties and much easier handling compared to inorganic electrolytes, a viable industrial-scale production of SPEs still needs to face some key challenges (**Figure 2.1**). These include achieving ionic conductivity of 1 $mS \cdot cm^{-1}$ or above at ambient temperature, a wide electrochemical stability window (ESW), high lithium-ion transference number (t_{Li+}) approaching unity, and mechanical robustness sufficient to suppress lithium dendrite growth [7]. Each of these parameters not only dictates the electrolyte's fundamental transport properties but also governs the electrochemical efficiency, safety, and mechanical integrity of the resulting battery cell. However, enhancing one of these properties often compromises others, making the optimization process a difficult task.

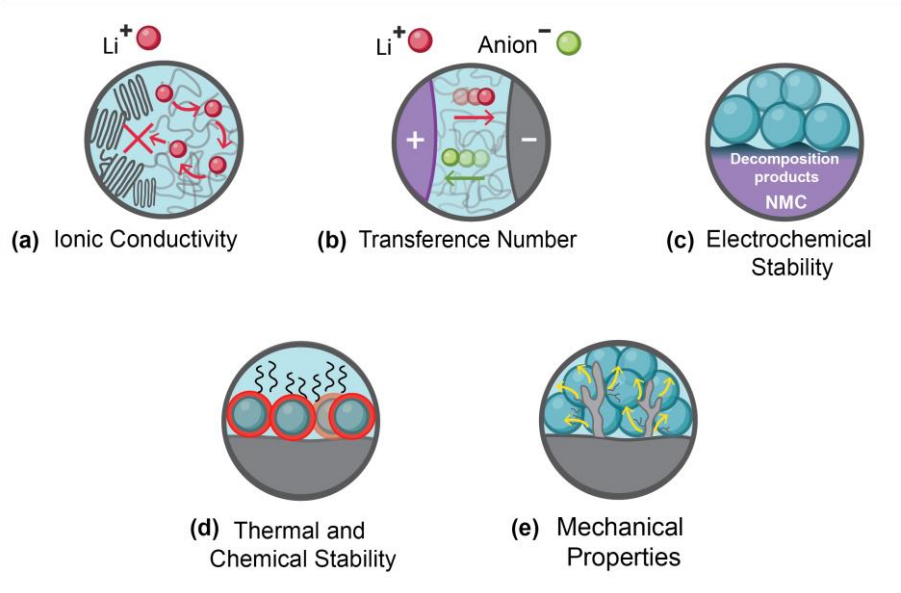

Figure 2.1 Schematic illustration of the main electrochemical parameters and physicochemical characteristics governing the performance of solid polymer-based electrolytes.

Ionic conductivity (σ) and Li^+ ion transference number (t_{Li+})

Ionic conductivity is amongst the most critical parameters in assessing the

practical operation of a given SPE. It determines the rate at which ions migrate through the polymer matrix, which in turn impacts the charge/discharge rate and the overall battery power capability. In polymer electrolytes, ions typically move through a segmental motion-assisted hopping mechanism, where lithium ions coordinate to and migrate along the polar sites of the polymer backbone within the amorphous phase [8]. For practical applications, especially at RT, a minimum conductivity threshold of 10^{-4} S·cm^{-1} is typically required. Common electrolytes display a high degree of crystallinity and the compact chain packing in semicrystalline domains typically prevents from efficiently transporting lithium ions, leading to low ionic conductivity at lower temperatures. Thus, the ionic conductivity of SPEs is generally lower than 10^{-4} S·cm^{-1} due to restricted polymer chain mobility, which consequently hinders ion transport through the bulk of the electrolyte. In some cases, poor lithium salt solubility and inefficient charge transfer at the electrode-electrolyte interface further exacerbate the problem [9]. Operating at temperatures above 40°C can partially alleviate these issues, but such harsh conditions could be detrimental to the overall cell functioning, as higher temperatures can accelerate decomposition, degrade mechanical properties, and pose limits for safe and practical battery cell operation [10].

While ionic conductivity is a measure of the electrolyte capability to conduct electricity *via* ion motions, the individual contribution of a particular ionic species to the total current can only be dissected by considering the ion transference number. The lithium-ion transference number (t_{Li+}) quantifies the fraction of the total ionic current carried by lithium ions. In conventional dual-ion SPEs, both Li^+ cations and counter-anions are mobile; however, in an ideal scenario, only Li^+ should participate in charge transport to maximise its efficiency. Indeed, low transference numbers result in concentration polarization and non-uniform Li deposition, ultimately compromising battery efficiency and safety [11]. Ideally, $t_{Li^+} = 1$, meaning the anions are fully immobilized, and only Li^+ ions contribute to charge transport, thereby minimizing concentration gradients and ensuring homogeneous lithium plating and stripping.

Two common methods are used to determine t_{Li^+}:

1. Evans, Vincent and Bruce proposed an electrochemical method that uses a symmetrical Li|SPE|Li cell under a small DC polarization (~10 mV). The transference number is then calculated by:

$$t_{Li^+} = \frac{I_s(\Delta V - I_0 R_0)}{I_0(\Delta V - I_s R_s)} \quad \text{[Eq 1]}$$

where I_0 and I_{ss} are initial and steady state current, R_0 and R_{ss} are initial and steady state resistance, and ΔV is the applied voltage.

2. The Pulsed Field Gradient NMR is a non-electrochemical method that determines the diffusion coefficients of Li^+ and anion (D_+ and D_-) with t_{Li^+} calculated as:

$$t_{Li^+} = \frac{D_+}{D_+ + D_-} \quad \text{[Eq 2]}$$

However, this method assumes negligible ion pairing or ion-ion correlations, an approximation that may not hold in concentrated or highly coordinated polymer electrolyte systems.

It is important to emphasize that different experimental approaches probe different definitions of t_{Li^+}. The electrochemical method provides an apparent steady-state value derived from macroscopic polarization behavior, whereas PFG-NMR yields a self-diffusion-based estimate that neglects ion-to-ion correlations. None of the two methods directly measures the true thermodynamic transference number, which formally depends on correlated ion motion and activity coefficients. Therefore, transference numbers obtained by different techniques are not strictly equivalent and should be compared with caution, particularly in concentrated or highly coordinated solid polymer electrolytes where ion correlations are significant.

Electrochemical stability window (ESW)

The electrochemical stability window (ESW) is the potential range over which the electrolyte is thermodynamically and kinetically stable against electrochemical oxidation and reduction, thus avoiding the onset of faradaic decomposition reactions, mainly occurring at the electrode/electrolyte interfaces. Extending as much as possible the ESW is particularly important to ensure stable and reliable operation when the electrolyte is coupled with high-voltage cathode materials. For example, poly(ethylene oxide) (PEO), one of the most studied SPE materials, has an upper voltage limit in the range of 3.8−4.0 V *vs.* Li^+/Li [12]. It poses concerns in coupling with high-energy 4V-class cathode materials, thus restricting its use to

materials such as lithium iron phosphate ($LiFePO_4$, or LFP), thus limiting the cell energy density due to its relatively low operating voltage. Improvements in oxidative (anodic) stability are essential for extending the use of polymer electrolytes to cathodes such as layered lithium transition metal oxides or spinels (*e.g.*, $LiNi_xMn_yCo_{1-x-y}O_2$ - NMC, or $LiNi_xMn_{2-x}O_4$ - LNMO), thereby allowing the development of high-energy density ASSLIMs.

Thermal and chemical stabilities

The structural integrity of SPEs must be preserved even under elevated temperatures to guarantee safe battery operation even in case of unexpected internal thermal events. The thermal stability of SPEs is typically evaluated using thermogravimetric analysis (TGA), with the desired performance exhibiting minimal mass loss or shrinkage below 150-200 °C.

The electrolyte must also show chemical stability, thus resisting degradation when in contact with reactive electrodes (e.g., Li metal and high-voltage cathodes) or other species that may be present within the cell environment. A poorly stable electrolyte can undergo decomposition processes and follow highly reactive pathways, which can eventually lead to gas evolution, thus posing safety risks while also reducing battery lifetime. Whether driven by electrochemical, chemical, thermal, or mechanical factors, degradation processes can jeopardize the long-term stability and the overall battery performance [13].

A comprehensive understanding of the underlying mechanisms at the molecular and interfacial levels is essential for outlining rational design strategies that can control and inhibit SPE degradation and improve their long-term chemical stability.

Mechanical integrity and interfacial compatibility

Mechanical integrity is critical to preventing lithium dendrite penetration and ensuring structural stability during cycling. Characterization is typically carried out using tensile testing and dynamic mechanical analysis (DMA), which provide key mechanical parameters such as Young's modulus, tensile strength, and elongation at break. High-modulus SPEs (>1 GPa) are often more effective in suppressing dendrites growth, however, excessive rigidity can compromise flexibility and interfacial contact with electrodes. Hence, achieving an optimal balance between toughness and flexibility is essential. Additionally, robust mechanical properties are

fundamental to ensuring adequate processability during battery manufacturing.

Interfacial compatibility refers to the ability of the SPE to form intimate and stable contact at the electrode surfaces. Insufficient adhesion leads to high interfacial resistance and can cause uneven lithium plating/stripping. This behaviour is typically assessed using electrochemical impedance spectroscopy (EIS) and morphological analysis (*e.g.*, SEM). Tailoring polymer chemistry or adding interface stabilizing or SEI forming additives is a common approach to enhance interfacial compatibility.

2.3 Common polymers for Li-metal batteries

In this section, the most common neat polymer systems used in SPEs are described, some of the sketched molecular structures of which are shown in **Figure 2.2**. Additionally, related main properties and electrochemical characteristics are summarised in **Table 2.1**.

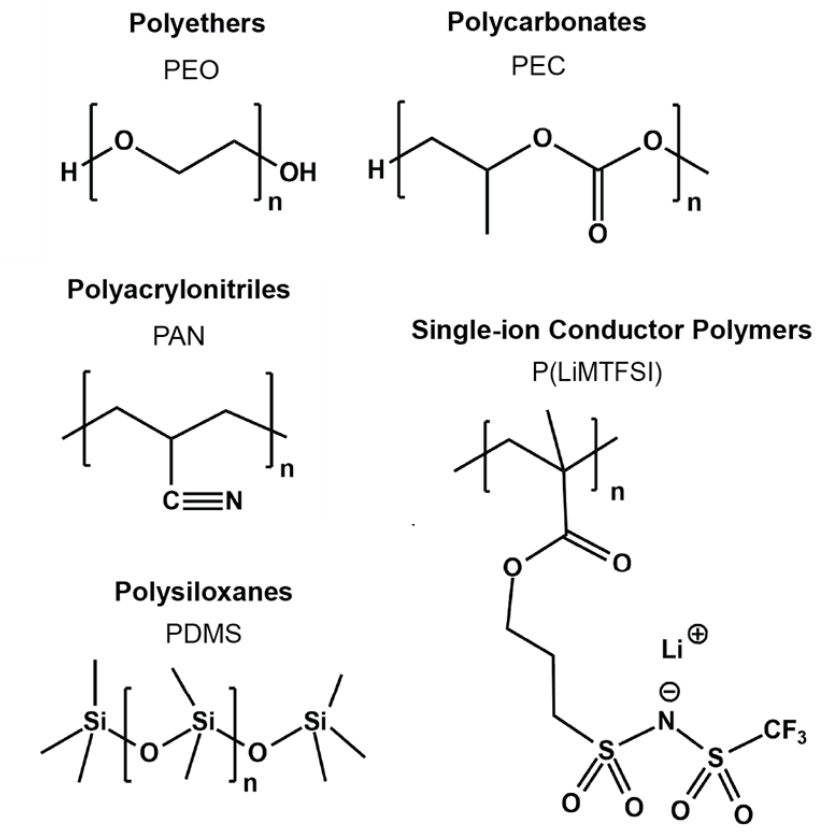

Figure 2.2 Sketched chemical structures of common polymer matrix employed in SPEs.

Poly(ethylene oxide) – PEO and polyethers. Among the various polymeric systems explored as SPEs, polyethers remain the most widely studied, with

poly(ethylene oxide) as the most representative example. Since the 1970s, PEO has attracted considerable attention due to its distinctive –CH_2–CH_2–O– (EO) backbone, the ether oxygens of which strongly coordinate Li^+ (and Na^+) and promote salt dissociation. The first evidence of significant ionic conductivity in PEO-salt complexes was reported by Fenton, Parker and Wright in 1973 and soon inspired Armand's vision of thin-film polymer batteries, which set ~10^{-5}/10^{-4} S cm^{-1} as the minimal practical ionic conductivity threshold. Despite its relatively low dielectric constant (ε ~ 5), PEO can dissolve a broad range of lithium salts [14,15]. The oxygen atoms contained in the backbone show high affinity for lithium ions, allowing a favorable coordination that promotes lithium salt solubility and enables cation transport *via* a hopping mechanism (see **Figure 2.3**) [6,16].

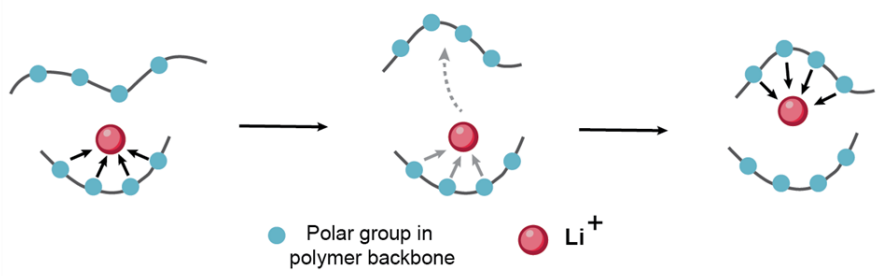

Figure 2.3 Schematic of the ion transport in the polymer amorphous phase via segmental motion-assisted hopping.

In this process, the free Li^+ ions released from the dissolved salt transiently coordinate with ether oxygen atoms along the polymer backbone. Ion transport occurs as Li^+ ions hop from one coordination site to another, both within and between polymer chains [8]. Although such strong Li-O complexation enhances salt solubility, it simultaneously restricts polymer segmental mobility, which is vital for effective ion transport. The result is a stable coordination structure that effectively hinders ion mobility, yielding low t_{Li+} (typically in the range of 0.1−0.2, *viz.* extremely far from unity for PEO-based SPEs). [17]. Furthermore, the high crystallinity of PEO at ambient conditions (T < 60°C) yields a rigid polymer structure with low chain mobility that negatively affects Li^+ hopping and mobility, representing a primary cause of its poor ionic conductivity at RT (~10^{-8} S cm^{-1} for PEO-LiTFSI, lithium bis(trifluoromethanesulfonyl)imide, far below the targeted ~10^{-4} S cm^{-1} threshold) [17–19]. Its semicrystalline morphology accounts for closely packed domains that obstruct access to efficient ion-transport pathways.

In addition, PEO-based SPEs typically exhibit narrow operating windows below 4 V *vs*. Li^+/Li, largely due to degradation of the ether backbone. These irreversible oxidative degradation processes at the cathode/electrolyte interface significantly reduce the cycle life of PEO-based SPEs paired to high-energy 4V-class cathodes, such as LCO or NMC [20]. Despite its historical relevance and favourable salt-solvation ability, pristine PEO suffers from several intrinsic limitations that hinder its widespread use as a standalone SPE material.

For these reasons, pristine PEO electrolytes have largely been replaced by more advanced formulations designed to disrupt the crystalline phase, weaken the strong Li-O coordination, and tune the PEO-anion interactions and reactivity. Such strategies collectively aim to enhance key performance metrics and bring PEO-based SPEs closer to practical viability in ASSB systems [21].

Polycarbonates. As reported in the literature, different families of polymers have been explored as alternatives to PEO as matrices for fabricating SPEs. Among these, aliphatic polycarbonates (pCs) are gaining popularity due to their amorphous nature and similar structure to organic-based solvents employed in traditional (*e.g.*, ethylene carbonate EC, propylene carbonate PC, and dimethyl carbonate DMC) [22–30]. pCs such as poly(ethylene carbonate) (pEC), poly(propylene carbonate) (pPC), poly(caprolactone-co-trimethylene carbonate) [p(CL-co-TMC)] have been exploited in lithium-based batteries with encouraging outcomes even at RT. In addition, polycarbonate-based electrolytes show good electrochemical stabilities, such as anodic oxidation threshold at voltages as high as 5 V and the ability to protect the cathode current collector [23]. Similarly to PEO, the high dielectric constants of pCs are beneficial to salt dissociation and solubility. In contrast to the strong Li-O coordination observed in polyethers, the weaker dipole moment of carbonate groups in pCs results in less pronounced Li^+ polymer interactions, thereby promoting higher ion transport [31]. Indeed, the t_{Li+} for pC-based systems is typically in the range of 0.4−0.6 with LiTFSI/LiFSI salt [32]. Ion transport properties in pCs are extremely sensitive to both the type and concentration of lithium salt employed [33]. Unlike polyethers, where high salt concentrations often lead to phase separation or increased crystallinity, tuning the salt content and anion identity in pC matrices can be advantageous. Some anions, such as TFSI, can exert plasticizing effect in the carbonate matrix, lowering the T_g and reducing the

crystalline fraction, thereby favoring ion mobility. For example, increasing the LiTFSI concentration to 80 wt.% (polymer-in-salt instead of salt-in-polymer) in pEC-based formulations has been shown to boost ionic conductivity to ~ 10^{-5} $S \cdot cm^{-1}$ at 30 °C [32]. While attractive for their high dielectric constant and ability to dissolve lithium salts, pure pCs face poor chemical stability against lithium metal, often leading to reduction at the interface and formation of unstable, resistive interphases. In addition, their limited mechanical strength can further promote dendrite penetration and poor cycling.

Polyacrylonitriles. Poly(acrylonitrile) - PAN is a well-established polymer host for SPEs in lithium metal batteries. Its promising application stems from the high polarity of its nitrile functional groups (−C≡N), which facilitate lithium salt dissociation and provide favorable ion transport properties. Compared to PEO, PAN demonstrates superior electrochemical stability and mechanical robustness, key attributes for maintaining structural integrity and suppressing lithium dendrite formation [34]. The thermal and oxidative stability allows PAN to operate across a wide ESW, with anodic breakdown voltage often above 4.5 V *vs.* Li^+/Li, which is advantageous for high-voltage cathode applications [35]. Despite their promising features, PAN-based SPEs have notable limitations that hinder their application. One of the major concerns is the chemical instability arising from spontaneous side reactions between the −C≡N group and Li metal [36]. These reactions lead to the formation of resistive interfacial layers on the Li surface, increasing resistance and limiting ion transport during cycling, ultimately compromising long-term performance. Nonetheless, the semicrystalline nature of PAN is the main factor responsible for its low ionic conductivity at room temperature (in the order of 10^{-6}–10^{-5} S cm^{-1}), as the restricted chain mobility hampers ion transport [37,38].

Polysiloxanes. Silicon-based polymers have attracted growing interest as alternatives to conventional SPEs, partly enabled by silicon ability to form carbon-analogous polymer architectures, while the Si–O framework provides distinct advantages in flexibility and interfacial/thermal stability. While silanes containing Si-Si bonds lack sufficient stability for electrochemical applications, siloxanes, which are characterized by robust Si-O bonds, form polymers with excellent chemical, thermal, and electrochemical stabilities [39,40]. First introduced in the

1980s as alternatives to polyethers, polysiloxanes (pS) were investigated for their high chain flexibility and low T_g, both of which promote ion mobility. Unfortunately, early studies showed that, unlike polyethers, the relatively non-polar siloxane backbone leads to weaker lithium-ion coordination and poor lithium salt solubility, thereby limiting charge carrier density and suppressing ionic conductivity [41,42]. To overcome these intrinsic limitations, various chemical functionalizations and composite design strategies have been developed to enhance ionic conductivity while preserving the excellent thermal and chemical stability of polysiloxanes.

One of the most compelling advantages of pS lies in the inherent safety and stability. The inorganic-like Si-O-Si backbone imparts non-flammability, non-toxicity, and excellent thermal resilience, enabling operation at elevated temperatures and improved tolerance to thermal runaway. In addition, pS-based SPEs exhibit good electrochemical stability against lithium metal and can operate at voltages up to 5 V *vs*. Li^+/Li, making them compatible with high-voltage cathodes [43]. However, their inherently soft and flexible nature, while advantageous for flexible or stretchable battery configurations, is typically insufficient to suppress lithium dendrite growth in LMBs.

Single-ion conducting polymers. Conventional SPEs, formed by dissolving lithium salts with small and mobile anions into a polymer host, operate as dual-ion conductors. In such systems, both lithium cations and counter-anions migrate in opposite directions under the effect of an electric field. This bidirectional ion movement leads to salt concentration gradients, leading to concentration polarization, diminished electrochemical performance, and ultimately premature cell failure [44]. For most commonly used polymer electrolytes, t_{Li+} remains below 0.3, which exacerbates these effects and contributes to uneven lithium deposition during cycling. According to the theoretical model developed by Newman, the cation transference number was identified as a critical parameter for suppressing ion concentration gradient and mitigating dendrite growth [45]. An effective strategy to improve t_{Li+} is to immobilize the anions by directly binding them to the polymer backbone [46]. This immobilization allows the system to behave as a lithium single-ion conductor (SIC), with t_{Li+} approaching unity, thereby minimizing concentration polarization, dendrite formation, and promoting uniform lithium deposition during cycling [47].

Synthetic approaches to single-ion conducting polymer (SICP) electrolytes can be broadly categorized into three methodologies, which include i) covalent attachment of anions to organic polymer backbones, ii) grafting anionic units onto inorganic backbones to form organic-inorganic hybrids, and iii) the use of anion-trapping agents to effectively immobilize anions within dual-ion conducting systems [53,72]. Incorporating TFSI or fluorosulfonylimide (FSI)-type tethered anions led to a 100- to 1000-fold increase in the ionic conductivity of SICPs compared to those with sulfonate or borate groups. Even though these anions weakly interact with lithium cations, the homopolymers still exhibit relatively high T_g, typically above 90 °C.

To address these limitations, researchers have pursued two main design strategies, which include copolymerizing the ionic monomers with neutral monomers bearing long, flexible oxyethylene chains, such as poly(ethylene glycol) methyl ether methacrylate (PEGM) [50], or synthesizing triblock copolymers, in which ionic segments were grown from central polyethylene oxide blocks of tunable molecular weights [51].

Table 2.1 Most common polymer hosts for SPEs with their main electrical/electrochemical features (ionic conductivity, lithium transference number, and ESW).

SPE	σ (S·cm^{-1})	t_{Li+}	ESW (V *vs.* Li^+/Li)	Advantages/ Disadvantages	Ref.
Poly(ethers)	10^{-7}–10^{-6} (25°C)	0.1 − 0.3	~ 4.0 V	Strong electron donating ability/Semi-crystalline, low ionic conductivity and t_{Li+}	[52,53]
Poly(carbonates)	10^{-9}–10^{-6} (30°C)	~ 0.5	~ 4.5 V	High dieletric constant and lower Li^+–polymer binding/Susceptible to thermal and chemical degradation (depolymerization)	[54]
Poly(acrylonitriles)	10^{-6}–10^{-5} (25°C)	0.2 − 0.3	> 4.5 V	Excellent oxidative stability, good ionic conductivity/C≡N group can react with lithium metal	[35]
SICPs	10^{-8}–10^{-6} (60°C)	~ 0.9	~4 V	High t_{Li+} and reduced dendrite formation/Low ionic conductivity and complex synthesis	[51,55]

Poly(siloxanes)	10^{-5} (25°C)	0.3 − 0.6	~ 5 V	High chain flexibility and good thermal and chemical stability/Low mechanical strength	[56]

2.4 Incorporating physical modifications to enhance ion transport and electrochemical stability

This section highlights physico-chemical modification strategies used to overcome the intrinsic limitations of neat polymer electrolytes in ASSLMBs (**Figure 2.4**).

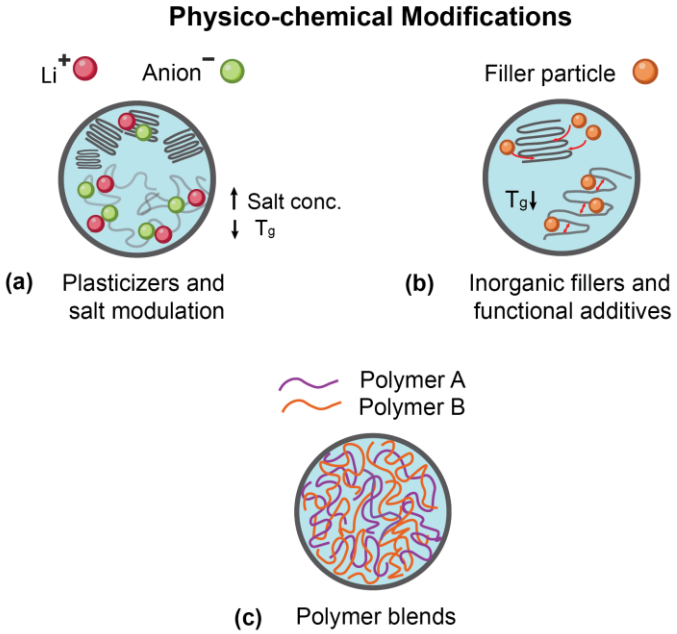

Figure 2.4 Representation of common physico-chemical modification strategies: (a) plasticizers and salt modulation; (b) inorganic and functional fillers; (c) polymer blends.

2.4.1 Salts modulation and plasticizers

To date, PEO is still regarded as the most attractive polymer hosts for solid polymer electrolytes, owing to its excellent ability to solvate lithium salts. Accordingly, a wide variety of PEO–LiX systems have been investigated (**Figure 2.5**), beginning with early studies employing salts such as $LiClO_4$. In general, a clear relationship has been established between the use of bulky, weakly

coordinating anions and enhanced ionic conductivity. Compared with conventionally used salts, such as $LiBF_4$ and $LiPF_6$, more recent generations of lithium salts containing more delocalized and bulkier anions such as trifluoromethanesulfonate (TFS^-), bis(trifluoromethanesulfonyl)imide ($TFSI^-$), bis(fluorosulfonyl)imide (FSI^-), as well as more recently developed fluoroborate-based anions [18], have demonstrated improved solubility, wider ESWs, and higher ionic conductivity.

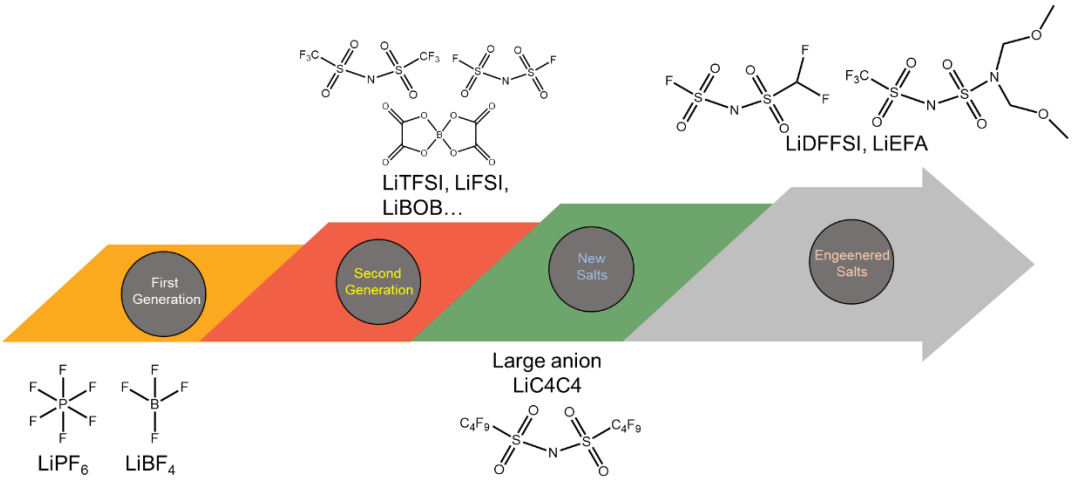

Figure 2.5 Evolution of lithium salts from the early LIB stages to the most recent literature reports.

More recently, a new generation of lithium salts has been developed in which the terminal $–CF_3$ group of conventional fluorinated anions is replaced by a longer perfluoroalkyl chain. Armand *et al.* proposed the utilization of a Teflon-like anion, bis(n-nonafluorobutanesulfonyl)imide ($[(n–C_4F_9SO_2)_2N]^-$ (LiC_4C_4) [57]. Mechanistic investigations, supported by chemical simulations and X-ray photoelectron spectroscopy (XPS) analyses, have suggested that the reductive decomposition of the corresponding NFSI-based anions leads to the formation of fluorinated oligomeric/polymeric species, together with LiF, within the SEI. In particular, the generation of fluorinated fragments of the type $(–CF_x–CF_x–)_n$, combined with LiF-rich domains, is believed to significantly improve the mechanical and chemical stability of the resulting interphase [58]. The development of lithium salts for polymer electrolytes has progressively evolved from conventional conducting salts toward engineered salts, in which the anion is molecularly designed not only to dissociate efficiently, but also to control ion transport and polymer–salt interactions. In this context, lithium salt with ether-

functionalized anion (LiEFA) is a representative example of this new design strategy. Owing to the charge-delocalized sulfonimide center and the presence of an electron-withdrawing $–CF_3$ group, the EFA anion behaves as a weakly coordinating species, favoring Li^+ dissociation. At the same time, its ethylene oxide (EO) unit promotes structural compatibility with PEO, enabling specific polymer–anion interactions and inducing nanoscale self-agglomeration of the anions. This combination suppresses anion mobility while maintaining efficient lithium transport. As a result, LiEFA/PEO electrolytes exhibit highly selective Li^+ ion mobility, with a Li-ion conductivity of 1.2×10^{-4} S cm^{-1} and an anionic conductivity significantly lower than that of analogous LiTFSI-based systems [58].

In parallel with salts modification, plasticization is widely used strategy to improve the ionic conductivity of SPEs. By increasing the amorphous phase content, plasticizers can elevate polymer chain mobility and facilitate the dissociation of ion pairs, leading to a higher population of free Li^+ ions available for conduction [59]. Nitrile-based additives have attracted significant attention in the development of advanced lithium battery electrolytes due to their high thermal and electrochemical stabilities and demonstrated enhancement in Li^+ conduction. Succinonitrile (SN), a widely employed plasticizer, is an organic, non-ionic compound that exhibits a plastic crystal phase within the temperature range of −40 to 60 °C. The presence of lattice defects in SN due to trans-gauche isomerism lowers the activation energy and enhances ionic conduction in the electrolyte. The high polarity of SN (dielectric constant ~ 56) enables it to dissolve various types of salts. SN is also prone to sublimation and may exhibit poor thermal stability, this issue being largely restrained when it is incorporated into a trap polymer matrix able to prevent unwanted sublimation [60]. An appropriate compromise between high ionic conductivity and sufficient mechanical stability can be achieved by optimizing the polymer/SN ratio [61].

Beyond solid plasticizers, room temperature ionic liquids (RTILs) have also become highly popular in the battery field for their ability to modulate the crystallinity of polymer-based electrolytes [62,63]. Unlike molecular solvents, which have high ionic conductivity but are volatile and highly flammable and therefore inherently unsafe, RTILs with enhanced thermal stability have been shown to dissolve lithium salts and improve the ionic conductivity of PEO-LiX. The selection of an adequate RTIL is crucial to achieve optimal compatibility with

the lithium metal anode. For example, RTILs based on the 1-ethyl-3-methylimidazolium (EMI) cation have many desirable properties, which includelow viscosity, wide ESW, and high ionic conductivity, but also poor stability toward Li metal. Other systems consisting of N-alkyl-N-methylpyrrolidinium cations and bis(trifluoromethanesulfonyl) imide anions ($Pyr_{NN}TFSI$) have high ionic conductivity and wide ESW, and can be combined with PEO, resulting in freestanding, easy-to-handle membranes with high conductivity at moderate temperatures [64].

2.4.2 Polymer blends

Polymer blending is considered an effective strategy to optimize electrochemical features of SPEs. Different types of polymers can be selected according to different type of applications [65]. Combining semicrystalline polymers like PEO with more amorphous ones can disrupt crystalline domains, increase the amorphous content, and enhance Li^+ mobility. Polycarbonates are often incorporated into PEO-based physical blends to achieve dual benefits: improving oxidative stability and lowering the T_g. In one representative formulation, PEO was blended with 50 wt.% pPC and LiTFSI ([EO]:[Li] = 18:1) [66]. The blending of PEO with amorphous pPC effectively increases the proportion of amorphous regions and inhibits the crystallization of PEO (**Figure 2.6a**). The DSC curve and related data indicate that as the content of pPC increases, the T_g and χc of the electrolyte start to decrease, reaching a minimum at the content of 50% PPC, lower T_g and χc are generally advantageous to the polymer electrolyte for batteries (**Figure 2.6b**). In particular, the crystallinity progressively declined from 48.07 to 22.10 % as pPC content exceeded 50 wt.%, while T_g dropped from −35. to −41.3 °C, enhancing segmental motion and ionic transport. Since the decrease in crystallinity promotes the migration of Li^+ in the amorphous region, the ionic conductivity is effectively improved. The resulting electrolyte showed a doubled ionic conductivity compared to neat PEO, reaching 2.04×10^{-5} and 2.82×10^{-4} $S \cdot cm^{-1}$ at 25 and 60 °C, respectively. Moreover, the ESW increased from 4.25 V (neat PEO) to 4.9 V *vs.* Li^+/Li, and Li plating/stripping tests showed lower interfacial resistance.

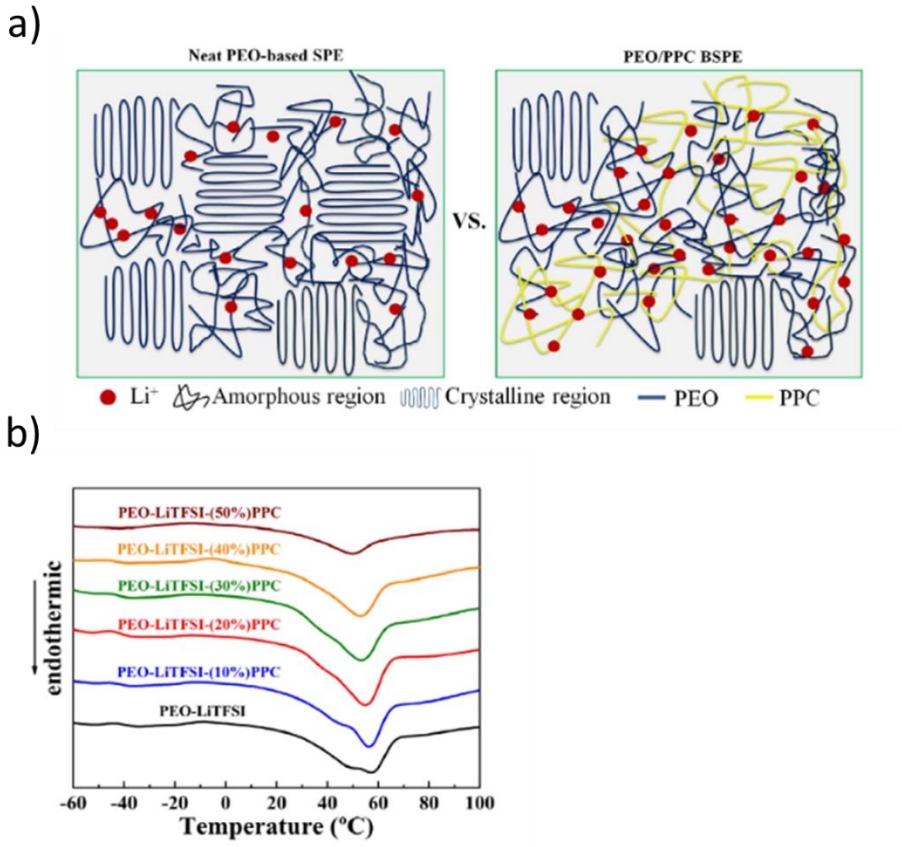

Figure 2.6 Schematic illustrations of neat PEO-based SPE and PEO/PPC blended SPE (a). DSC profiles of the PEO-PPC blend (b). Reproduced and readapted with permission from ref. [66].

Similarly, Li *et al.* prepared a new type of blended polymer by mixing microcrystalline PVDF-HFP with PEO using a solvent casting method [67]. Thermal analysis of the SPE revealed that the crystallinity of PEO-PVDF-HFP greatly reduced compared to neat-PEO. The addition of PVDF-HFP breaks up the chain structure of the PEO crystalline region and increases the amount of amorphous phase, thus promoting the Li^+ migration and improving the conductivity of the electrolyte.

2.4.3 Inorganic additives

Inorganic fillers are widely used to boost the performance of SPEs by increasing ionic conductivity, enhancing mechanical robustness, and improving electrochemical stability. Typical ceramic oxides include TiO_2, Al_2O_3, SiO_2, and ZrO_2, which can suppress polymer crystallinity, reinforce the electrolyte matrix, and in some formulations facilitate Li^+ transport while broadening the ESW. Two primary mechanisms have been identified as key for conductivity enhancement: (i) salt dissociation *via* Lewis acid-base interactions established between the fillers and

the electrolyte anions, thus promoting salt dissociation and increasing free Li^+ concentration; (ii) disruption of polymer crystallinity as a result of the local reorganization induced by the fillers, thereby favoring chain segmental motion and facilitating ion transport [68]. The pioneering work of Weston and Steele in 1982 demonstrated the potential of inorganic fillers by incorporating α-Al_2O_3 into a PEO matrix, resulting in a significant increase in ionic conductivity [69]. Since then, numerous fillers, such as SiO_2 [70], Al_2O_3 [71], CeO_2 [72], ZnO [73], ZrO_2 [74] as well as novel advanced materials, like covalent organic frameworks (COFs) [75] and metal-organic frameworks (MOFs) [76], have been explored in recent years. Tambelli *et al.* further confirmed the benefits of using Al_2O_3 as a filler, observing that incorporating alumina effectively reduced the T_g and crystallinity of PEO [77]. Song *et al.* designed a PEO-based composite polymer electrolyte (CPE) incorporating SN and two-dimensional γ-Al_2O_3 nanosheets to overcome the low ionic conductivity and limited Li^+ mobility typical of conventional PEO electrolytes [78]. The γ-Al_2O_3 nanosheets enhanced lithium salt dissociation and promoted Li^+ transport through Lewis acid-base interactions, resulting in a high ionic conductivity of 2.02×10^{-4} S cm^{-4} at 25 °C. A Li-metal cell using a LFP cathode exhibited remarkable electrochemical performance at 60 °C.

2.5 Restructuring the polymer chemical frameworks towards tailored electrochemical features

Considerable efforts have been directed toward molecular engineering of polymer electrolytes to overcome the intrinsic limitations of conventional SPEs. By redesigning polymer backbones and side chains, key parameters can be simultaneously tuned, which include segmental dynamics, Li^+ coordination and transport pathways, mechanical integrity, and interfacial stability against high-energy 4V-class cathodes. This section surveys the main chemical modification strategies, illustrated in **Figure 2.7**, including copolymerization, grafting, crosslinking, and the introduction of ion-conducting or ion-coordinating functionalities. Such structure-driven design enables SPEs with deliberately tailored electrochemical responses, supporting safer, higher-performance, and durable ASSLMBs.

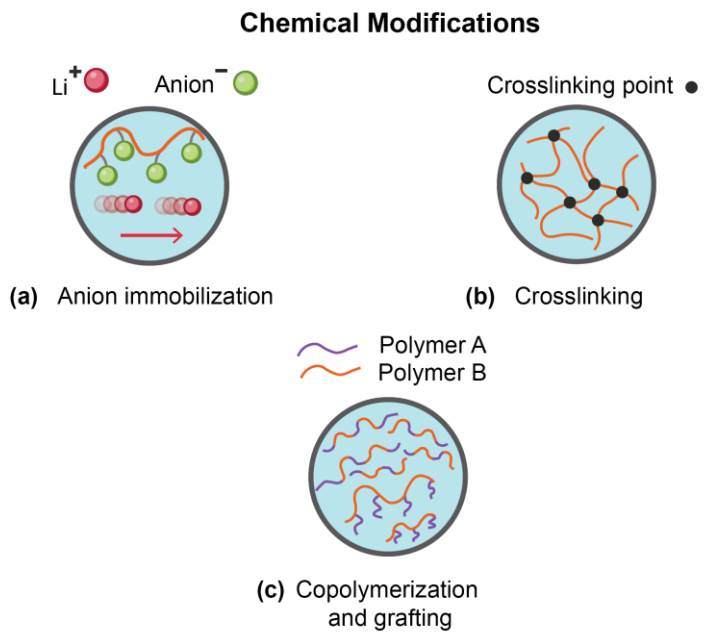

Figure 2.7 Schematic representation of possible chemical modification strategies reviewed in this work, including: (a) anion immobilization, (b) crosslinking, (c) copolymerization or grafting.

2.5.1 Chemical immobilization of anion

Despite the advantages of the various SPE systems discussed in the previous section, conventional salt-in-polymer electrolytes remain affected by several important limitations. These materials are classified as dual-ion conductors, meaning that both cations and anions are mobile within the polymer host matrix (**Figure 2.8a**). However, lithium ions typically exhibit lower mobility than their corresponding anions. This imbalance in ion transport can lead to the development of concentration gradients across the electrolyte during repeated charge and discharge cycles. Single Ion Conducting Polymers (SICPs) have emerged as one of the most promising strategies for improving the effective current delivered by the cell while mitigating issues associated with anion accumulation at the electrode/electrolyte interface [51]. In this class of materials, the anionic moieties are chemically immobilized within the polymer framework, whereas only the lithium cations remain mobile. As a result, ion transport is predominantly carried by Li^+, which can significantly reduce concentration polarization and enhance electrochemical performance. Incorporating lithium ions directly into the polymer structure, rather than relying on lithium salt dissolution, results in a high lithium transference number (t_{Li+} ~0.8). Specifically, McCloskey and coworkers found that a modest increase in t_{Li+} is beneficial for achieving a higher state of charge in

batteries, even if overall conductivity is reduced [79]. Current strategies for synthesizing SICP electrolytes mainly involve two approaches: covalently binding the anions to the polymer backbone and covalently attaching anionic groups to inorganic frameworks to form organic-inorganic hybrid structures [80] (**Figure 2.8b**).

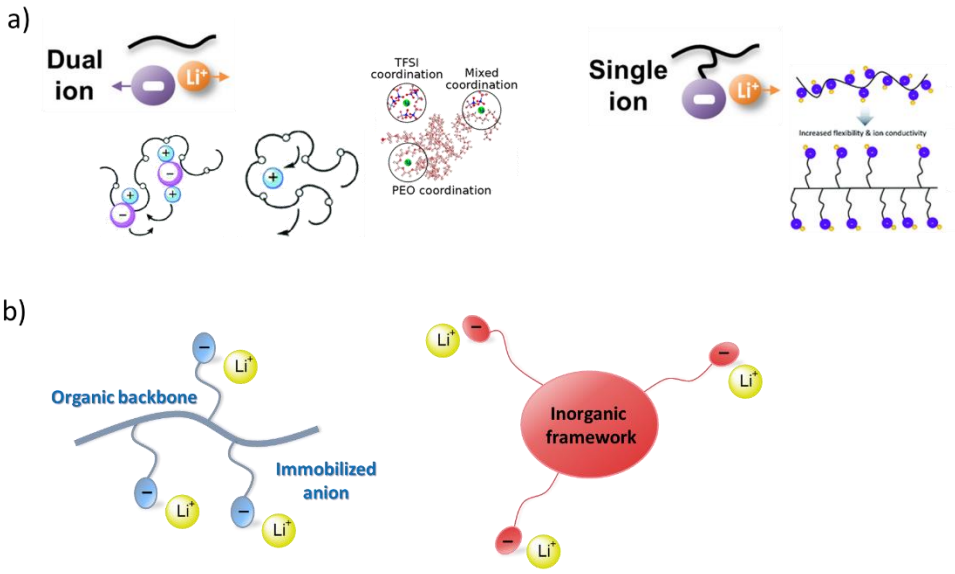

Figure 2.8 Illustration of dual-ion vs. single-ion conductor (a). Method to achieve single Li^+ ion transport features: polyanions and organic/inorganic hybrid (b).

Binding the anion to a polymer backbone. Two primary strategies are used to synthesize SICP electrolytes with polymer backbones, *viz.* i) polymerizing monomers that contain lithium salts, and ii) chemically modifying pre-existing polymers. For polymerizing lithium salt monomers, the monomer must contain a functional group capable of undergoing polymerization, typically an acrylate, methacrylate, or styrene group. The polymerization is conceptually simple: it starts with the addition of an alkali metal salt to a monomer containing polymerizable groups; then, cation exchange is performed, replacing the alkali ions with Li^+ ions to produce a lithium salt monomer; eventually, a polymerization reaction is conducted to synthesize the SICP electrolytes. A recently synthesized SICP electrolyte, *i.e.*, lithium poly[(cyano)(4-styrenesulfonyl)imide] (LiPCSI), exhibits an extremely high t_{Li+} of 0.84 as well as an oxidation potential exceeding 5 V *vs.* Li^+/Li due to the presence of a highly delocalized anion moiety and oxidation-resistant cyano groups [81].

However, the SICP electrolytes obtained from these strategies often exhibit regions where Li^+ cannot readily move, leading to very low conductivity. The

partial incompatibility between ionic and neutral blocks can result in a microphase-separated morphology, causing the formation of nanoscale domains and concentrating the ionic species inside the ion-conducting channels [82]. To overcome this issue, other polymers with Lewis base groups (such as EO groups) are co-polymerized or blended to help dissolving and transporting Li^+.

SICPEs with inorganic backbone. An organic-inorganic SICP electrolyte is realized when inorganic moieties constitute the main backbone (*e.g.*, siloxane-, phosphazene-, or borate/oxide-rich frameworks) and are covalently linked to organic segments. Unlike conventional "salt-in-polymer" SPE, these materials enable decoupling of mechanical integrity from ion transport through rational backbone design, side-chain engineering, and controlled crosslinking. In parallel, nano-sized inorganic building blocks and hybrid domains (including *in situ*-formed clusters or grafted nanoparticles) can be integrated to further enhance salt dissociation, suppress crystallinity, and reinforce the electrolyte without sacrificing processability. Overall, inorganic-backbone SICPs offer a versatile platform to combine close-to-unity t_{Li^+}, improved thermal/mechanical robustness, and tuneable interfacial chemistry for ASSLMBs.

2.5.2 Crosslinking methodologies

Polymer crosslinking is commonly implemented either by thermal activation of initiators or by UV-induced photopolymerization, both of which generate reactive species (typically radicals) that form covalent bonds (bridges) between polymer chains, typically yielding a robust three-dimensional (3D) network. Beyond improving mechanical integrity, crosslinking can suppress chain packing and crystallization, increasing the amorphous fraction, and, consequently, facilitating segmental dynamics and ion transport. Importantly, the crosslinking density provides a practical handle to balance ionic conductivity against modulus, dimensional stability, and tensile strength, which are critical under stack pressure and during long-term cycling. Crosslinking can also mitigate leakage of liquid components (if any), reduce interfacial contact loss, and in some formulations improve resistance to dendrite penetration by increasing shear modulus and maintaining uniform current distribution. Overall, crosslinked SPEs offer a versatile route to simultaneously tailor transport, mechanics, and interfacial robustness for solid-state LMBs [83,84].

Polyethers can be converted into 3D networks under UV irradiation using light-sensitive type II photoinitiators, such as benzophenone, which generate radicals that promote interchain coupling, without the need for additional crosslinking agents. Under UV irradiation, the photoinitiator induces chain fragmentation and subsequent crosslinking through hydrogen abstraction from the PEO backbone (**Figure 2.9**) [85].

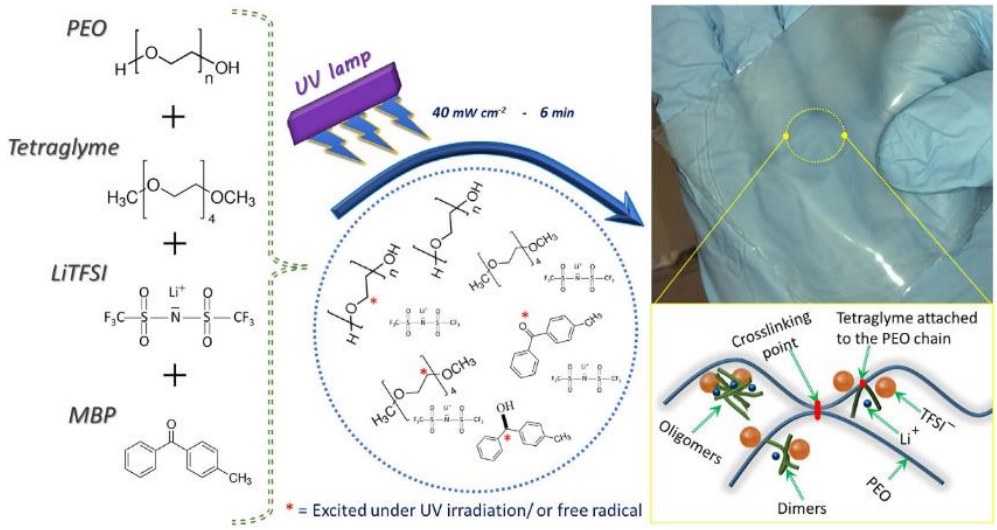

Figure 2.9 Sketched representation of crosslinked SPE preparation along with used materials, and plausible illustration of interconnected PEO chains. Reproduced and readapted with permission from ref. [85].

Fu and co-workers developed a dual-salt PEO-based polymer electrolyte with a crosslinked polymer network formed through *in-situ* polymerization, employing tetraethylene glycol dimethyl ether (TEGDME) in a 1.5:1 ratio with respect to PEO [86]. Crosslinking significantly enhances the amorphous regions of PEO, reducing crystallinity to 6.29 % and resulting in a SPE providing high ionic conductivity (5.7×10^{-4} S·cm^{-1} at 30 °C) and compatibility with the lithium metal electrode.

2.5.3 Copolymerization and grafting techniques

Copolymerization offers another strategy for tailoring the properties of polymer electrolytes. The polymerization of different monomers to produce polymers, can break the ordered structure of the homopolymer and reduce the crystallinity, thus increasing the ionic conductivity. Meabe *et al.* explored the polycondensation of PEO and pCs by varying the EO units from 2 to 45 between carbonate groups [87]. Solvent casting from acetonitrile yielded amorphous or semicrystalline polymer electrolytes, depending on EO content. Polymer with shorter EO chains (x = 2–6)

remained amorphous, while others displayed melting temperature ranging from 29 to 52 °C. The sample PEO_{34}-pC exhibited the highest ionic conductivity 4×10^{-5} $S \cdot cm^{-1}$ at 25 °C with 30 wt.% LiTFSI (corresponding to the lowest T_g of –48 °C), while PEO_{34} without copolymerization showed a conductivity of 10^{-5} $S \cdot cm^{-1}$. The salt concentration significantly impacted the performance: lower levels restricted ion mobility due to crystallinity, while higher concentrations increased T_g and hindered ion transport. A random P(EC–EO) copolymer containing 5–120 mol.% LiFSI was synthesized: a single T_g peak in DSC and absence of melting peaks confirmed its amorphous phase. The best formulation (53% EO, 120 mol.% LiFSI) was coupled to LFP delivering good performances at 40 °C [88].

References

[1] A. Manthiram, X. Yu, S. Wang, Lithium battery chemistries enabled by solid-state electrolytes, Nat. Rev. Mater. 2 (2017) 16103. https://doi.org/10.1038/natrevmats.2016.103.

[2] Q. Zhao, S. Stalin, C.Z. Zhao, L.A. Archer, Designing solid-state electrolytes for safe, energy-dense batteries, Nat. Rev. Mater. 5 (2020) 229–252. https://doi.org/10.1038/s41578-019-0165-5.

[3] L. Fan, S. Wei, S. Li, Q. Li, Y. Lu, Recent Progress of the Solid-State Electrolytes for High-Energy Metal-Based Batteries, Adv. Energy Mater. 8 (2018) 1702657. https://doi.org/10.1002/aenm.201702657.

[4] Y. An, X. Han, Y. Liu, A. Azhar, J. Na, A.K. Nanjundan, S. Wang, J. Yu, Y. Yamauchi, Progress in Solid Polymer Electrolytes for Lithium-Ion Batteries and Beyond, Small 18 (2022) 2103617. https://doi.org/10.1002/smll.202103617.

[5] L. Long, S. Wang, M. Xiao, Y. Meng, Polymer electrolytes for lithium polymer batteries, J. Mater. Chem. A Mater. 4 (2016) 10038–10069. https://doi.org/10.1039/c6ta02621d.

[6] D.E. Fenton, M. Parker, P. V Wright, Complexes of alkali metal ions with poly(ethylene oxide), Polymer (Guildf). 14 (1973) 589. https://doi.org/https://doi.org/10.1016/0032-3861(73)90146-8.

[7] W. Zhao, J. Yi, P. He, H. Zhou, Solid-State Electrolytes for Lithium-Ion Batteries: Fundamentals, Challenges and Perspectives, Electrochemical Energy Reviews 2 (2019) 574–605. https://doi.org/10.1007/s41918-019-00048-0.

[8] Y. An, X. Han, Y. Liu, A. Azhar, J. Na, A.K. Nanjundan, S. Wang, J. Yu, Y. Yamauchi, Progress in Solid Polymer Electrolytes for Lithium-Ion Batteries and Beyond, Small 18 (2022). https://doi.org/10.1002/smll.202103617.

[9] Z. Li, R. Yu, S. Weng, Q. Zhang, X. Wang, X. Guo, Tailoring polymer electrolyte ionic conductivity for production of low- temperature operating quasi-all-solid-state lithium metal batteries, Nat. Commun. 14 (2023). https://doi.org/10.1038/s41467-023-35857-x.

[10] H. Yang, N. Wu, Ionic conductivity and ion transport mechanisms of solid-state lithium-ion battery electrolytes: A review, Energy Sci. Eng. 10 (2022) 1643–1671. https://doi.org/10.1002/ese3.1163.

[11] M. Jia, M. Khurram Tufail, X. Guo, Insight into the Key Factors in High Li+ Transference Number Composite Electrolytes for Solid Lithium Batteries, ChemSusChem 16 (2023). https://doi.org/10.1002/cssc.202201801.

[12] L. Herbers, J. Minář, S. Stuckenberg, V. Küpers, D. Berghus, S. Nowak, M. Winter, P. Bieker, The Influence of Polyethylene Oxide Degradation in Polymer-Based Electrolytes for NMC and Lithium Metal Batteries, Advanced Energy and Sustainability Research 4 (2023). https://doi.org/10.1002/aesr.202300153.

[13] S. Choudhury, Z. Tu, A. Nijamudheen, M.J. Zachman, S. Stalin, Y. Deng, Q. Zhao, D. Vu, L.F. Kourkoutis, J.L. Mendoza-Cortes, L.A. Archer, Stabilizing polymer electrolytes in high-voltage lithium batteries, Nat. Commun. 10 (2019). https://doi.org/10.1038/s41467-019-11015-0.

[14] J.R. Nair, L. Imholt, G. Brunklaus, M. Winter, Lithium Metal Polymer Electrolyte Batteries: Opportunities and Challenges You may also like Fast Charging of Energy-Dense Lithium Metal Batteries in Localized Ether-Based Highly Concentrated Electrolytes, Electrochem. Soc. Interface 28 (2019). https://doi.org/10.1149/2.F05192if.

[15] X. Su, X.P. Xu, Z.Q. Ji, J. Wu, F. Ma, L.Z. Fan, Polyethylene Oxide-Based Composite Solid Electrolytes for Lithium Batteries: Current Progress, Low-Temperature and High-Voltage Limitations, and Prospects, Electrochemical Energy Reviews 7 (2024). https://doi.org/10.1007/s41918-023-00204-7.

[16] M. Armand, Polymer solid electrolytes - an overview, Solid State Ion. 9–10 (1983) 745–754. https://doi.org/10.1016/0167-2738(83)90083-8.

[17] J. Mindemark, M.J. Lacey, T. Bowden, D. Brandell, Beyond PEO—Alternative host materials for Li+-conducting solid polymer electrolytes, Prog. Polym. Sci. 81 (2018) 114–143. https://doi.org/10.1016/j.progpolymsci.2017.12.004.

[18] G. Wang, X. Zhu, A. Rashid, Z. Hu, P. Sun, Q. Zhang, L. Zhang, Organic polymeric filler-amorphized poly(ethylene oxide) electrolyte enables all-solid-state lithium-metal batteries operating at 35 °c, J. Mater. Chem. A Mater. 8 (2020) 13351–13363. https://doi.org/10.1039/d0ta00335b.

[19] H. Zhang, C. Liu, L. Zheng, F. Xu, W. Feng, H. Li, X. Huang, M. Armand, J. Nie, Z. Zhou, Lithium bis(fluorosulfonyl)imide/poly(ethylene oxide) polymer electrolyte, Electrochim. Acta 133 (2014) 529–538. https://doi.org/10.1016/j.electacta.2014.04.099.

[20] J. Li, Y. Ji, H. Song, S. Chen, S. Ding, B. Zhang, L. Yang, Y. Song, F. Pan, Insights Into the Interfacial Degradation of High-Voltage All-Solid-State Lithium Batteries, Nanomicro Lett. 14 (2022). https://doi.org/10.1007/s40820-022-00936-z.

[21] Z. Xue, D. He, X. Xie, Poly(ethylene oxide)-based electrolytes for lithium-ion batteries, J. Mater. Chem. A Mater. 3 (2015) 19218–19253. https://doi.org/10.1039/c5ta03471j.

[22] B. Sun, J. Mindemark, K. Edström, D. Brandell, Polycarbonate-based solid polymer electrolytes for Li-ion batteries, Solid State Ion. 262 (2014) 738–742. https://doi.org/10.1016/j.ssi.2013.08.014.

[23] Z. Li, J. Mindemark, D. Brandell, Y. Tominaga, A concentrated poly(ethylene carbonate)/poly(trimethylene carbonate) blend electrolyte for all-solid-state Li battery, Polym. J. 51 (2019) 753–760. https://doi.org/10.1038/s41428-019-0184-5.

[24] J. Mindemark, B. Sun, D. Brandell, Hydroxyl-functionalized poly(trimethylene carbonate) electrolytes for 3D-electrode configurations, Polym. Chem. 6 (2015) 4766–4774. https://doi.org/10.1039/c5py00446b.

[25] K. Kimura, J. Motomatsu, Y. Tominaga, Highly concentrated polycarbonate-based solid polymer electrolytes having extraordinary electrochemical stability, J. Polym. Sci. B Polym. Phys. 54 (2016) 2442–2447. https://doi.org/10.1002/polb.24235.

[26] P.N. Didwal, Y.N. Singhbabu, R. Verma, B.J. Sung, G.H. Lee, J.S. Lee, D.R. Chang, C.J. Park, An advanced solid polymer electrolyte composed of poly(propylene carbonate) and mesoporous silica nanoparticles for use in all-solid-state lithium-ion batteries, Energy Storage Mater. 37 (2021) 476–490. https://doi.org/10.1016/j.ensm.2021.02.034.

[27] K. Xu, Nonaqueous liquid electrolytes for lithium-based rechargeable batteries, Chem. Rev. 104 (2004) 4303–4417. https://doi.org/10.1021/cr030203g.

[28] B. Sun, J. Mindemark, K. Edström, D. Brandell, Polycarbonate-based solid polymer electrolytes for Li-ion batteries, Solid State Ion. 262 (2014) 738–742. https://doi.org/10.1016/j.ssi.2013.08.014.

[29] L. Zhu, J. Li, Y. Jia, P. Zhu, M. Jing, S. Yao, X. Shen, S. Li, F. Tu, Toward high performance solid-state lithium-ion battery with a promising PEO/PPC blend solid polymer electrolyte, Int. J. Energy Res. 44 (2020) 10168–10178. https://doi.org/10.1002/er.5632.

[30] Y.C. Jung, M.S. Park, D.H. Kim, M. Ue, A. Eftekhari, D.W. Kim, Room-Temperature Performance of Poly(Ethylene Ether Carbonate)-Based Solid Polymer Electrolytes for All-Solid-State Lithium Batteries, Sci. Rep. 7 (2017). https://doi.org/10.1038/s41598-017-17697-0.

[31] J. Bao, G. Shi, C. Tao, C. Wang, C. Zhu, L. Cheng, G. Qian, C. Chen, Polycarbonate-based polyurethane as a polymer electrolyte matrix for all-solid-state lithium batteries, J. Power Sources 389 (2018) 84–92. https://doi.org/10.1016/j.jpowsour.2018.04.020.

[32] Y. Tominaga, V. Nanthana, D. Tohyama, Ionic conduction in poly(ethylene carbonate)-based rubbery electrolytes including lithium salts, Polym. J. 44 (2012) 1155–1158. https://doi.org/10.1038/pj.2012.97.

[33] Y. Tominaga, K. Yamazaki, V. Nanthana, Effect of Anions on Lithium Ion Conduction in Poly(ethylene carbonate)-based Polymer Electrolytes, J. Electrochem. Soc. 162 (2015) A3133–A3136. https://doi.org/10.1149/2.0211502jes.

[34] W. Liu, N. Liu, J. Sun, P.C. Hsu, Y. Li, H.W. Lee, Y. Cui, Ionic Conductivity Enhancement of Polymer Electrolytes with Ceramic Nanowire Fillers, Nano Lett. 15 (2015) 2740–2745. https://doi.org/10.1021/acs.nanolett.5b00600.

[35] X. Liu, Z. Bi, Y. Wan, X. Guo, Composition regulation of polyacrylonitrile-based polymer electrolytes enabling dual-interfacially stable solid-state lithium batteries, J. Colloid Interface Sci. 665 (2024) 582–591. https://doi.org/10.1016/j.jcis.2024.03.166.

[36] P. Hu, J. Chai, Y. Duan, Z. Liu, G. Cui, L. Chen, Progress in nitrile-based polymer electrolytes for high performance lithium batteries, J. Mater. Chem. A Mater. 4 (2016) 10070–10083. https://doi.org/10.1039/c6ta02907h.

[37] S. Mu, W. Huang, W. Sun, N. Zhao, M. Jia, Z. Bi, X. Guo, Heterogeneous electrolyte membranes enabling double-side stable interfaces for solid lithium batteries, Journal of Energy Chemistry 60 (2021) 162–168. https://doi.org/10.1016/j.jechem.2020.12.026.

[38] Z. Zhang, M. Zhang, J. Wu, X. Hu, B. Fu, X. Zhang, B. Luo, K. Khan, Z. Fang, Z. Xu, M. Wu, Interfacial Plasticization Strategy Enabling a Long-Cycle-Life Solid-

State Lithium Metal Battery, Small 20 (2024). https://doi.org/10.1002/smll.202304234.
[39] Q. Wang, H. Zhang, Z. Cui, Q. Zhou, X. Shangguan, S. Tian, X. Zhou, G. Cui, Siloxane-based polymer electrolytes for solid-state lithium batteries, Energy Storage Mater. 23 (2019) 466–490. https://doi.org/10.1016/j.ensm.2019.04.016.
[40] H. Wang, S. Chen, Y. Li, Y. Liu, Q. Jing, X. Liu, Z. Liu, X. Zhang, Organosilicon-Based Functional Electrolytes for High-Performance Lithium Batteries, Adv. Energy Mater. 11 (2021). https://doi.org/10.1002/aenm.202101057.
[41] K. Nagaoka, H. Naruse, I. Shinohara, M. Watanabe, High Ionic Conductivity in Poly(dimethy1 Siloxane-co-Ethylene Oxide) Dissolving Lithium Perchlorate, Journal of Polymer Science: Polymer Letters Edition 22 (1984) 659–663. https://doi.org/https://doi.org/10.1002/pol.1984.130221205.
[42] R. Spindler, D.F. Shriver, Synthesis, NMR Characterization, and Electrical Properties of Siloxane-Based Polymer Electrolytes, Kirimura, J. Bull. Ser. Exp. Stn 21 (1988) 16. https://pubs.acs.org/sharingguidelines.
[43] J.Y. Lee, Y.M. Lee, B. Bhattacharya, Y.C. Nho, J.K. Park, Solid polymer electrolytes based on crosslinkable polyoctahedral silsesquioxanes (POSS) for room temperature lithium polymer batteries, Journal of Solid State Electrochemistry 14 (2010) 1445–1449. https://doi.org/10.1007/s10008-009-0968-1.
[44] D. Zhou, D. Shanmukaraj, A. Tkacheva, M. Armand, G. Wang, Polymer Electrolytes for Lithium-Based Batteries: Advances and Prospects, Chem 5 (2019) 2326–2352. https://doi.org/10.1016/j.chempr.2019.05.009.
[45] J. Newman, K.E. Thomas, H. Hafezi, D.R. Wheeler, Modeling of lithium-ion batteries, in: J. Power Sources, 2003: pp. 838–843. https://doi.org/10.1016/S0378-7753(03)00282-9.
[46] R. Bouchet, S. Maria, R. Meziane, A. Aboulaich, L. Lienafa, J.P. Bonnet, T.N.T. Phan, D. Bertin, D. Gigmes, D. Devaux, R. Denoyel, M. Armand, Single-ion BAB triblock copolymers as highly efficient electrolytes for lithium-metal batteries, Nat. Mater. 12 (2013) 452–457. https://doi.org/10.1038/nmat3602.
[47] Y. Lu, M. Tikekar, R. Mohanty, K. Hendrickson, L. Ma, L.A. Archer, Stable cycling of lithium metal batteries using high transference number electrolytes, Adv. Energy Mater. 5 (2015). https://doi.org/10.1002/aenm.201402073.
[48] Y. Tominaga, K. Yamazaki, Fast Li-ion conduction in poly(ethylene carbonate)-based electrolytes and composites filled with TiO2 nanoparticles, Chemical Communications 50 (2014) 4448–4450. https://doi.org/10.1039/c3cc49588d.
[49] S.S. Park, Y. Tulchinsky, M. Dinca, Single-Ion Li+, Na+, and Mg2+ Solid Electrolytes Supported by a Mesoporous Anionic Cu-Azolate Metal-Organic Framework, J. Am. Chem. Soc. 139 (2017) 13260–13263. https://doi.org/10.1021/jacs.7b06197.
[50] L. Porcarelli, P.S. Vlasov, D.O. Ponkratov, E.I. Lozinskaya, D.Y. Antonov, J.R. Nair, C. Gerbaldi, D. Mecerreyes, A.S. Shaplov, Design of ionic liquid like monomers towards easy-accessible single-ion conducting polymer electrolytes, Eur. Polym. J. 107 (2018) 218–228. https://doi.org/10.1016/j.eurpolymj.2018.08.014.

[51] R. Bouchet, S. Maria, R. Meziane, A. Aboulaich, L. Lienafa, J.P. Bonnet, T.N.T. Phan, D. Bertin, D. Gigmes, D. Devaux, R. Denoyel, M. Armand, Single-ion BAB triblock copolymers as highly efficient electrolytes for lithium-metal batteries, Nat. Mater. 12 (2013) 452–457. https://doi.org/10.1038/nmat3602.

[52] L. Yue, J. Ma, J. Zhang, J. Zhao, S. Dong, Z. Liu, G. Cui, L. Chen, All solid-state polymer electrolytes for high-performance lithium ion batteries, Energy Storage Mater. 5 (2016) 139–164. https://doi.org/10.1016/j.ensm.2016.07.003.

[53] X. Yang, M. Jiang, X. Gao, D. Bao, Q. Sun, N. Holmes, H. Duan, S. Mukherjee, K. Adair, C. Zhao, J. Liang, W. Li, J. Li, Y. Liu, H. Huang, L. Zhang, S. Lu, Q. Lu, R. Li, C.V. Singh, X. Sun, Determining the limiting factor of the electrochemical stability window for PEO-based solid polymer electrolytes: Main chain or terminal -OH group?, Energy Environ. Sci. 13 (2020) 1318–1325. https://doi.org/10.1039/d0ee00342e.

[54] J. Mindemark, M.J. Lacey, T. Bowden, D. Brandell, Beyond PEO—Alternative host materials for Li+-conducting solid polymer electrolytes, Prog. Polym. Sci. 81 (2018) 114–143. https://doi.org/10.1016/j.progpolymsci.2017.12.004.

[55] S. Feng, D. Shi, F. Liu, L. Zheng, J. Nie, W. Feng, X. Huang, M. Armand, Z. Zhou, Single lithium-ion conducting polymer electrolytes based on poly[(4-styrenesulfonyl)(trifluoromethanesulfonyl)imide] anions, Electrochim. Acta 93 (2013) 254–263. https://doi.org/10.1016/j.electacta.2013.01.119.

[56] Q. Wang, H. Zhang, Z. Cui, Q. Zhou, X. Shangguan, S. Tian, X. Zhou, G. Cui, Siloxane-based polymer electrolytes for solid-state lithium batteries, Energy Storage Mater. 23 (2019) 466–490. https://doi.org/10.1016/j.ensm.2019.04.016.

[57] B. Tong, Z. Song, W. Feng, J. Zhu, H. Yu, X. Huang, M. Armand, Z. Zhou, H. Zhang, Design of a Teflon-Like Anion for Unprecedently Enhanced Lithium Metal Polymer Batteries, Adv. Energy Mater. 13 (2023). https://doi.org/10.1002/aenm.202204085.

[58] H. Zhang, F. Chen, O. Lakuntza, U. Oteo, L. Qiao, M. Martinez-Ibañez, H. Zhu, J. Carrasco, M. Forsyth, M. Armand, Suppressed Mobility of Negative Charges in Polymer Electrolytes with an Ether-Functionalized Anion, Angewandte Chemie 131 (2019) 12198–12203. https://doi.org/10.1002/ange.201905794.

[59] Y. Zhao, L. Wang, Y. Zhou, Z. Liang, N. Tavajohi, B. Li, T. Li, Solid Polymer Electrolytes with High Conductivity and Transference Number of Li Ions for Li-Based Rechargeable Batteries, Advanced Science 8 (2021). https://doi.org/10.1002/advs.202003675.

[60] M.A.A. Sunita, B. Sundaresan, S. Jeya, Plastic crystal as a plasticizer for enhancing Li+ ion conductivity in PMMA–LiTf polymer electrolyte, J. Non. Cryst. Solids 646 (2024). https://doi.org/10.1016/j.jnoncrysol.2024.123243.

[61] L.Z. Fan, J. Maier, Composite effects in poly(ethylene oxide)-succinonitrile based all-solid electrolytes, Electrochem. Commun. 8 (2006) 1753–1756. https://doi.org/10.1016/j.elecom.2006.08.017.

[62] M. Forsyth, L. Porcarelli, X. Wang, N. Goujon, D. Mecerreyes, Innovative Electrolytes Based on Ionic Liquids and Polymers for Next-Generation Solid-State Batteries, Acc. Chem. Res. 52 (2019) 686–694. https://doi.org/10.1021/acs.accounts.8b00566.

[63] I. Osada, H. de Vries, B. Scrosati, S. Passerini, Ionic-Liquid-Based Polymer Electrolytes for Battery Applications, Angewandte Chemie 128 (2016) 510–523. https://doi.org/10.1002/ange.201504971.

[64] J.-H. Shin, W.A. Henderson, S. Passerini, PEO-Based Polymer Electrolytes with Ionic Liquids and Their Use in Lithium Metal-Polymer Electrolyte Batteries, J. Electrochem. Soc. 152 (2005) A978. https://doi.org/10.1149/1.1890701.

[65] N. Yazie, D. Worku, N. Gabbiye, A. Alemayehu, Z. Getahun, M. Dagnew, Development of polymer blend electrolytes for battery systems: recent progress, challenges, and future outlook, Mater. Renew. Sustain. Energy 12 (2023) 73–94. https://doi.org/10.1007/s40243-023-00231-w.

[66] L. Zhu, J. Li, Y. Jia, P. Zhu, M. Jing, S. Yao, X. Shen, S. Li, F. Tu, Toward high performance solid-state lithium-ion battery with a promising PEO/PPC blend solid polymer electrolyte, Int. J. Energy Res. 44 (2020) 10168–10178. https://doi.org/10.1002/er.5632.

[67] J. Li, L. Zhu, J. Xu, M. Jing, S. Yao, X. Shen, S. Li, F. Tu, Boosting the performance of poly(ethylene oxide)-based solid polymer electrolytes by blending with poly(vinylidene fluoride-co-hexafluoropropylene) for solid-state lithium-ion batteries, Int. J. Energy Res. 44 (2020) 7831–7840. https://doi.org/10.1002/er.5476.

[68] F. Croce, L. Persi, B. Scrosati, F. Serraino-Fiory, E. Plichta, M.A. Hendrickson, Role of the ceramic fillers in enhancing the transport properties of composite polymer electrolytes, Electrochim. Acta 46 (2001) 2457–2461. https://doi.org/https://doi.org/10.1016/S0013-4686(01)00458-3.

[69] J.E. Weston, B.C.H. Steele, Effects of Inert Fillers on the Mechanical and Electrochemical Properties of Lithium Salt-Poly (Ethylene Oxide) Polymer Electrolytes, Solid State Ion. 7 (1982) 75–79. https://doi.org/https://doi.org/10.1016/0167-2738(82)90072-8.

[70] V. Marangon, Y. Tominaga, J. Hassoun, An alternative composite polymer electrolyte for high performances lithium battery, J. Power Sources 449 (2020). https://doi.org/10.1016/j.jpowsour.2019.227508.

[71] Y. Song, L. Yang, J. Li, M. Zhang, Y. Wang, S. Li, S. Chen, K. Yang, K. Xu, F. Pan, Synergistic Dissociation-and-Trapping Effect to Promote Li-Ion Conduction in Polymer Electrolytes via Oxygen Vacancies, Small 17 (2021). https://doi.org/10.1002/smll.202102039.

[72] H. Chen, D. Adekoya, L. Hencz, J. Ma, S. Chen, C. Yan, H. Zhao, G. Cui, S. Zhang, Stable Seamless Interfaces and Rapid Ionic Conductivity of Ca–CeO2/LiTFSI/PEO Composite Electrolyte for High-Rate and High-Voltage All-Solid-State Battery, Adv. Energy Mater. 10 (2020). https://doi.org/10.1002/aenm.202000049.

[73] W. Bao, L. Zhao, H. Zhao, L. Su, X. Cai, B. Yi, Y. Zhang, J. Xie, Vapor phase infiltration of ZnO quantum dots for all-solid-state PEO-based lithium batteries, Energy Storage Mater. 43 (2021) 258–265. https://doi.org/10.1016/j.ensm.2021.09.010.

[74] F. Croce, G.B. Appetecchi, L. Persi, B. Scrosati, Nanocomposite polymer electrolytes for lithium batteries, Nature 394 (1998) 456–458. https://doi.org/https://doi.org/10.1038/28818.

[75] A. Saleem, R. Iqbal, M.K. Majeed, A. Hussain, A.R. Akbar, Z. Hussain, B. Jabar, S. Rauf, L.L. Shaw, Boosting lithium-ion conductivity of polymer electrolyte by selective introduction of covalent organic frameworks for safe lithium metal batteries, Nano Energy 128 (2024). https://doi.org/10.1016/j.nanoen.2024.109848.

[76] L. Xu, X. Xiao, H. Tu, F. Zhu, J. Wang, H. Liu, W. Huang, W. Deng, H. Hou, T. Liu, X. Ji, K. Amine, G. Zou, Engineering Functionalized 2D Metal-Organic Frameworks Nanosheets with Fast Li+ Conduction for Advanced Solid Li Batteries, Advanced Materials 35 (2023). https://doi.org/10.1002/adma.202303193.

[77] C.C. Tambelli, A.C. Bloise, A. V Rosário, E.C. Pereira, C.J. Magon, J.P. Donoso, Characterisation of PEO-Al2O3 composite polymer electrolytes, Electrochim. Acta 47 (2002) 1677–1682. https://doi.org/https://doi.org/10.1016/S0013-4686(01)00900-8.

[78] J. Song, Y. Xu, Y. Zhou, P. Wang, H. Feng, J. Yang, F. Zhuge, Q. Tan, Incorporating 2D γ-Al2O3 nanosheets into the flexible PEO-based solid electrolyte for lithium metal batteries, Electrochim. Acta 437 (2023). https://doi.org/10.1016/j.electacta.2022.141504.

[79] K.M. Diederichsen, E.J. McShane, B.D. McCloskey, Promising Routes to a High Li+ Transference Number Electrolyte for Lithium Ion Batteries, ACS Energy Lett. 2 (2017) 2563–2575. https://doi.org/10.1021/acsenergylett.7b00792.

[80] H. Wang, L. Sheng, G. Yasin, L. Wang, H. Xu, X. He, Reviewing the current status and development of polymer electrolytes for solid-state lithium batteries, Energy Storage Mater. 33 (2020) 188–215. https://doi.org/10.1016/j.ensm.2020.08.014.

[81] H. Yuan, J. Luan, Z. Yang, J. Zhang, Y. Wu, Z. Lu, H. Liu, Single Lithium-Ion Conducting Solid Polymer Electrolyte with Superior Electrochemical Stability and Interfacial Compatibility for Solid-State Lithium Metal Batteries, ACS Appl. Mater. Interfaces 12 (2020) 7249–7256. https://doi.org/10.1021/acsami.9b20436.

[82] S. Inceoglu, A.A. Rojas, D. Devaux, X.C. Chen, G.M. Stone, N.P. Balsara, Morphology-conductivity relationship of single-ion-conducting block copolymer electrolytes for lithium batteries, ACS Macro Lett. 3 (2014) 510–514. https://doi.org/10.1021/mz5001948.

[83] J.R. Nair, I. Shaji, N. Ehteshami, A. Thum, Di. Diddens, A. Heuer, M. Winter, Solid Polymer Electrolytes for Lithium Metal Battery via Thermally Induced Cationic Ring-Opening Polymerization (CROP) with an Insight into the Reaction Mechanism, Chemistry of Materials 31 (2019) 3118–3133. https://doi.org/10.1021/acs.chemmater.8b04172.

[84] Y. Guo, X. Qu, Z. Hu, J. Zhu, W. Niu, X. Liu, Highly elastic and mechanically robust polymer electrolytes with high ionic conductivity and adhesiveness for high-performance lithium metal batteries, J. Mater. Chem. A Mater. 9 (2021) 13597–13607. https://doi.org/10.1039/d1ta02579a.

[85] L. Porcarelli, C. Gerbaldi, F. Bella, J.R. Nair, Super Soft All-Ethylene Oxide Polymer Electrolyte for Safe All-Solid Lithium Batteries, Sci. Rep. 6 (2016). https://doi.org/10.1038/srep19892.

[86] F. Fu, Y. Zheng, N. Jiang, Y. Liu, C. Sun, A. Zhang, H. Teng, L. Sun, H. Xie, A Dual-Salt PEO-based polymer electrolyte with Cross-Linked polymer network for

High-Voltage lithium metal batteries, Chemical Engineering Journal 450 (2022). https://doi.org/10.1016/j.cej.2022.137776.

[87] L. Meabe, T.V. Huynh, N. Lago, H. Sardon, C. Li, L.A. O'Dell, M. Armand, M. Forsyth, D. Mecerreyes, Poly(ethylene oxide carbonates) solid polymer electrolytes for lithium batteries, Electrochim. Acta 264 (2018) 367–375. https://doi.org/10.1016/j.electacta.2018.01.101.

[88] Y. Tominaga, K. Nakano, T. Morioka, Random copolymers of ethylene carbonate and ethylene oxide for Li-Ion conductive solid electrolytes, Electrochim. Acta 312 (2019) 342–348. https://doi.org/10.1016/j.electacta.2019.05.004.

Chapter 3
Materials and Methods

3.1 Materials

Poly(ethylene oxide) (PEO, M_w of 4×10^5 g mol^{-1} and 4×10^6 g mol^{-1}, CAS: 25322-68-3) was purchased from Sigma Aldrich. Poly(ethylene carbonate) (pEC, CAS: 25608-11-1) and poly(propylene carbonate) (pPC, CAS: 25511-85-7) were received from Specific Polymers. Bis(trifluoromethane) sulfonamide lithium salt (LiTFSI) was purchased from Sigma-Aldrich (CAS: 90076-65-6). All polymers were dried for 3 days under vacuum at 60 °C. LiTFSI was dried under vacuum for one day at room temperature, two days at 70 °C, and finally two hours at 110 °C. Anhydrous N-methyl pyrrolidone (NMP, CAS: 872-50-4) and succinonitrile (SN, CAS 110-61-2) were obtained from Merck and used as received.

2-Chloroethanesulfonyl chloride (98%, Acros Organics), trifluoromethanesulfonylamide ($CF_3SO_2NH_2$, 97%, ABCR), triethylamine (TEA, for synthesis, Merck), diisopropylamine (DIPA, ≥99.5%, Sigma-Aldrich), 2-mercaptoethanol (98%, Sigma-Aldrich), 6-mercapto-1-hexanol (>98.0%, TCI Europe), 4-methoxyphenol (MEHQ, 99%, Merck), poly(ethylene glycol) methyl ether methacrylate (PEGM, Mn approx 500 g mol^{-1}, Merck), 4-cyano-4-(phenylcarbonothioylthio)pentanoic acid (CPADB, 99%, Sigma-Aldrich), lithium chloride (LiCl, 99%, Acros Organics), silver nitrate ($AgNO_3$, >99%, Acros Organics), 1-butyl-3-methylimidazolium bromide (BMImBr, 99%, IoLiTec), magnesium sulfate ($MgSO_4$, 99.5%, Acros Organics), phosphorus pentoxide (P_2O_5, Sicapent®, Merck), activated charcoal (Acros Organics).

Conductive carbon black (C65, Imerys) and poly(vinylidene fluoride) (PVdF, Solef 6020, Solvay) were used without further purification. Lithium iron phosphate ($LiFePO_4$, LFP) cathode powder was provided by BASF. Lithium nickel manganese cobalt oxides (NMC622) cathode powder was provided by MSE Supplies. Carbon-coated aluminum foil (GELON) and lithium metal foil (Li, high purity lithium metal, Albemarle) were used as received.

Methacryloyl chloride (C_4H_5ClO, 98%, Sigma-Aldrich) was purified by atmospheric distillation. Potassium carbonate (K_2CO_3, 99.2%, BLDpharm) was dried at 140 °C for 6 h before use. Azobisisobutyronitrile (AIBN, 99%, Sigma-Aldrich) was recrystallized from methanol.

Acetonitrile (AcN, anhydrous, 99.5%, Acros Organics), methanol (MeOH, anhydrous, 99.5%, Acros Organics), tetrahydrofurane (THF, 99.8%, unstabilized, Thermo Fisher), ethyl acetate (EtAc, 99%, Fisher), diethylether (Et_2O, 99%, Fisher), dichloromethane (DCM, 99.5%), N,N-dimethylformamide (DMF, anhydrous 99.8%, Acros), isopropanol (iPrOH, 99%, Fisher), and acetone (99%, Fisher) were used as received. Ultrapure deionized water was obtained using Sartorius Arium® Comfort smart station.

NMR solvents and standards: dimethyl sulfoxide-d6 (DMSO-d6, 99.9 atom%D, Sigma-Aldrich) was dried over 4Å molecular sieves; hexafluorobenzene (C_6F_6, 99%, Acros Organics) was used as received.

3.2. Methods

3.2.1 Membrane Preparation

The following instruments were used for polymer electrolyte membrane preparation. The procedure or synthesis will be described in detail in the following experimental chapters.

Extrusion

A mini-compounder (Haake MiniLab II – Thermo Fischer Scientific) was used to prepare the formulations. The extruder is designed to produce small quantities (approximately 7 cm^3) of polymer, composite, or nanocomposite materials. The tool consists of two co-rotational twin screws with controllable rotation speed. The compounder allowed the proper mixing of the polymer components and salt without

using solvents, melting the polymer into the compounder's chamber and recirculating it many times (**Figure 3.1**).

Figure 3.1 Extruder employed for polymer electrolyte preparation.

Hot-press

The membrane of polymer electrolyte was obtained by hot-pressing the blended polymer at 70 °C and different pressure (5-25 bar) (**Figure 3.2**).

Figure 3.2 Hydraulic press used to heat and press the polymer membrane.

UV-crosslinking

For the process of UV-crosslinking, a DMAX ECE 5000 flood UV lamp was employed. The photopolymerization (UV-curing, UV-crosslinking) was carried out at around 70 °C for 3 min on each side under the lamp (40 mW cm^{-2}) (**Figure 3.3**).

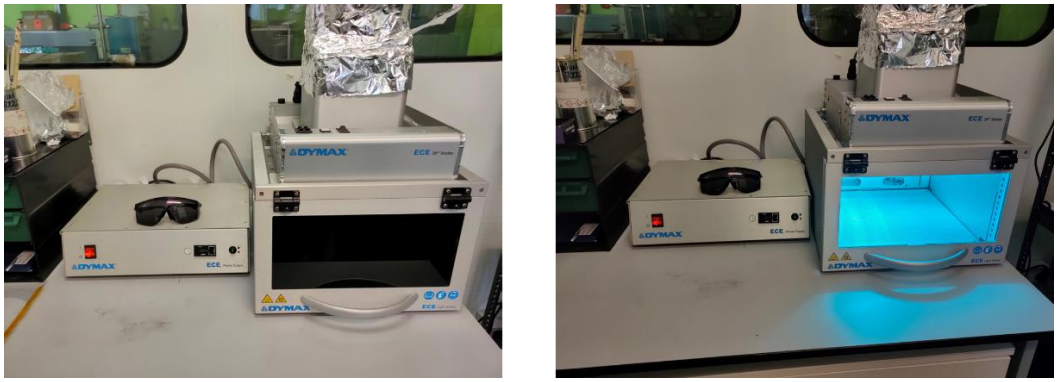

Figure 3.3 UV-lamp used for crosslinking of polymer membrane.

3.2.2 Thermal, Morphological and Physical Characterizations

The following tests were carried out to characterize the thermal properties of the polymer-based electrolytes developed in this PhD work.

Thermogravimetric analysis (TGA) was performed with a Netzsch TG 209 F3. The measure was conducted between 25 °C and 600 °C under a nitrogen atmosphere, using a heating ramp of 10 °C min^{-1}. The temperature at which the degradation process starts was fixed when 5 % of loss in weight is reached.

Differential Scanning Calorimetry (DSC, Netzsch 214 Polyma Equipment) was carried out to evaluate the degree of crystallinity anf transition temperatures (glass transition and melting). The measurements were conducted in a temperature range between −50 and 100 °C with a heating rate of 10 °C min^{-1} in a nitrogen atmosphere (40 mL min^{-1}). The crystallinity degree was calculated as described in Equation 1, using the value of 205 J g^{-1} as melting enthalpy (ΔH_m^0) for 100% crystalline PEO [40,41].

$$Crystallinity\ (\%) = \frac{\Delta H_m}{\Delta H_m{}^0} * 100 \qquad \text{(Eq. 1)}$$

The **Dynamic Mechanical Thermal Analysis** (DMTA) was performed with a Q800 by TA Intruments. The dynamo-mechanical and viscoelastic properties and the relaxation temperatures of the polymer blends were evaluated by applying an

isofrequency of 1 Hz with a ramp of temperature from –60 to 60 °C at 3 °C min^{-1} using bar specimens obtained from the membranes. From DMTA, storage modulus, loss modulus, and relaxation temperatures (taken as peaks temperature in the loss modulus curves) were obtained.

Scanning Electron Microscopy (SEM, Solaris X, Tescan) was used to characterize the surface and cross-section morphology of the prepared membrane, using a beam energy of 5 keV. The cross-section was obtained by breaking the membranes after having soaked them in liquid nitrogen for 1 minute.

Infrared Spectroscopy (IR) was performed to measure the optical transmittance of the SPE membranes using a spectrometer (Nicolet™ iS50 FTIR, ThermoFisher).

The **X-ray Photoelectron Spectroscopy** (XPS) experiments were performed with a Thermofisher Nexsa G2. X-ray beam: Al Kα, E = 1486.6 eV. Photoelectron emission take-off angle: 0°with respect to the surface normal

Binding Energy was referenced on the C-(C,H) component @ 285 eV. The samples have been transfered under argon from a glove box into the XPS spectrometer.

Gel content was calculated to evaluate the percentage of non-crosslinked polymeric chains still present after UV-curing. The sample (around 0.65 g) was weighed, closed in a metal grid (500 mesh), and soaked in 50 mL of ethyl acetate (EtOAc) for 1 h under stirring at room temperature. Then, the solvent was changed with another 50 mL of fresh EtOAc and kept for 24 h under stirring at room temperature before the third extraction with another 50 mL of fresh solvent for 3 h. The sample was recovered and dried in a vacuum oven until constant weight. The same procedure was repeated on the same sample using AcN as solvent. The gel content was evaluated according to Equation 2.

$$Gel\ Content\ (\%) = \frac{w_d}{w_i} * 100 \qquad \text{(Eq. 2)}$$

where w_d and w_i are the weight after drying and the initial weight, respectively.

Nuclear magnetic resonance (NMR) spectra were recorded on Avance III HD 600MHz (Bruker) spectrometer (^{1}H NMR at 600 MHz, ^{7}Li NMR at 233 MHz, ^{13}C NMR at 151 MHz, and ^{19}F at 565 MHz) at 25°C in the indicated deuterated solvent and are listed in ppm. The signals corresponding to the residual protons and carbons

of the deuterated solvent were used as an internal standard for ^{1}H and ^{13}C NMR, respectively. C_6F_6 (−164.9 ppm) was utilized as an external standard for ^{19}F NMR.

Size exclusion chromatography (SEC) / Gel Permeation Chromatography (GPC) was used to determine the number-average molecular weights (M_n) and M_w/M_n ratios. The study was performed on a 1200 Infinity gel permeation chromatograph (Agilent Technologies) equipped with PLgel 5µm MIXED-D column (Agilent Technologies, USA), PLgel 5µm (Agilent Technologies) pre-column and an integrated refractive index (IR) detector. The system was operated at 50 °C and 1.0 mL min^{-1} flow using 0.1 M LiTFSI solution in DMF as an eluent. Poly(methyl methacrylate) standards (EasiVial PM, Agilent Technologies, Mp = 550 – 1558 × 10^3) were used to perform calibration.

3.2.3 Electrical and Electrochemical Characterizations

Ionic conductivity (σ_i) was measured by electrochemical impedance spectroscopy (EIS) with a VMP-3 research-grade multichannel potentiostat/galvanostat with frequency response analyser for high-end EIS measurements (Biologic, France). To avoid any influence of moisture/humidity on the conductivity of polymer-based electrolytes, the latter were preliminary dried at 80 °C/0.1 mbar for 12 h in a B-585 oven (Buchi Glass Drying Oven, Switzerland) filled with P_2O_5 and were transferred under vacuum inside an argon-filled glovebox (MBRAUN MB-Labstar, H_2O and O_2 content <0.5 ppm). An electrolyte sample disk of 16 mm in diameter, with a thickness of about 150 µm, was sandwiched between two stainless-steel (SS-316) blocking electrodes in a SS||electrolyte||SS configuration. For each SPE, the thickness was accurately measured before and after tests using a precision micrometer (Mitutoyo). EIS data were recorded on the VMP-3 electrochemical workstation in a frequency range of 0.1 Hz – 1 MHz by applying a sinusoidal voltage of 20 mV at various temperatures (normally, 0 – 80 °C) and storing the cells in an environmentally controlled climatic chamber (MK 53 E2 from BINDER, Germany). The cells were kept for 120 min at each temperature with intervals of 10 °C for proper thermal equilibration. Nyquist plots were analysed using the Biologic EC-Lab® advanced software for electrochemical research. The ionic conductivity (σ_i) was determined according to Equation 3:

$$\sigma_i = D/AR \quad \text{(Eq. 3)}$$

where D represents the thickness (cm), A the area (cm^2), and R (Ω) the total resistance of the electrolytes under study.

Cyclic voltammetry (CV), **Linear Sweep Voltammetry (LSV)** and **Chronoamperometry (CA)** were used to determine the electrochemical stability window (ESW) of the polymer-based electrolytes under study. The VMP3 multipotentiostat (20 V, ±400 mA) and ECC-Std test cells (EL-Cell GmbH) were used to carry out the electrochemical characterization. The two-electrode cells were assembled by sandwiching a SPE membrane between a working electrode and a lithium metal foil, which served as the reference and the counter electrode, simultaneously. Separate tests were performed for the determination electrochemical stability using stainless steel disks or Aluminium Carbon Coated (CC) as working electrodes. Potential sweeps were carried out between OCV and 5.8 V vs. Li^+/Li at a constant rate of 0.1 mV s^{-1}.

Lithium-ion transference number (t_{Li+}) was determined in a symmetric Li/electrolyte/Li cell, which was subjected to a 20 mV polarization bias (ΔV) with the aim to determine the initial (I_o) and the steady state (I_{ss}) currents. EIS was performed on the VMP3 multipotentiostat by applying a 20 mV perturbation between 300 kHz and 0.01 Hz at OCV conditions to obtain the resistance of the passivation layer before ($R_{SEI+CT,o}$) and after ($R_{SEI+CT,ss}$) polarization. The t_{Li+} was calculated using the Evans/Vincent/Bruce equation [1]:

$$t_{Li+} = \frac{I_{ss}\cdot(\Delta V - I_o\cdot R_{SEI+CT,o})}{I_o\cdot(\Delta V - I_{ss}\cdot R_{SEI+CT,ss})} \quad \text{(Eq 4)}$$

where t_{Li+} is the Li transference number, ΔV is the potential applied across the cell (20 mV), $R_{SEI+CT,o}$ and $R_{SEI+CT,ss}$ are the initial and steady-state resistances of the passivating layer, I_o and I_{ss} are the initial and steady-state currents.

3.3 Lithium Metal Cell Assembly and Testing

Lab-scale symmetric (Li/electrolyte/Li) cells and/or Li-metal ($LiFePO_4$ or $LiNi_xMny Co_{1-x-y}O_2$/electrolyte/Li) cells were galvanostatically cycled on an Arbin

BT2000 battery tester at different temperatures. Cells were cycled between 2.5 and 4 V vs. Li^+/Li for LFP and between 3 and 4.2 V vs. Li^+/Li for NMC-based composite cathodes with different charge/discharge current regimes up to C/3, where the rate is denoted as C/n, corresponding to a full discharge or full charge of the theoretical cathode capacity in n hours.

Lithium plating/stripping tests were performed at different temperatures in symmetrical Li||electrolyte||Li configuration. Reversible galvanostatic cycling was performed at various current densities of 0.025, 0.050, 0.100, 0.200, 0.300 and 0.400 mA cm^{-2} with a fixed plated/stripped areal capacity per half/cycle of 0.2 mAh cm^{-2} depending on the cell. These tests enabled assessment of interface stability and polarization behaviour under varying current loads. For long-term stability testing, the plated/stripped areal capacity was fixed at 0.20 or 0.10 mAh cm^{-2}.

Composite cathode (catholyte) preparation

To prepare the different cathode films used in this work the following compositions were used:

- $LiFePO_4$ (LFP) catholyte materials was received by Blue Solutions, produced by a proprietary patented dry process and including PEO:LiTFSI electrolyte as the active binder (Chapter 5).
- 80 wt.% of LFP, 10 wt.% of C_{65} carbon black and 10 wt.% of PVDF (Chapter 6).
- 70 wt% of NMC622, 10 wt.% of C_{65} carbon black and 20 wt.% of PEC/PMLiTFSI (9:1) (Chapter 6)
- 60 wt.% of LFP, 10 wt.% of C_{65} carbon black and 30 wt.% of PEO and Li salt (EO:Li/20:1) as binder (Chapter 7).
- 60 wt.% of carbon coated LFP, 10 wt.% of C_{65} carbon black and 27 wt.% of coPIL and 3% of PVDF as binder (Chapter 8).

Briefly, LFP or NMC active material powders and C_{65} carbon black were gently mixed in a hand mortar and, successively added to the ca. 5 wt.% solution of binder in NMP upon stirring. The magnetic stirring continued at ambient temperature for 1 h, whereupon the resultant suspension was additionally homogenized using an Ultra-Turrax mixer (IKA-Werke GmbH & Co. KG) for 10 min. The obtained dense slurry was casted onto an aluminum current collector foil using a doctor-blade with a blade height of 300 μm (**Figure 3.4**).

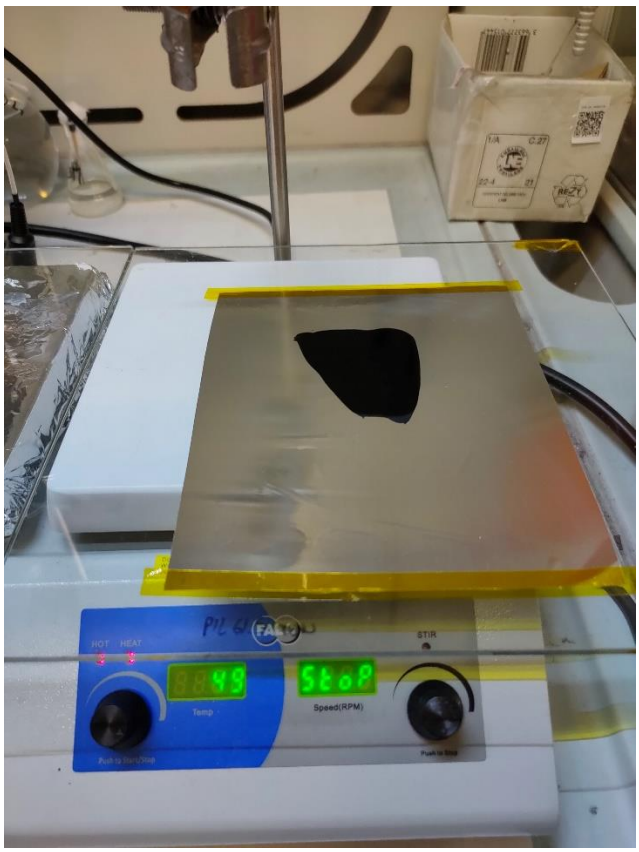

Figure 3.4 Casting of slurry on Al-foil.

NMP solvent was removed by evaporation at ambient temperature for 12 h and further drying at 60 °C/1 mm Hg for 24 h in the B-585 oven (Buchi Glass Drying Oven) filled with P_2O_5. To avoid contamination with atmospheric moisture, the cathode tape was further transferred under vacuum inside the argon-filled glovebox. After drying, the obtained composite cathode (catholyte) films had a thickness of 100±2 µm and active mass loading of 3 to 4 mg cm^{-2}.

Li-metal cells assembly and galvanostatic cycling

Lab-scale Li‖electrolyte‖LFP or NMC battery prototypes were assembled inside an Ar-filled glovebox using ECC-Std test cells (EL-Cell GmbH) (**Figure 3.5**).

Figure 3.5 ECC-Std wiring setup for testing.

In case of SICP electrolyte based cells, a round Teflon spacer (100 µm thick, 12 mm inner diameter) was placed on top of the composite cathode tape, whereupon a layer of electrolyte was applied manually directly on the composite cathode surface within the internal diameter of the spacer. In case of SPE based cells, neither spacers or other protecting tools and/or additives or liquid molecular transporter additions were used and the SPE disk was directly sandwiched in between the anode and cathode disks. In all cases, the assembly was completed by placing a lithium metal disk anode (14 mm diameter) on top of the electrolyte. The assemblies were housed in ECC-Std test cells and connected to the ARBIN BT2000 for constant-current (galvanostatic) charge/discharge testing at different temperatures and current regimes as detailed in the various Chapters following. These tests were used to evaluate electrochemical cycling stability, rate capability and operational life of the SPEs in real battery cell configuration.

All electrolyte/materials preparations and processing steps as well as cell assembly procedures were conducted under the inert atmosphere of an argon-filled glovebox (O_2 and H_2O <0.1 ppm, M-Braun UniLab) unless otherwise stated (**Figure 3.6**).

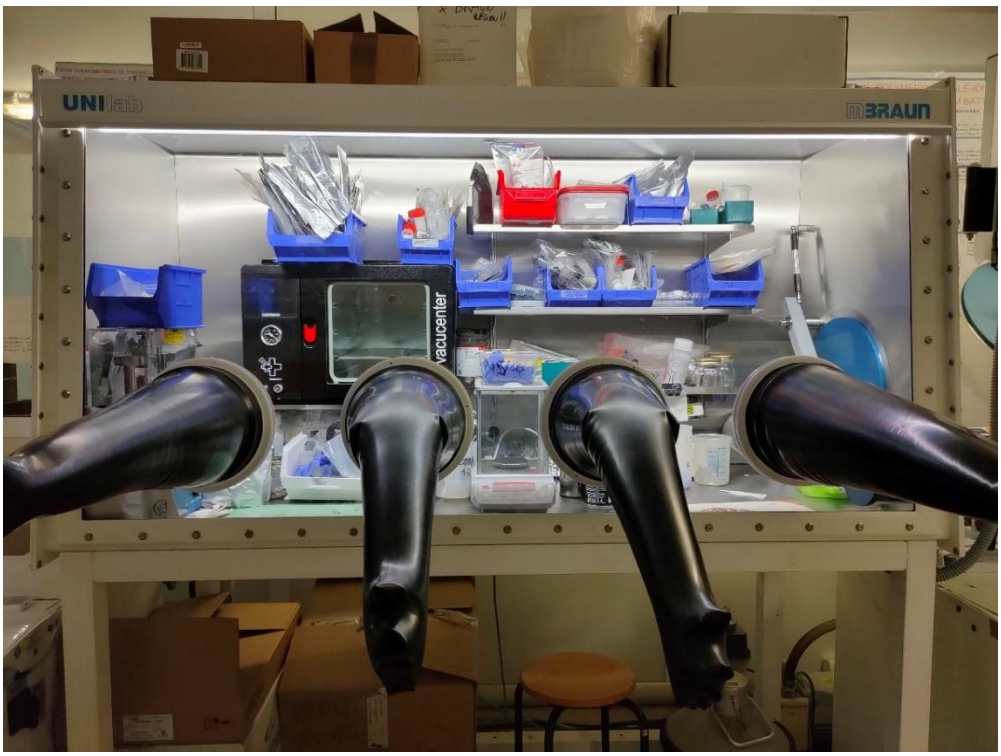

Figure 3.6 Argon-filled glovebox (M-Braun UniLab) used to stock electrolyte and for cell preparation.

References

[1] J. Evans, C.A. Vincent, P.G. Bruce, Electrochemical measurement of transference numbers in polymer electrolytes, Polymer (Guildf). 28 (1987) 2324–2328.

Chapter 4

Formulating PEO-Polycarbonate Blends As Solid Polymer Electrolytes By Solvent-Free Extrusion

The growing demand for safe, high-performance, and sustainable energy storage systems has stimulated research into advanced lithium battery technologies [1–3], and particularly solid polymer-based electrolytes should allow addressing major limitations of conventional liquid electrolytes, including safety concerns, limited electrochemical stability, mechanical properties, and scalability [4–12]. As detailed in Chapter 2, among polymer hosts PEO remains a benchmark material due to its ability to solvate lithium salts through coordination between Li^+ ions and ether oxygen atoms, enabling ion transport via polymer chain motion [13–15]. However, its practical application is hindered by high crystallinity at moderate temperatures, which limits ionic conductivity below about 60 °C, together with modest mechanical strength and limited electrochemical stability [16,17].

Aliphatic polycarbonates have recently emerged as promising blending partners because of their mainly amorphous nature and the presence of carbonate groups, similar to those found in conventional carbonate-based liquid electrolytes, which accounts for enhanced ionic conductivity towards practical values of 10^{-4} S cm^{-1} at moderately low temperature (40 °C), and electrochemical stability

exceeding 4.5 V vs. Li^+/Li, thus in principle compatible with high-energy 4V-class cathodes [18,19].

In this scenario, the initial work detailed in the present Chapter investigates an efficient, economical, and solvent-free approach to blending PEO with polycarbonates (pCs). Actually, a systematic study of the optimal PEO/pC ratio and of the most promising pC candidates is still lacking. The aim is to combine the favorable ion-solvating ability of PEO with the amorphous character and electrochemical advantages of pCs to obtain blends with an improved balance of ionic conductivity, mechanical strength, and thermal stability for potential application as SPEs. In addition, the blends are prepared by solvent-free extrusion, a process that avoids flammable solvents, simplifies manufacturing, reduces cost and environmental impact, and yields homogeneous materials even in the presence of inorganic fillers [20,21]. Overall, this study examines the preparation, characterization, and performance of PEO/PC blends for their possible use as electrolytes in next-generation ASSLMBs. These results have been published in the scientific research article F. Gambino *et al.*, J. Power Sources Adv. 30 (2024), and are reproduced/readapted in the following sections.

4.1 Preparation of blend PEO/PC SPEs

The PEO, PCs, and LiTFSI were weighted in the M-Braun glove box. All components were loaded in the mini-extruder with a continuous flow of N_2 to avoid moisture contamination (however, note that the extrusion equipment is placed inside an environmentally controlled dry-room with R.H. <2% ± 1 at 20 °C, produced by SOIMAR). Firstly, half of the PEO/PC was introduced in the extruder, then LiTFSI was added little by little, and then the last part of the polymer blend was added. The mixtures were left for 15 min of mixing into the compounder chamber to reach proper homogeneity. The operating conditions during extrusion process were 140 °C and 130 rpm. After mixing, the blended polymer was extracted from the extruder, sealed under vacuum, and transferred into the glovebox. The final SPE membrane was obtained by hot-pressing the blended polymer at 70 °C and 10 bar. Before use, SPEs were dried under vacuum at 40 °C for 12 h in the B-585 oven (Buchi Glass Drying Oven) and then transferred under vacuum inside the argon-filled M-Braun dry glovebox to minimize the presence of residual

moisture/humidity. The extrusion process and an example of the resulting SPE membrane are shown in **Figure 4.1**.

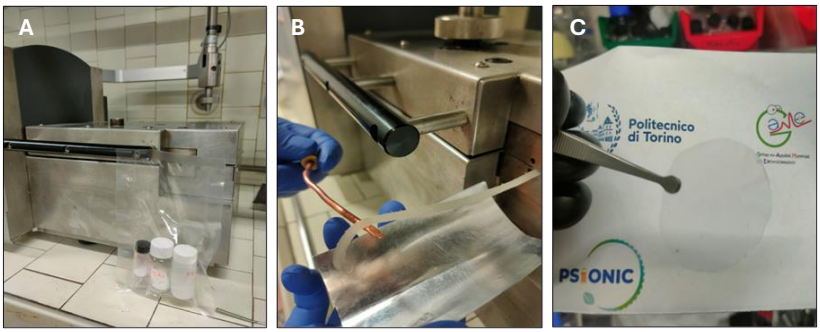

Figure 4.1 Different steps of the extrusion process. Precursor materials (A) were introduced into the extruder. After 15 min of mixing at 140°C and 130 rpm, the blend was extracted from the extruder (B). The formulation was then hot-pressed to obtain the final self-standing SPE membrane (C).

4.2 Design of Experiment

The production of polymer blends involves interplay among various parameters. In this case, three experimental variables were selected (polycarbonate type, polyethylene oxide molecular weight, and blend composition) that are relevant to the production of the blend. Each of these factors can significantly impact the final properties of the polymer electrolyte membrane, such as the conductivity, the electrochemical stability (in the following paragraph is indicated as voltage), as well as the crystallinity. The objective of the study is to systematically investigate the influence of these key factors on the production of a PEO/PC polymer blend. Regarding the type of PEO, the effects induced by the variation of molecular weight were explored by using two distinct PEOs with M_w of 4×10^5 g mol^{-1} (400k) and 4×10^6 g mol^{-1} (4M) respectively, which can influence the blend's viscosity and chain entanglement. At the same time, the influence of employing two different types of polycarbonates was examined, namely polyethylene carbonate (PEC) and polypropylene carbonate (PPC). The blend composition ratio and the relative effects on the final properties were also investigated, varying the percentage of PEO (0, 30, 50, 70, and 100%) in the formulation with PC. To evaluate the influence of these factors and their correlations, a Design of Experiment (DoE) approach was used, which offers several advantages over traditional one-factor-at-a-time experimentation [22]. A full factorial design (**Figure 4.2**) was used to investigate the combination of

experimental factors leading to the production of 20 different samples (2×2×5 combinations) with four SPEs prepared in replicate, to evaluate the experimental variability (the set of experiments is reported in **Table 4.1**).

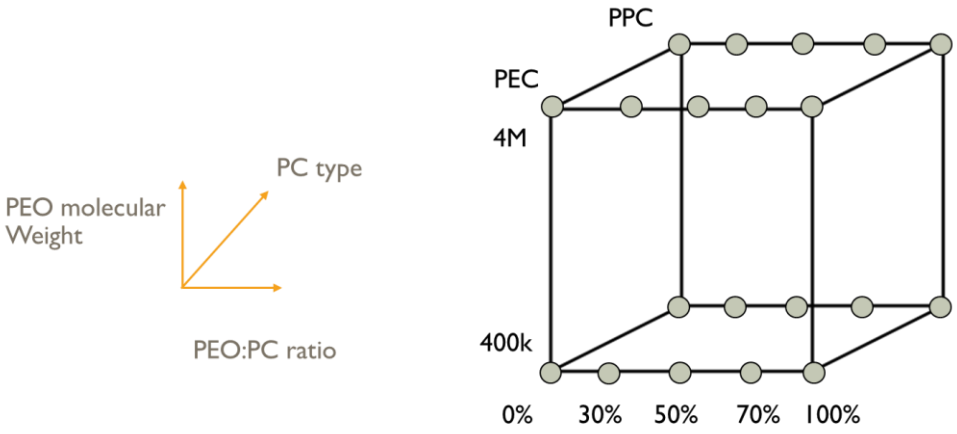

Figure 4.2 Full-factorial design considering three factors: i) PEO molecular weight, ii) polycarbonate (pC) type, iii) ratio of the two polymers.

A multivariate analysis based on multiple linear regression (MLR) was performed to quantify the effects of the experimental variables on the blend properties [23]. For each property (conductivity, voltage, and crystallinity), a regression model has been calculated (at a 90 % confidence level) which is able to describe their variation over the experimental domain investigated.

Table 4.1 Set of Experiments for DoE with the composition of the membranes produced and the three results taken into account.

Exp Name	*PC*	*PEO*	*%PEO*	*Voltage (V)*	*Conductivity (S cm^{-1})*	*Crystallinity (%)*
N1	PEC	400k	0	4.13	3.22×10^{-9}	0
N2	PEC	400k	30	4.66	9.42×10^{-6}	0
N3	PEC	400k	70	4.51	3.4×10^{-5}	30.7
N4	PEC	400k	100	4.48	3.15×10^{-5}	37.0
N5	PEC	4M	0	4.13	5×10^{-10}	0
N6	PEC	4M	30	4.66	7.42×10^{-6}	3.0
N7	PEC	4M	70	4.51	1.43×10^{-5}	22.7
N8	PEC	4M	100	4.64	4.57×10^{-5}	35.9
N9	PPC	400k	0	4.42	5×10^{-10}	0

N10	PPC	400k	30	4.53	5.89×10^{-6}	0
N11	PPC	400k	70	4.54	3.4×10^{-5}	30.9
N12	PPC	400k	100	4.48	2.13×10^{-5}	29.0
N13	PPC	4M	0	4.42	8.19×10^{-10}	0
N14	PPC	4M	30	4.50	1.8×10^{-6}	0
N15	PPC	4M	70	4.65	2.98×10^{-5}	31.7
N16	PPC	4M	100	4.64	2.06×10^{-5}	33.4
N17	PEC	400k	70	4.63	2.83×10^{-5}	17.9
N18	PEC	4M	30	4.65	5.31e-06	0
N19	PPC	400k	30	4.38	1.28×10^{-6}	0
N20	PPC	4M	70	4.54	2.49×10^{-5}	21.6
N21	PEC	400k	50	4.66	4.58×10^{-5}	15.6
N22	PEC	4M	50	4.66	2.39×10^{-5}	1.31
N23	PPC	400k	50	4.66	1.36×10^{-5}	21.6
N24	PPC	4M	50	4.69	9.36×10^{-6}	18.6

4.3 Thermal properties

Thermal analyses were performed to evaluate the thermal stability of the prepared membrane. TGA thermograms (**Figure 4.3**) pointed out that PEO shows a start in decomposition around 370 – 375 °C for both M_ws, while PCs start decomposing at lower temperatures, namely 218 °C for PEC and 240 °C for PPC.

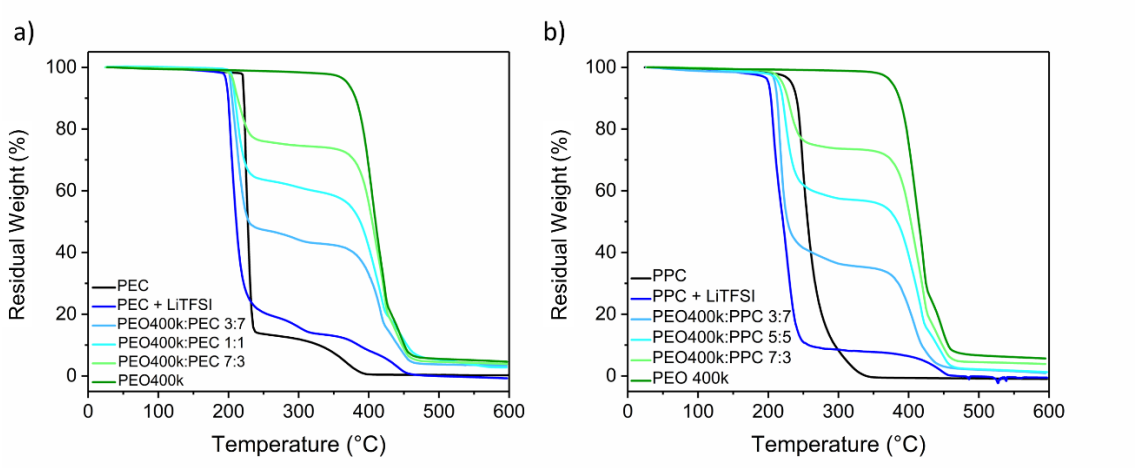

Figure 4.3 TGA thermograms of the polymer under N_2 from 0 to 600 °C for PEO400k mixed with different ratio of PEC (a) and PPC (b).

The addition of LiTFSI influences the thermal stability of PEO and PCs differently. For PEO, the thermogram evidences a two-step decomposition at 380 – 390 °C and 430 °C. The first decomposition step, which is slightly shifted, is related to the chain scission of the polymer. The second decomposition step is caused by complexation of LiTFSI with ethylene oxide units [24,25]. On the contrary, a reduction to 200 °C was observed for PCs, generally associated with the use of PCs and the catalytic activity of LiTFSI in triggering the depolymerization process at high temperatures [26,27]. The overall effect of the PC addition is a slight reduction in the thermal stability of about 20 °C. However, the TGA thermal stability of all the compositions remains up to 190 °C, which is considered sufficiently since the operative temperature of cells is not expected to exceed 100 °C, assuring high safety levels in normal conditions as well as in case of thermal runaways [28,29]. As expected, the thermograms of the PEO-PC mixtures evidence two main degradation steps, the first associated with PCs degradation and the second related to PEO and LiTFSI degradation. The mass loss relative to the two polymer degradations agrees with the PEO:PCs formulations ratio introduced in the extruder. The residual mass at 600 °C is associated with the LiTFSI residue, and the differences among samples are related to the slightly different quantities of salt used to maintain the same [EO]:[Li] ratio at 20:1.

DSC analyses were carried out to evaluate the effects of LiTFSI salt and the influence of PCs on the crystallinity degree (**Figure 4.4**). Both types of neat PEO showed a crystallinity degree of 70 %, and the addition of LiTFSI salt halved the crystallinity, thanks to the high solubility and interaction of Li^+ with the polymer

chains and the plasticizing effect of $TFSI^-$ anion [30]. The bis(fluorosulfonyl)imide anion interacts with PEO chains preventing dense packing of the polymer segments and increasing the chain mobility [31,32]. This disruption of the crystalline structure increases the amorphous region within the polymer matrix.

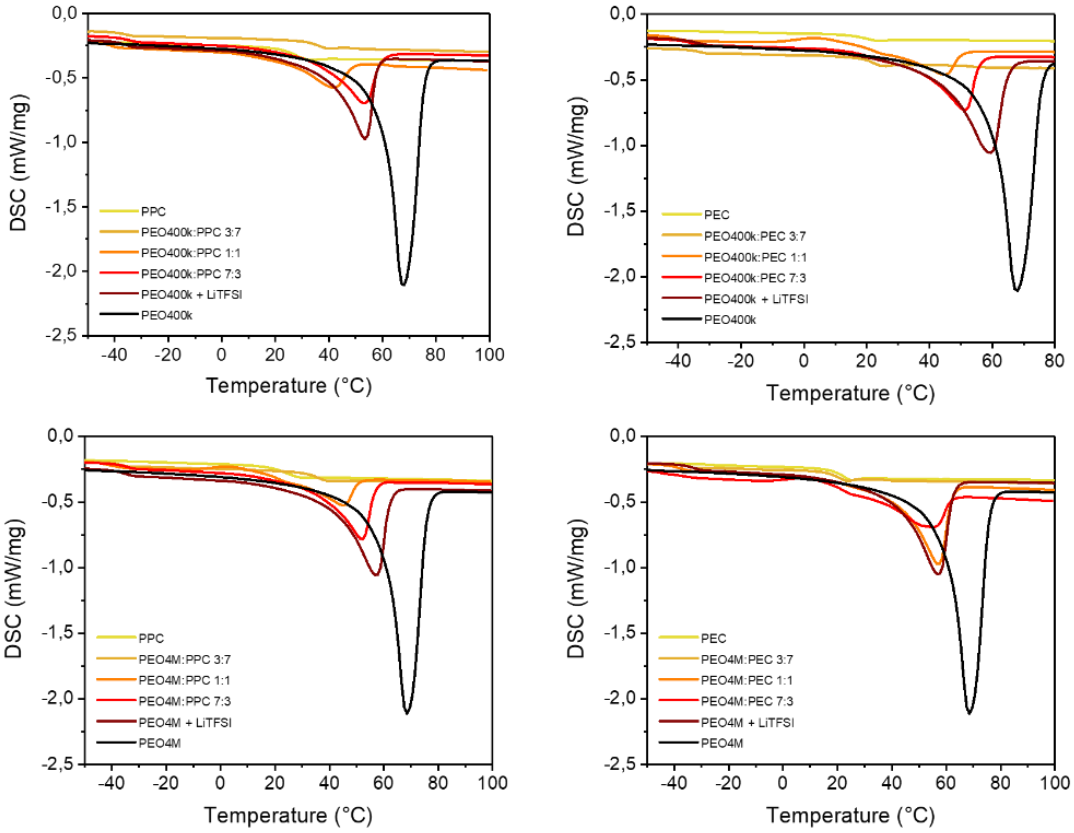

Figure 4.4 DSC thermograms under N_2 recorded from -50 to 100 °C at a heating rate of 10 °C min^{-1}.

Moreover, as highlighted in **Figure 4.5a**, the intensity of the melting peaks decreases and shifts to lower temperatures when the polycarbonate ratio increases [33]. The multivariate analysis of the crystallinity values measured for the different blend compositions (**Table 4.2**) evidence that the amount of PEO is the sole relevant variable influencing this parameter (**Figure 4.5b**). In particular, the crystallinity degree decreases proportionally to the percentage of PEO in the blend. The predicted variation of crystallinity shows that the blend becomes completely amorphous at values equal to or lower than 40 % (**Figure 4.5c**) of PEO.

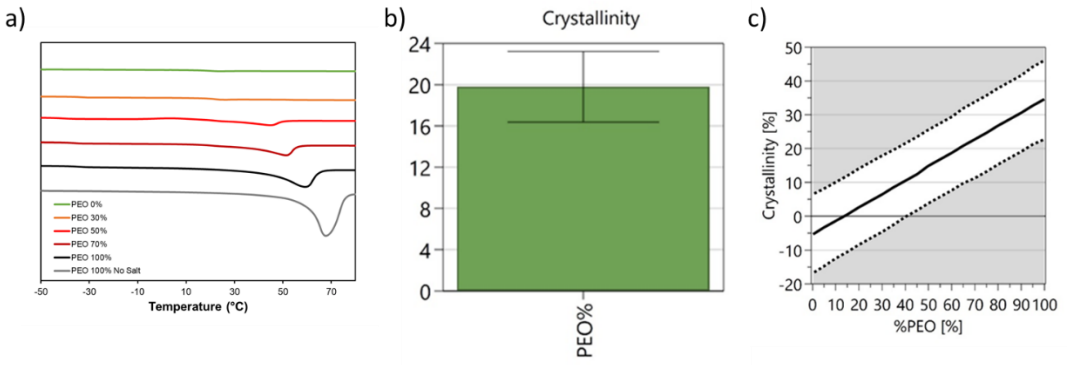

Figure 4.5 a) Detail of DSC measurements of PEO/PEC blends under N_2 from −50 to 100 °C; b) regression coefficients plot for the conductivity and crystallinity models; model equation for crystallinity (%) y = 14.62 + 19.79 * % PEO, (R^2 = 0.82); c) effect of the % of PEO on the crystallinity calculated from DoE analysis. In this case, the mathematical fitting goes below 0 % of crystallinity, which has no physical sense due to the impossibility of setting a lower limit.

On the contrary, the molecular weight of PEO and the structural unit of PC did not seem to affect the resulting crystallinity. Moving toward the use of these polymer membranes as SPEs, a reduced crystallinity is expected to increase the lithium-ion conductivity, particularly at room temperature. Among the two types of polycarbonate tested, the formulations containing PEC showed a higher reduction in crystallinity values, most likely associated with the lower T_g of the PEC polymer. Instead, no significant changes in the T_α values (obtained from DMA analysis) were observed in all formulations, as reported in **Table 4.2**. The presence of both relaxation peaks of PEO and PCs pointed out that the polymers are slightly soluble.

Table 4.1. T_α values (obtained from DMA) and percentage of crystallinity (cryst.%, obtained from DSC) for all samples.

PC (%)	PEO 4M /PEC formulations			PEO 4M /PPC formulations			PEO 400k /PEC formulations			PEO 400k /PPC formulations		
	T_α PEO (°C)	T_α PEC (°C)	Cryst. (%)	T_α PEO (°C)	T_α PPC (°C)	Cryst. (%)	T_α PEO (°C)	T_α PEC (°C)	Cryst. (%)	T_α PEO (°C)	T_α PPC (°C)	Cryst. (%)
0	-30	-	35	-30	-	35	-32	-	33	-32	-	33
30	-33	22	33	-34	37	19	-33	25	24	-34	36	22
50	-36	-	1	-31	40	9	-33	23	8	-31	39	11
70	-36	23	0	-33	40	0	-33	21	0	-32	40	0
100	-	21	0	-	26	0	-	21	0	-	26	0

Relevant information about the T_g values of the tested formulations can be obtained from DSC measurements, even if, in most cases, the melting peak overlaps

the signal related to PC's T_g. Firstly, the addition of LiTFSI increased the T_g of PEO from −50 to −35 °C, as reported in the literature [34], whereas the T_g of PCs was less affected by the salt addition, changing from 14 to 20 °C for PEC and from 27 to 25 °C for PPC. The presence of two different T_gs is in agreement with the DMA analysis, confirming that PEO and PEC/PPC are not miscible, suggesting phase separation within the blend. Finally, the addition of PCs to the LiTFSI-PEO system allows it to reach lower crystallinity values.

4.4 Mechanical and Morphological Characterization

DMA thermograms were performed in a temperature range from −60 to 60 °C for the formulation containing 50 wt.% of PEC and PEO 400k, which can be compared to the pure PEO 400k formulation. Due to the quite similar storage and loss modulus values, resulting in limited significance in evaluating the best formulation, the DMA thermograms are considered only to assess the T_α of the materials (corresponding values are reported in **Table 4.2**). In this case, two different T_α can be pointed out for the two-component formulation, indicating a phase separation.

The SPE films obtained after hot-pressing were flexible, self-standing, and homogeneous by naked eye. Morphologies of the three polymer blends composed of PEO and PEC at varying weight ratios (30, 50, and 70 wt.% of PEC, respectively) were investigated by SEM analysis. SEM images of the polymer blends revealed that all three compositions exhibited a smooth and homogeneous surface. No distinct domains or phase boundaries attributable to PEO or PEC can be observed, irrespective of the weight ratios, at the reported magnification (**Figure 4.6**).

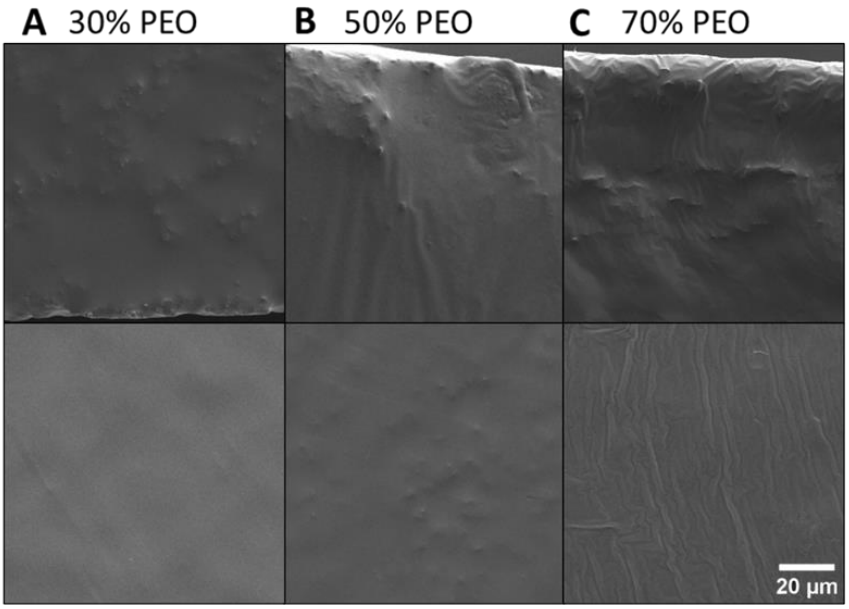

Figure 4.6 SEM micrographs of the cross-section (top) and the surface (bottom) of the PEO/PEC blend with 30 % (A), 50 % (B), and 70 % (C) of PEO.

The micrographs obtained from the surface analysis displayed a uniform and continuous appearance, suggesting that the PEO and PEC components should be well-homogenised on a microscale level. The cross-sectional study of the polymer blends yielded similar results to the surface analysis. It indicates that the manufacturing process resulted in highly uniform blends. The phase separation observed by DSC and DMA might be visible only at higher magnification and resolution in SEM images. However, obtaining better quality images is out of the scope of the present work, which is related to optimising the thermal and electrochemical properties of the polymer blends.

4.5 Electrochemical Properties

The practical utility of SPEs is influenced by their ionic conductivity, which can be determined by EIS analysis. All Arrhenius plots of PEO 400k/PEC formulations in a temperature range of 0 – 80 °C are shown in **Figure 4.7a**.

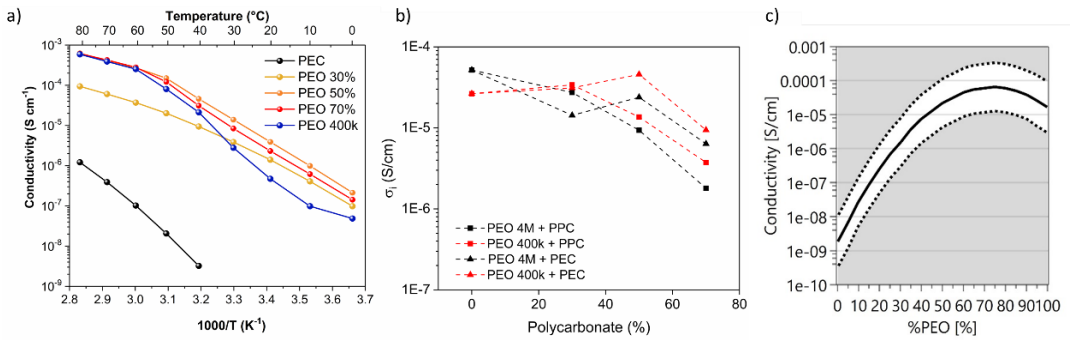

Figure 4.7 Arrhenius plot of ionic conductivity versus inverse temperature determined by EIS in the range of 0−80 °C for PEO 400k/PEC formulations (a). Comparison of the conductivity values at 40 °C varying the percentual of polycarbonate in the blend (b). Effect of the % PEO on the conductivity calculated from DoE analysis (c).

At temperatures above 50 °C, PEO displayed similar conductivity to the blends due to the melting of PEO crystalline domains that occur at around 50 °C. Above this temperature, the material is completely amorphous which improves ion mobility. However, at lower temperatures, the electrolytes made of PEO/PC show better ionic conductivity compared to the pure PEO. This is related to the reduction in crystallinity of PEO in the system, as demonstrated by the DSC thermograms. Thus, at lower temperatures, the blend of PEO with amorphous PCs possesses higher ion conduction properties.

Moreover, the slope of the profile in the high-temperature region (80 – 50 °C) is different from the slope in the low-temperature region (50 – 0 °C). The reason behind this effect is the recrystallisation of PEO that occurs at temperatures lower than 50 °C. This effect is less pronounced in the profiles of the PEO/PC blends due to the lower crystallinity of these systems. The σ_i values at 40 °C are shown in **Figure 4.7b**. In addition, it is observable that in all blends, SPEs with PEO 400k showed slightly higher conductivity compared to those containing PEO 4M. Low molecular weight PEO has shorter polymer chains, which generally result in higher segmental mobility [55]. This increased mobility facilitates ion transport, enhancing ionic conductivity. This is in accordance with the study of Teran et al., who found that the conductivity is proportional to $1/M_w$ in a PEO/LiTFSI electrolyte [56].

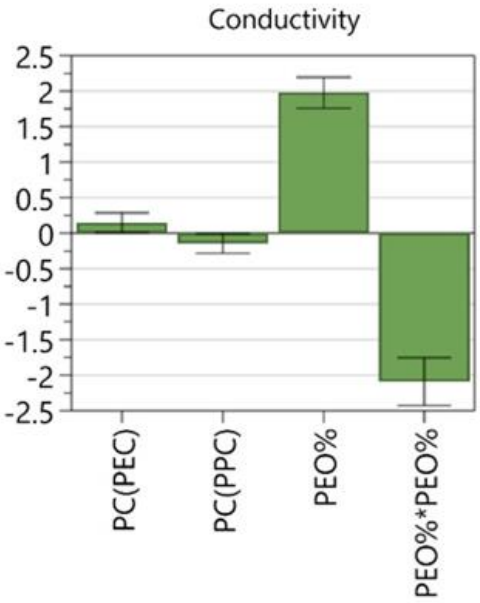

Figure 4.8 Regression coefficients plot for the conductivity models. Model equations for conductivity (S cm^{-1}) Log(y) = - 4.67 + 1.94 * % PEO - 2.04 * % PEO * % PEO + 0.15* PC (PEC) – 0.15 * PC (PPC), (R^2 = 0.95)

The effects of PC and PEO types, as well as the % PEO, on the conductivity were evaluated at 40 °C through DoE analysis. Among them, the main influential variable is the percentage of PEO in the blend (**Figure 4.8**). Generally, conductivity at values 40 °C improved from 10^{-9} to 10^{-5} S cm^{-1} with increasing the quantity of PEO from 0 to 50 %, respectively. The blends with 50% of PCs displayed the best conductivity in the range of 10^{-5} S cm^{-1} at 40 °C. This value is comparable with the PEO and PCs electrolyte obtained by co-polymerization or solvent casting blend reported by other authors in the literature [57,58]. Above such percentage, the values remained quite stable, and only a slight decrease is observed with pure PEO (**Figure 4.5c**). In addition to % of PEO, the type of PC shows a lower effect on the conductivity, where the use of PEC, instead of PPC, leads to slightly higher values. Contrary to previous observations, molecular weight is not considered a significant factor in DoE analysis. Among all the polyelectrolytes tested, PEO 400k:PEC 1:1 exhibited the highest ionic conductivity (4.58×10^{-5} S cm^{-1}).

When comparing SPEs with the same polycarbonate content, it is evident that the type of polycarbonate plays a role in determining ionic conductivity. PEC-based SPEs generally exhibited higher conductivity compared to PPC-based ones and the reason can be attributed to the intrinsic higher conductivity of the pure PEC, which is higher than PPC (**Figure A1**). Moreover, the molecular weight of PEO influenced the conductivity of the electrolyte when considering samples with only PEO.

Despite a high conductivity of PEO 4M, SPEs with PEO 400k showed close conductivity compared to the same blends made with PEO 4M.

The electrochemical stability window of PEO/PC blends was evaluated using linear sweep voltammetry at 40 °C. By applying This characterization technique aimed at demonstrating the potential threshold for electrolyte degradation up to a certain cut-off voltage. Oxidation stability of all blends was compared to observe any effects resulting from the factors examined. The results of the LSV curve for the blend of PEO 4M and PEC are shown in **Figure 4.9a**. It can be observed that the potential of neat PEO-based SPE starts to increase around 4.3 V vs. Li^+/Li; as the voltage is increased, the oxidation current increases sharply. However, it is evident that upon the addition of amorphous PEC, the voltage at which oxidative decomposition takes place increases gradually. A value of 4.64 V vs. Li^+/Li is reached when 70 % of PEC is added. These findings indicate that the electrochemical stability of blend SPEs can be enhanced by adding PEC, with the stability improvement being directly related to PEC content. This enhancement is attributed to the wide ESW of PCs [30]. Notably, the oxidation peak of water is not observable in all samples, meaning that the drying process is efficient enough to remove all traces of water that can eventually be contained in both PEO and LiTFSI components.

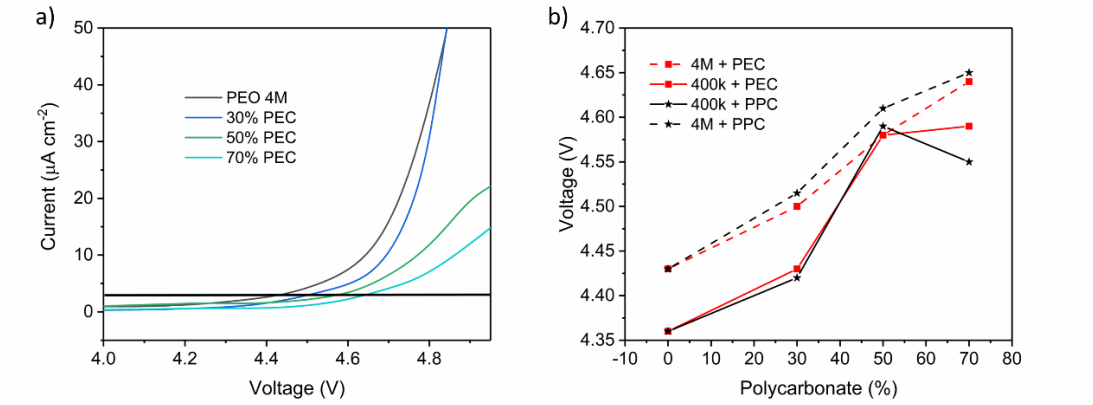

Figure 4.9 Linear sweep voltammetry (LSV) for neat PEO and PEO-PEC blends (a). Comparison of the voltage value varying the percentage of polycarbonate; cut-off current threshold: 3 µA cm^{-2} (b).

This result, along with no substantial weight loss at around 100 °C in the TGA, suggests that the extrusion process allowed the production of polymer blends without water contamination or degradation of the polymers. Then, the oxidation stability was evaluated for all the blends **Figure 4.9b** shows the voltage stability evaluated at the threshold of a leak current of 3 µA cm^{-2}. The evaluation has excluded the LSV of pure PC membranes due to the much lower ionic conductivity

at 40 °C of polycarbonates, which influences the obtained values. For this reason, it was not possible to conduct a multivariate analysis for this parameter because of the lack of data. The figure shows that the % PC is the most influential variable. Among the experimental trials, PEO 4M:PPC 3:7 exhibited the highest anodic stability (4.65 V). Varying the weight ratio of PEO and PC within the polymer blend leads to a variation in the electrochemical stability with a general improvement, reaching a maximum around the ratio 3:7 of PEO/PC. On the contrary, PC type and PEO's molecular weight have a lower impact on voltage stability. Varying the molecular weight of PEO was shown to influence voltage stability, with blends containing PEO 4M displaying improved stability. Differently, the type of PC has a lower influence on the oxidation potential, and the SPEs containing PPC are proven to have slightly better electrochemical stability. This result, along with no substantial weight loss at around 100 °C in the TGA, suggests that the extrusion process allowed the production of salt-in-polymer blends without water contamination or degradation of the polymers, with promising prospects as SPEs in ASSLMBs.

4.6 Concluding Remarks

In this initial experimental Chapter, results were reported regarding the development of a series of truly-solid SPEs by incorporating two types of polycarbonates, viz. polyethylene and polypropylene carbonate, in a PEO-based matrix encompassing LiTFSI salt. Different molecular weight PEOs and compositions (from 0 to 100 % of PEO) were investigated to optimize the final polyelectrolyte properties, such as crystallinity, electrochemical stability window, and ionic conductivity. Blend SPEs were successfully produced by employing a mini-compounder to mix the precursors materials in one pot, homogeneously and efficiently. The process is fully solvent-free as it avoids the use of organic solvents and is easily up-scalable, thus ready to find practical industrial applications. Homogeneous mixing of the component was confirmed by SEM images, which did not reveal any distinct domain at the micrometer scale.

The addition of amorphous PC led to a substantial decrease in crystallinity, which is attested to around 10 % when 50 % of PEO is used. No relevant effect was induced by the type of PC used. In addition, all blends exhibited improved ionic conductivity up to a threshold of 50 % of PEO, while further decrease in the PEO

percentage was detrimental to conductivity. The sample PEO400k, with 50 % of PEC, displayed the best ionic conductivity among the series with 4.6×10^{-5} S cm^{-1} at 40 °C, showing an increase of 57 % with respect to the SPE with only PEO 400k. The ESW also took advantage of the addition of PCs, reaching a maximum in the anodic stability for the formulation with 70 % of PEO. Enhanced breakdown value of 4.65 V was reached for PEO 4M with 70 % of PPC, indicating a beneficial role of PCs. The statistical analyses of the experimental results by a DoE approach confirmed that the most important parameter that should be taken into account is the quantity of PEO, showing an excellent trade-off among all properties for a ratio of PEO 400k:PEC 1:1. The possibility of readily scale up the solvent-free production process and the improved mechanical and electrochemical performances make the LiTFSI-PEO/PC blended SPE a promising candidate for next-generation solid-state Li-based energy storage technologies.

References

[1] J.B. Goodenough, K.S. Park, The Li-ion rechargeable battery: A perspective, J. Am. Chem. Soc. 135 (2013) 1167–1176. https://doi.org/10.1021/ja3091438.

[2] T. Cai, Y. Wang, F. Zhao, Z. Ma, P. Kumar, H. Xie, C. Sun, J. Wang, Q. Li, Y. Guo, J. Ming, Graphic, Quantitation, Visualization, Standardization, Digitization, and Intelligence of Electrolyte and Electrolyte-Electrode Interface, Adv. Energy Mater. 14 (2024) 2400569. https://doi.org/10.1002/aenm.202400569.

[3] B. Dunn, H. Kamath, J.-M. Tarascon, Electrical Energy Storage for the Grid: A Battery of Choices, Science 334 (2011) 928–935. https://doi.org/10.1126/science.1212741.

[4] S. Zhang, K. Ueno, K. Dokko, M. Watanabe, Recent Advances in Electrolytes for Lithium-Sulfur Batteries, Adv. Energy Mater. 5 (2015) 1500117. https://doi.org/10.1002/aenm.201500117.

[5] J.I. Lee, M. Shin, D. Hong, S. Park, Efficient Li-Ion-Conductive Layer for the Realization of Highly Stable High-Voltage and High-Capacity Lithium Metal Batteries, Adv. Energy Mater. 9 (2019) 1803722. https://doi.org/10.1002/aenm.201803722.

[6] Y. Liu, D. Lin, Z. Liang, J. Zhao, K. Yan, Y. Cui, Lithium-coated polymeric matrix as a minimum volume-change and dendrite-free lithium metal anode, Nat. Commun. 7 (2016) 10992. https://doi.org/10.1038/ncomms10992.

[7] Y. Chen, Z. Ma, Y. Wang, P. Kumar, F. Zhao, T. Cai, Z. Cao, L. Cavallo, H. Cheng, Q. Li, J. Ming, Trace ethylene carbonate-mediated low-concentration ether-based electrolytes for high-voltage lithium metal batteries, Energy Environ. Sci. 17 (2024) 5613. https://doi.org/10.1039/d4ee01831a.

[8] H. Liang, Z. Ma, Y. Wang, F. Zhao, Z. Cao, L. Cavallo, Q. Li, J. Ming, Solvent-Solvent Interaction Mediated Lithium-Ion (De)intercalation Chemistry in Propylene Carbonate Based Electrolytes for Lithium-Sulfur Batteries, ACS Nano 17 (2023) 18062–18073. https://doi.org/10.1021/acsnano.3c04790.

[9] D. Lv, Y. Shao, T. Lozano, W.D. Bennett, G.L. Graff, B. Polzin, J. Zhang, M.H. Engelhard, N.T. Saenz, W.A. Henderson, P. Bhattacharya, J. Liu, J. Xiao, Failure mechanism for fast-charged lithium metal batteries with liquid electrolytes, Adv. Energy Mater. 5 (2015) 1400993. https://doi.org/10.1002/aenm.201400993.

[10] X. Zheng, L. Huang, X. Ye, J. Zhang, F. Min, W. Luo, Y. Huang, Critical effects of electrolyte recipes for Li and Na metal batteries, Chem 7 (2021) 2312–2346. https://doi.org/10.1016/j.chempr.2021.02.025.

[11] A. Manthiram, X. Yu, S. Wang, Lithium battery chemistries enabled by solid-state electrolytes, Nat. Rev. Mater. 2 (2017) 16103. https://doi.org/10.1038/natrevmats.2016.103.
[12] Q. Zhao, S. Stalin, C.Z. Zhao, L.A. Archer, Designing solid-state electrolytes for safe, energy-dense batteries, Nat. Rev. Mater. 5 (2020) 229–252. https://doi.org/10.1038/s41578-019-0165-5.
[13] L. Fan, S. Wei, S. Li, Q. Li, Y. Lu, Recent Progress of the Solid-State Electrolytes for High-Energy Metal-Based Batteries, Adv. Energy Mater. 8 (2018) 1702657. https://doi.org/10.1002/aenm.201702657.
[14] Y. An, X. Han, Y. Liu, A. Azhar, J. Na, A.K. Nanjundan, S. Wang, J. Yu, Y. Yamauchi, Progress in Solid Polymer Electrolytes for Lithium-Ion Batteries and Beyond, Small 18 (2022) 2103617. https://doi.org/10.1002/smll.202103617.
[15] L. Long, S. Wang, M. Xiao, Y. Meng, Polymer electrolytes for lithium polymer batteries, J. Mater. Chem. A Mater. 4 (2016) 10038–10069. https://doi.org/10.1039/c6ta02621d.
[16] G. Wang, X. Zhu, A. Rashid, Z. Hu, P. Sun, Q. Zhang, L. Zhang, Organic polymeric filler-amorphized poly(ethylene oxide) electrolyte enables all-solid-state lithium-metal batteries operating at 35 °C, J. Mater. Chem. A Mater. 8 (2020) 13351–13363. https://doi.org/10.1039/d0ta00335b.
[17] W. Zhou, Z. Wang, Y. Pu, Y. Li, S. Xin, X. Li, J. Chen, J.B. Goodenough, Double-Layer Polymer Electrolyte for High-Voltage All-Solid-State Rechargeable Batteries, Advanced Materials 31 (2019) 1805574. https://doi.org/10.1002/adma.201805574.
[18] J. Mindemark, M.J. Lacey, T. Bowden, D. Brandell, Beyond PEO—Alternative host materials for Li+-conducting solid polymer electrolytes, Prog. Polym. Sci. 81 (2018) 114–143. https://doi.org/10.1016/j.progpolymsci.2017.12.004.
[19] Z. Xue, D. He, X. Xie, Poly(ethylene oxide)-based electrolytes for lithium-ion batteries, J. Mater. Chem. A Mater. 3 (2015) 19218–19253. https://doi.org/10.1039/c5ta03471j.
[20] L. Stolz, S. Hochstädt, S. Röser, M.R. Hansen, M. Winter, J. Kasnatscheew, Single-Ion versus Dual-Ion Conducting Electrolytes: The Relevance of Concentration Polarization in Solid-State Batteries, ACS Appl. Mater. Interfaces 14 (2022) 11559–11566. https://doi.org/10.1021/acsami.2c00084.
[21] H.M.J.C. Pitawala, M.A.K.L. Dissanayake, V.A. Seneviratne, B.E. Mellander, I. Albinson, Effect of plasticizers (EC or PC) on the ionic conductivity and thermal properties of the (PEO)9LiTf: Al2O3 nanocomposite polymer electrolyte system, Journal of Solid State Electrochemistry 12 (2008) 783–789. https://doi.org/10.1007/s10008-008-0505-7.
[22] R. Leardi, Experimental design in chemistry: A tutorial, Anal. Chim. Acta 652 (2009) 161–172. https://doi.org/10.1016/j.aca.2009.06.015.
[23] M. Sergent, D. Mathieu, R. Phan-Tan-Luu, G. Drava, Chemometrics and intelligent laboratory systems Tutorial Correct and incorrect use of

multilinear regression, Chemometrics and Intelligent Laboratory Systems 27 (1995) 153–162.
[24] Y. Tominaga, V. Nanthana, D. Tohyama, Ionic conduction in poly(ethylene carbonate)-based rubbery electrolytes including lithium salts, Polym. J. 44 (2012) 1155–1158. https://doi.org/10.1038/pj.2012.97.
[25] B.N. Choi, J.H. Yang, Y.S. Kim, C.H. Chung, Effect of morphological change of copper-oxide fillers on the performance of solid polymer electrolytes for lithium-metal polymer batteries, RSC Adv. 9 (2019) 21760–21770. https://doi.org/10.1039/c9ra03555a.
[26] B. Commarieu, A. Paolella, S. Collin-Martin, C. Gagnon, A. Vijh, A. Guerfi, K. Zaghib, Solid-to-liquid transition of polycarbonate solid electrolytes in Li-metal batteries, J. Power Sources 436 (2019) 226852. https://doi.org/10.1016/j.jpowsour.2019.226852.
[27] A. Buchheit, M. Grünebaum, B. Teßmer, M. Winter, H.D. Wiemhöfer, Polycarbonate-Based Lithium Salt-Containing Electrolytes: New Insights into Thermal Stability, Journal of Physical Chemistry C 125 (2021) 4371–4378. https://doi.org/10.1021/acs.jpcc.0c09968.
[28] K. Kimura, J. Hassoun, S. Panero, B. Scrosati, Y. Tominaga, Electrochemical properties of a poly(ethylene carbonate)-LiTFSI electrolyte containing a pyrrolidinium-based ionic liquid, Ionics (Kiel). 21 (2015) 895–900. https://doi.org/10.1007/s11581-015-1370-x.
[29] L. Porcarelli, C. Gerbaldi, F. Bella, J.R. Nair, Super Soft All-Ethylene Oxide Polymer Electrolyte for Safe All-Solid Lithium Batteries, Sci. Rep. 6 (2016). https://doi.org/10.1038/srep19892.
[30] H. Zhang, C. Liu, L. Zheng, F. Xu, W. Feng, H. Li, X. Huang, M. Armand, J. Nie, Z. Zhou, Lithium bis(fluorosulfonyl)imide/poly(ethylene oxide) polymer electrolyte, Electrochim. Acta 133 (2014) 529–538. https://doi.org/10.1016/j.electacta.2014.04.099.
[31] H. Zhang, C. Liu, L. Zheng, F. Xu, W. Feng, H. Li, X. Huang, M. Armand, J. Nie, Z. Zhou, Lithium bis(fluorosulfonyl)imide/poly(ethylene oxide) polymer electrolyte, Electrochim. Acta 133 (2014) 529–538. https://doi.org/10.1016/j.electacta.2014.04.099.
[32] A. Vallèe, S. Besner, J. Prud'homme, Comparative study of poly(ethylene oxide) electrolytes made with LiN(CF3SO2)2, LiCF3SO3 and LiClO4: Thermal properties and conductivity behaviour, Elctrochimica Acta 37 (1992) 1579–1583.
[33] C. Li, Q. Kong, Q. Fan, Y. Xia, Crystallization behavior of polycarbonate/poly(ethylene oxide) blends studied by DSC, Mater. Lett. 59 (2005) 773–778. https://doi.org/10.1016/j.matlet.2004.11.018.
[34] M. Polaskova, P. Peer, R. Cermak, P. Ponizil, Effect of thermal treatment on crystallinity of poly(ethylene oxide) electrospun fibers, Polymers 11 (2019) 1384. https://doi.org/10.3390/polym11091384.

Chapter 5

Effect of UV-crosslinking on poly(ethylene oxide)-polycarbonate solid-state electrolytes

Following the results presented in the previous Chapter 4, where solvent-free extrusion enabled the preparation of homogeneous PEO/polycarbonate truly solid polymer electrolytes with improved crystallinity, ionic conductivity, and electrochemical stability compared with neat PEO. The present Chapter investigates a further step to enhance their practical performance. In particular, the PEO/PEC blends obtained by extrusion showed a promising balance of properties, but their application is still limited by the intrinsic drawbacks of PEO-based electrolytes, including modest oxidative stability, low room-temperature conductivity, and degradation phenomena at the electrode/electrolyte interfaces, especially under high-voltage or prolonged thermal operating conditions [1–6].

Blending with polycarbonates is attractive because these polymers are largely amorphous, electrochemically more stable than PEO, and able to support lithium-ion transport while preserving processability and low cost [7–10]. However, polycarbonates such as PEC may themselves undergo degradation in the presence of lithium salts, owing to the combination of strong Lewis-acidic lithium ions and weakly coordinating anions such as $TFSI^-$ [11]. Therefore, once the composition and solvent-free processing route were optimized in Chapter 4, improving the

chemical and interfacial stability of the extruded PEO/PEC system became the next key objective.

To address this issue, this Chapter introduces a UV-induced crosslinking step after extrusion by adding a fluorinated benzophenone derivative, selected for its compatibility with the processing temperature of extrusion and its dual role as hydrogen abstractor and photoinitiator [12–14]. The aim was to suppress or limit PEC degradation, stabilize the polymer matrix, and further improve the electrochemical behavior of the SPEs. The resulting UV-cured SPEs were investigated in terms of thermal and electrochemical stability, lithium plating/stripping behavior, and compatibility with LFP cathodes (obtained in the form of a catholyte as detailed in Chapter 3) and lithium metal, while NMR analysis was used to directly compare degradation processes in cured and non-cured systems. Overall, the results detailed in this Chapter demonstrate how the combination of solvent-free extrusion and post-processing photopolymerization can extend the performance of PEO/PEC-based SPEs toward more reliable truly ASSLMBs. These results have been published in the scientific research article M. Gastaldi, F. Gambino *et al.*, Mater. Today Energy 52 (2025) 101947 and are reproduced/readapted in the following sections.

5.1 Preparation of the UV-crosslinked SPEs

All formulations were prepared under inert atmosphere following the optimised solvent-free procedure in the mini extruder detailed in Section 4.1 in Chapter 4 [15]. However, in this case after introducing into the extruder a first portion of the PEO/PEC formulation followed by LiTFSI salt, the photoinitiator 4-4'-difluorobenzophenone was added in the case of the UV-crosslinkable SPE formulation; eventually, the last part of the PEO/PEC formulation was then added. The extruded formulations in the form of filaments were used to prepare the blend SPEs (namely, PEO-PEC, ~10 cm in diameter films having a thickness of about 100 μm). To crosslinked samples (PEO-PEC-UV) by the same hot-pressing procedure, followed by UV-induced photopolymerization at 40 mW cm^{-2} for 3 min on each side of the SPE (**Figure 5.1**).

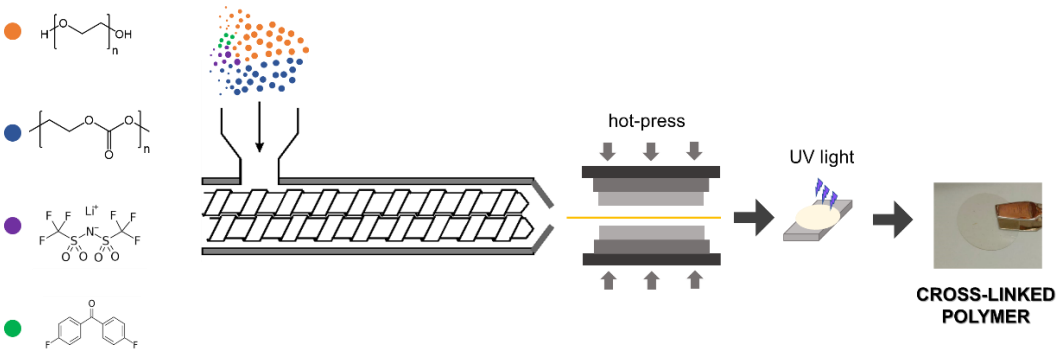

Figure 5.1 Different steps of the preparation method for UV-crosslinked PEO-PEC-UV SPEs. From left to right: the starting materials were introduced into the extruder; after 15 minutes of mixing at 140°C and 130 rpm, the blend was extracted from the extruder in the form of filament; then, the formulation was hot-pressed and exposed to UV light to obtain the truly-solid, ready-to-use, cross-linked SPE.

All SPEs underwent another drying step at 40 °C under vacuum for 12 h in the B-585 oven and then were stored in the glove box before use. The ratio between [EO] and [Li^+] units was fixed at 20:1, reported as optimal in terms of ionic conductivity at high temperatures and reduced stickiness [16], while the best ratio (1:1) among PEO and PEC, reported in Chapter 4, was used here for the polymer fraction. Both the non-UV-cured and UV-cured (crosslinked) SPE samples appear as quasi-transparent and homogeneous SPE membranes.

5.2 Thermomechanical Characterization

Thermogravimetric analysis (TGA) was conducted in an inert atmosphere, simulating the working conditions of the battery, for both the PEO-PEC and PEO-PEC-UV SPEs. From the comparison between the resulting thermograms (**Figure 5.2**), the $T_{d5\%}$ can be increased by around 15 °C after crosslinking, thanks to the new covalent bonds linking the polymer chains. In both cases, degradation starts at temperatures around 200 °C, which are usually not reached under standard operation.

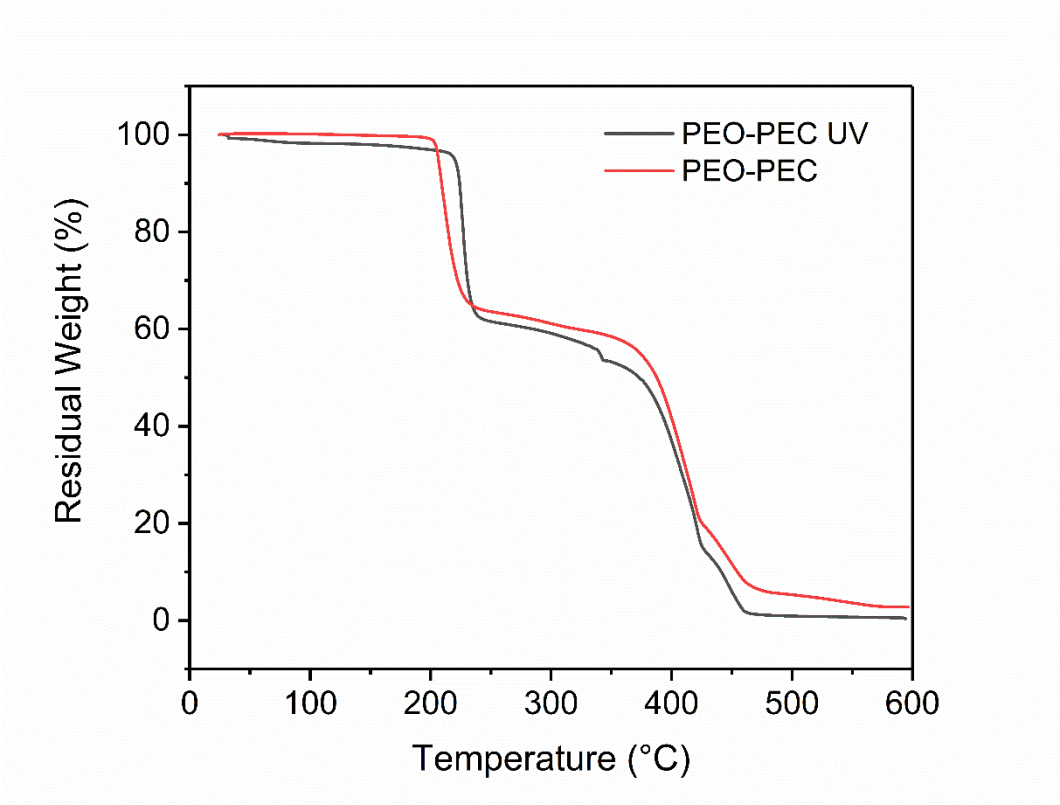

Figure 5.2 TGA thermograms of PEO-PEC (red) and PEO-PEC-UV (black).

These results agree with the reported data [9] for non-extruded materials and demonstrate that no degradations or damage to the polymeric material in the extrusion process took place. As reported previously in Chapter 4, TGA analysis of pure PEO and PEC compounds confirms that both materials exhibit thermal stability up to 200 °C, even in the presence of lithium salt.

Differential scanning calorimetry (DSC) was performed to evaluate the crystallinity of SPE. It is commonly known that crystalline regions should be avoided to enhance the ionic conductivity in the polymer network [13,17,18]. Crosslinking is a suitable method to reduce or even eliminate crystalline regions that hinder ionic conductivity while simultaneously enhancing mechanical properties [19,20].

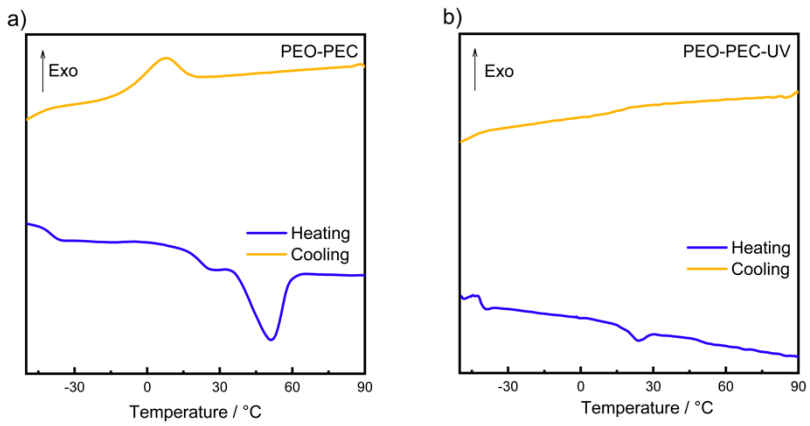

Figure 5.3 DSC thermograms under N_2 from -50 to 90 °C with a heating rate of 10 °C min^{-1} of PEO-PEC (a) and PEO-PEC-UV (b).

As shown in **Fig. 5.3a** for the PEO-PEC, the presence of a melting peak in the range of 40 – 60 °C suggests the presence of crystalline regions, around 8%. Moreover, the presence of two distinct T_g peaks at –39.9 and 22.2 °C, respectively, points out the lithium salt effect in increasing the T_g for PEO [21,22] without affecting the one of PEC, as well as the limited solubility of the two polymers. Indeed, the presence of two different T_g, shown in both thermograms in **Figure 5.3a,b**, highlights the non-miscibility of the two polymers, which remain as two different phases that cannot be distinguished by naked eye nor with SEM pictures, as reported in Chapter 4. For PEO-PEC-UV, instead, the absence of any melting peak in **Figure 5.3b** accounts for the crosslinking effect in avoiding the crystallisation of the sample, making it completely amorphous and revealing only the two different T_g values of PEO and PEC.

Dynamic mechanical analysis was carried out to evaluate the mechanical properties before and after UV-curing (**Figure 5.4**). The presence of two distinct peaks in the E'' curves confirms the immiscibility of PEO and PEC, as discussed in DSC measurements. The first transition at around –30 °C is related to the T_g of PEO, while the second one at 20 °C to PEC. The increase in the T_g value from the pristine PEO (around –60 °C) is related to the addition of LiTFSI that induces coordination among the Li^+ cation and the PEO chains, obtaining a more rigid structure[23].

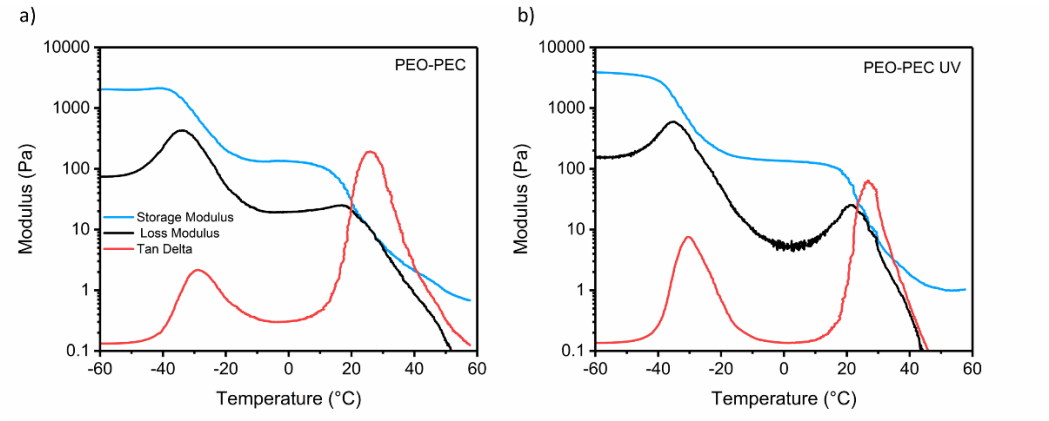

Figure 5.4 DMA curves of PEO-PEC (a) and PEO-PEC-UV (b) SPEs.

The resulting moduli of the polymers above 40 °C are rather low to ensure good mechanical properties and avoid/limit the lithium dendrite formation, but high enough to confer self-standing ability and easy handling to the SPE.

To further investigate the crosslinking procedure, the gel content analysis was carried out by soaking the samples in two different solvents, EtOAc and ACN, which were chosen evaluating the reported solubility of the two polymers. Indeed, while PEC is soluble in the former (as reported in the Technical Data Sheet provided by the supplier), PEO is soluble in the latter, as reported in the literature [24]. As a result, after soaking the sample in EtOAc and drying it until constant weight, 97.9 % of the polymer remains undissolved, while 94.1 % remains after ACN soaking. Part of the weight loss is related to the salt and the photoinitiator included in the formulation, meaning that the crosslinking procedure is effective in covalently linking the polymer chains, trapping part of the lithium salt and the photoinitiator into the matrix. In contrast, the same procedure applied to the PEO-PEC results in its complete dissolution.

5.3 Ionic Conductivity and Electrochemical Characterization

The ionic conductivity was measured from 0 to 80 °C to assess how the introduction of PEC and crosslinking affect the material's properties. As shown in **Figure 5.5a**, pure PEO shows a characteristic change in slope around 60 – 50 °C, corresponding to the melting of its crystalline domains. In contrast, pure PEC shows very low conductivity, even at 80 °C, and becomes undetectable below 40 °C. A

less pronounced slope change is observed for PEO-PEC, with an even smoother curve for PEO-PEC-UV. These results confirm the reduction in crystalline regions from pure PEO to the fully amorphous, PEO-PEC-UV sample. However, a slight reduction in the conductivity values is observed for both PEO-PEC and PEO-PEC-UV at temperatures above 60 °C, attributed to the presence of PEC, which has lower ionic conductivity. Conversely, between 50 and 0 °C, PEC enhances the electrolyte conductivity due to its ability to dissolve lithium salt without forming stable complexes that would otherwise hinder chain mobility. As a result of reduced chain mobility in the PEO-PEC-UV sample, the ionic conductivity at 70 °C decreases from 8.5×10^{-4} S cm^{-1} for the pristine PEO to 4.2×10^{-4} S cm^{-1} for the PEO-PEC sample, and further to 1.8×10^{-4} S cm^{-1} for PEO-PEC-UV, which is a reasonably high value for a truly solid crosslinked polymer electrolyte and its operation in practical Li-metal battery cells.

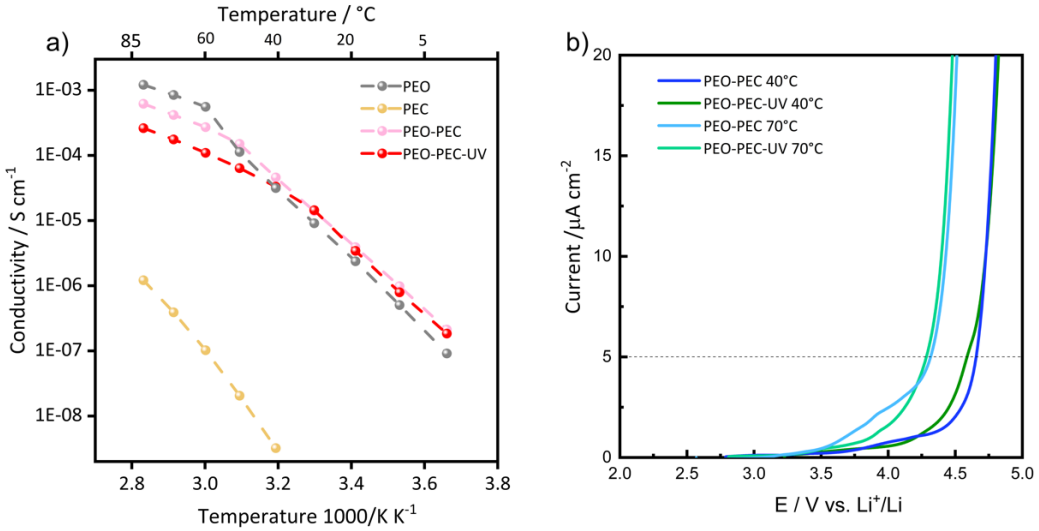

Figure 5.5 Ionic conductivity of PEO-PEC, and PEO-PEC-UV SPEs (a), produced maintaining the same [EO]:[Li$^+$] ratio across all formulations. Electrochemical stability (anodic) in oxidation for both PEO-PEC and PEO-PEC-UV at 40 and 70 °C (b).

Based on the ionic conductivity results, two different temperatures were selected to evaluate the electrochemical performance at 40 and 70°C, to investigate the effect of crosslinking, and assess the thermal stability of the electrolyte, respectively. The electrochemical stability window (ESW) was tested to determine the applicability of these materials as SPEs in lithium metal cells [25,26]. Linear sweep voltammetry (LSV) was employed to evaluate the potential at which possible degradations of the polymeric material occur (**Fig. 5.5b**). At both temperatures, no

significant difference between the PEO-PEC and PEO-PEC-UV samples is detected, with onset potentials of ~ 4.6 V and 4.3 V at 40 °C and 70 °C, respectively, considering a threshold fixed at 5 μA cm^{-2}. While a slight reduction in the oxidation stability is noted as the temperature increases to 70 °C, SPEs still exhibit suitable stability for LFP cathodes.

The Li^+ transference number (t_{Li^+}) reflects the proportion of charge carried by lithium ions and plays a crucial role in controlling the deposition morphology of lithium metal. As shown in **Figure 5.6**, the t_{Li^+} of the electrolyte was determined using the Bruce–Vincent–Evans method. The obtained t_{Li^+} value is 0.17, which is consistent with previously reported values [27].

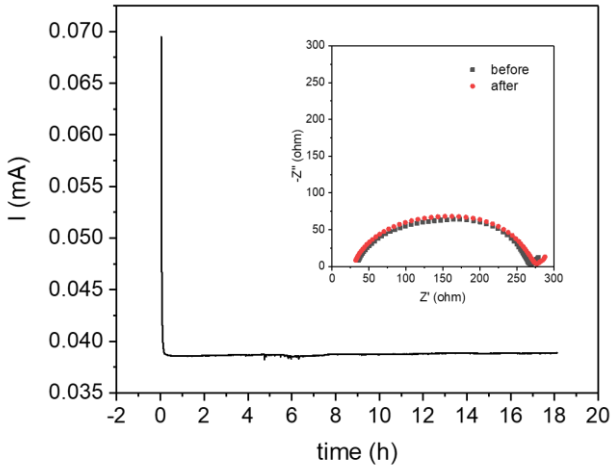

Figure 5.6 Lithium transference number measurement of the PEO-PEC-UV electrolyte at 70 °C.

5.4 Compatibility with the Lithium Metal Electrode

The stability and compatibility of the SPEs at the interface with the lithium metal electrode were investigated through galvanostatic lithium plating/stripping experiments performed at both 40 and 70 °C. At 40 °C, the PEO-PEC SPE fails to sustain even the first plating and stripping cycle (**Figure 5.7a**). In contrast, the crosslinked PEO-PEC-UV withstands testing under the same cell configuration with progressively increasing current densities from 0.025 to 0.2 mA cm^{-2} at both temperatures (**Figure 5.7,c**). At 40 °C, the electrolyte shows good cycling reversibility up to 0.1 mA cm^{-2}, with a maximum overpotential of 0.4 V. When the current is increased to 0.2 mA cm^{-2}, the overpotential exponentially increases;

however, no short circuit occurs (**Figure 5.7b**). The PEO-PEC-UV SPE demonstrates improved rate performance for lithium plating/stripping at 70 °C. As the current density increases from 0.025 to 0.100 mA cm^{-2}, the overpotential rises from 0.02 to 0.11 V (**Figure 5.7c**). Stable cycling is still achieved at 0.2 mA cm^{-2}, with the overpotential increasing to 0.3 V. To ensure the long-term durability and safety of PEO-PEC-UV in lithium metal cells, a prolonged plating/stripping test was conducted at a constant current density of 0.050 mA cm^{-2} (**Figure 5.7d**). Throughout the test, no significant increase in overpotential is observed compared to the initial value, nor are there any sudden or unexpected current spikes or drifts accounting for uneven dendrite formation. During the first hundreds of hours, a slight decrease in overpotential is observed, likely due to the stabilisation process of the cell. Afterward, the cell shows stable behaviour for 600 h, with a steady overpotential of 0.025 V.

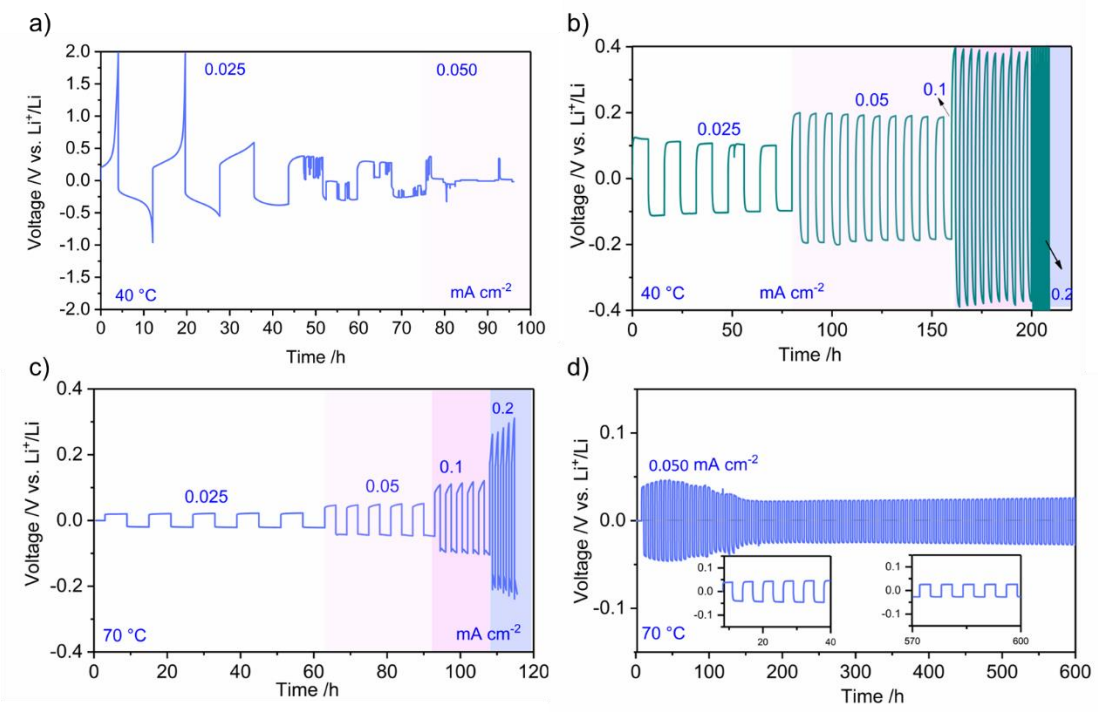

Figure 5.7 Voltage vs. time profiles of galvanostatic plating/stripping in symmetric Li cells, current densities ranging from 0.025 to 0.200 mA cm^{-2} (capacity per half cycle of 0.2 mAh cm^{-2}). The cell employed (a) PEO-PEC at 40 °C, (b) PEO-PEC-UV at 40 °C and (c) PEO-PEC-UV at 70 °C. (d) Long-term reversible cycling performances of PEO-PEC-UV at 0.050 mA cm^{-2} (capacity per half cycle of 0.2 mAh cm^{-2}) at 70 °C.

5.5 Performance of SPE-based Lithium Metal Battery Cells

The practical application of the PEO-PEC-UV SPE in lithium metal cells was tested with a LFP-based electrode, in a high-loading (around 10 mg cm^{-2}) catholyte configuration. **Figure 5.8a** shows the discharge capacity as a function of the current density at C/20, C/10, C/5, and back to C/20 in the 2.5 - 4.0 V vs. Li^+/Li voltage window. During the initial cycle, the cell exhibits a charge capacity of 172.5 mAh g^{-1} with a Coulombic efficiency (CE) of 89.5%. However, after a few cycles, the capacity stabilises at around 168.6 mAh g^{-1} with a CE of 99.9%. These results indicate that the truly solid-state cell delivers excellent rate performance at all tested C-rates, maintaining the same specific charge capacity when the current rate is increased to C/10, with a CE of 99%. At C/5, the capacity slightly drops to 157 mAh g^{-1} with a CE of 98-99%. Meanwhile, the increase in polarisation voltage at different current densities, even after cycling up to 40 cycles, as shown in **Figure 5.8b** and **5.8c**, is negligible, further demonstrating its good cycling reversibility. The promising rate performance of the Li||PEO-PEC-UV||LFP cell with a high-loading cathode can be attributed to the high Li^+ conductivity of the crosslinked SPE, along with excellent electrode-electrolyte compatibility, which promotes homogeneous Li^+ deposition and stable SEI layer formation.

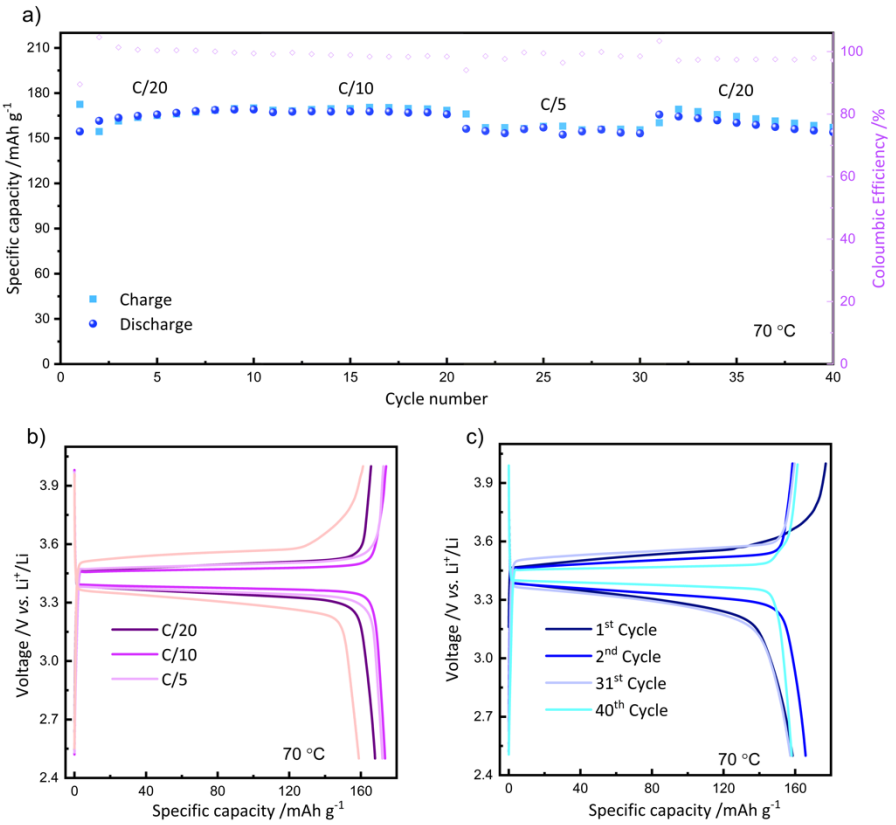

Figure 5.8 Rate capability upon galvanostatic charge/discharge cycling of the Li||PEO-PEC-UV||LFP battery cell at 70 °C (a) and the corresponding voltage vs. specific capacity curves upon charge and discharge (b, c).

Further measurements were performed on PEO-PEC-UV SPE in lithium-metal cells, which were tested with an LFP-based electrode in a high-loading (around 8 mg cm^{-2}) catholyte configuration at a lower temperature (40 °C), as shown in **Figure 5.9**. As can be observed, the cell exhibits an initial charge capacity of 165.5 mAh g^{-1} with an initial CE of 77.7% at C/50. After activation and stabilisation of the electrode-electrolyte interface, the capacity remains stable with a CE of 99% at both C/50 and C/20. However, the cell shows a capacity drop at C/10 and a slight decrease when returning to C/20 after 40 cycles. From these results, we can conclude that the crosslinking enhances the mechanical properties, limiting the lithium dendrites formation and growth, thus enabling stable cell cycling.

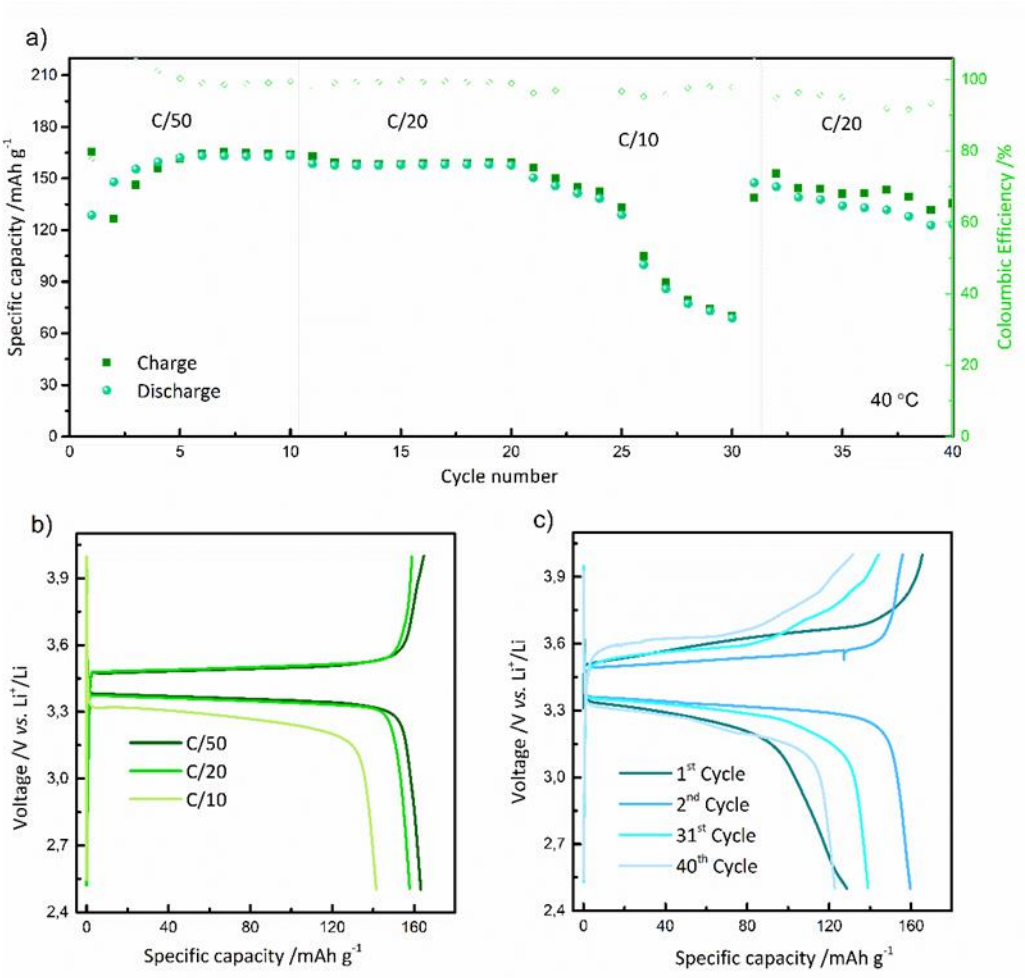

Figure 5.9 Rate capability upon galvanostatic charge/discharge cycling of the Li/PEO-PEC-UV/LFP battery at 40 °C (a) and the corresponding voltage vs. specific capacity curves upon charge (b) and discharge (c).

Moreover, the electrochemical behaviour observed at both temperatures indicates that PEO-PEC-UV remains stable without showing depolymerisation, even when in contact with lithium metal or in the presence of lithium salt. A deep investigation about the degradation and depolymerisation process is described in the following section.

5.6 Degradation of Polymer Electrolyte

Polycarbonates are known to depolymerise into their monomers in the presence of lithium ions, lithium metal, and at high temperatures [28]. The degradation of PEC leads to the production of ethylene carbonate (EC), a liquid monomer above 40 °C, which can dissolve the polymer network, allowing for direct contact between the lithium and the cathode, in turn causing short-circuiting. This degradation explains the poor performance of non-crosslinked

PEO-PEC SPEs. To shed more light on this phenomenon, battery cells were opened in a glove box after cycling for visual inspection of the different components, particularly the electrolyte, and following NMR analysis for characterization of any degradation phenomena (**Figure 5.10**).

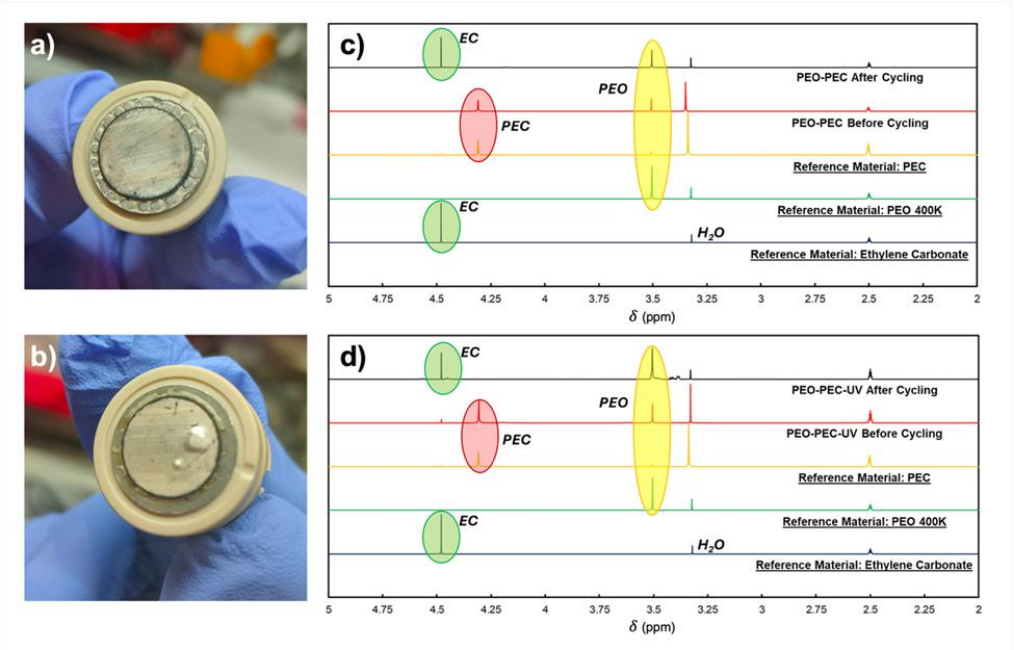

Figure 5.10 Digital photographs of PEO-PEC (a) and PEO-PEC-UV (b) SPEs after lithium plating/stripping cycling (cells were opened after the PEO-PEC cell short circuited); corresponding NMR spectra of PEO-PEC (c) and PEO-PEC-UV (d).

Figure 5.10a,b shows the aspect of PEO-PEC and the PEO-PEC-UV SPEs in symmetrical Li||Li cells after the lithium plating/stripping tests. Both cells underwent the same testing procedure: cycling at 70 °C and stopping at the same time when the cell with the PEO-PEC short-circuited (indeed, the one with PEO-PEC-UV was still operating properly). As shown in **Figure 5.10a**, PEO-PEC becomes liquid after cycling, indicating depolymerisation into EC monomer. In contrast, PEO-PEC-UV (**Figure 5.10b**) maintains its solid form, demonstrating enhanced mechanical robustness and stability over temperature. Upon NMR analysis, the PEO-PEC sample before cycling (**Figure 5.10c**) shows peaks related to PEO and PEC. After cycling, PEC degrades into EC monomers, which, at 70 °C, act as a solvent and dissolve the polymer matrix. For PEO-PEC-UV (**Figure 5.10d**), the UV crosslinking process prevents complete dissolution of the polymer network; indeed, only a small amount of PEC that is not crosslinked is degraded to EC. Notably, while the crosslinking maintains the membrane integrity, the resulting small amount of EC produced is encompassed in the

crosslinked polymeric matrix, acting as a plasticiser and enhancing lithium-ion conductivity.

These results are further supported by the ATR-FTIR spectra shown in **Figure 5.11**, which compares the spectra of PEO-PEC-UV before and after lithium plating/stripping cycles with those of the pristine materials containing LiTFSI.

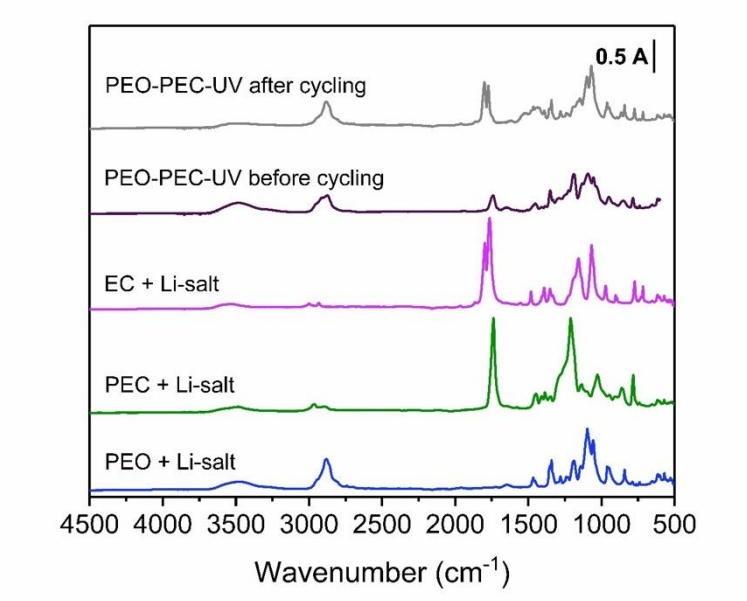

Figure 5.11 ATR-FTIR spectra of PEO-PEC-UV before and after lithium plating/stripping cycles, compared with those of PEO, PEC, and EC mixed with LiTFSI.

The single peak at 1737 cm^{-1} is associated to the C=O stretching of carbonate groups in PEC-LiTFSI, while the same reflection is splitted in liquid EC-LiTFSI. As expected, the crosslinked PEO-PEC-UV SPE before cycling only shows the features of PEC in the 1700–1800 cm^{-1} range. After cycling, the distinct splitted EC signal also emerges, which overlaps with the peak at 1737 cm^{-1} of PEC, accounting for only a partial degradation of PEC to EC as for the NMR results.

5.7 Interfacial Stability

To better understand the kinetics of the charge and discharge processes, electrochemical impedance spectroscopy was employed. EIS measurements were conducted by collecting a series of spectra during the oxidation and reduction phases of the initial cycle, with bias potentials incremented in small steps of 50 mV across the potential range of 2.5 to 4.0 V. These measurements were performed at 70 °C using Li||PEO-PEC-UV||LFP catholyte cell. **Figure 5.12a,b** shows selected

sequences of Nyquist plots acquired for the cell. When the cell is within the voltage range of 2.5 V ≤ E ≤ 3.8 V, the following contributions to the overall impedance can be identified in the Nyquist plots and assigned to specific steps in the electronic/ionic transport, from high to low frequencies: (i) the intercept with the real axis represents the ionic resistance of the SPE layer (R_s), which depends on the ionic conductivity and thickness of the layer; (ii) two convoluted arcs in the high-to-middle frequencies are caused by the resistances at the planar interfaces (R_{int}), which may either correspond to ion or electron transfer, depending on the type of interface; (iii) the Warburg diffusion element (W) is evidenced by the sloped line at the lowest-frequency limit, describing the diffusion of Li^+ ions to a blocking electrode [29–31]. However, when the voltage range is 3.8 V ≤ E ≤ 4.0 V, the shape of the curve in the low-frequency region of the Nyquist plots indicates the composite nature of the cathode, which can be accurately described using a Transmission Line Model (TLM) [32]. To capture the response at very low frequencies, a Warburg open element (WO) is incorporated in series with the TLM. As a result, the spectra during charge and discharge were fitted with two distinct equivalent circuits, as illustrated in **Figure 5.12c,d**. To account for deviations from ideal behavior caused by electrode inhomogeneity or roughness, all capacitance (C) elements were substituted with constant-phase elements (Q) during the fitting procedure. This fitting was performed using the RelaxIS software by rhd Instruments. The interfacial resistances within the cell (Catholyte/SPE/Li) hinder the transport of Li^+ and electrons (**Figure 5.12f**). The composite cathode consists of the cathode active material (CAM), a carbon additive, and the catholyte. The catholyte often contains a solid polymer analogous to the one used in the SPE. The TLM used follows the approach described by Wurster et al. [29], incorporating electronic resistance (R_{el}), ionic resistance (R_{ion}), and R-CPE elements to represent the CAM-catholyte interface, with the charge transfer resistance (R_{ct}) being proportional to the CAM surface area. **Figure 5.12e** shows the calculated resistance values for R_{sol} and R_{int} during both charge and discharge cycles (60 data points). In agreement with the Nyquist plots, R_{sol} and R_{int} exhibit a slight increase during charge from 2.5 to 3.5 V. These values then stabilise between 3.5 and 3.8 V, followed by a decrease from 3.8 to 4.0 V. However, as the intercalation progresses and the potential decreases from 4.0 to 3.2 V vs. Li^+/Li, the resistance values start to increase but then remain constant until the end of discharge. These changes in

the R_{int} may result from alterations in the near-surface region of the active material, modifications in the interfacial region of the electrolyte, or the formation of an interlayer [29].

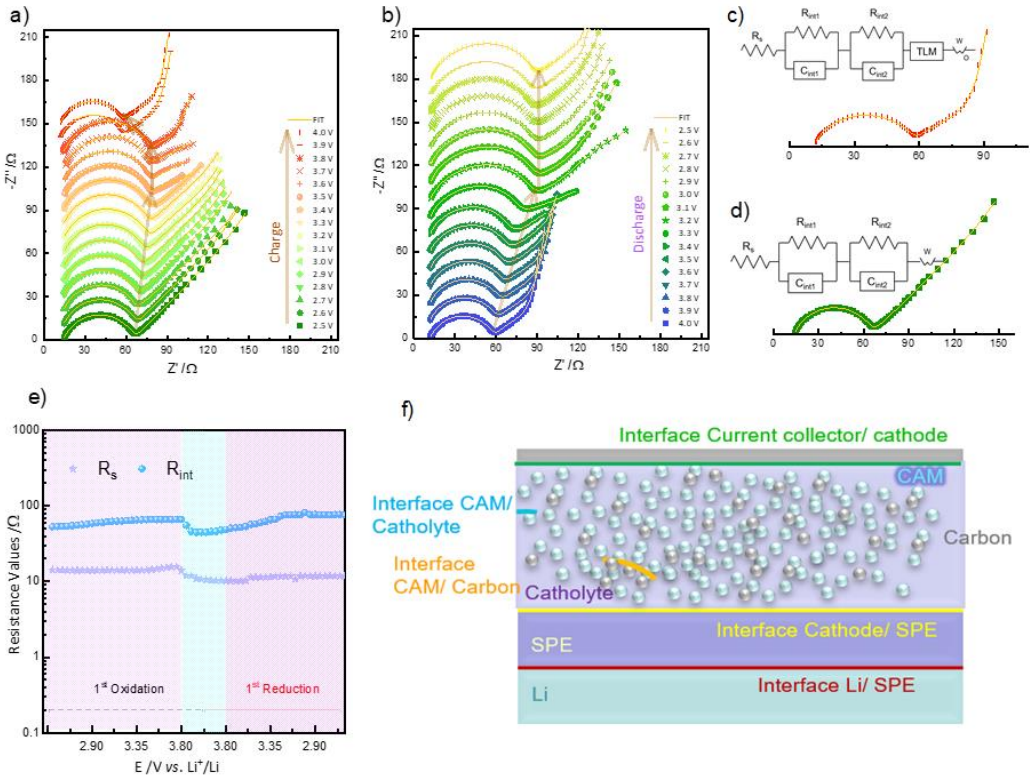

Figure 5.12 The corresponding Nyquist plots recorded at selected potentials during the first oxidation (a) and the first reduction (b); The equivalent circuits used to simulate the data (c,d); the fitted resistance values during the first charge and discharge (e); schematic illustration of various interfaces in a Li||PEO-PEC-UV||LFP catholyte cell (f).

5.8 Concluding remarks

This chapter provided a detailed overview of the successful preparation of an advanced solid polymer electrolyte composed of a poly(ethylene oxide)/poly(ethylene carbonate) network with dissolved LiTFSI, offering superior performance compared to conventional PEO-based electrolytes due to an UV-curing process applied to induce crosslinking of the polymer chains, thus enhancing the thermomechanical and electrochemical properties, improving thermal stability, and reducing crystallinity.. To minimise environmental impact, the electrolyte is produced using an extrusion process that eliminates organic solvents and liquid components, preventing potential leaching and reducing costs. This method

employs polymers with low environmental impact, and is scalable for industrial application.

Symmetric Li||Li cells assembled with the PEO-PEC-UV SPE demonstrate outstanding stripping/plating performance across a current density range of 0.025 to 0.2 mA cm^{-2} at 40 and 70 °C, with stable cycling for over 600 hours at 0.05 mA cm^{-2} and no issues related to lithium dendrite growth. Furthermore, rate capability tests were conducted at both 40 and 70 °C in truly solid-state lab-scale lithium metal polymer cells, assembled with a high-loading LFP-based composite catholyte (~8-10 mg cm^{-2}), demonstrating outstanding galvanostatic charge/discharge performance at low C-rates. Degradation phenomena are also investigated, revealing that the UV-crosslinking stabilises the system; in addition, the in-situ produced small amount of liquid ethylene carbonate enhances the electrochemical performance of the resulting electrolyte while being trapped in the polymeric matrix. The presented findings confirm that the proper combination of dry extrusion coupled with UV-induced crosslinking can pave the way for the truly solvent-free, simple and scalable production of greener and more sustainable SPEs, with enhanced thermomechanical and electrochemical properties, suitable for future applications in batteries at near ambient temperature operating conditions.

References

[1] J. Mindemark, M.J. Lacey, T. Bowden, D. Brandell, Beyond PEO—Alternative host materials for Li+-conducting solid polymer electrolytes, Prog. Polym. Sci. 81 (2018) 114–143. https://doi.org/10.1016/j.progpolymsci.2017.12.004.

[2] M.A. Cabañero Martínez, N. Boaretto, A.J. Naylor, F. Alcaide, G.D. Salian, F. Palombarini, E. Ayerbe, M. Borras, M. Casas-Cabanas, Are Polymer-Based Electrolytes Ready for High-Voltage Lithium Battery Applications? An Overview of Degradation Mechanisms and Battery Performance, Adv. Energy Mater. 12 (2022) 2201264. https://doi.org/10.1002/aenm.202201264.

[3] L. Herbers, J. Minář, S. Stuckenberg, V. Küpers, D. Berghus, S. Nowak, M. Winter, P. Bieker, The Influence of Polyethylene Oxide Degradation in Polymer-Based Electrolytes for NMC and Lithium Metal Batteries, Advanced Energy and Sustainability Research 4 (2023) 2300153. https://doi.org/10.1002/aesr.202300153.

[4] B. Guo, Y. Fu, J. Wang, Y. Gong, Y. Zhao, K. Yang, S. Zhou, L. Liu, S. Yang, X. Liu, F. Pan, Strategies and characterization methods for achieving high performance PEO-based solid-state lithium-ion batteries, Chemical Communications 58 (2022) 8182–8193. https://doi.org/10.1039/d2cc02306g.

[5] Q. Han, S. Wang, W. Kong, W. Ren, Y. Liu, H. Wang, Realizing compatibility of high voltage cathode and poly (ethylene oxide) electrolyte in all-solid-state lithium batteries by bilayer electrolyte design, Chemical Engineering Journal 454 (2023) 140104. https://doi.org/10.1016/j.cej.2022.140104.

[6] Y. He, Y. Dong, L. Qiao, C.M. Costa, S. Lanceros-Méndez, J. Han, W. He, Recent progress in ultra-thin solid polymeric electrolytes for next-generation lithium batteries, Energy Storage Mater. 67 (2024) 103329. https://doi.org/10.1016/j.ensm.2024.103329.

[7] Y. Zhao, Y. Bai, W. Li, M. An, Y. Bai, G. Chen, Design strategies for polymer electrolytes with ether and carbonate groups for solid-state lithium metal batteries, Chemistry of Materials 32 (2020) 6811–6830. https://doi.org/10.1021/acs.chemmater.9b04521.

[8] Z. Cui, V. Marangon, J. Hassoun, Y. Tominaga, Polycarbonate-based composite polymer electrolytes with Al2O3 enhanced by in situ polymerized electrolyte Interlayers for all-solid-state lithium-metal batteries, J. Power Sources 611 (2024). https://doi.org/10.1016/j.jpowsour.2024.234760.

[9] N. Soontornnon, K. Kimura, Y. Tominaga, A highly salt concentrated ethylene carbonate-based self-standing copolymer electrolyte for solid-state lithium metal batteries, J. Mater. Chem. A Mater. 12 (2024) 20278–20287. https://doi.org/10.1039/d4ta03543g.

[10] T. Li, P.K. Panda, C. Te Hsieh, Y.A. Gandomi, P.C. Yang, Lithium iron phosphate cathode supported solid lithium batteries with dual composite solid electrolytes

enabling high energy density and stable cyclability, J. Energy Storage 81 (2024) 110444. https://doi.org/10.1016/j.est.2024.110444.
[11] A. Buchheit, M. Grünebaum, B. Teßmer, M. Winter, H.D. Wiemhöfer, Polycarbonate-Based Lithium Salt-Containing Electrolytes: New Insights into Thermal Stability, Journal of Physical Chemistry C 125 (2021) 4371–4378. https://doi.org/10.1021/acs.jpcc.0c09968.
[12] M. Falco, L. Castro, J.R. Nair, F. Bella, F. Bardé, G. Meligrana, C. Gerbaldi, UV-Cross-Linked Composite Polymer Electrolyte for High-Rate, Ambient Temperature Lithium Batteries, ACS Appl. Energy Mater. 2 (2019) 1600–1607. https://doi.org/10.1021/acsaem.8b02185.
[13] M. Falco, C. Simari, C. Ferrara, J.R. Nair, G. Meligrana, F. Bella, I. Nicotera, P. Mustarelli, M. Winter, C. Gerbaldi, Understanding the effect of UV-induced cross-linking on the physicochemical properties of highly performing PEO/LiTFSI-based polymer electrolytes, Langmuir 35 (2019) 8210–8219. https://doi.org/10.1021/acs.langmuir.9b00041.
[14] L. Porcarelli, C. Gerbaldi, F. Bella, J.R. Nair, Super Soft All-Ethylene Oxide Polymer Electrolyte for Safe All-Solid Lithium Batteries, Sci. Rep. 6 (2016). https://doi.org/10.1038/srep19892.
[15] F. Gambino, M. Gastaldi, A. Jouhara, S. Malburet, S. Galliano, N. Cavallini, G. Colucci, M. Zanetti, A. Fina, G.A. Elia, C. Gerbaldi, Formulating PEO-polycarbonate blends as solid polymer electrolytes by solvent-free extrusion, Journal of Power Sources Advances 30 (2024). https://doi.org/10.1016/j.powera.2024.100160.
[16] K. Platen, F. Langer, J. Schwenzel, Influence of Screw Design and Process Parameters on the Product Quality of PEO:LiTFSI Solid Electrolytes Using Solvent-Free Melt Extrusion, Batteries 10 (2024) 183. https://doi.org/10.3390/batteries10060183.
[17] H. Wang, X. Cui, C. Zhang, H. Gao, W. Du, Y. Chen, Promotion of ionic conductivity of PEO-based solid electrolyte using ultrasonic vibration, Polymers (Basel). 12 (2020) 1889. https://doi.org/10.3390/POLYM12091889.
[18] Z. Wang, B. Al Alwan, W. Fawaz, K.Y.S. Ng, Novel PEO-based composite solid electrolytes for All-Solid-State Li-S battery, Journal of Electroanalytical Chemistry 954 (2024) 118017. https://doi.org/10.1016/j.jelechem.2023.118017.
[19] J. Li, X. Chen, S. Muhammad, S. Roy, H. Huang, C. Yu, Z. Ullah, Z. Wang, Y. Zhang, K. Wang, B. Guo, Development of solid polymer electrolytes for solid-state lithium battery applications, Mater. Today Energy 43 (2024) 101574. https://doi.org/10.1016/j.mtener.2024.101574.
[20] Y. Ji, Y.H. Zhang, F.N. Shi, L.N. Zhang, UV-derived double crosslinked PEO-based solid polymer electrolyte for room temperature, J. Colloid Interface Sci. 629 (2023) 492–500. https://doi.org/10.1016/j.jcis.2022.09.089.
[21] Y. Tominaga, V. Nanthana, D. Tohyama, Ionic conduction in poly(ethylene carbonate)-based rubbery electrolytes including lithium salts, Polym. J. 44 (2012) 1155–1158. https://doi.org/10.1038/pj.2012.97.
[22] K. Platen, F. Langer, R. Bayer, R. Hollmann, J. Schwenzel, M. Busse, Influence of Molecular Weight and Lithium Bis(trifluoromethanesulfonyl)imide on the Thermal

Processability of Poly(ethylene oxide) for Solid-State Electrolytes, Polymers (Basel). 15 (2023) 3375. https://doi.org/10.3390/polym15163375.
[23] A. Nishimoto, K. Agehara, N. Furuya, T. Watanabe, M. Watanabe, High Ionic Conductivity of Polyether-Based Network Polymer Electrolytes with Hyperbranched Side Chains, Macromolecules 32 (1999) 1541–1548. https://doi.org/10.1021/ma981436q.
[24] M.A. Munshi, B.B. Owens, Ionic Transport in Poly(ethylene oxide) (PEO)-LiX Polymeric Solid Electrolyte, Polym. J. 20 (1988) 577–586.
[25] Z. Chen, Y. Zhang, B. Zhu, J. Wang, J. Hu, J. Zou, Z. Jin, X. Li, Y. Zhang, C. Zhang, Construction of high-performance solid-state electrolytes for lithium metal batteries by UV-curing technology, Polym. Test. 132 (2024) 108386. https://doi.org/10.1016/j.polymertesting.2024.108386.
[26] S. Huo, L. Sheng, W. Xue, L. Wang, H. Xu, H. Zhang, X. He, Challenges of polymer electrolyte with wide electrochemical window for high energy solid-state lithium batteries, InfoMat 5 (2023) e12394. https://doi.org/10.1002/inf2.12394.
[27] E. Quartarone, P. Mustarelli, Electrolytes for solid-state lithium rechargeable batteries: Recent advances and perspectives, Chem. Soc. Rev. 40 (2011) 2525–2540. https://doi.org/10.1039/c0cs00081g.
[28] B. Sun, C. Xu, J. Mindemark, T. Gustafsson, K. Edström, D. Brandell, At the polymer electrolyte interfaces: the role of the polymer host in interphase layer formation in Li-batteries, J. Mater. Chem. A Mater. 3 (2015) 13994–14000. https://doi.org/10.1039/c5ta02485d.
[29] V. Wurster, C. Engel, H. Graebe, T. Ferber, W. Jaegermann, R. Hausbrand, Characterization of the Interfaces in LiFePO4/PEO-LiTFSI Composite Cathodes and to the Adjacent Layers, J. Electrochem. Soc. 166 (2019) A5410–A5420. https://doi.org/10.1149/2.0621903jes.
[30] H. Darjazi, I. Madinabeitia, M. Zarrabeitia, E. Gonzalo, B. Acebedo, S. Javad Rezvani, F.J. Fernández-Carretero, F. Nobili, A. García-Luis, M.Á. Muñoz-Márquez, LiNi0.5Mn1.5O4 Thin Films Grown by Magnetron Sputtering under Inert Gas Flow Mixtures as High-Voltage Cathode Materials for Lithium-Ion Batteries, ChemElectroChem 10 (2023) e202201004. https://doi.org/10.1002/celc.202201004.
[31] H. Darjazi, S.J. Rezvani, S. Brutti, F. Nobili, Improvement of structural and electrochemical properties of NMC layered cathode material by combined doping and coating, Electrochim. Acta 404 (2022) 139577. https://doi.org/10.1016/j.electacta.2021.139577.
[32] J. Euler, W. Nonnenmacher, Stromverteilung in porösen elektroden, Electrochim. Acta 2 (1960) 268–286.

Chapter 6

Role of Succinonitrile in Enhancing PEO-PEC Electrolytes for High-Voltage Lithium Metal Batteries

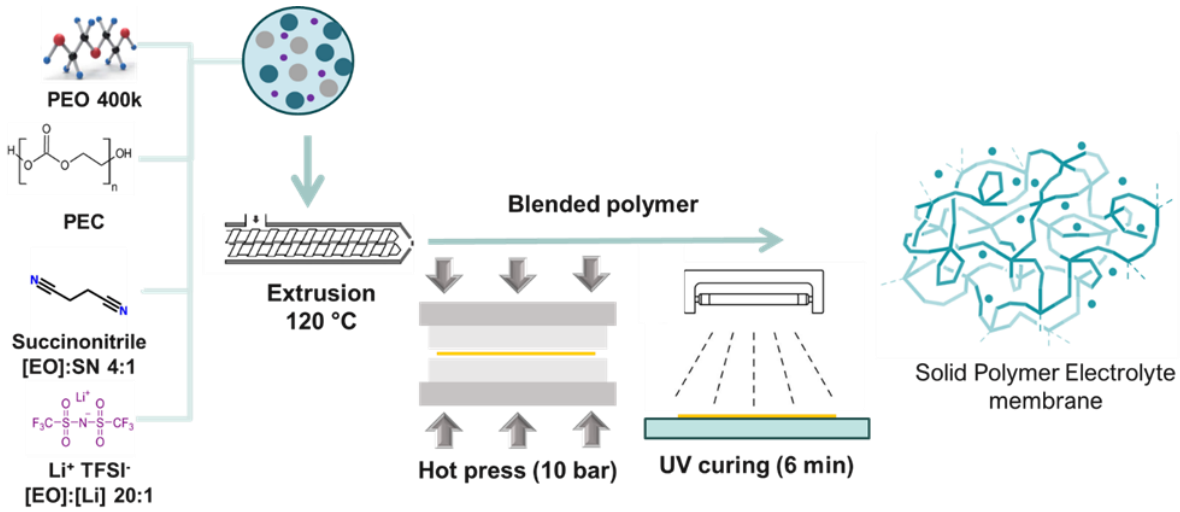

Chapters 4 and 5 established a solvent-free strategy for the development of PEO/polycarbonate solid polymer electrolytes based on readily scalable melt extrusion and subsequent UV-induced crosslinking. The first step demonstrated that homogeneous PEO/PEC blends can be successfully processed without solvents, leading to improved structural and electrochemical properties compared with neat PEO. The second showed that UV curing effectively stabilizes the extruded polymer matrix, mitigates polycarbonate degradation, and enhances the interfacial behavior of the electrolyte in lithium metal cells.

Building on this platform, the present Chapter addresses a further key limitation of these systems, namely the need to improve ionic transport at moderate temperature while preserving the thermomechanical and interfacial stability achieved through crosslinking. To this end, succinonitrile (SN) was introduced as a solid plasticizing component within the UV-cured PEO/PEC framework. Owing to its plastic-crystalline character, SN is expected to enhance chain mobility, promote lithium salt dissociation, and suppress residual crystallinity, thereby improving conductivity at 40 °C [1–7]. However, excessive SN loading (>10 wt%) has been shown to severely compromise the mechanical properties of the polymer matrix [8]. These findings highlight a critical trade-off: while plasticizers such as SN can markedly enhance ionic conductivity, they may simultaneously undermine structural integrity. To address this challenge, cross-linking strategies have been employed to construct a three-dimensional polymer framework that reinforces the matrix and preserves mechanical strength without sacrificing ionic transport [9,10].

The use of the previously optimized crosslinked PEO/PEC matrix provides a suitable means to accommodate this trade-off, combining the stabilizing effect of the three-dimensional polymer network with the beneficial transport properties introduced by SN. On this basis, SN-containing UV-cured PEO/PEC electrolytes are investigated, which were prepared through a fully solvent-free route, with particular attention to the role of polymer composition in determining ionic conductivity, anodic stability, and compatibility with lithium metal. The practical relevance of the optimized formulation is finally assessed in solid-state lithium metal cells employing both LFP and, remarkably, high-energy 4V-class NMC

cathodes at 40 °C. Overall, this study represents the natural continuation of the previous Chapters and demonstrates how plasticization can further extend the performance of the solvent-free PEO/PEC electrolyte platform toward more efficient solid-state lithium metal batteries.

6.1 Solid Polymer Electrolyte Membrane Preparation

The preparation procedure was optimised and reported in previous Chapters [11]. The molar ratio between [EO] and [Li^+] units was fixed at 20:1, as this composition was previously identified as optimal for achieving high ionic conductivity at elevated temperatures while minimizing electrolyte stickiness. The PEO-PEC ratios selected for this study were also based on previously reported optimized compositions [12]. Here, three electrolyte formulations were investigated: (i) PEO–PEC (1:1), (ii) PEO–PEC (1:1) incorporating SN, and (iii) PEO–PEC (7:3) incorporating SN. The structures of the components for the formulation of PEO-based electrolytes are summarized in **Figure 6.1**. For SN-containing systems, the SN content was fixed at molar ration of EO/SN = 4/1. PEO–PEC (1:1), PEO–PEC (1:1) incorporating SN, and PEO–PEC (7:3) incorporating SN were designated as SPE, SPE(1:1)+SN, and SPE(7:3)+SN, respectively.

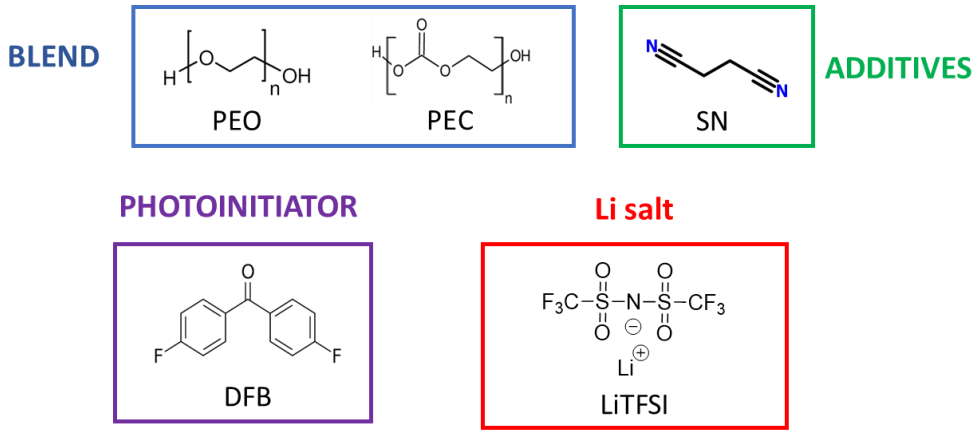

Figure 6.1 Chemical structure of the PEO and PEC polymers forming the blend (blue panel), additives added to the polymer matrix (green panel), photoinitiator used for cross-linking (violet panel) and lithium salt added (red panel).

6.2 Electrolyte Characterization

Figure 6.2a shows a photograph of the SPE(1:1) + SN SPE, which appears quasi-transparent, homogeneous, elastic, and self-standing, indicating its suitability for subsequent structural and electrochemical characterization. The effect of UV exposure on SN was investigated using FT-IR spectroscopy. **Figure 6.2b** displays the FT-IR spectra of pristine SN and the SPE(1:1) + SN electrolyte before UV exposure, after 1 min of irradiation, and after 3 min of irradiation. The SN-containing SPE was exposed to UV light under the same conditions employed for electrolyte preparation.

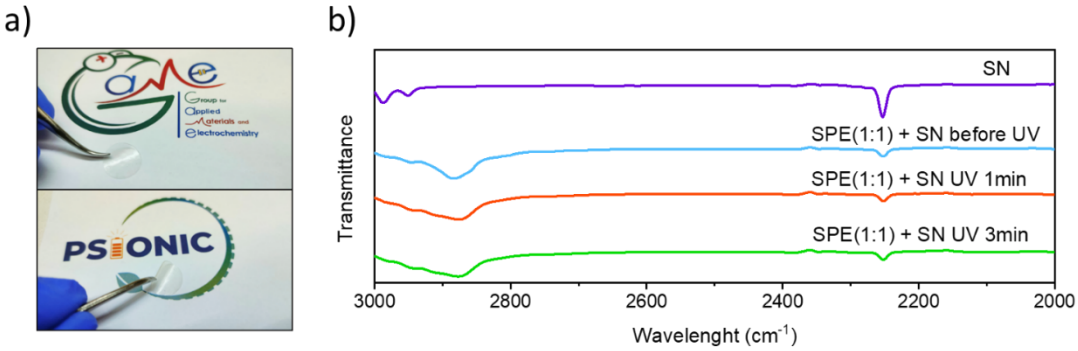

Figure 6.2 a) Digital photograph of the self-standing, flexible, and quasi-transparent SPE(1:1)+SN SPE. b) FT-IR spectra of pristine SN and the SPE(1:1)+SN electrolyte recorded before UV exposure and after 1 min and 3 min of UV irradiation, respectively.

As shown in **Figure 6.2b**, the characteristic absorption band at 2252 cm^{-1}, assigned to the cyano (C≡N) stretching vibration, remains essentially unchanged even after three minutes of UV exposure. This observation indicates that the cyano functional groups of SN are largely preserved during the UV-curing process, confirming the chemical stability of SN under the applied irradiation conditions.

To investigate thermal properties and crystallinity of SPEs, DSC measurements were performed. Since Li^+ ion conduction primarily occurs in the amorphous phase, suppression of crystallinity is essential for achieving high ionic conductivity [13]. **Figure 6.3a** shows the DSC thermograms of PEO/LiTFSI, SPE(1:1) + SN, and SPE(7:3) + SN. The PEO/LiTFSI SPE reveals a characteristic endothermic transition at −32 °C, attributed to a solid-solid transition associated with the transition of crystalline PEO into a more amorphous or ordered-amorphous (plastic crystalline) phase, along with a melting peak at around 60 °C. As previously

reported, this SPE displays a semi-crystalline nature, with a crystallinity degree of approximately 33% [11]. In contrast, no distinct melting or crystallization peaks are observed for the SN-based SPEs, indicating a predominantly amorphous structure. The incorporation of PEC disrupts the formation of crystalline domains in PEO, while UV-induced cross-linking generates a network structure that further suppresses PEO recrystallization [14]. Both SN-based SPEs show two T_g, located at −50 °C (PEO-rich phase) and −10 °C (PEC-rich phase), indicating phase separation between the two polymer components.

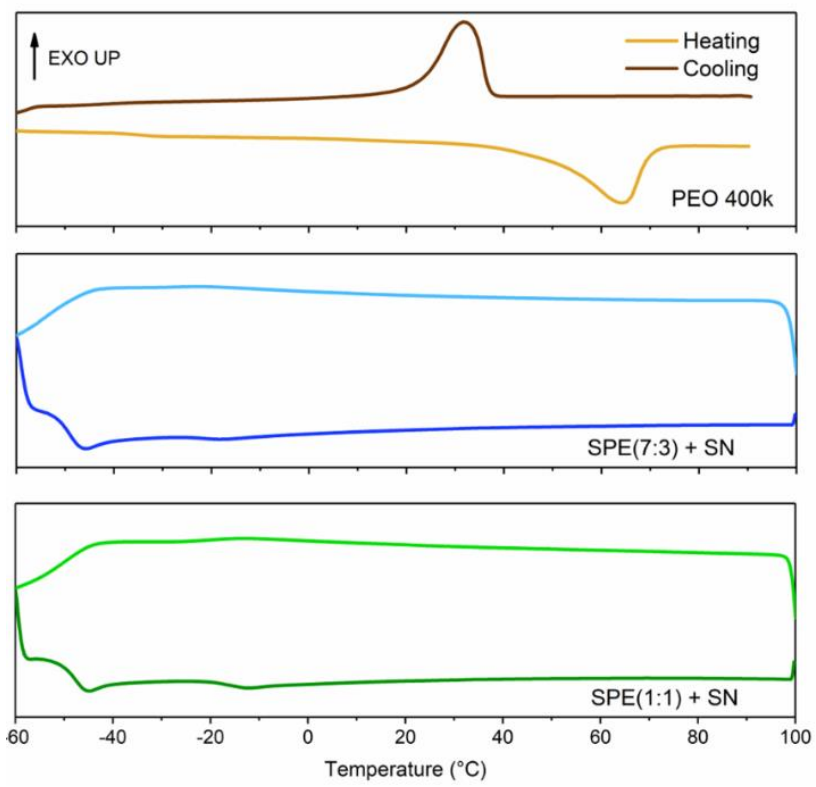

Figure 6.3 DSC thermograms of PEO/LiTFSI, SPE(1:1)+SN, and SPE(7:3)+SN recorded at a heating rate of 10 °C min^{-1}.

TGA analysis was carried out in the temperature range of 25–800°C to evaluate the thermal stability of the SN-containing SPEs, as shown in **Figure 6.4a**. The SPEs exhibit thermal stability up to around 136 °C, corresponding to 5% weight loss, while the plasticizer-free SPE shows the onset of degradation over 200 °C. The initial weight loss observed at around 130 °C can be attributed to sublimation of SN [15]. Nevertheless, the $T_{95\%}$ of 136 °C for the plasticized SPEs confirm their adequate thermal robustness for operation under moderately elevated temperatures in practical applications. Moreover, this result indicates that the extrusion process at ~120 °C did not induce chemical degradation of the polymer matrix. The TGA

curves of both SPE formulations reveal three distinct weight-loss stages. The initial mass loss observed between 130 and 220 °C is mainly attributed to the sublimation of SN. Above 220 °C, degradation of the aliphatic polycarbonate chains begins. The final weight-loss stage, occurring above 350 °C, is associated with the decomposition of the PEO polymer backbone and its complexes with LiTFSI. Typically, salt-doped PEO systems exhibit a two-step decomposition behaviour: the first step, occurring around 380 °C, corresponds to polymer chain scission, while the second decomposition event at approximately 430 °C is related to the breakdown of LiTFSI ethylene oxide coordination complexes [16].

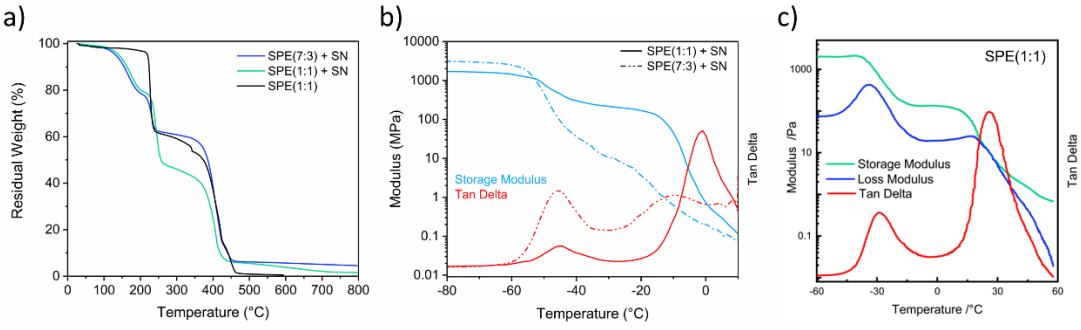

Figure 6.4 a) TGA curves of SPE(1:1)+SN, SPE(7:3)+SN and SPE(1:1) obtained under N_2 atmosphere at a heating rate of 10 °C min^{-1}. b) DMA curves of SPE(1:1)+SN, SPE(7:3)+SN and c) plasticizer-free SPE(1:1).

DMA was performed to evaluate the mechanical behaviour of the plasticized SPEs. The measurements reveal a reduction in the T_g and further confirm the partial immiscibility between the PEO and PEC phases (**Figure 6.4b**). The Tan Delta curve exhibits two distinct α-relaxation peaks for both SPEs, corresponding to the glass transitions of the individual PEO-rich and PEC-rich domains. Compared with the system without SN addition (**Figure 6.4c**), both T_g values decrease by approximately 20–30 °C. These transition temperatures are approximately 20 °C lower than those observed for plasticizers-free systems (–30 °C and +20 °C, respectively), demonstrating the effective plasticizing action of SN, which promotes increased chain mobility and softening of both polymer phases[12,17].

The temperature dependence of the ionic conductivity for the investigated SPEs is presented in **Figure 6.5**. The SPE(7:3) + SN SPE exhibits slightly higher ionic conductivity across the entire temperature range, reaching values of 2×10^{-4} S cm^{-1} and 3.2×10^{-5} S cm^{-1} at 70 and 40 °C respectively. This enhancement can be directly attributed to the pronounced plasticizing effect of SN, which reduces the

T_g, suppresses residual crystallinity, and increases the free volume within the polymer matrix. These combined effects promote enhanced segmental chain mobility, thereby facilitating Li^+ transport [7]. A comparison between the two SN-containing systems further highlights the critical role of polymer composition. The SPE(7:3) + SN electrolyte consistently outperforms the corresponding 1:1 formulation that displays a conductivity of 3.2×10^{-5} S cm^{-1} at 40 °C, indicating that the higher PEO fraction provides a greater density of ether oxygen coordination sites for Li^+ migration. Meanwhile, PEC and SN synergistically inhibit PEO recrystallization, preserving an amorphous structure favorable for efficient ionic conduction.

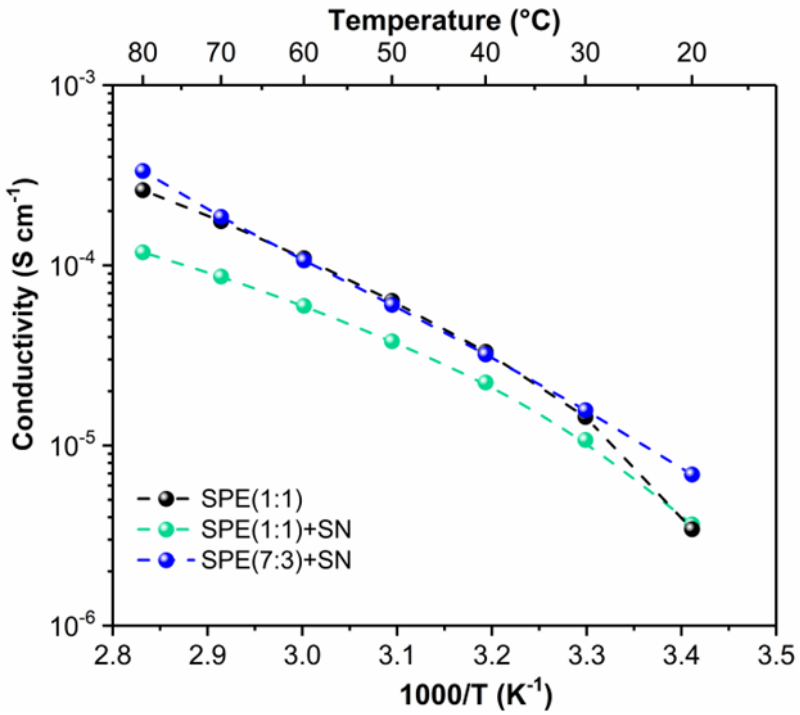

Figure 6.5 Arrhenius plots of ionic conductivity vs. inverse temperature of SPEs under study.

The ESW of the investigated SPEs is a critical parameter for practical application, as it determines compatibility with high-voltage cathode materials, thus potentially enabling the development of high-energy-density lithium batteries. Figure 3b shows the anodic stability of the SN-containing SPEs, assessed through the current response during a stepwise potential sweep from 3 V to 5 V vs. Li^+/Li at 40 °C. Each voltage step produces an initial current spike followed by a gradual decay toward a quasi-steady-state value with no significant current flow of the investigated electrolytes up to 4.9 vs. Li^+/Li, which can meet the requirement of typical high-voltage cathode materials. Using a threshold of ~5 μA cm^{-2}, no significant current increase is observed for the SN-containing SPEs up to 4.8 V vs.

Li^+/Li, which is notably higher than that of the pristine SPE [12]. This observation is consistent with the addition of an additive with high oxidation stability like SN, which has contributed to increase the ESW of the material [18]. Moreover, the LSV profile shown in the inset of **Figure 6.6** for the SPE(7:3)+SN electrolyte, shows the onset of a current increase at approximately 4.8 V, in good agreement with the behavior observed in the CA. At the same time, there is no distinct sign of redox features attributable to SN during the scan, excluding the potential hazards of cyanide formation in practical applications [19]. Notably, the PEO–PEC (1:1) composition exhibits slightly lower anodic current densities compared to the 7:3 formulation, which can be attributed to its higher PEC fraction [20]. This enhanced oxidative stability exceeds that of the pristine SPE and satisfies the operational requirements of typical high-energy density 4V-class cathode materials.

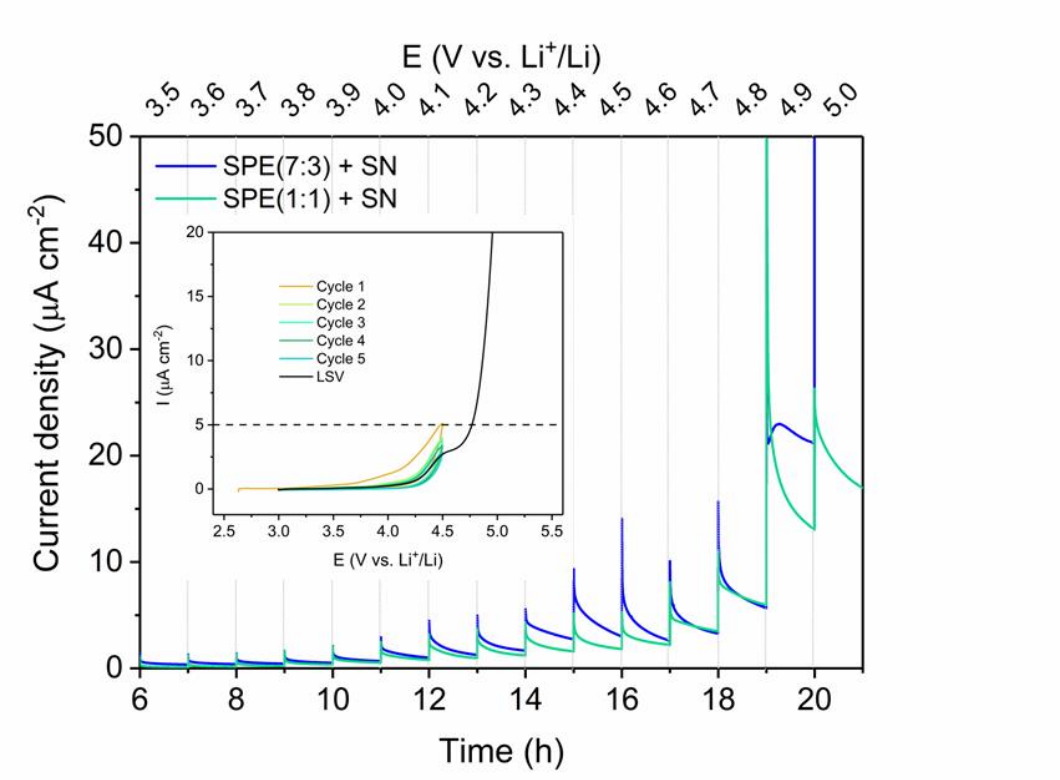

Figure 6.6 CA of SN-containing SPEs using a Li/SPE/Al-CC cell during stepwise anodic polarization at 40 °C; inset: LSV profile of SPE(7:3)+SN at 40 °C (scan rate of 0.1 mV s^{-1}).

Figures 6.7a and **6.7b** present the lithium plating/stripping behavior of the SPE(7:3)+SN SPE evaluated at 40 °C under various current densities ranging from 25 to 150 µA cm^{-2}, as well as during long-term cycling at 25 µA cm^{-2}. The SPE exhibits low polarization across different current densities, with an overpotential of 0.4 V at the highest tested current density of 150 µA cm^{-2}. An initial gradual

increase in overpotential is observed within the first few hundred hours, which is attributed to the progressive formation of a stable SEI at the lithium surface. Once a uniform and ionically conductive SEI is established, the overpotential reaches a steady-state value and remains nearly constant over 1400 h of continuous cycling, demonstrating highly stable interfacial behavior and effective suppression of dendritic growth. In contrast, the SPE (1:1) + SN SPE (**Figure 6.7c**) exhibits a progressive increase in overpotential even at the lowest applied current density (25 µA cm^{-2}), followed by pronounced voltage polarization upon increasing the current density and eventual short-circuit failure.

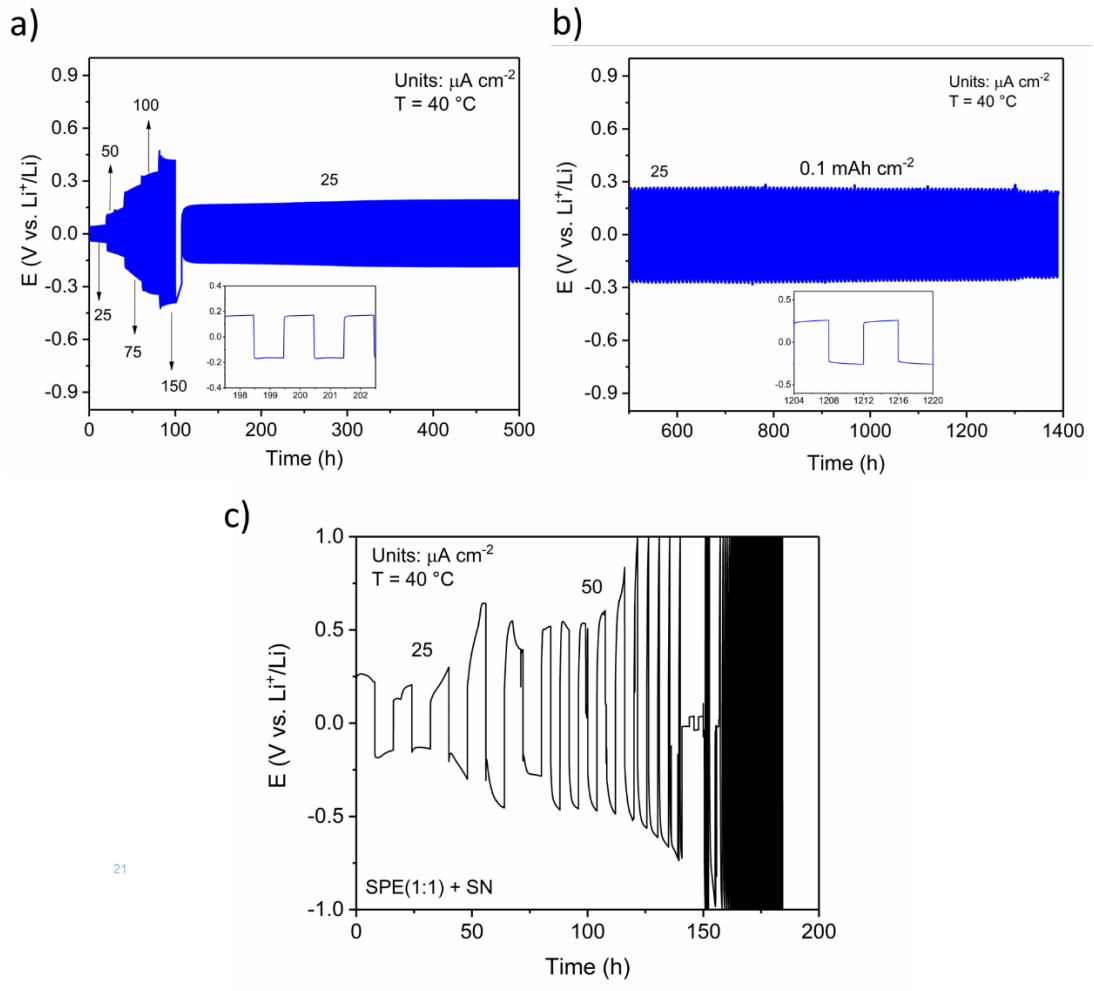

Figure 6.7 a) Galvanostatic lithium plating/stripping cycling in symmetric Li‖Li cells employing SPE(7:3)+SN at current densities ranging from 25 to 150 µA cm^{-2} (step time of 1 hour per half cycle, corresponding to a plated/stripped capacity per half cycle of 25 to 150 mAh cm^{-2}). b) Long-term lithium plating/stripping stability of SPE(7:3)+SN at 25 µA cm^{-2}. c) Plating/stripping cycling employing SPE(1:1)+SN at current densities ranging from 25 to 50 µA cm^{-2} (T = 40 °C).

The lower interfacial stability observed for the SPE(1:1) + SN electrolyte at 40 °C can be attributed to its higher PEC content and comparatively lower ionic

conductivity at this temperature. The reduced ionic conductivity limits efficient Li^+ transport across the interface, leading to increased local polarization and inhomogeneous lithium deposition. Such conditions promote uneven current distribution and enhance the likelihood of parasitic interfacial reactions. It can be attributed to the intrinsic chemical reactivity of PEC and SN toward lithium metal [21]. Similarly, succinonitrile, upon contact with Li metal, can undergo partial reduction of the nitrile groups, producing electronically insulating but ionically heterogeneous decomposition products [22]. In contrast, the SPE(7:3) + SN formulation benefits from both a higher PEO fraction and the synergistic plasticizing effect of SN. The increased PEO content provides a greater density of ether oxygen coordination sites for Li^+ transport, while SN enhances segmental mobility by reducing the glass transition temperature and suppressing residual crystallinity. This synergistic effect results in improved ionic conductivity at 40 °C, enabling efficient Li^+ transport under moderate operating conditions. Consequently, more homogeneous lithium plating/stripping is achieved, promoting the formation of a stable and ionically conductive solid electrolyte interphase. These combined factors account for the superior interfacial stability and long-term cycling performance observed for the SPE(7:3) + SN electrolyte.

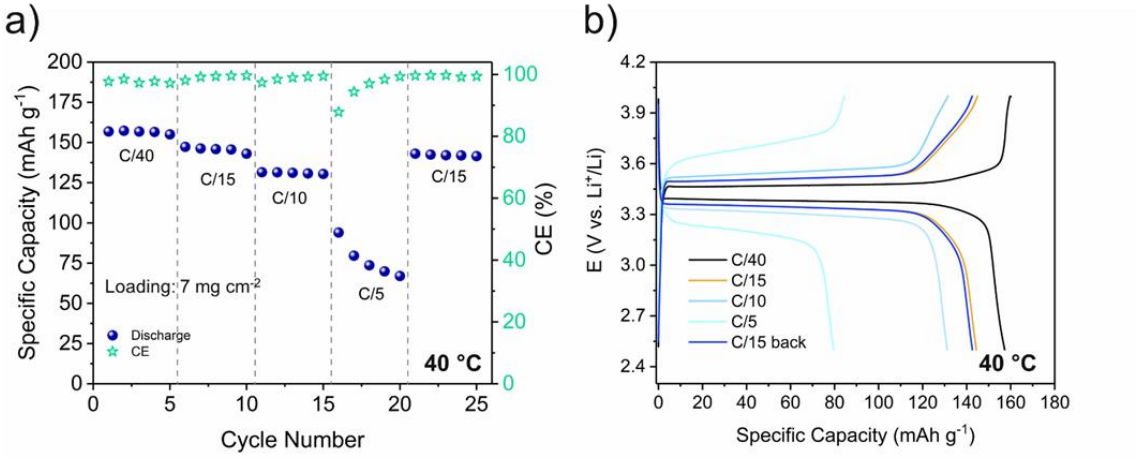

Figure 6.8 Electrochemical performance of Li‖SPE(7:3) + SN‖ LiFePO4 cells (T = 40 °C): (a) rate capability evaluated at C-rates ranging from C/40 to C/5; (b) representative charge–discharge voltage profiles at the different C-rates. All tests were performed within a voltage window of 2.5 and 4.0 V.

Laboratory-scale all-solid-state lithium metal cells were assembled to evaluate the electrochemical performance of the optimized SPE in combination with both moderate- (LFP) and high-voltage (NMC) cathode materials at 40 °C. Figure 4a shows the rate capability of the Li‖SPE(7:3) + SN‖LFP cell cycled at 40 °C at progressively increasing C-rates from C/40 to C/5. At a low current density (C/40),

the cell delivers a high specific discharge capacity of 157 mAh g^{-1}, which is close to the theoretical capacity of the commercial LFP used as cathode active material. Upon increasing the rate, the cell maintains discharge capacities of 147 and 135 mAh g^{-1} at C/15 and C/10, respectively. At C/5, a more pronounced capacity drops to 94 mAh g^{-1} is observed, which can be attributed to increased polarization arising from kinetic limitations typical of solid-state systems. Nevertheless, when the current density is reduced back to C/15, the discharge capacity largely recovers, confirming the absence of significant irreversible degradation. The initial Coulombic efficiency is ~98%; at C/10, the CE stabilizes at ~99.2%. Upon returning to C/15 in the subsequent cycles, the CE further improves, reaching values as high as 99.7%. The relatively small capacity decay demonstrates that the SPE(7:3) + SN electrolyte provides sufficient ionic conductivity and low interfacial resistance to sustain operation at higher current densities. The representative galvanostatic charge-discharge profiles at different C-rates (**Figure 6.8b**) show that voltage polarization remains relatively low, indicating efficient charge transfer enabled by good interfacial contact between the SPE and the active material at low and intermediate rates. However, as the current density increases, the polarization gradually rises, as expected for SPEs. Nevertheless, no abnormal voltage profiles are observed, indicating homogeneous Li^+ transport and stable interfacial behavior. Performance is clearly higher than that observed for the pristine electrolyte, which exhibited a considerable capacity drop under similar conditions. (**Figure 6.9**).

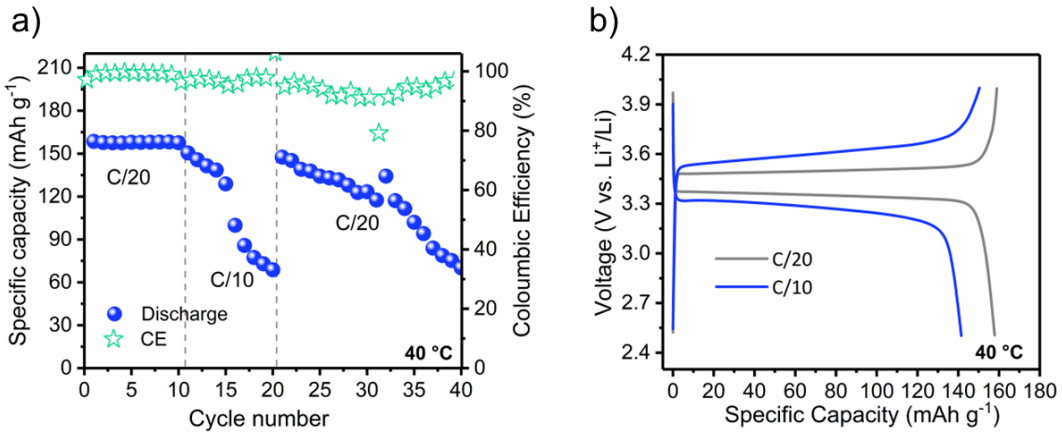

Figure 6.9 Rate capability of the pristine electrolyte employing a Li/SPE(1:1)/LFP cell upon reversible galvanostatic cycling at 40 °C (a) and the corresponding voltage vs. specific capacity curves at C/20 and C/10 rates (b).

6.3 Electrochemical Behavior of Solid Polymer Electrolyte with High Voltage Cathode

To further verify the feasibility of the SN-containing SPE for practical applications, laboratory-scale Li-metal battery cells comprising a catholyte-electrolyte integrated NMC electrode and lithium metal anode were assembled. The performance of the SPE(7:3) + SN SPE was evaluated using a commercial NMC662 cathode cycled between 3.0 and 4.2 V vs. Li^+/Li at 40 °C. As shown in **Figure 6.10a**, the cell delivers a reversible discharge capacity of approximately 145 mAh g^{-1} at C/15, demonstrating that the electrolyte can operate stably under oxidative potentials exceeding 4.0 V. Upon increasing the current density to C/10 and C/5, a gradual decrease in capacity is observed, which is primarily associated with increased polarization rather than electrolyte degradation. This interpretation is supported by the recovery of the capacity when the current density is returned to C/15. The voltage profiles reported in **Figure 6.10b** exhibit smooth and sloping charge–discharge curves typical of layered NMC cathodes. At lower current densities, the profiles display limited polarization and good reversibility, whereas higher rates lead to increased overpotential, particularly near the upper cutoff voltage. Importantly, no abrupt voltage drops or indications of parasitic oxidation are observed, suggesting that the presence of SN and PEC improves the oxidative stability of the electrolyte. Noteworthy, the pristine SPE, both at 40 and 70 °C, was found to operate reliably only with the LFP cathode and not with high-voltage cathodes.

Long-term cycling stability of the SPE(7:3) + SN SPE at C/15 is shown in Figures **6.10c** and **6.10d**. Remarkably, the cell maintains a stable discharge capacity over prolonged cycling, with only gradual and limited capacity fading. The corresponding CE remains in the range of 98-99% throughout the test, indicating highly reversible lithium insertion and extraction processes. Selected voltage profiles collected at different cycle numbers overlap closely, confirming that polarization does not significantly increase upon cycling and that the electrode–electrolyte interfaces remain stable over time.

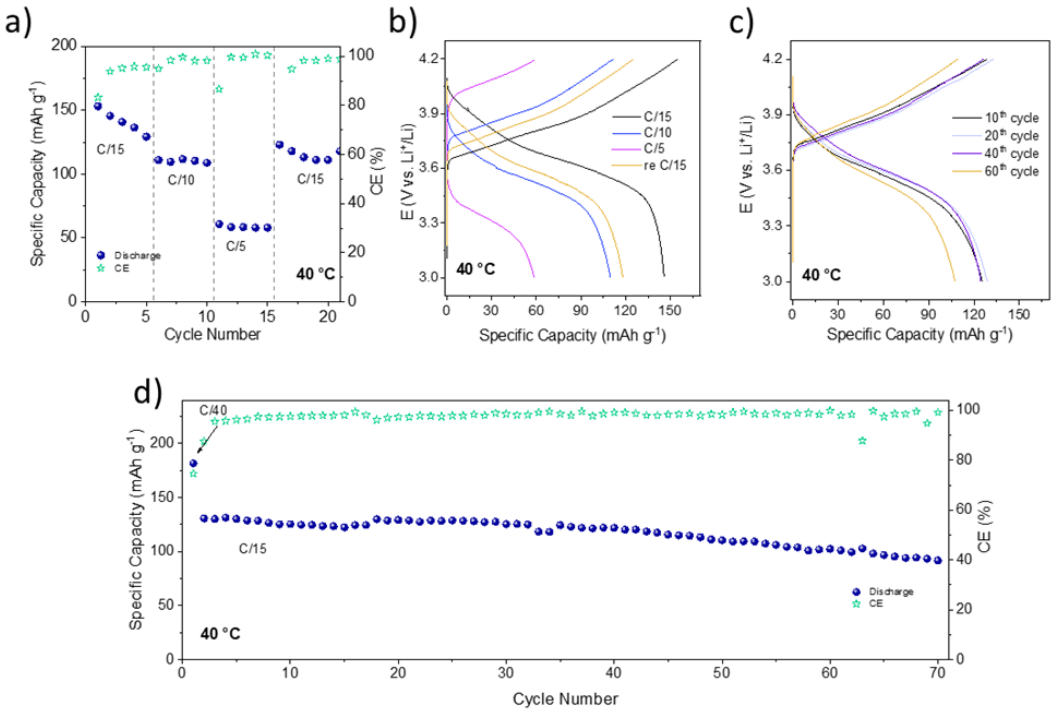

Figure 6.10 Electrochemical performance of Li‖ SPE(7:3) + SN‖NMC622 cells (T = 40 °C): (a) rate capability evaluated at C-rates ranging from C/15 to C/5; (b) representative charge–discharge voltage vs. specific capacity profiles at the different C-rates; (c) representative charge–discharge voltage vs. specific capacity profiles at C/15; (d) long-term cycling at C/15. All tests were performed within a voltage range of 3 and 4.2 V.

For comparison, a Li‖NMC622 cell employing the SPE(1:1) + SN SPE was also assembled (**Figure 6.10**). In this case, the cell exhibits significantly lower performance. An initial discharge capacity of ~120 mAh g^{-1} is achieved at C/15, followed by rapid capacity fading and pronounced polarization at higher current densities, with only partial recovery when returning to lower rates. The higher PEC content in the 1:1 SPE likely results in insufficient ion transport and reduced interfacial stability at high voltages, ultimately preventing sustained operation with NMC cathodes.

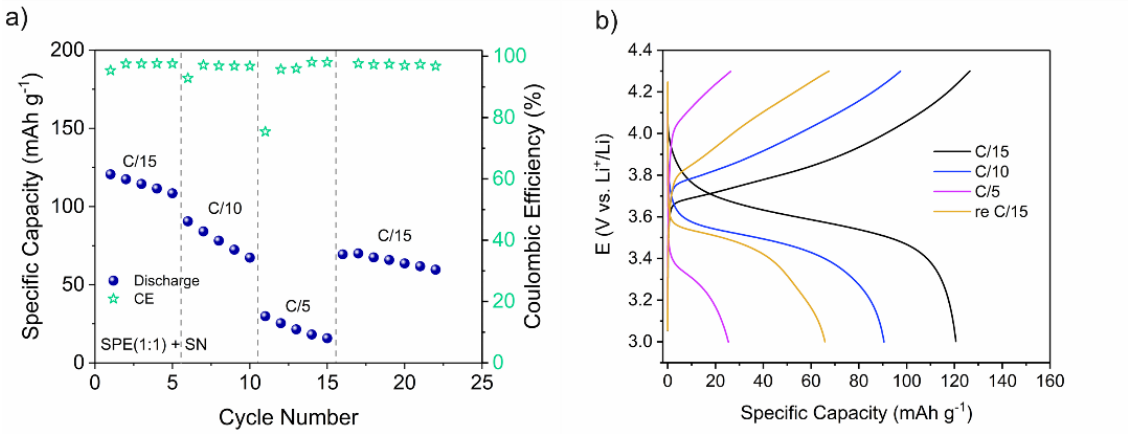

Figure 6.11 Rate capability of Li-metal cell employing SPE(1:1) + SN with NMC622-based cathode: (a) evaluation of the rate capability at C rates ranging from C/15 to C/5 (T = 40 °C); (b) selected dis-/charge profiles obtained at the different C rates.

6.4 Concluding remarks

In summary, this Chapter builds on the solvent-free, UV-cured PEO/PEC electrolyte platform established in the previous Chapters and demonstrates that the introduction of succinonitrile provides an effective step further towards the enhancement of its performance at moderate temperature. Within this already optimized and scalable processing framework, SN proved particularly effective in promoting ionic transport and broadening the electrochemical applicability of the electrolyte, while the systematic investigation of the PEO/PEC ratio identified a PEO-rich composition as the most favorable compromise between conductivity, mechanical robustness, and interfacial stability toward lithium metal.

The optimized SPE(7:3)+SN formulation combined efficient Li^+ transport with sufficient structural integrity for reliable cell assembly and operation. Most importantly, it enabled highly reversible lithium plating/stripping for more than 1400 h in symmetric Li‖Li cells at 40 °C, with moderate and stable overpotentials, indicating the formation of a durable and homogeneous electrolyte/electrode interphase. This result confirms that the combined action of UV-crosslinking and SN plasticization can effectively stabilize the lithium interface while preserving the solid-state character of the SPE.

The practical relevance of this electrolyte was further validated in laboratory-scale solid-state lithium metal batteries employing both LFP and high-voltage NMC cathodes. In both configurations, the cells delivered near-practical specific capacities and stable cycling at 40 °C, while the oxidative stability of the optimized

electrolyte was sufficient to sustain operation up to 4.2 V vs. Li^+/Li with acceptable polarization and rate capability. Overall, these findings show that the synergistic combination of an established solvent-free processing route, crosslinked PEO/PEC networks, and SN plasticization represents a viable strategy to extend the performance of polymer electrolytes toward moderate-temperature operation. More broadly, this work highlights how targeted formulation advances, built on a scalable processing platform, can effectively bridge ionic transport, interfacial stability, and practical cell performance in next-generation solid-state lithium metal batteries.

References

[1] P.J. Alarco, Y. Abu-Lebdeh, A. Abouimrane, M. Armand, The plastic-crystalline phase of succinonitrile as a universal matrix for solid-state ionic conductors, Nat. Mater. 3 (2004) 476–481. https://doi.org/10.1038/nmat1158.

[2] L.Z. Fan, Y.S. Hu, A.J. Bhattacharyya, J. Maier, Succinonitrile as a versatile additive for polymer electrolytes, Adv. Funct. Mater. 17 (2007) 2800–2807. https://doi.org/10.1002/adfm.200601070.

[3] F. Chen, W. Zha, D. Yang, S. Cao, Q. Shen, L. Zhang, D.R. Sadoway, All-Solid-State Lithium Battery Fitted with Polymer Electrolyte Enhanced by Solid Plasticizer and Conductive Ceramic Filler, J. Electrochem. Soc. 165 (2018) A3558–A3565. https://doi.org/10.1149/2.1371814jes.

[4] V. van Laack, F. Langer, A. Hartwig, K. Koschek, Succinonitrile-Polymer Composite Electrolytes for Li-Ion Solid-State Batteries─The Influence of Polymer Additives on Thermomechanical and Electrochemical Properties, ACS Omega 8 (2023) 9058–9066. https://doi.org/10.1021/acsomega.2c02174.

[5] W. Zha, J. Li, W. Li, C. Sun, Z. Wen, Anchoring succinonitrile by solvent-Li+ associations for high-performance solid-state lithium battery, Chemical Engineering Journal 406 (2021) 126754. https://doi.org/10.1016/j.cej.2020.126754.

[6] Y. Liu, Y. Zhao, W. Lu, L. Sun, L. Lin, M. Zheng, X. Sun, H. Xie, PEO based polymer in plastic crystal electrolytes for room temperature high-voltage lithium metal batteries, Nano Energy 88 (2021) 106205. https://doi.org/10.1016/j.nanoen.2021.106205.

[7] S. Xu, Z. Sun, C. Sun, F. Li, K. Chen, Z. Zhang, G. Hou, H.M. Cheng, F. Li, Homogeneous and Fast Ion Conduction of PEO-Based Solid-State Electrolyte at Low Temperature, Adv. Funct. Mater. 30 (2020) 2007172. https://doi.org/10.1002/adfm.202007172.

[8] B. Chen, Z. Huang, X. Chen, Y. Zhao, Q. Xu, P. Long, S. Chen, X. Xu, A new composite solid electrolyte PEO/Li10GeP2S12/SN for all-solid-state lithium battery, Electrochim. Acta 210 (2016) 905–914. https://doi.org/10.1016/j.electacta.2016.06.025.

[9] M. Falco, C. Simari, C. Ferrara, J.R. Nair, G. Meligrana, F. Bella, I. Nicotera, P. Mustarelli, M. Winter, C. Gerbaldi, Understanding the effect of UV-induced cross-linking on the physicochemical properties of highly performing PEO/LiTFSI-based polymer electrolytes, Langmuir 35 (2019) 8210–8219. https://doi.org/10.1021/acs.langmuir.9b00041.

[10] D.F. Miranda, C. Versek, M.T. Tuominen, T.P. Russell, J.J. Watkins, Cross-linked block copolymer/ionic liquid self-assembled blends for polymer gel electrolytes with high ionic conductivity and mechanical strength, Macromolecules 46 (2013) 9313–9323. https://doi.org/10.1021/ma401302r.

[11] F. Gambino, M. Gastaldi, A. Jouhara, S. Malburet, S. Galliano, N. Cavallini, G. Colucci, M. Zanetti, A. Fina, G.A. Elia, C. Gerbaldi, Formulating PEO-polycarbonate blends as solid polymer electrolytes by solvent-free extrusion, Journal of Power Sources Advances 30 (2024) 100160. https://doi.org/10.1016/j.powera.2024.100160.

[12] M. Gastaldi, F. Gambino, H. Darjazi, A. Jouhara, S. Malburet, M. Zanetti, G. Saracco, G.A. Elia, C. Gerbaldi, Dry extrusion of poly(ethylene oxide)-polycarbonate all-solid-state electrolytes for Li-metal batteries: effect of UV-crosslinking on the electrochemical performance, Mater. Today Energy 52 (2025) 101947. https://doi.org/10.1016/j.mtener.2025.101947.

[13] Z. Xue, D. He, X. Xie, Poly(ethylene oxide)-based electrolytes for lithium-ion batteries, J. Mater. Chem. A Mater. 3 (2015) 19218–19253. https://doi.org/10.1039/c5ta03471j.

[14] L. Porcarelli, C. Gerbaldi, F. Bella, J.R. Nair, Super Soft All-Ethylene Oxide Polymer Electrolyte for Safe All-Solid Lithium Batteries, Sci. Rep. 6 (2016) 19892. https://doi.org/10.1038/srep19892.

[15] R. He, M. Echeverri, D. Ward, Y. Zhu, T. Kyu, Highly conductive solvent-free polymer electrolyte membrane for lithium-ion batteries: Effect of prepolymer molecular weight, J. Memb. Sci. 498 (2016) 208–217. https://doi.org/10.1016/j.memsci.2015.10.008.

[16] H. Beyer, S. Meini, N. Tsiouvaras, M. Piana, H.A. Gasteiger, Thermal and electrochemical decomposition of lithium peroxide in non-catalyzed carbon cathodes for Li-air batteries, Physical Chemistry Chemical Physics 15 (2013) 11025–11037. https://doi.org/10.1039/c3cp51056e.

[17] Z. Yang, Y. Luo, X. Gao, R. Wang, High-Safety All-Solid-State Lithium-Ion Battery Working at Ambient Temperature with In Situ UV-Curing Polymer Electrolyte on the Electrode, ChemElectroChem 7 (2020) 2599–2607. https://doi.org/10.1002/celc.202000411.

[18] D. Bao, W. Zhao, Z. Li, Y. Tao, Y. Zhong, Z. Tang, Z. Gao, H. Wang, H. Zhang, X. Sun, A solid-like succinonitrile-based polymer electrolyte with superior mechanical strength for high performance lithium metal batteries, J. Energy Storage 91 (2024) 112016. https://doi.org/10.1016/j.est.2024.112016.

[19] D. Lin, P.Y. Yuen, Y. Liu, W. Liu, N. Liu, R.H. Dauskardt, Y. Cui, A Silica-Aerogel-Reinforced Composite Polymer Electrolyte with High Ionic Conductivity and High Modulus, Advanced Materials 30 (2018) 1802661. https://doi.org/10.1002/adma.201802661.

[20] Z. Li, J. Mindemark, D. Brandell, Y. Tominaga, A concentrated poly(ethylene carbonate)/poly(trimethylene carbonate) blend electrolyte for all-solid-state Li battery, Polym. J. 51 (2019) 753–760. https://doi.org/10.1038/s41428-019-0184-5.

[21] B. Sun, C. Xu, J. Mindemark, T. Gustafsson, K. Edström, D. Brandell, At the polymer electrolyte interfaces: the role of the polymer host in interphase layer formation in Li-batteries, J. Mater. Chem. A Mater. 3 (2015) 13994–14000. https://doi.org/10.1039/c5ta02485d.

[22] Y. Liu, Y. Zhao, W. Lu, L. Sun, L. Lin, M. Zheng, X. Sun, H. Xie, PEO based polymer in plastic crystal electrolytes for room temperature high-voltage lithium

metal batteries, Nano Energy 88 (2021) 106205. https://doi.org/10.1016/j.nanoen.2021.106205.

Chapter 7
Low Melting Non-Corrosive Asymmetric Thioether-TFSI Li Salts for Solid Polymer Electrolytes

Among lithium salts for poly(ethylene oxide)-based solid polymer electrolytes, a major breakthrough was the introduction of lithium bis(trifluoromethylsulfonyl)imide (LiTFSI, **Scheme 1**), featuring a weakly coordinating, highly charge-delocalized $TFSI^-$ anion [1]. Weak coordination enhances Li^+ mobility while enabling high ionic conductivity (3.9×10^{-4} S cm^{-1} at 70°C , the typical operating temperature of LiMP batteries), along with thermal and chemical stability, prompting extensive efforts to replace the widely used but less thermally stable and more hazardous $LiPF_6$ [2–4]. However, LiTFSI still exhibits several well-known drawbacks in PEO-based SPEs (**Table 1**), relatively low Li^+ transference number (t_{Li^+} = 0.22) [5], lower ionic conductivity compared to $LiPF_6$/PEO systems [6], poor long-term interfacial stability toward Li metal due to unstable SEI formation, and pronounced corrosion of aluminum current collectors (**Figure 7.1, Table 7.1**) [3,7]. These limitations have driven intensive research into $TFSI^-$ anion modification and the development of new weakly coordinating anions, aiming to produce SPEs with higher ionic conductivity, improved Li-anode interfacial stability, and enhanced cycling performance with aluminum current

collectors [5,8–11]. One promising strategy involves Li salts that are liquid at battery operating temperatures, as reduced melting points (T_m) can plasticize the PEO matrix, suppress crystallization. Early studies in this field focused on how the length and symmetry of fluoroalkyl chains within the TFSI-like anion influence the properties of the resulting Li salts and their SPEs (**Scheme 1**; e.g., LiBETI [12], LiFTFSI [5], Li bis[(nonafluorobutyl)-sulfonyl]imide (LiC4C4) [13], Li (trifluoromethylsulfonyl)-N-(nona-fluorobutylsulfonyl)imide (C1C4) [14] etc.). It was demonstrated that the length of the perfluoroalkyl chains improves the interfacial compatibility of SPEs with both anode materials (e.g., Li metal and graphite) and cathode electrodes (**Table 7.1**). However, this structural variation increased T_m of salts, exerted opposing effects on ionic conductivity of Li salt/PEO materials, and does not enhance lithium-ion transport, as the highly fluorinated groups interact only weakly with PEG chains [15].

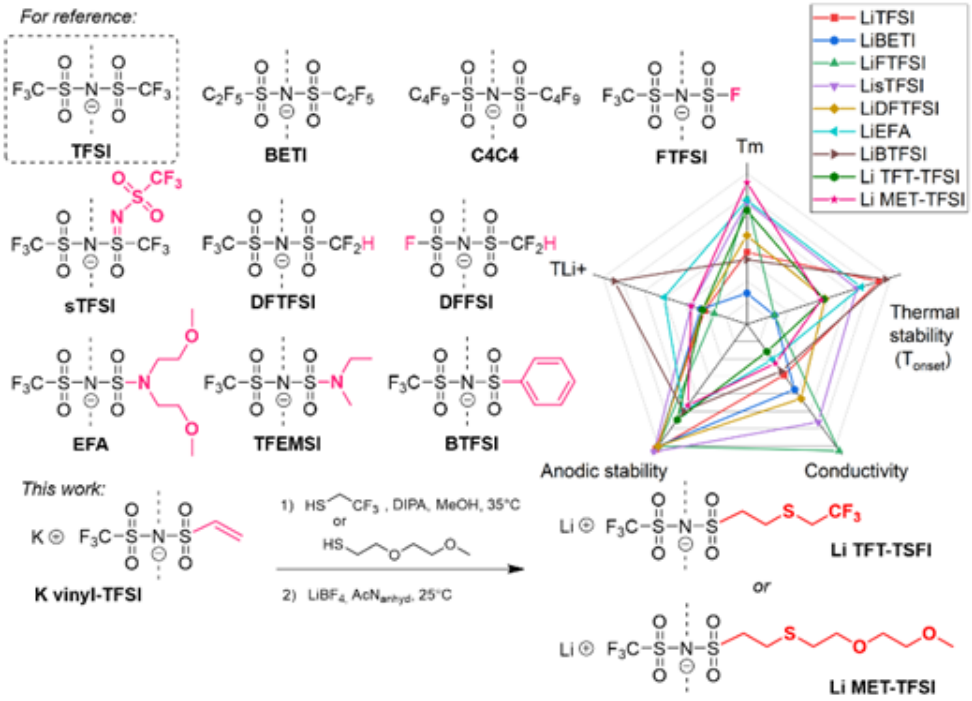

Figure 7.1 Reference structures of TFSI and previously reported asymmetrically modified TFSI anions selected for comparison; and synthetic pathway overview of the two novel asymmetric thioether-TFSI Li salts.

In contrast, introducing asymmetry into the TFSI anion was found to substantially reduce T_m while simultaneously improving other SPE properties [16–19]. A notable example is LisTFSI (super-TFSI) (**Scheme 1**) [16,17], it exhibits a dramatically reduced melting point (118 °C vs. 233 °C) which enables higher ionic conductivity and slightly improved Li^+ transference numbers without

compromising electrochemical stability, although stable cycling has mainly been demonstrated in ionic liquid-based systems [20].

Combined with asymmetry, several studies have further explored the introduction of a positive dipole into the anion structure, leading to the development of DFTFSI [6,19,21] and DFFSI [18] anions, in which one fluorine atom is substituted by hydrogen. This modification results in only a modest reduction in the T_m of the Li salts; however, LiDFTFSI/PEO and LiDFFSI/PEO SPEs exhibit approximately a 1.5-fold increase in ionic conductivity (compared to LiTFSI/PEO), reduced interfacial resistance, improved compatibility with Li-metal anodes and remarkably suppressed Al corrosion compared to LiTFSI/PEO.

A similar strategy combining anion asymmetry with enhanced interactions with the host polymer matrix was further exploited in the design of the EFA [22] and TFEMSI [23] anions, in which a tertiary amine group is directly attached to the sulfonyl moiety. The incorporation of short PEG chains significantly reduced the melting temperature of LiEFA to 112 °C (**Table 7.1**) and increased the Li^+ transference number up to 0.43, owing to segmental entanglement of the anion-tethered methoxyethyl chains, which are likely immobilized by PEO via hydrogen bonding [22]. However, this modification led to a reduced electrochemical stability toward the Li anode (≈4 V) and a slight loss of thermal stability.

Finally, LiBTFSI [24] achieves one of the highest reported Li^+ transference numbers (0.69) in PEO-based SPEs, attributed to π–π stacking between aromatic groups that promotes anion aggregation and suppresses anion mobility, resulting in improved cycling stability despite moderate conductivity and limited anodic stability.

In this context, the present Chapter investigates two novel asymmetric thioether-TFSI lithium salts designed as alternative conducting salts for PEO-based solid polymer electrolytes. Their molecular design combines an asymmetric TFSI framework with thioether-containing substituents in order to lower the salt melting point, limit aluminum corrosion, and tune the interactions between anion and polymer matrix. The resulting salts, Li TFT-TFSI and Li MET-TFSI, were synthesized and incorporated into PEO-based electrolytes, the thermal and electrochemical properties of which were systematically compared with those of the conventional LiTFSI/PEO system.

Table 7.1 Thermal and electrochemical properties of Li salts and respective Li salt/PEO SPEs

Li salt	Neat Li salt		Li salt/PEO polyelectrolyte[a]		
	T_m[b] (°C)	T_{onset}[c] (°C)	σ 70°C (S cm^{-1})	LSV[d] 70°C (V)	T_{Li^+}[e] 70°C
Li TFT-TFSI	136	240	2.1×10^{-4}	4.3	0.23
Li MET-TFSI	71	235	3.0×10^{-4}	3.8	0.29
For comparison:					
Li TFSI[6,14]	233	356	3.9×10^{-4}	4.8-5.1	0.22
Li BETI[13]	328	n.d	5.0×10^{-4}	n.d	0.24
Li C_4C_4[13]	352	334	2.2×10^{-4}	5.3	0.29
Li FTFSI[5]	110	150	9.7×10^{-4}	5.2	0.17
Li sTFSI[17]	118	300	7.5×10^{-4}	5.4	0.29
Li DFFSI[18]	n.d.	184	6.6×10^{-4}	n.d	0.23
Li DFTFSI[19]	194	242	5.7×10^{-4}	5.2	0.35
Li EFA[22]	112	308	2.7×10^{-4}	4.0	0.43
Li TFEMSI[24]	181	318	3.5×10^{-4}	n.d	0.64
Li BTFSI[25]	n.d.	352	3.6×10^{-4}	4.0	0.69

[a] The Li salts/PEO blends composition was fixed at [EO]/[Li^+] = 20 (note: PEO with different molecular weights may be used). [b] Melting point (T_m) determined by DSC under N_2 (note: heating rates of 5 or 10°C min^{-1} may be employed). [c] Onset weight loss temperature determined by TGA in air (note: heating rates of 5 or 10°C min^{-1} may be employed). [d] Anodic stability by linear sweep voltammetry (LSV) at 70°C. [e] Li-ion transference number measured at 70°C.

Particular attention was devoted to ionic conductivity, lithium-ion transference number, compatibility with lithium metal, and cycling performance in Li‖$LiFePO_4$ cells, together with the passivation behavior toward aluminum current collectors. Overall, this study aimed at assessing the practical potential of low-melting, non-corrosive asymmetric lithium salts as promising alternatives to conventional conducting salts for solid polymer electrolytes. Within the broader framework of this thesis, this Chapter well fits as it highlights how the design of new lithium salts is a key strategy to overcome the limitations of conventional polymer electrolytes while also guiding the development of more sustainable battery chemistries.

These results have been published in the scientific research article V. Y. Shevtsov, F. Gambino et al., Chemm. Comm (2026) (under press) and are reproduced/readapted in the following sections.

7.1 Synthesis Overview

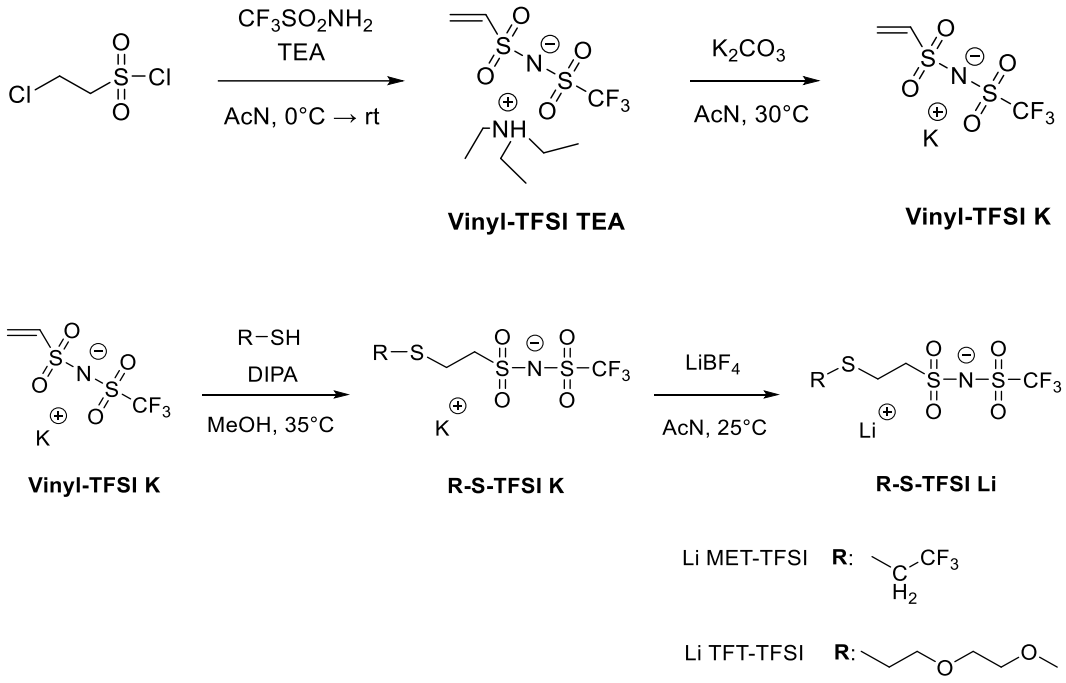

Figure 7.2 General synthetic route for the preparation of Li MET-TFSI and Li TFT-TFSI salts.

Synthesis of **Vinyl-TFSI TEA**

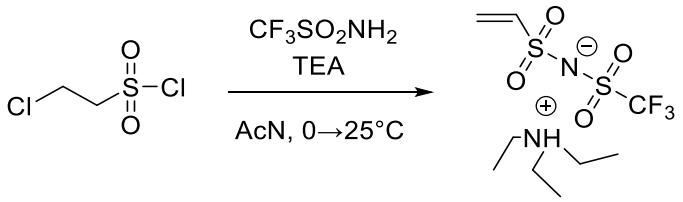

$CF_3SO_2NH_2$ (27.4 g, 0.184 mol) and triethylamine (TEA, 59.6 g, 0.589 mol) were dissolved in 60 mL of anhydrous acetonitrile (AcN) at RT under an inert atmosphere. The resulting solution was then precooled to 0 °C using an ice bath. A separate solution of 2-chloroethanesulfonyl chloride (30.0 g, 0.184 mol) in 200 mL of anhydrous AcN was prepared and added dropwise to the amine solution while maintaining the temperature at 0 °C. After the addition was complete, the ice bath was removed, and the reaction mixture was allowed to warm gradually to RT. Stirring was continued at 25 °C for 12 hours and the formation of a white precipitate

of triethylammonium chloride ($(CH_3CH_2)_3NH^+Cl^-$) was observed. The precipitate was filtered and the solvent was then evaporated. The resulting oil was dissolved in 50 mL of anhydrous ethyl acetate (EtAc) and the additional precipitation of $(CH_3CH_2)_3NH^+Cl^-$ was observed. The solid was filtered off, the solvent was subsequently removed under reduced pressure, yielding the brown oily product. It was finally dried at 40 °C/0.2 mbar for 12 h in a Büchi B-585 glass drying oven equipped with a P_2O_5 moisture trap. Yield: 57.5 g (92 %); NMR **Figure A1**

Synthesis of **Vinyl-TFSI K**

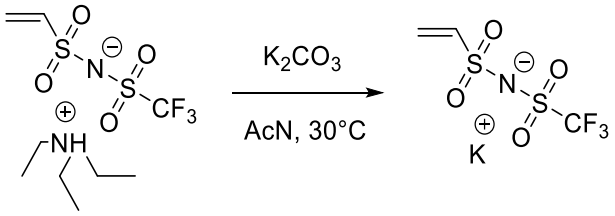

The freshly dried K_2CO_3 powder (58.3 g, 0.422 mol) was added in one portion to a solution of vinyl-TFSI TEA (57.5 g, 0.169 mol) in anhydrous AcN (200 mL). The suspension was then stirred for 12 h at 30°C under an inert atmosphere. The residual powder was filtered off and the solvent evaporated. The obtained beige powder was washed with anhydrous diethyl ether (3 × 35 mL) and further dried at 40°C/0.2 mbar for 15 h. Yield: 40.5 g (86 %); NMR **Figure A2**

Synthesis of **CF_3-CH_2-S-TFSI K**

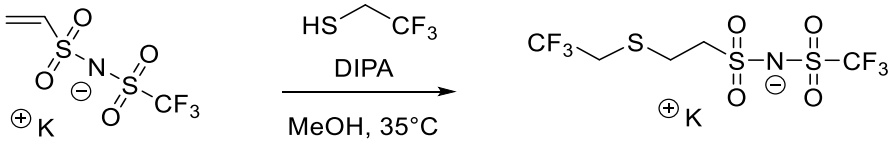

Vinyl-TFSI K (4.93 g, 17.8 mmol), 2,2,2-trifluoroethanethiol (2.68 g, 23.0 mmol), DIPA (0.36 g, 3.9 mmol), and anhydrous MeOH (20 mL) were charged into a high-pressure glass reactor, which was subsequently flushed with Ar and sealed. After complete dissolution at room temperature, the reaction mixture was stirred for 5 h at room temperature and then for an additional 15 h at 35 °C. Upon completion, the solution was concentrated to approximately half of its initial volume by evaporating 6 mL of methanol under reduced pressure (40 °C/100 mbar). The concentrated solution was then precipitated into an excess of anhydrous diethyl

ether (60 mL) under vigorous stirring, affording beige powder. The solid was isolated by decantation, washed with anhydrous diethyl ether (3 × 25 mL), and dried at 30 °C/0.15 mbar for 12 h. Yield: 4.80 g (68%); **NMR Figure A3**

Synthesis of CF_3-CH_2-S-TFSI Li (**Li TFT-TFSI**)

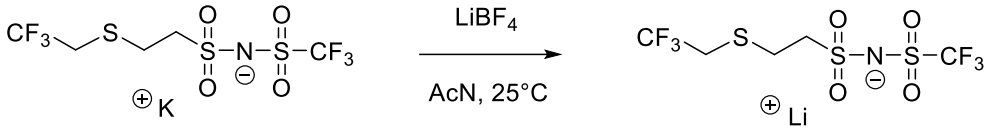

CF_3-CH_2-S-TFSI K (2.50 g, 6.3 mmol) and anhydrous $LiBF_4$ (0.60 g, 6.3 mmol) were dissolved in anhydrous AcN (20 mL) under an argon atmosphere. The resulting solution was stirred at 25 °C for 24 h, during which the formation of a KBF_4 precipitate was observed. The suspension was subsequently filtered to afford a clear solution. The solvent was removed under reduced pressure to obtain white powder. The product was dried at 50 °C/0.1 mbar for 12 h. Yield: 1.82 g (91 %); NMR **Figure A4−6**; Anal. calcd. for $C_5H_6F_6LiNO_4S_3$ (361.22): C, 16.63 %; H, 1.67 %; N, 3.88 %. Found: C, 16.69 %; H, 1.84 %; N, 3.98 %; T_g = -2.9 °C (DSC, 5 °C min^{-1}); T_m = 135.9 °C (DSC, 5 °C min^{-1}).

Synthesis of **CH_3-(O-CH_2-CH_2)$_2$-S-TFSI K**

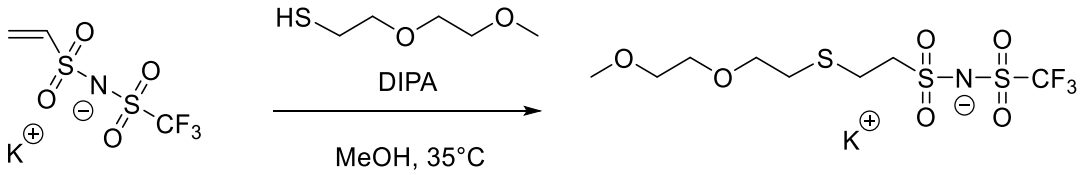

Vinyl-TFSI K (4.0 g, 14.4 mmol), 2-(2-methoxyethoxy)ethane-1-thiol (2.56 g, 18.7 mmol), DIPA (0.44 g, 4.3 mmol), and anhydrous MeOH (20 mL) were charged into a high-pressure glass reactor, which was subsequently flushed with Ar and sealed. After complete dissolution at room temperature, the reaction mixture was stirred for 5 h at room temperature and then for an additional 15 h at 35 °C. Upon completion, the solution was concentrated to approximately half of its initial volume by evaporating 7 mL of methanol under reduced pressure (40 °C/100 mbar). The concentrated solution was then precipitated into an excess of anhydrous diethyl ether (60 mL) under vigorous stirring, affording beige powder. The solid was

isolated by decantation, washed with anhydrous diethyl ether (3 × 25 mL), and dried at 30 °C/0.15 mbar for 12. Yield: 4.70 g (78%); **Figure A7**.

Synthesis of CH_3-(O-CH_2-CH_2)$_2$-S-TFSI Li (**Li MET-TFSI**)

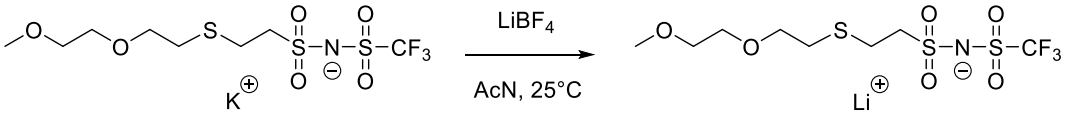

CH_3-(O-CH_2-CH_2)$_2$-S-TFSI K (4.70 g, 11.4 mmol) and anhydrous $LiBF_4$ (1.06 g, 11.4 mmol) were dissolved in anhydrous acetonitrile (40 mL) under an argon atmosphere. The resulting solution was stirred at 25 °C for 24 h, during which the formation of a KBF_4 precipitate was observed. The suspension was subsequently filtered to afford a clear solution. The solvent was removed under reduced pressure to obtain white powder. The product was dried at 50 °C/0.1 mbar for 12 h. Yield: 3.7 g (89 %); **Figure A8−13**; Anal. calc. for $C_8H_{15}F_3LiNO_6S_3$ (381.32): C, 25.20 %; H, 3.97 %; N, 3.67 %. Found: C, 24.57 %; H, 4.00 %; N, 3.68 % ; T_g = −3.9 °C (DSC, 5 °C min^{-1}); T_m = 71.4 °C (DSC, 5 °C min^{-1}).

7.2 Salt Characterization

To address the demand for non-corrosive lithium salts featuring weakly coordinating anions, low T_m, and SPEs with high ionic conductivity and elevated t_{Li^+}, a straightforward synthetic strategy based on thiol-ene click chemistry was here developed (**Figure 7.2**) [25]. This approach employs the commercially available potassium salt of (trifluoromethylsulfonyl)-N-(ethenesulfonyl)-imide (vinyl-TFSI) [26] and enables the modular design of a broad family of asymmetric anions through a two-step reaction sequence with selected thiols. Moreover, the proposed synthesis method is distinguished by its simplicity, consistently high reaction yields, straightforward product isolation, and the attainment of a high level of purity suitable for electrochemical applications. In details, vinyl-TFSI K was reacted with two thiols: 2,2,2-trifluoroethanethiol and 2-(2-methoxyethoxy)-ethane-1-thiol (**Figure 7.2**). The former was chosen to generate the smallest asymmetric anion bearing a fluorinated functional group (-CH_2-CF_3), while the latter introduces two consecutive ethylene oxide (EO) units that, analogously to the EFA anion, are expected to interact with PEO chains, thereby reducing anion mobility. Subsequent cation exchange from potassium to lithium afforded the target thioether-TFSI

lithium salts: lithium ((2-((2,2,2-trifluoroethyl)thio)ethyl)sulfonyl)-N-(trifluorome-thylsulfonyl)imide (abbreviated Li TFT-TFSI) and lithium ((2-((2-(2-methoxy-ethoxy)ethyl)thio)ethyl)sulfonyl)-N-(trifluorome-thylsulfonyl)-imide (Li MET-TFSI). A combination of ^{1}H NMR, ^{7}Li NMR, ^{13}C NMR, ^{19}F NMR and FT-IR spectroscopy and elemental analysis were used to confirm the structures and purity of newly synthesized compounds (Figure A1−A11). Additionally, 2D NMR techniques, such as HSQC and HMBC were used to identify the structure and correctly assign the protons and carbons of Li MET-TFSI (**see Fig. A12−A13**).

DSC traces of the newly synthesized salts reveal melting points (T_m, observed during the 1st heating) at 136 and 71 °C for Li TFT-TFSI and Li MET-TFSI, respectively (**Figure A14–A15**), with the latter representing the lowest T_m reported to date for TFSI-type Li salts (**Figure 7.3a**). This pronounced T_m reduction is attributed to the methoxyethoxy-thioethyl substituent on the TFSI anion, the steric and conformational effects of which hinder efficient anion packing and suppress crystallization.

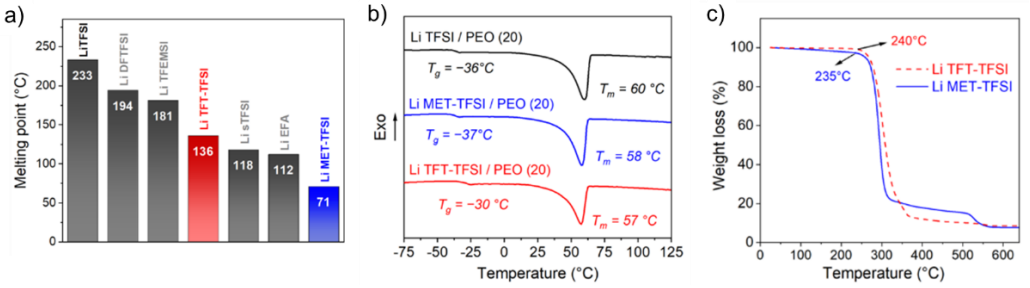

Figure 7.3 Physical and thermal, properties of neat Li salts and LiX/PEO polyelectrolytes (X = TFT-TFSI, MET-TFSI, or TFSI; [EO/Li$^+$] = 20): a) Summary of melting points of asymmetric sulfonimide Li salts; b) DSC traces of salt-in-polymer electrolytes; c) TGA plots of neat Li salts in air.

This interpretation is supported by the second DSC cycle, in which no crystallization was observed even upon slow cooling, and only a $T_g \approx -3.0$ °C was detected.

Switching from Li salts to their PEO-based SPEs with [EO]/[Li$^+$] = 20 by mol ratio resulted in the formation of self-standing semi-transparent membranes, the thermal properties of which were evaluated by DSC. **Figure 7.3b** shows the DSC curves from the first heating scan of the newly developed Li TFT-TFSI/PEO and Li MET-TFSI/PEO SPEs, benchmarked against the conventional LiTFSI/PEO system. All samples exhibit two characteristic thermal transitions: a glass transition in the range of −37.4 to −29.6 °C and a melting transition (T_m) associated with crystalline PEO between 57.3 and 60.5 °C. The T_g values decreased in the following

order: −29.6 °C (Li TFT-TFSI/PEO) > −35.7 °C (LiTFSI/PEO) > −37.4 °C (Li MET-TFSI/PEO). This trend indicates a stronger plasticizing effect of Li MET-TFSI compared to Li TFT-TFSI and the reference LiTFSI salt. Analysis of the PEO melting transition revealed the following order of T_m values: 60.5 °C (LiTFSI/PEO) > 58.0 °C (Li MET-TFSI/PEO) > 57.3 °C (Li TFT-TFSI/PEO), which correlates well with the corresponding melting enthalpies (ΔH_m): 68.5 J g^{-1} (LiTFSI/PEO) > 66.2 J g^{-1} (Li MET-TFSI/PEO) > 54.1 J g^{-1} (Li TFT-TFSI/PEO). These results clearly indicate a reduced degree of PEO crystallinity in the Li MET-TFSI/PEO and Li TFT-TFSI/PEO systems compared to the conventional LiTFSI/PEO SPE. The reduced crystallinity can be attributed both to the lower intrinsic melting points of the newly developed lithium salts and to their enhanced ability to plasticize the PEO matrix. Furthermore, the suppressed recrystallization of PEO can be rationalized by the increased flexibility of the modified TFSI-type anions, which is governed by the nature of the substituent groups attached to the sulfur atom [5,17,21]. In particular, the larger side groups in Li MET-TFSI and Li TFT-TFSI relative to LiTFSI are expected to promote PEO segmental mobility, thereby hindering crystallization in the blended SPEs. TGA in air further revealed an onset of weight loss above 235 °C (**Figure 7.3c**), indicating sufficient thermal stability for practical use, as LMB typically operate below 100 °C.

7.3 Electrochemical Behavior of Novel Lithium Salts

Figure 7.4a shows Arrhenius plots of the total ionic conductivity (σ_i), reflecting the combined transport of Li^+ cations and anions, for Li TFT-TFSI/PEO, Li MET-TFSI/PEO, and LiTFSI/PEO SPEs. In the near-ambient temperature range (20–30 °C), Li MET-TFSI/PEO shows the highest conductivity (5.4×10^{-7} S cm^{-1}), exceeding LiTFSI/PEO (4.7×10^{-7} S cm^{-1}) and Li TFT-TFSI/PEO (2.0×10^{-8} S cm^{-1}).

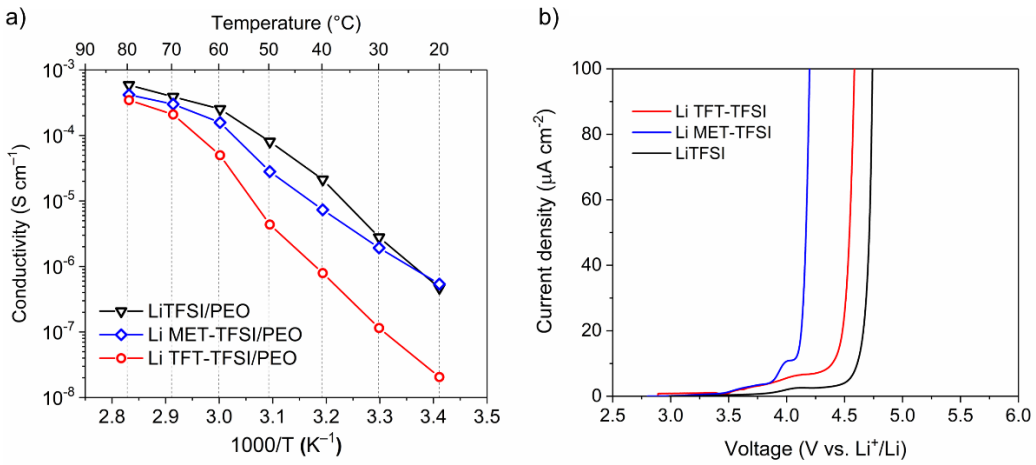

Figure 7.4 Electrical and electrochemical behavior of Li TFT-TFSI/PEO (red), Li MET-TFT/PEO (blue), and Li TFSI/PEO (black). Arrhenius plots of ionic conductivity vs. inverse temperature for polyelectrolytes determined by EIS in the range 20-80 °C (a) and linear sweeping voltammetry profiles measured in a Li‖Lix/PEO‖Al carbon-coated configuration at a scan rate of 0.1 mV s^{-1} at 70 °C (b).

However, ionic conductivity values of all three systems remain insufficient for LMBs, mainly due to crystalline PEO domains that strongly hinder ion transport. Upon heating above 60 °C, conductivity increased sharply for all SPEs, reaching ~10^{-4} S cm^{-1}, which is attributed to melting-induced amorphization of the PEO matrix that enables continuous ion-conducting pathways and enhances ion mobility [27]. At 70 °C, the total ionic conductivity increased with decreasing effective anion volume in the following order (**Table 7.1):** 2.1 × 10^{-4} S cm^{-1} (Li TFT-TFSI/PEO) < 3.0 × 10^{-4} S cm^{-1} (Li MET-TFSI/PEO) ≤ 3.9 × 10^{-4} S cm^{-1} (LiTFSI/PEO). The LSVs of the SPEs are compared in **Figure 7.4b.** All SPEs show anodic breakdown at ~4 V vs. Li/Li^+, attributed to oxidative degradation of the PEO matrix [28]. Increasing the potential to ~4.8 V resulted in a sharp increase in polarization current, indicating the onset of oxidative decomposition involving the thioether anions, possibly together with PEO. Nonetheless, both newly developed Li salts exhibit sufficient anodic stability for operation in LFP batteries.

To evaluate the suitability of thioether-TFSI lithium salts for application in LMBs, the electrochemical properties of Li TFT-TFSI/PEO and Li MET-TFSI/PEO were systematically investigated with particular attention to thir t_{Li^+}, compatibility with the Li metal electrode, and cycling performance in Li°‖Li_x/PEO‖$LiFePO_4$ (LFP) cells. The Li-ion transference number of the SPEs was determined using the Evans−Vincent−Bruce method (**Figure 7.5**).

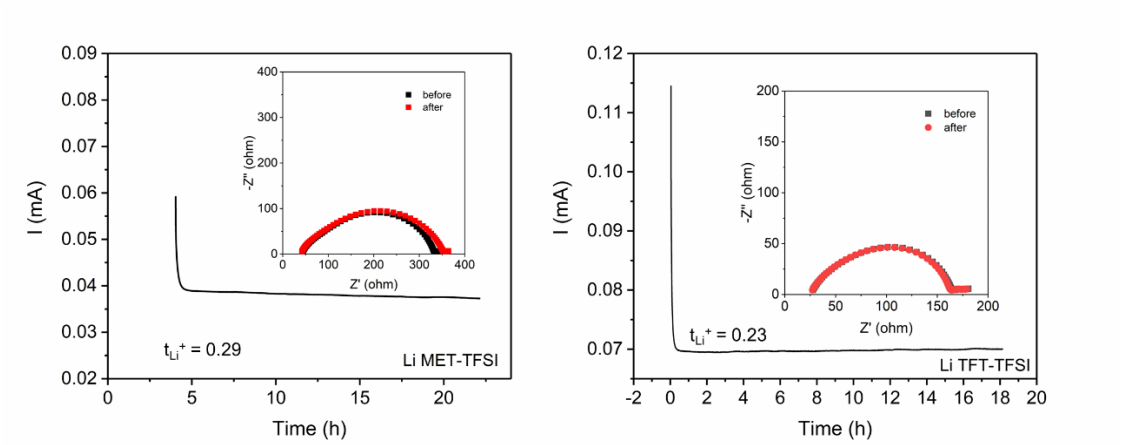

Figure 7.5 Lithium transference number measurements of Li MET-TFSI/PEO (left) and Li TFT-TFSI/PEO (right) at 70°C (EO/Li = 20), including chronoamperometry and EIS before and after polarization.

Notably, Li MET-TFSI/PEO exhibited a higher t_{Li}^+ value (0.29) compared to LiTFSI/PEO (0.22) and Li TFT-TFSI/PEO (0.23). This enhanced t_{Li}^+ can be attributed to a combination of two effects: (i) increased mobility of Li^+-containing species resulting from the lower T_g of the SPE, enabled by the stronger plasticizing effect of Li MET-TFSI, and (ii) reduced mobility of the MET-TFSI anions due to their stronger interactions with the PEO matrix.

Figure 7.6a shows galvanostatic lithium plating/stripping in Li^0 symmetric cells at 70 °C and different current densities. While LiTFSI/PEO exhibits pronounced voltage instabilities already at 0.1 mA cm^{-2}, the TFT-TFSI- and MET-TFSI-based SPEs allow stable cycling at 0.2 mA cm^{-2} with lower overpotentials than the reference system. During long-term cycling at 0.05 mA cm^{-2} (**Figure 7.6b**), the Li TFT-TFSI/PEO and Li MET-TFSI/PEO cells remained stable for over 600 h, whereas the LiTFSI-based cell short-circuited after ~250 h, indicating markedly improved Li^0 electrode stability due to reduced concentration polarization and suppressed dendritic lithium growth.

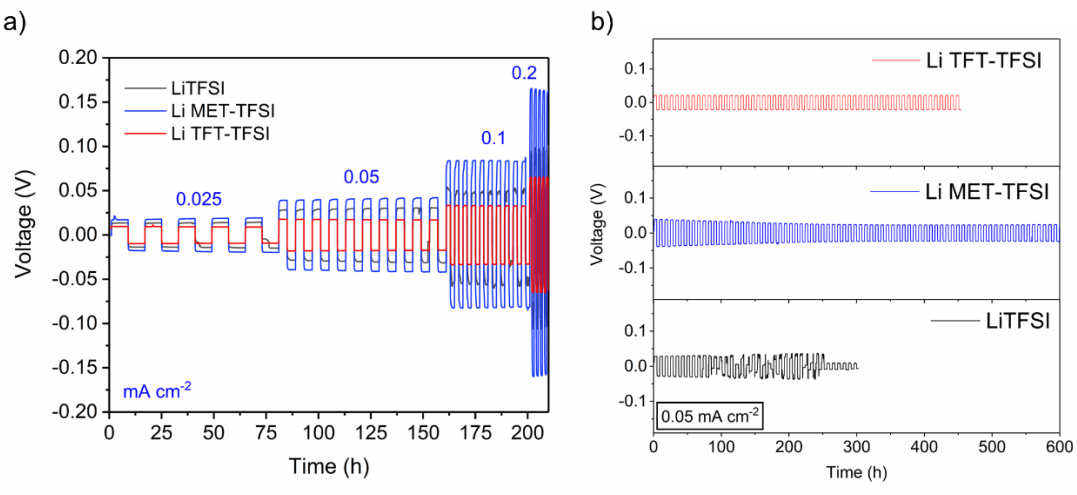

Figure 7.6 Galvanostatic cycling of Li°‖ Lix/PEO ‖Li° symmetric cells at different current densities (total plated/stripped capacity of 0.2 mAh cm^{-2} per half cycle); d) long-term cycling performances of Li symmetric cell at 0.050 mA cm^{-2}.

In addition, symmetric Li^0 cell was used to test the critical current density of SPEs. The current density increases from 0.15 to 0.4 mA cm^{-2} at 70 °C (**Figure 7.7**). The PEO/LiTFSI electrolyte experiences a short circuit during the first cycles, while SPEs based on Li TFT-TFSI and Li MET-TFSI sustain higher current densities and shorting at 0.31 mA cm^{-2} and 0.39 mA cm^{-2} respectively, corroborating the compatibility of the SPEs with the Li metal anode.

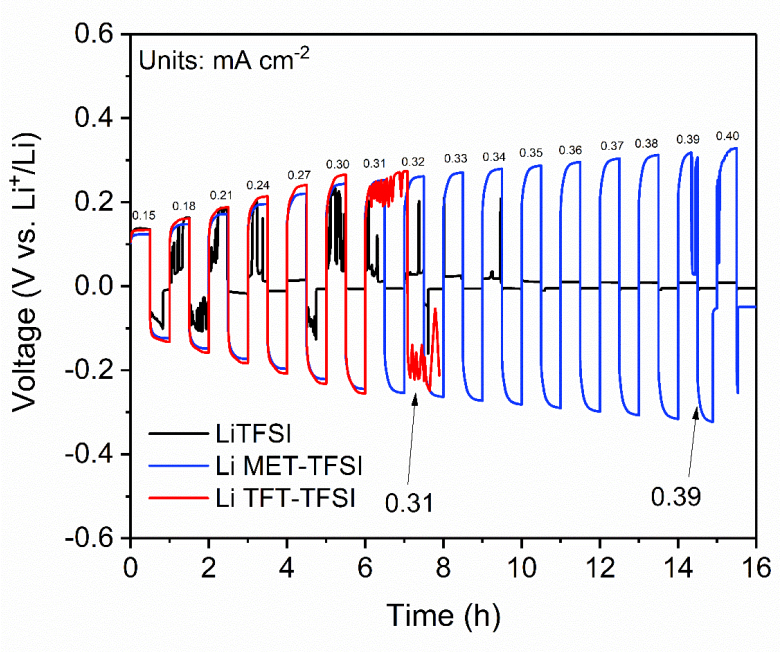

Figure 7.7 Critical current density (CCD) test at 70 °C for the SPEs with new salts under study vs LiTFSI reference.

In **Figure 7.8a** is shown the discharge capacity as a function of current density (stepwise increase from C/20, C/15, C/10, C/5, and back to C/15) for Li°‖Lix/PEO‖$LiFePO_4$ cells. SPEs based on Li TFT-TFSI and Li MET-TFSI display

stable charge/discharge behavior across all C-rates, together with excellent cycling stability and high Coulombic efficiency. Both SPEs maintain capacities close to the theoretical value of $LiFePO_4$ (≈160 mAh g^{-1}), with CE above 98% at all tested rates, whereas the conventional LiTFSI/PEO electrolyte delivers significantly lower capacities of ~130–140 mAh g^{-1} under identical conditions.

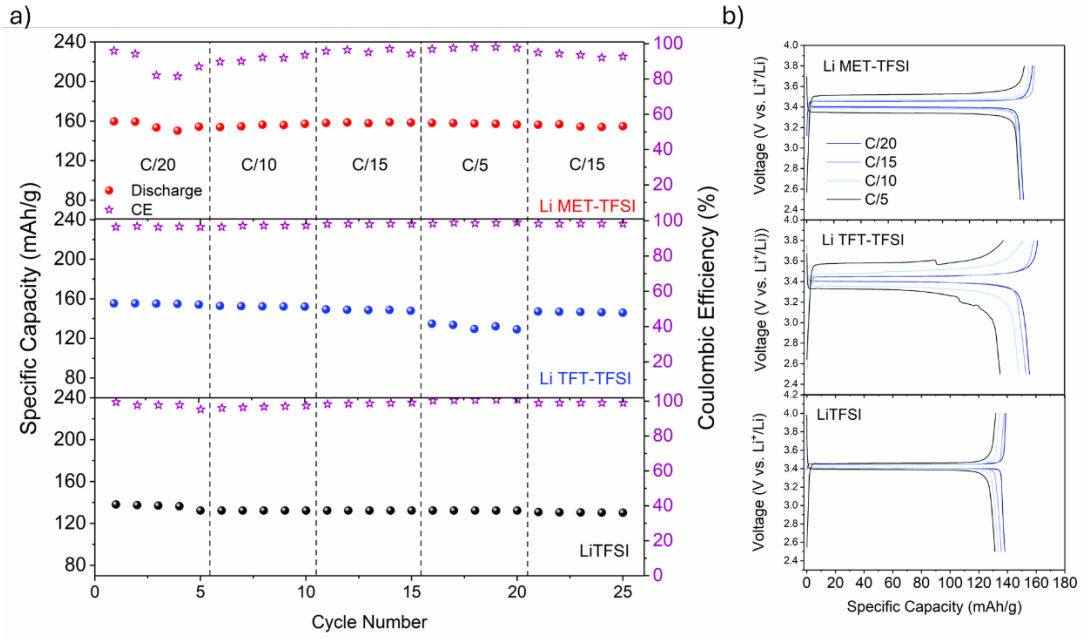

Figure 7.8 Specific capacity and Coulombic efficiency as a function of cycle number for Li°‖ Li_x/PEO ‖$LiFePO_4$ cells at variable C-rates (a); Potential vs. specific capacity profiles of Li°‖Li_x/PEO‖$LiFePO_4$ at 70 °C and variable C-rates (b).

Anodic dissolution tests were performed using 1 M Li salt solutions in EC/DMC (1:1 v/v) with uncoated Al discs by holding the potential 1.3 V above the open-circuit potential of the corresponding half-cell (**Figure 7.9**). During the first cycle, current densities of ~0.9 and ~0.1 µA cm^{-2} were recorded for Li MET-TFSI and Li TFT-TFSI, respectively, which are negligible compared to LiTFSI, for which a sustained current density of ~15 mA cm^{-2} was observed. This pronounced response for LiTFSI clearly indicates anodic dissolution of the Al° current collector [6]. In contrast, the very low currents for Li MET-TFSI and Li TFT-TFSI are attributed to the formation of a highly resistive passivation layer on the Al surface, effectively suppressing anodic dissolution [6,29,30].

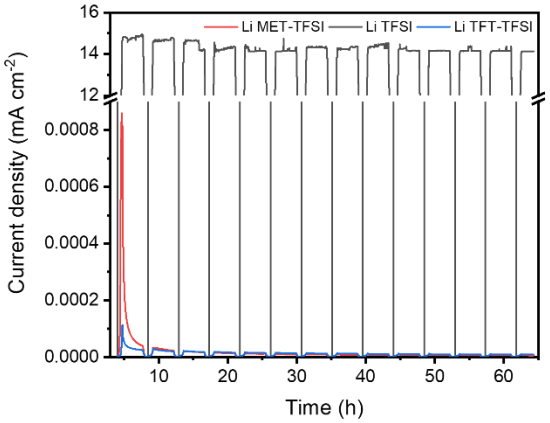

Figure 7.9 Anodic dissolution behavior of aluminium in 1 M Li salt in EC-DMC (1:1 v/v) liquid electrolytes measured in a two-electrode configuration (Al working electrode, activated carbon counter electrode) using a Whatman GF/A glass fiber separator.

To gain a deeper understanding of the chemical composition and morphology of the formed SEI, XPS, and FESEM analyses were conducted on Al disk. Strongly reduced corrosion was observed by FESEM: severe pitting is visible for LiTFSI after cycling (**Figure 7.10a**), whereas no pitting features were detected on Al discs from Li MET-TFSI or Li TFT-TFSI electrolytes (**Figure 7.10b,c**).

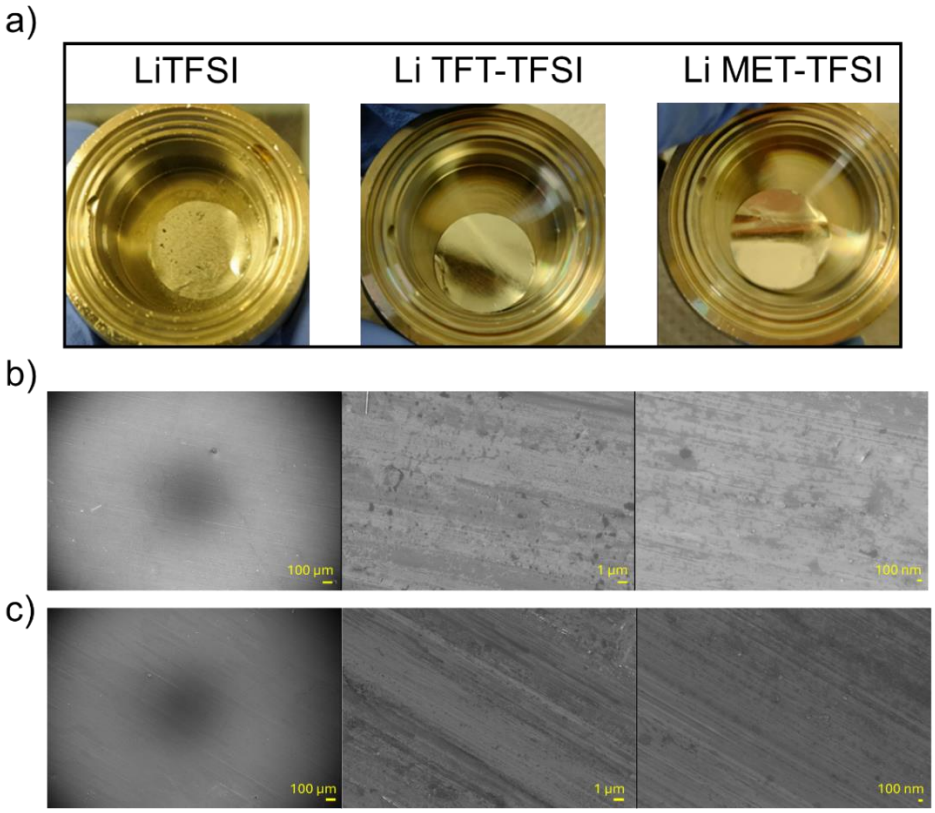

Figure 7.10. Digital photographs of aluminium disks after anodic dissolution tests in 1 M Li salt/EC–DMC (1:1 v/v) liquid electrolytes, showing visible corrosion pits on the Al surface in the presence of LiTFSI (a). FESEM images of the Al disk surface after anodic dissolution test in 1 M Li TFT-TFSI/EC–

DMC (1:1 v/v) liquid electrolyte (b). FESEM images of the Al disk surface after anodic dissolution test in 1 M Li MET-TFSI/EC–DMC (1:1 v/v) liquid electrolyte (c).

The surface elemental composition **(Figure 7.11)** and corresponding XPS peak fitting of the Al 2p, F 1s, and S 2p regions (**Figure 7.12**) consistently reveal that the nature of the interphase strongly depends on the salt chemistry. In all cases, the presence of C, O, F, N, S, Li, and Al indicates the formation of a mixed organic/inorganic layer arising from both solvent and salt decomposition. For LiTFSI, the relatively high C and O content, together with F 1s and S 2p signals dominated by components assigned to intact TFSI species, indicates that the surface layer is largely composed of solvent-derived species with a significant contribution from residual salt. In contrast, Li TFT-TFSI and especially Li MET-TFSI lead to a marked increase in F-containing species, consistent with a greater contribution from salt decomposition.

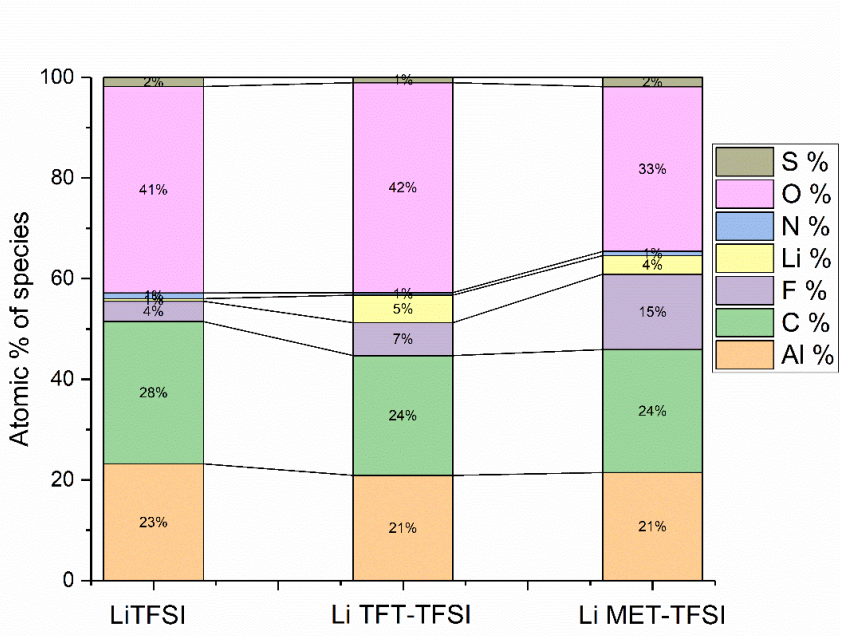

Figure 7.11 Surface elemental composition of Al disk after anodic dissolution using the developed Li MET-TFSI and Li TFT-TFSI salt vs LiTFSI reference.

This is corroborated by the F 1s spectra, which shows an increasing contribution of lower binding energy components assigned to the species F-metal (LiF and AlF_3), while the higher contribution in CF_x for LiTFSI indicates that the salt structure is partially kept. In addition, in the S 2p region, a slight increase in the peaks at lower energy, associated with sulphite and SO_x species, is observed for the Li TFT-TFSI and Li MET-TFSI. Among the three systems, Li MET-TFSI exhibits the highest fluorine content and the strongest F-metal contribution; together with Li TFT-TFSI, forms a thicker LiF and AlF_3 protective layer protecting the surface against corrosion.

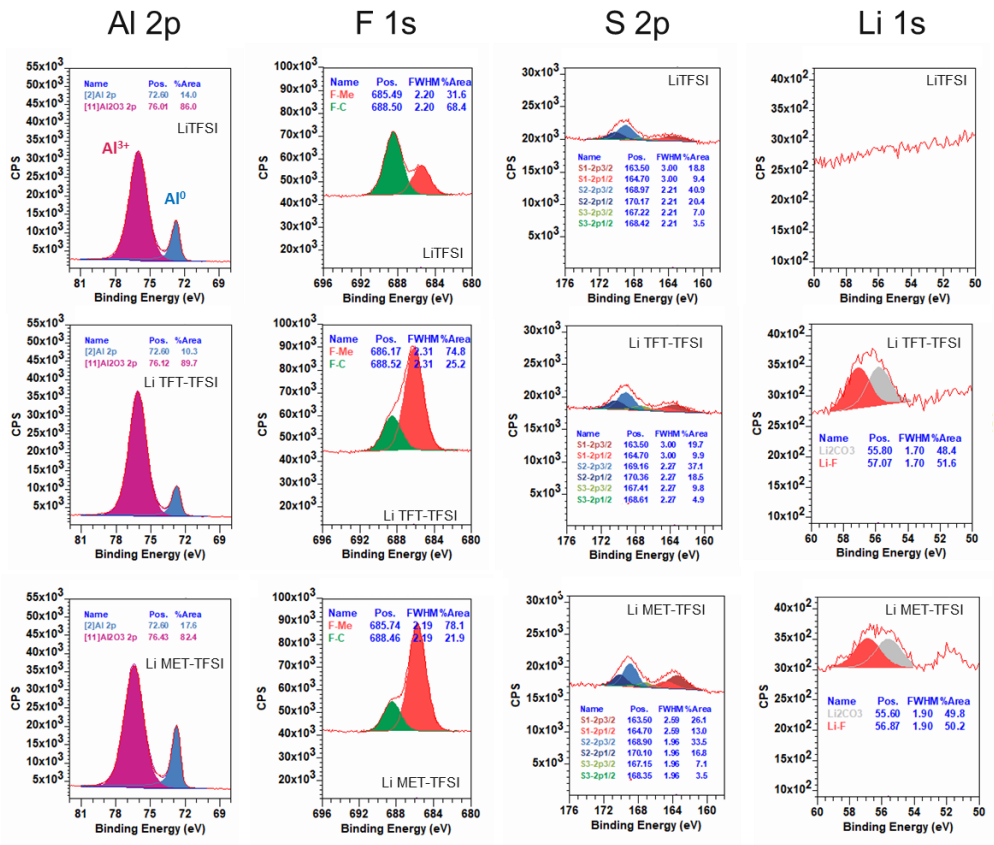

Figure 7.12 Al 2p, F 1s, S 2p, and Li 1s XPS core levels of Al disk after anodic dissolution test using LiTFSI (up), Li TFT-TFSI (middle) and Li MET-TFSI (bottom).

7.4 Concluding remarks

In summary, two asymmetric thioether-TFSI lithium salts were developed to overcome key limitations of conventional LiTFSI-based PEO electrolytes. Their low melting points suppress PEO crystallinity, enabling enhanced plasticization, maintained ionic conductivity, and improved Li^+ transference without sacrificing thermal or electrochemical stability. Notably, both salts suppress aluminium current-collector corrosion via formation of a stable passivation layer. When incorporated into PEO-based SPEs, these properties yield improved compatibility with lithium metal and stable long-term cycling in Li‖$LiFePO_4$ cells with high capacity retention and Coulombic efficiency. The modular thiol-ene synthesis additionally allows structural tunability with reduced fluorine content, supporting scalability and regulatory compliance.

Within the broader framework of this thesis, this Chapter is particularly relevant because it shows that, alongside polymer and processing optimization, rational lithium-salt design has become a key lever for simultaneously tuning ion transport, interfacial stability, and current-collector compatibility in solid polymer

electrolytes, while also responding to the growing drive toward lower-fluorine and more sustainable battery chemistries.

References

[1] S. Callens, J.-F. Le Nest, A. Gandini, M. Armand, A novel solid polymer electrolyte: Synthesis and characterization, Polym. Bull. 25 (1991) 443–450. https://doi.org/10.1007/BF00310235.

[2] A. Hammami, N. Raymond, M. Armand, Runaway risk of forming toxic compounds, Nature 424 (2003) 635–636.

[3] J.-M. Tarascon, M. Armand, Issues and challenges facing rechargeable lithium batteries, Nature 414 (2001) 359–367.

[4] Q. Wang, P. Ping, X. Zhao, G. Chu, J. Sun, C. Chen, Thermal runaway caused fire and explosion of lithium ion battery, J. Power Sources 208 (2012) 210–224. https://doi.org/10.1016/j.jpowsour.2012.02.038.

[5] B. Tong, P. Wang, Q. Ma, H. Wan, H. Zhang, X. Huang, M. Armand, W. Feng, J. Nie, Z. Zhou, Lithium fluorinated sulfonimide-based solid polymer electrolytes for Li || LiFePO4 cell: The impact of anionic structure, Solid State Ion. 358 (2020) 115519. https://doi.org/10.1016/j.ssi.2020.115519.

[6] L. Qiao, U. Oteo, M. Martinez-Ibañez, A. Santiago, R. Cid, E. Sanchez-Diez, E. Lobato, L. Meabe, M. Armand, H. Zhang, Stable non-corrosive sulfonimide salt for 4-V-class lithium metal batteries, Nat. Mater. 21 (2022) 455–462. https://doi.org/10.1038/s41563-021-01190-1.

[7] L.J. Krause, W. Lamanna, J. Summerfield, M. Engle, G. Korba, R. Loch, R. Atanasoski, Corrosion of aluminum at high voltages in non-aqueous electrolytes containing perfluoroalkylsulfonyl imides; new lithium salts for lithium-ion cells, J. Power Sources 68 (1997) 320–325. https://doi.org/10.1016/S0378-7753(97)02517-2.

[8] G. Guzmán-González, M. Alvarez-Tirado, J.L. Olmedo-Martínez, M.L. Picchio, N. Casado, M. Forsyth, D. Mecerreyes, Lithium Borate Ionic Liquids as Single-Component Electrolytes for Batteries, Adv. Energy Mater. 13 (2023) 2202974. https://doi.org/10.1002/aenm.202202974.

[9] D. Flachard, J. Rolland, M.M. Obadia, A. Serghei, R. Bouchet, E. Drockenmuller, A 1,2,3-triazolate lithium salt with ionic liquid properties at room temperature, Chem. Commun. 54 (2018) 9035–9038. https://doi.org/10.1039/C8CC04463E.

[10] M.B. Herath, S.E. Creager, R.V. Rajagopal, O.E. Geiculescu, D.D. DesMarteau, Ionic conduction in polyether-based lithium arylfluorosulfonimide ionic melt electrolytes, Electrochimica Acta 54 (2009) 5877–5883. https://doi.org/10.1016/j.electacta.2009.05.050.

[11] S. Bhowmick, M. Ahmed, A. Filippov, L.C. Loaiza, F.U. Shah, P. Johansson, Ambient temperature liquid salt electrolytes, Chem. Commun. 59 (2023) 2620–2623. https://doi.org/10.1039/D3CC00318C.

[12] G.B. Appetecchi, S. Passerini, Poly(ethylene oxide)-LiN (SO2CF2CF3)2 Polymer Electrolytes: II. Characterization of the Interface with Lithium, J. Electrochem. Soc. (n.d.).

[13] B. Tong, Z. Song, W. Feng, J. Zhu, H. Yu, X. Huang, M. Armand, Z. Zhou, H. Zhang, Design of a Teflon-Like Anion for Unprecedently Enhanced Lithium Metal Polymer Batteries, Adv. Energy Mater. 13 (2023) 2204085. https://doi.org/10.1002/aenm.202204085.

[14] F. Castiglione, G. Raos, G. Battista Appetecchi, M. Montanino, S. Passerini, M. Moreno, A. Famulari, A. Mele, Blending ionic liquids: how physico-chemical properties change, Phys. Chem. Chem. Phys. 12 (2010) 1784. https://doi.org/10.1039/b921816e.
[15] N. Nishi, Y. Yasui, T. Uruga, H. Tanida, T. Yamada, S. Nakayama, H. Matsuoka, T. Kakiuchi, Ionic multilayers at the free surface of an ionic liquid, trioctylmethylammonium bis(nonafluorobutanesulfonyl)amide, probed by x-ray reflectivity measurements, J. Chem. Phys. 132 (2010) 164705. https://doi.org/10.1063/1.3398029.
[16] H. Zhang, H. Han, X. Cheng, L. Zheng, P. Cheng, W. Feng, J. Nie, M. Armand, X. Huang, Z. Zhou, Lithium salt with a super-delocalized perfluorinated sulfonimide anion as conducting salt for lithium-ion cells: Physicochemical and electrochemical properties, J. Power Sources 296 (2015) 142–149. https://doi.org/10.1016/j.jpowsour.2015.07.026.
[17] H. Zhang, Z. Song, W. Yuan, W. Feng, J. Nie, M. Armand, X. Huang, Z. Zhou, Impact of Negative Charge Delocalization on the Properties of Solid Polymer Electrolytes, ChemElectroChem 8 (2021) 1322–1328. https://doi.org/10.1002/celc.202100045.
[18] L. García, D. Fraile-Insagurbe, I. Serna, I. Aldalur, L. Meabe, M. Arrese-Igor, R. Cid, J. Etxabe, M. Armand, M. Martinez-Ibañez, Engineering a Stable Solid–Electrolyte Interphase through a Novel Trifluoromethyl-Free Lithium Salt for Lithium Metal Polymer Batteries, ENERGY Environ. Mater. (2025) e70143. https://doi.org/10.1002/eem2.70143.
[19] H. Zhang, U. Oteo, H. Zhu, X. Judez, M. Martinez-Ibañez, I. Aldalur, E. Sanchez-Diez, C. Li, J. Carrasco, M. Forsyth, M. Armand, Enhanced Lithium-Ion Conductivity of Polymer Electrolytes by Selective Introduction of Hydrogen into the Anion, Angew. Chem. Int. Ed. 58 (2019) 7829–7834. https://doi.org/10.1002/anie.201813700.
[20] H. Zhang, X. Cheng, Q. Ma, W. Feng, L. Zheng, J. Nie, X. Huang, M. Armand, Z. Zhou, New ionic liquids based on a super-delocalized perfluorinated sulfonimide anion: physical and electrochemical properties, Electrochimica Acta 207 (2016) 66–75. https://doi.org/10.1016/j.electacta.2016.03.201.
[21] H. Zhang, U. Oteo, X. Judez, G.G. Eshetu, M. Martinez-Ibañez, J. Carrasco, C. Li, M. Armand, Designer Anion Enabling Solid-State Lithium-Sulfur Batteries, Joule 3 (2019) 1689–1702. https://doi.org/10.1016/j.joule.2019.05.003.
[22] H. Zhang, F. Chen, O. Lakuntza, U. Oteo, L. Qiao, M. Martinez-Ibañez, H. Zhu, J. Carrasco, M. Forsyth, M. Armand, Suppressed Mobility of Negative Charges in Polymer Electrolytes with an Ether-Functionalized Anion, Angew. Chem. Int. Ed. 58 (2019) 12070–12075. https://doi.org/10.1002/anie.201905794.
[23] M. Martinez-Ibañez, E. Sanchez-Diez, U. Oteo, I. Gracia, I. Aldalur, H.B. Eitouni, M. Joost, M. Armand, H. Zhang, Anions with a Dipole: Toward High Transport Numbers in Solid Polymer Electrolytes, Chem. Mater. 34 (2022) 3451–3460. https://doi.org/10.1021/acs.chemmater.2c00285.
[24] L. Qiao, S. Rodriguez Peña, M. Martínez-Ibañez, A. Santiago, I. Aldalur, E. Lobato, E. Sanchez-Diez, Y. Zhang, H. Manzano, H. Zhu, M. Forsyth, M. Armand, J. Carrasco, H. Zhang, Anion π–π Stacking for Improved Lithium Transport in Polymer Electrolytes, J. Am. Chem. Soc. 144 (2022) 9806–9816. https://doi.org/10.1021/jacs.2c02260.

[25] TFSI-functional thioether compounds for electrochemical applications, LU601870, 2025.
[26] H.T. Ho, M. Rollet, T.N.T. Phan, D. Gigmes, “Michael addition” reaction onto vinyl sulfonyl(trifluoromethylsulfonyl)imide: An easy access to sulfonyl(trifluoromethylsulfonyl)imide-based monomers and polymers, Eur. Polym. J. 107 (2018) 74–81. https://doi.org/10.1016/j.eurpolymj.2018.07.042.
[27] Z. Xue, D. He, X. Xie, Poly(ethylene oxide)-based electrolytes for lithium-ion batteries, J. Mater. Chem. A 3 (2015) 19218–19253. https://doi.org/10.1039/C5TA03471J.
[28] X. Yang, M. Jiang, X. Gao, D. Bao, Q. Sun, N. Holmes, H. Duan, S. Mukherjee, K. Adair, C. Zhao, J. Liang, W. Li, J. Li, Y. Liu, H. Huang, L. Zhang, S. Lu, Q. Lu, R. Li, C.V. Singh, X. Sun, Determining the limiting factor of the electrochemical stability window for PEO-based solid polymer electrolytes: main chain or terminal –OH group?, Energy Environ. Sci. 13 (2020) 1318–1325. https://doi.org/10.1039/D0EE00342E.
[29] S. Porporato, J.L. Gómez-Urbano, A. Piovano, G.A. Elia, C. Gerbaldi, A. Balducci, UV-crosslinked glyoxal-methacrylate electrolytes for quasi-solid electric double layer capacitors, Electrochimica Acta 525 (2025) 146096. https://doi.org/10.1016/j.electacta.2025.146096.
[30] R.-S. Kühnel, M. Lübke, M. Winter, S. Passerini, A. Balducci, Suppression of aluminum current collector corrosion in ionic liquid containing electrolytes, J. Power Sources 214 (2012) 178–184. https://doi.org/10.1016/j.jpowsour.2012.04.054.

Chapter 8

Click Chemistry Approach to Synthesize Advanced Single-Ion Conductors for Li Batteries

As introduced in Chapter 2, single-ion-conducting polyelectrolytes (SICPs) are a relatively new subclass of solid-state polymer electrolytes where the anionic species are covalently anchored to the polymer backbone and only Li^+ remains mobile [1–6]. Since the anions in SICPs are chemically bonded to the polymer backbone, only Li^+ ions contribute to sustained charge transport. Unfortunately, up to date, a competitive LMB that utilizes SICP has still not been developed, and one of the major reasons for that is insufficient ionic conductivity of these polyelectrolytes: typically way below that of salt-in-PEO polymer electrolytes ($4 \times 10^{-5} – 9 \times 10^{-4}$ S cm^{-1} at 25 °C) [7], which accounts for poor cycling performance and rapid specific capacity decay of the resulting batteries.

One common approach to overcome these limitations is synthesis of specialized ionic liquid monomers (ILM)s. In contrast to two conventional and most used ILMs: lithium styrene (trifluoromethane)sulfonylimide (Li STFSI) and lithium methacrylate (trifluoromethane)sulfonylimide (Li MTFSI) that characteristically have short chain linkers (also known as spacers) between anionic moiety (e.g. TFSI−) and polymerizable group[4,8,9], the second generation ILMs are being designed to have: a) long and flexible spacers not containing chemically “rigid” moieties, such as benzene rings, b) polar oxygen species within these spacers’

chains (i.e., ether C−O–C and ester –C(=O)–O–C functional groups), and c) no electrochemically unstable groups in the spacer (e.g. C=C double bonds). These monomers are usually directly polymerized into SICPs and do not require the use of complex and elaborate block-copolymerization techniques [10–14].

For instance, Shaplov's group recently, designed and synthesized another ionic monomer [10]. Denoted M(PEG)TFSI, its unique feature was the 10-repeating-units-long poly(ethylene glycol) (PEG) spacer connecting the methacrylate group and TFSI anion, which allowed to dramatically enhance segmental mobility and thus Li+ transport. Most importantly, the SICP prepared using this ILM demonstrated good anodic stability (4.5 V vs Li^+/Li at 70 °C) and stable cycling behavior. The one significant downside of that approach, however, was tedious and elaborate multi-step synthetic pathway required to obtain M(PEG)TFSI monomer limiting its rapid implementation in production of solid-state $LiFePO_4$ (LFP)-based LMBs.

One of the most intriguing works in this realm was done by the group of Matyjaszewski that employed alkyne-azide click chemistry approach to further elongate the spacer of PEGylated methacrylate and attach TFSI moiety allowing highly conductive "one-of-a-kind" ILM [14]. Furthermore, it was demonstrated that homopolymer of this ILM can be directly used as SICP, and that it was capable of undergoing continuous 300 h Li plating-stripping in Li|SICP|Li configuration at 90 °C. On the other hand, no actual Li-cell cycling was demonstrated for this particular SICP, while the synthesis of this unique monomer still required multiple precursor preparatory steps prior to alkyne−azide cycloaddition.

In this context, thiol-ene click chemistry has attracted an intensive attention by researchers for the facile synthesis of polymer due to their high reactivity, good selectivity and mild reaction conditions [15–17]. Thiol-ene reactions offer several notable advantages: they proceed with high reactivity and excellent selectivity, operate under mild conditions, tolerate oxygen and moisture, and are compatible with large-scale synthesis using readily available starting materials. In recent years, thioether polymers with diverse functional groups and excellent comprehensive properties have been synthesized by thiol-click chemistry as an efficient and rapid synthesis method and employed in LMBs [18–23]. In addition, thiol-ene chemistry introduces beneficial structural features into the resulting polymers. Tew et al. synthesized a series of thiol-conjugated polymers via a thiol-ene click chemistry

and prepared solid polymer electrolyte [22]. It was shown that the introduction of a sulfur atom can increase the ionic conductivity at room temperature. The relatively long C–S bond, the lower electronegativity of sulfur, and its moderate coordinating ability enhance segmental mobility within the polymer matrix [18].

Inspired by the 2018 finding that vinyl-functionalized TFSI anion, namely, (trifluoromethylsulfonyl)-N-(ethenesulfonyl)imide (vinyl-TFSI or TVA) can be easily synthesized with high yields and in high purity (in form of potassium salt) as reported by Gigmes *et al.* [24], and, moreover, that it is now commercialized (in form of lithium salt), in this Chapter It is demonstrated that novel, elongated ionic monomers containing thio-ether group in the spacer's structure can be obtained in a facile, straightforward, two-step chemical procedure (**Figure 8.1**), by means of:

1) "clicking" the easily accessible vinyl-TFSI with a desired hydroxy-thiol (in this study, two reagents were selected – 2-mercapto-ethanol and 6-mercapto-1-hexanol) via thiol-ene Michael addition reaction, and;

2) esterifying the obtained compounds using methacryloyl chloride into the designed ILMs.

Two newly as-synthesized monomers were denoted BMIM ILM1 and BMIM ILM2 and further used to prepare a series of poly(ionic liquid)s (PIL)s by means of their copolymerization with PEGM in different molar ratios (denoted BMIM coPIL1 and BMIM coPIL2) and their subsequent ionic exchange from organic cation to Li cation, thus obtaining desired series of SICPs – Li coPIL1 and Li coPIL2 (**Figure 8.2**). These materials were thoroughly investigated in terms of their physical and electrochemical properties, and the best-performing SICPs of two series were utilized as actual all-solid-state polyelectrolytes within laboratory-scale Li battery cells in configuration of metallic Li anode | SICP | $LiFePO_4$ cathode.

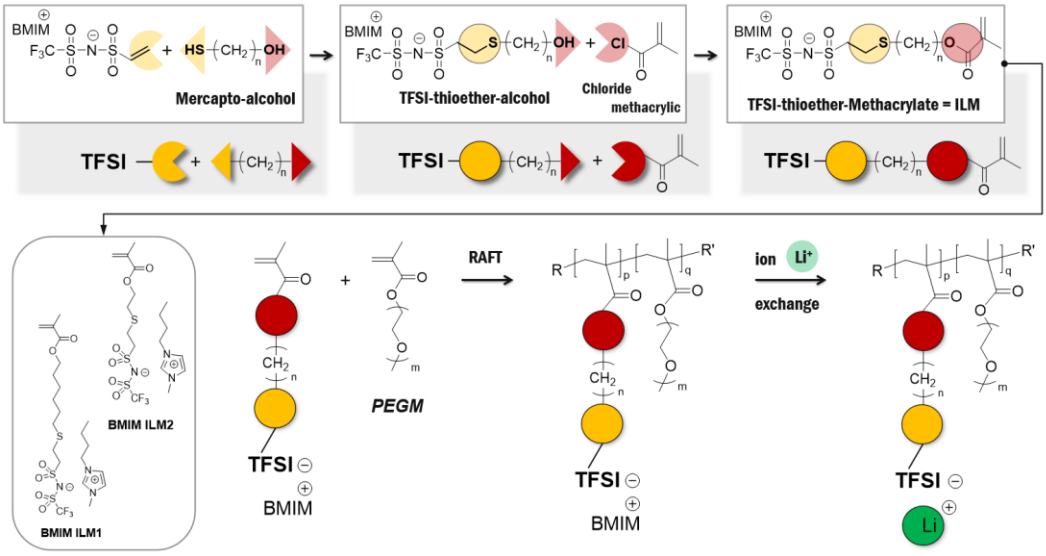

Figure 8.1 Facile synthesis of new family of ILMs with thioether spacer utilizing thiol-ene click approach towards improved SICPs.

8.1 Synthesis of Ionic Monomer

Two ionic liquid-like monomers were designed with a vision to straightforwardly and effortlessly incorporate sulfur atom within the elongated alkyl chain connecting polymerizable methacrylate group and anionic TFSI moiety - ILM1 (eight-methylene-chain) and ILM2 (four-methylene-chain) as can be seen in **Figure 8.1**.

First, 1-butyl-3-methylimidazolium (BMIM) vinyl-TFSI was successfully synthesized using slightly modified previously reported procedure [25] by addition-elimination reaction between 2-chloroethanesulfonyl chloride and $CF_3SO_2NH_2$ followed by a series of ion exchange reactions. Ultimately, BMIM organic cation was chosen due to its convenient solubility properties and ease of handling.

Then, thiol-ene Michael addition was performed via clicking BMIM vinyl-TFSI with preselected 2-mercapto-ethanol and 6-mercapto-1-hexanol. Michael mechanism for addition was chosen over more common free-radical addition mechanism due to the very strong electron-withdrawing effect of TFSI anion adjacent to vinyl functional group, which prevents effective thiyl radical addition across this carbon-carbon double bond [26]. Michael mechanism, one the other hand, allows to easily "click" highly electron-deficient vinyl compounds with the help of organic base catalysts, such as amines or phosphines (here, diisopropyl amine was chosen due to its moderate nucleophilicity and high selectivity), via thiol deprotonation and formation of anionic intermediates [27,28]. Indeed, both

reactions (with short-alkyl and longer-alkyl hydroxythiols) proceeded with very high efficiency, ultimately achieving 100% conversion (**Figures A17 and A18**).

Finally, the as-obtained hydroxy-TFSI compounds were reacted with methacryloyl chloride in the presence of triethylamine (TEA) acting as a catalyst and proton scavenger, thus, effectively esterifying respective alcohols into desired methacrylates (**Figure 8.2**).

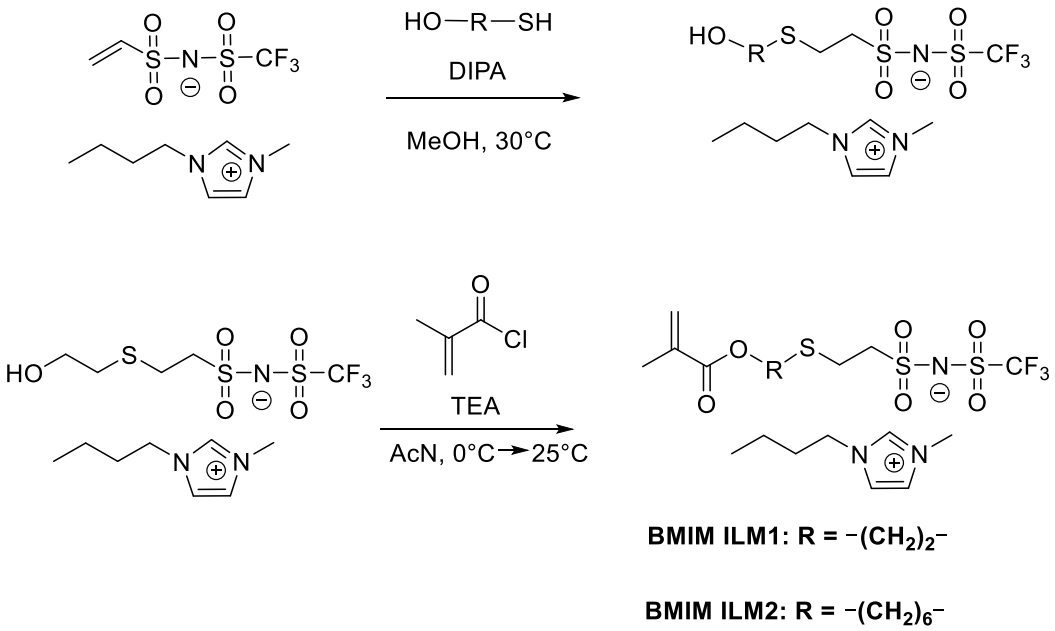

Figure 8.2 Synthesis procedure of BMIM ILM1 and BMIM ILM2.

These new ionic monomers were denoted BMIM ILM1 and BMIM ILM2 and their chemical structure and purity were thoroughly investigated using multiple analytical techniques, such as ^{1}H, ^{13}C, and ^{19}F NMR spectroscopy, elemental analysis, and differential scanning calorimetry; for more details reader is referred to Appendix and **Figures A19-A21** and **A22-A24**. Both newly synthesized monomers appeared as viscous yellowish liquids with T_g of −65.0 °C (BMIM ILM1) and −58.4 °C (BMIM ILM2).

8.2 Controlled radical polymerization of the synthesized ILMs

A series of homo- and co-polymerizations of the novel BMIM ILM1 and BMIM ILM2 monomers were performed via Reversible Addition-Fragmentation

chain Transfer (RAFT) polymerization technique in DMF solvent using AIBN radical initiator.

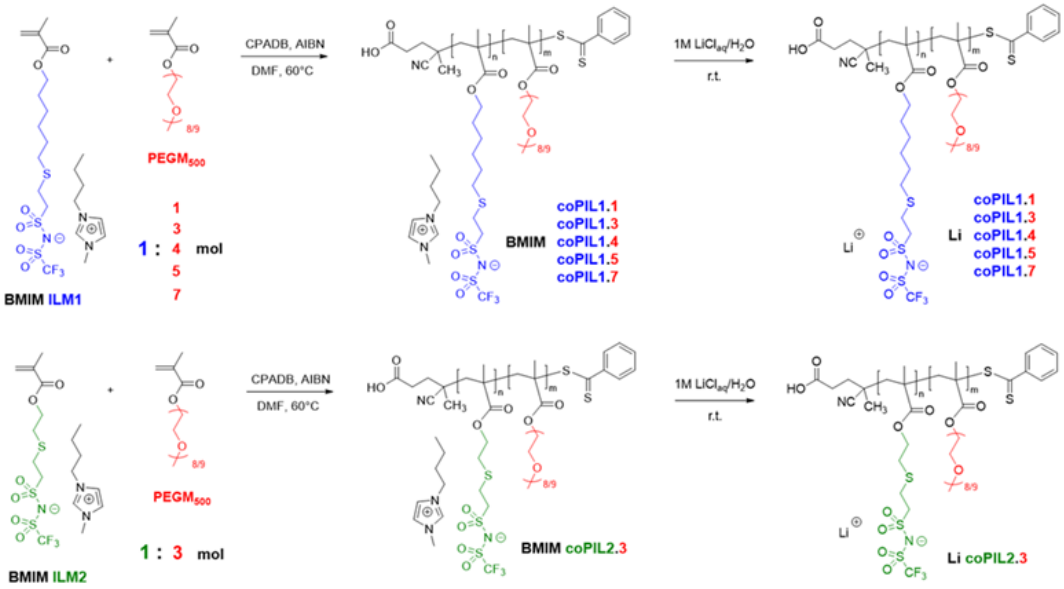

Figure 8.3 RAFT copolymerizations towards novel Li SICPs.

As shown in **Figure 8.3**, the range of products of random copolymerization of BMIM ILM1 with PEGM (in 5 different molar ratios) were denoted BMIM coPIL1, and a product of random copolymerization of BMIM ILM2 with PEGM was denoted BMIM coPIL2. To analyze the molecular weights and polydispersity of as-obtained (co)polymers Gel Permeation Chromatography (GPC) in 0.1 M LiTFSI solution in DMF was done. As can be seen from Table S1, for all polymers, the determined Mn values were relatively high, ranging from 30 kDa to 35 kDa (which were in the range of targeted M_{ns} in RAFT calculations), while determined M_w/M_n ratios were relatively small, ranging from 1.2 to 1.8 indicating narrow molecular weight distributions characteristic of RAFT polymerization method.

Lastly, all copolymers were subjected to ion exchange in aqueous solution of LiCl inside dialysis membranes substituting BMIM cation to Li cation thus obtaining desired polyelectrolytes denoted Li coPIL1 and Li coPIL2, accordingly. Structures of synthesized SICPs were confirmed by ^{1}H, ^{7}Li, and ^{19}F NMR and GPC (**Table 8.1, Figures A25-A34**). All synthesized (co)polymers appeared as soft pink honey-like materials, that can easily form coatings.

Table 8.1 Selected coPILs properties.

No	Abbrev.	Polyelectrolytes synthesis and properties								
		[PEGM]/[ILM] (ratio)		$M_w \times 10^3$ (g mol^{-1})[b]	M_w/M_n[b]	T_g (°C)[c]	T_d (°C)[d]	σ_i (S cm^{-1})		Anodic Stability, (V)[e]
		theoretical	experimental[a]					25 °C	70 °C	
1	Li coPIL1.1	1	1.11	38.0	1.2	−20	255	5.5×10^{-8}	4.1×10^{-6}	
2	**Li coPIL1.3**	**3**	**3.05**	**37.4**	**1.3**	**−45**	**235**	$\mathbf{1.1\times10^{-6}}$	$\mathbf{1.8\times10^{-5}}$	**5.1**
3	Li coPIL1.4	4	4.30	39.1	1.3			1.2×10^{-6}	1.7×10^{-5}	
4	Li coPIL1.5	5	5.19	38.8	1.2	−50	230	1.3×10^{-6}	1.9×10^{-5}	
5	Li coPIL1.7	7	7.13	39.9	1.4	−54		1.3×10^{-6}	1.6×10^{-5}	
6	**Li coPIL2.3**	**3**	**3.11**	**35.4**	**1.2**	**−44**	**185**	$\mathbf{9.9\times10^{-7}}$	$\mathbf{1.6\times10^{-5}}$	**4.9**
References for comparison:										
7	**copoly(Li MTFSI)**	3	2.90	44.6	1.6	−21		7.5×10^{-7}	1.0×10^{-5}	4.0
8	**copoly(Li MESTTFSI)[11]**	7	7.00	416.0	4.9	−55	230	1.9×10^{-6}	1.1×10^{-5}	4.2
9	**copoly(Li M-PEG-TFSI)[10]**	2	2.80	83.9	5.6	−46	200	3.0×10^{-6}	3.8×10^{-5}	4.5

[a]*Actual copolymer composition was determined by equation S2 using ^1H NMR spectroscopic analysis.*
[b]*By GPC in in 0.1 M LiTFSI solution in DMF at 50°C with PMMA standards.*
[c]*By DSC, on heating, 5° min^{-1} heating rate.*
[d]*By TGA, 5° min^{-1} heating rate.*
[e]*Determined by cyclic voltammetry at 70°C (aluminium carbon coated as the working electrode and Li foil as the counter and reference electrodes, scan rate 0.1 mV s^{-1}).*

8.3 Thermal Characterization

Thermogravimetric analysis was conducted in an inert atmosphere, simulating the working conditions in a battery cell, for both the polymers (**Figure 8.4a**). The comparison reveals that Li coPIL1.3 is stable until 235 °C, while Li coPIL2.3 until 185 °C, temperature is high enough to assure the thermal stability. In **Figure 8.4b** the differential scanning calorimetry data are shown, which were recorded for the system Li coPIL1.3 and Li coPIL2.3. Both SICP exhibit a very T_g in the range of

−45 °C, indicating that the T_g is essentially independent from the length of the chain of the ionic monomer.

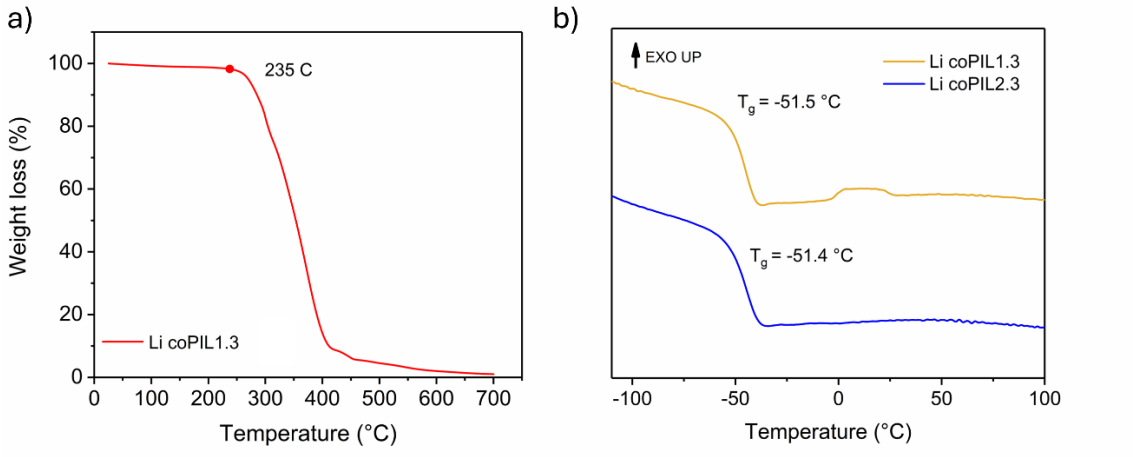

Figure 8.4 TGA thermograms of the coPILs under air from 25 to 700 °C (a) and DSC traces with a heating rate of 10 °C min^{-1} (b).

The RAFT random copolymerization of PEGM and ILM1 in different ratios led to a similar decrease in T_g of the obtained Li coPIL1.X copolymers **Figure A35-38**). The value ranged in the following order:

T_g in °C: Li coPIL1.1 (−20) < Li coPIL1.3 (−45) < Li coPIL1.5 (−50) < Li coPIL1.7 (−54)

As the PEGMA monomer content increases, these flexible segments disrupt interchain packing, increasing free volume, and reducing the intermolecular interactions that constrain segmental motion causing the decrease of T_g.

8.4 Ionic Conductivity Measurements

Ionic conductivity (σ_i) as a function of temperature of all synthesized polymers was studied by EIS. **Figure 8.4** summarizes ionic conductivity features of different coPILs highlighting the influence of copolymer formulation and side-chain chemistry on the ion transport.

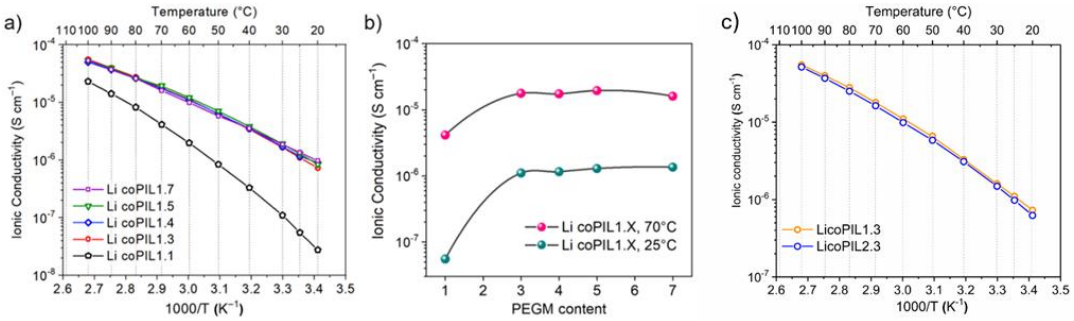

Figure 8.5 Ionic conductivity (σ_i) vs temperature (from 20 to 100 °C) of anhydrous polyelectrolyte samples of Li coPIL1.X series, b) σ_i (at 25 and 70°C) dependence of Li coPIL1.X series on the content of PEGM (molar, with respect to ILM), and c) σ_i vs temperature (from 20 to 100 °C) of anhydrous Li coPIL2.3.

In the field of all-solid-state SICP research, it is generally accepted that two factors contribute mainly to the ionic conductivity of a PIL: overall segmental mobility of the polymer and its ability to solvate and coordinate mobile ions. Often, PEGM is a comonomer of choice due to its well-known beneficial effect with regard to the abovementioned factors: generally, it reduces the T_g of a resulting copolymer and enhances the mobility of Li cations via coordination with oxyethylene side chains. **Figure 8.5a** provides evidence of Li coPIL1.X polyelectrolyte series benefiting from incorporation of PEGM. Sample Li coPIL1.1 demonstrated lower σ_{DC} (5.5×10^{-8} S cm^{-1} at 25 ºC and 4.1×10^{-6} S cm^{-1} at 70 ºC) than all other samples due to the insufficient amount of PEGM; meanwhile, samples Li coPIL1.3 to Li coPIL1.7 show ionic conductivities of approximately 1.2×10^{-7} S cm^{-1} at 25 ºC and 1.7×10^{-5} S cm^{-1} at 70 ºC, which can be considered decently high if compared to the nearest analogues (see **Table 8.1**, entries **7** – **9**).

Figure 8.5b was plotted to clearly see the impact of PEGM comonomer addition to the system: amounts greater than 3:1 (with respect to ILM1) did not lead to increase in sample's ionic conductivity either at 25 ºC or at 70 ºC, a clear plateau behavior was observed. Thus, for this type of SICP optimum PEGM content is established to be 3:1 because at this ratio the maximum in σ_{DC} was achieved, and, hence, further "dilution" of coPIL would not bring any positive effect but would negatively impact thermal and electrochemical stability.

As can be seen in **Figure 8.5c**, Li coPIL2.3 (copolymer based on slightly shorter-spacer ILM2) demonstrated conductivity slightly lower than Li coPIL1.3 (9.9×10^{-7} S cm^{-1} vs 1.1×10^{-6} S cm^{-1} at 25 ºC). Considering the content of PEGM to be optimal in these coPILs (**Table 8.1**, entries No. **2**, **6**, **7**, and **9**) a conclusion can be made that the chemical nature of an ILM's spacer plays a significant role

through influencing the segmental mobility of the system, therefore, governing the ionic transport:

σ copoly(LiM-PEG-TFSI) > σ Li coPIL1.3 > σ Li coPIL2.3 > σ copoly(LiMTFSI).

8.5 Electrochemical Stability, Li Transference Number and Compatibility with Li Metal

The polymers based on Li coPIL2.3 and Li coPIL1.3 were selected for subsequent electrochemical testing. This composition was chosen to minimize the PEGM content, as its ethylene oxide units are known to undergo oxidative degradation at potentials above ~4.0 V. Reducing the proportion of PEGM therefore limits the risk of high-voltage instability [30]. The anodic stability of the electrolytes is evaluated by measuring the current evolution during a stepwise potential sweep from 4.0 V to 5.5 V vs. Li^+/Li, increasing by 0.1 V each one hour (**Figure 8.6a,b**).

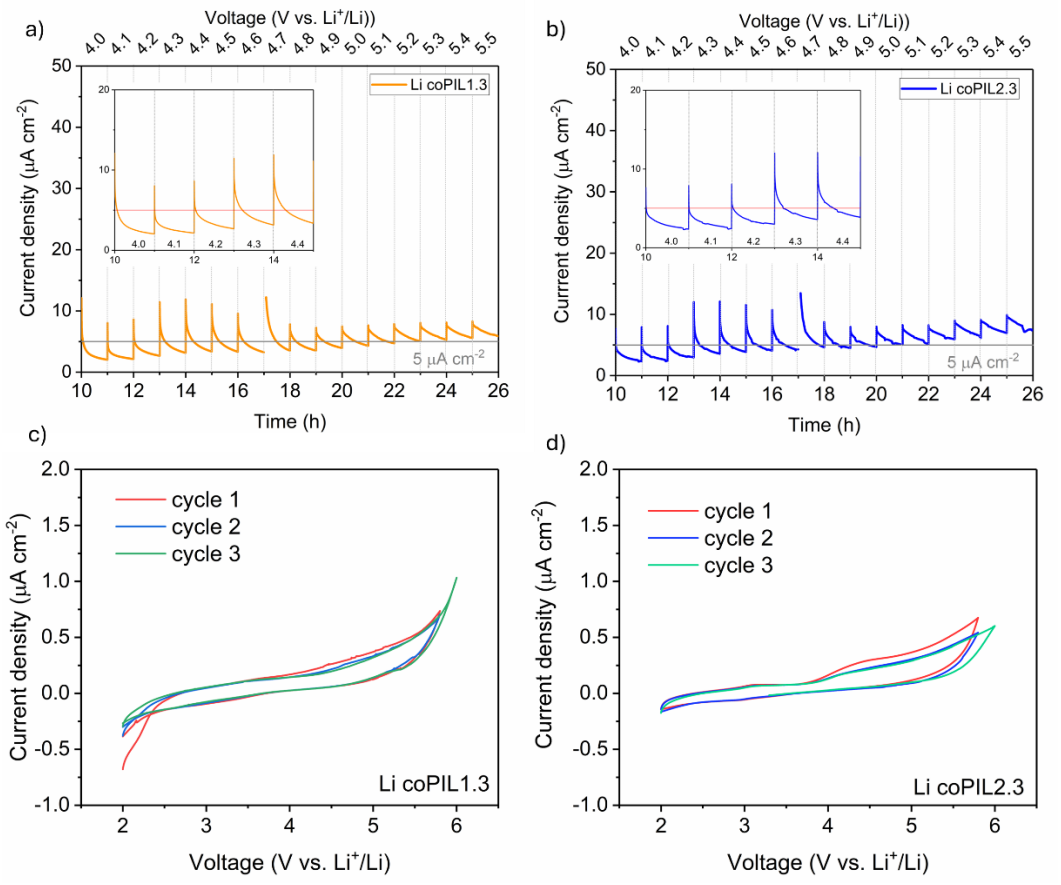

Figure 8.6 a,b) Chronoamperometric analysis (current density vs. time profiles) of the Li/PIL/Al-CC cells subjected to a stepwise potential sweep. c,d) Current density vs. potential plot upon cyclic voltammetry of Li/PIL/SS cells at a scan rate of 0.1 mV s^{-1}.

Each voltage step induces an initial current spike followed by a gradual decay toward a quasi-steady-state value, with no significant current flow of the investigated electrolytes up to 5.5 V vs. Li^+/Li. The Li coPIL1.3 electrolyte shows a current density below the imposed cutoff of 5 µA cm^{-2} up to 5.2 V vs. Li^+/Li and a maximum value of about 5.8 mA cm^{-2} at 5.5 V vs. Li^+/Li. Conversely, Li coPIL2.3 shows negligible current flow up to 4.9 V vs. Li^+/Li, while at the highest potential a value of about 7.4 mA cm^{-2} is obtained. Overall, Li coPIL1.3 shows better electrochemical stability, with current flowing below 5 µA cm^{-2} up to 5.2 V vs. Li^+/Li. As expected, also the cyclic voltammetry (CV) tests of the investigated electrolytes performed at a scan rate of 0.1 mV s^{-1}, well confirms the data obtained by the stepwise potential measurement, evidencing no sudden increase in the current density up to 6 V after 3 cycles (**Figure 8.6c,d**). The promising prospects of the newly developed SICP electrolyte were further corroborated by evaluating the lithium-ion transference number (t_{Li^+}), determined by the methods of Evans et al. [31].

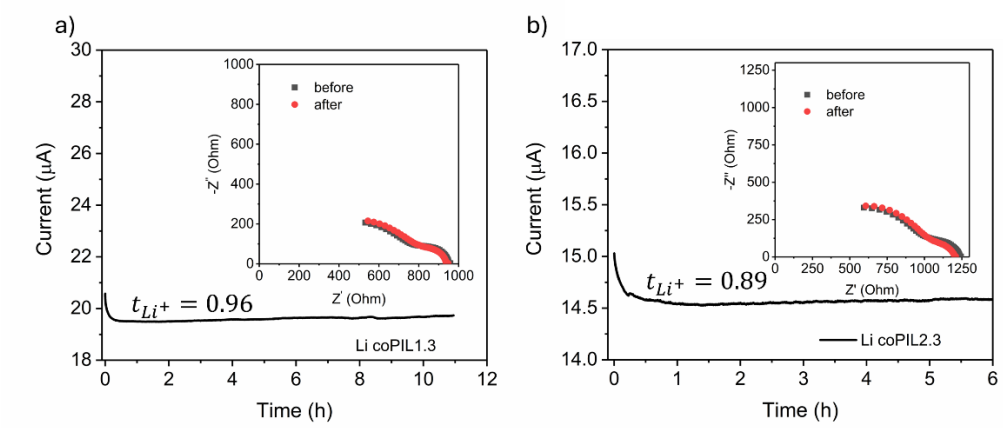

Figure 8.7 Determination of the lithium-ion transference number via a combination of chrononamperometry and EIS analysis for (a) Li coPIL1.3 and (b) Li coPIL2.3. All measurements were performed at 70 °C.

The results are presented in **Figure 8.7** revealing a lithium-ion transference number of 0.96 and 0.89 for Li coPIL1.3 and Li coPIL2.3, respectively, which is fairly close to unity. Slight deviation from unity is frequently observed in SICPEs and can be an be attributed to minor reactions [32] or the formation of an interphase at the Li electrode | SICP electrolyte interface and the charge transport across this

interphase [33]. Overall, values are high enough to prevent the formation and growth of inhomogeneous lithium dendritic structures and correspondingly guaranteeing safe and stable long-term operation in LMBs.

In this respect, the compatibility with lithium metal was investigated by galvanostatic lithium stripping/plating experiments in symmetric Li‖Li cells at 70 °C (**Figure 8.8**). When applying increasingly higher current densities, ranging from 0.05 to 0.4 mA cm^{-2} (corresponding to plated/stripped capacities per half-cycle ranging from 0.05 to 0.4 mAh cm^{-2}), a very stable overpotential is observed for Li coPIL1.3, that is as small as 49 mV at 0.05 mA cm^{-2} and increases slowly to 243 mV at 0.250 mA cm^{-2}, 287 mV at 0.3 mA cm^{-2} and 407 mV at 0.4 mA cm^{-2} (**Figure 8.8a**). Li coPIL2.3, shows similar results but, when a current density of 0.4 mA cm^{-2} was applied, the voltage showed irregular profile and peaks and then dropped. Aiming at supporting the durability and safe operation of the Li coPIL1.3 polyelectrolyte in lithium metal cells, a prolonged plating/stripping test was performed at a fixed current density regime of 0.05 mA cm^{-2}. The cell exhibits an essentially constant overpotential of about 70 mV for more than 1400 h without observing either an increase in overpotential over time with respect to the initial value or any abrupt or unexpected current spikes/drifts, which can be related to irregular dendrite growth (**Figure 8.8b**). EIS measurements were collected at selected cycling times, as indicated by the dashed lines, and the corresponding Nyquist plots are shown below. The semicircle in the low frequency region, which can be attributed to the combined charge-transfer resistance and interfacial processes at the Li/electrolyte interface, exhibits only marginal variation over extended cycling, indicating a stable interfacial resistance and suppressed interfacial degradation.

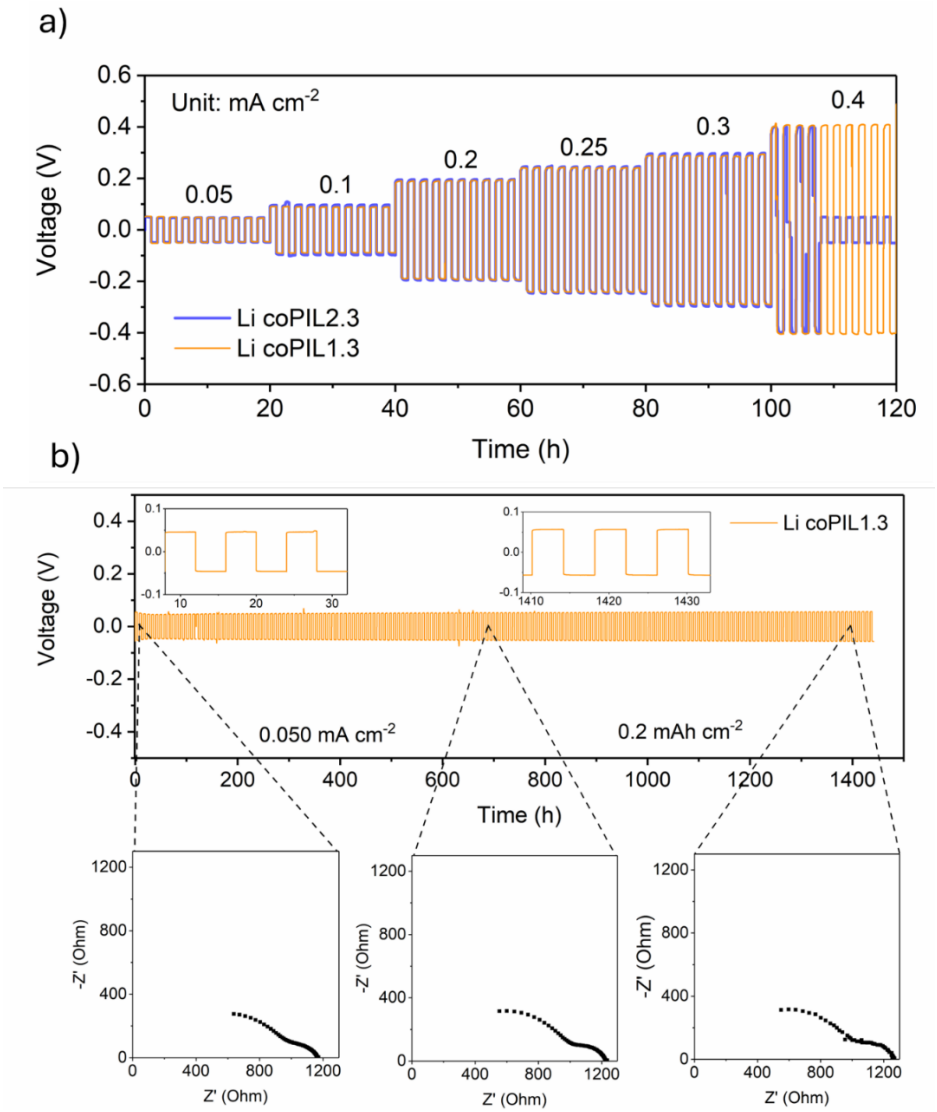

Figure 8.8 Lithium stripping/plating tests conducted on symmetric Li‖Li cells employing Li coPIL1.3 and Li coPIL2.3 as the electrolyte at a) varying current densities, ranging from 0.05 to 0.3 mA cm^{-2} (plated/stripped capacity per half cycle: 0.05 to 0.4 mAh cm^{-2}); b) selected lithium stripping/plating cycles of Li coPIL1.3 at constant current densities, T = 70 °C, each stripping and plating step lasted for 4 h (the insets show a magnification of selected cycles at beginning and end of test).

8.6 Electrochemical Behavior in Laboratory-scale Lithium Metal Battery Cell

This electrochemical response shown in the previous section accounts for a very good compatibility of the Li coPIL1.3 electrolyte with lithium metal and an excellent interfacial stability. Both electrolyte systems provide rather stable overpotentials, as expected for a SICP electrolyte. However, the cells employing Li coPIL1.3 show generally lower overpotential, due to the higher t_{Li^+} of this polyelectrolyte. For this reason, Li coPIL1.3 was selected as system in Li‖$LiFePO_4$

cells **(Figure 8.9**). The LFP-based electrode was prepared in the form of a catholyte using Li coPIL1.3 as an active binder to enhance the interfacial contact between solid polymer electrolyte and electrode active materials as reported in the experimental part. The lab-scale Li-metal cell was assembled without any further treatment of the electrodes or in the absence of any plasticizers/enhancers (e.g., solvents, salts). The galvanostatic cycling of the all-solid-state lab-scale cell at 70 °C and increasingly high C rates (C/n, n = 20, 15 10, 5, 3, and back to 15) is displayed in Figure 5a. For instance, the cell provides a specific capacity of 160 mAh g^{-1}, which slightly decreases to 110 mAh g^{-1} at C/3. An excellent coulombic efficiency that stabilizes after few cycles at around 99% is achieved, highlighting the good performance of Li coPIL1.3. For comparison, the galvanostatic performance of previously reported SICP electrolytes, namely Li/copoly(LiMESTTFSI)/LFP and Li/copoly(LiM-PEG-TFSI)/LFP cells, is shown in **Figure A39**. Although both systems were tested under similar conditions (70 °C and comparable C-rates), they display noticeably poorer electrochemical behavior compared to the Li coPIL1.3–based cell investigated in this work.

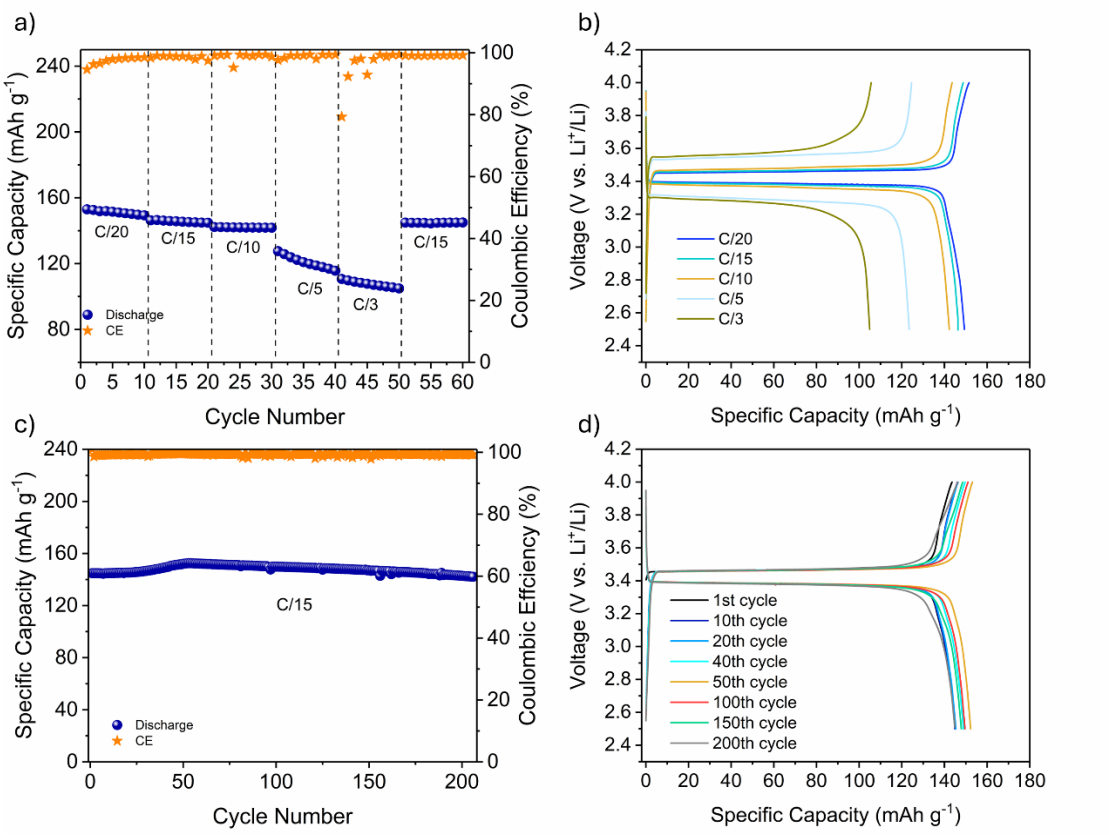

Figure 8.9 Comparison of the performance of Li‖$LiFePO_4$ cells employing Li coPIL1.3 as the electrolyte: (a) evaluation of the rate capability at C rates ranging from C/20 to C/3 (T = 70 °C); (b) selected discharge profiles obtained at the different C rates; (c) plot of the specific discharge capacity upon long-term

constant current cycling at C/15 (T = 70 °C); (d) selected discharge profiles at C/15 from the 1st to the 100th cycle. All tests were performed within cutoff voltages of 2.5 and 4.0 V.

The corresponding voltage vs. specific capacity profiles at the various C-rates (**Figure 8.9b**) show well-defined charge/discharge plateaus, with only minor polarization increases at higher rates. In addition, a truly solid state battery cell assembled with the Li coPIL1.3 SICP electrolyte can withstand stable reversible galvanostatic charge/discharge cycling for hundreds of cycles with a remarkable capacity retention of 92% at C/15 (**Figure 8.9c**). Representative voltage vs specific capacity profiles collected from cycle 1 to cycle 150 (**Figure 8.9d**) confirm the excellent stability of the cell, as the shape and polarization remain essentially unchanged over extended operation. The nearly overlapping curves demonstrate that interfacial resistance does not significantly increase over time and that the electrolyte maintains its structural and electrochemical integrity during prolonged cycling.

8.7 Concluding remarks

In summary, results detailed in this Chapter demonstrate that the development of high-performance single-ion conducting polymer electrolytes is not only a matter of increasing ionic conductivity, but of rationally balancing ion transport, electrochemical stability, and interfacial compatibility with lithium metal. In this context, the new family of ionic liquid-like monomers developed here, based on thioether-containing spacers and accessible through a simple thiol–ene click chemistry route, provides an effective platform for the preparation of advanced SICPs with improved transport properties and excellent processability. The introduction of sulfur atoms and flexible elongated spacers proved particularly beneficial in promoting segmental mobility without compromising the intrinsic oxidative stability required for solid-state lithium metal batteries.

Among the investigated materials, Li coPIL1.3 emerged as the most promising electrolyte, combining high ionic conductivity (10^{-6} and 10^{-5} S cm^{-1} at 25 and 70 °C, respectively), a lithium-ion transference number close to unity (0.96 at 70 °C), remarkable anodic stability (>5.0 V vs. Li^+/Li), and excellent compatibility with lithium metal. When implemented in truly solid-state Li‖$LiFePO_4$ cells, this electrolyte enabled highly reversible cycling, limited polarization even at elevated rates, and outstanding long-term stability over 200 charge/discharge cycles.

Overall, the obtained results highlight why SICPs remain such a compelling direction for next-generation LMBs: by immobilizing the anion, they offer a direct route toward reduced concentration polarization, more homogeneous lithium deposition, and intrinsically safer cell operation. In this context, the present study shows that click-chemistry-enabled molecular design can move SICPs beyond their traditional conductivity limitations and turn them into realistic candidates for high-energy, truly solid-state batteries.

References

[1] J. Zhu, Z. Zhang, S. Zhao, A.S. Westover, I. Belharouak, P.F. Cao, Single-Ion Conducting Polymer Electrolytes for Solid-State Lithium–Metal Batteries: Design, Performance, and Challenges, Adv. Energy Mater. 11 (2021). https://doi.org/10.1002/aenm.202003836.

[2] H. Yuan, J. Luan, Z. Yang, J. Zhang, Y. Wu, Z. Lu, H. Liu, Single Lithium-Ion Conducting Solid Polymer Electrolyte with Superior Electrochemical Stability and Interfacial Compatibility for Solid-State Lithium Metal Batteries, ACS Appl. Mater. Interfaces 12 (2020) 7249–7256. https://doi.org/10.1021/acsami.9b20436.

[3] G. Lingua, P. Grysan, P.S. Vlasov, P. Verge, A.S. Shaplov, C. Gerbaldi, Unique Carbonate-Based Single Ion Conducting Block Copolymers Enabling High-Voltage, All-Solid-State Lithium Metal Batteries, Macromolecules 54 (2021) 6911–6924. https://doi.org/10.1021/acs.macromol.1c00981.

[4] R. Bouchet, S. Maria, R. Meziane, A. Aboulaich, L. Lienafa, J.P. Bonnet, T.N.T. Phan, D. Bertin, D. Gigmes, D. Devaux, R. Denoyel, M. Armand, Single-ion BAB triblock copolymers as highly efficient electrolytes for lithium-metal batteries, Nat. Mater. 12 (2013) 452–457. https://doi.org/10.1038/nmat3602.

[5] L. Porcarelli, A.S. Shaplov, F. Bella, J.R. Nair, D. Mecerreyes, C. Gerbaldi, Single-Ion Conducting Polymer Electrolytes for Lithium Metal Polymer Batteries that Operate at Ambient Temperature, ACS Energy Lett. 1 (2016) 678–682. https://doi.org/10.1021/acsenergylett.6b00216.

[6] C. Cao, Y. Li, Y. Feng, C. Peng, Z. Li, W. Feng, A solid-state single-ion polymer electrolyte with ultrahigh ionic conductivity for dendrite-free lithium metal batteries, Energy Storage Mater. 19 (2019) 401–407. https://doi.org/10.1016/j.ensm.2019.03.004.

[7] Z. Xue, D. He, X. Xie, Poly(ethylene oxide)-based electrolytes for lithium-ion batteries, J. Mater. Chem. A Mater. 3 (2015) 19218–19253. https://doi.org/10.1039/c5ta03471j.

[8] C. Jangu, A.M. Savage, Z. Zhang, A.R. Schultz, L.A. Madsen, F.L. Beyer, T.E. Long, Sulfonimide-Containing Triblock Copolymers for Improved Conductivity and Mechanical Performance, Macromolecules 48 (2015) 4520–4528. https://doi.org/10.1021/acs.macromol.5b01009.

[9] L. Porcarelli, M.A. Aboudzadeh, L. Rubatat, J.R. Nair, A.S. Shaplov, C. Gerbaldi, D. Mecerreyes, Single-ion triblock copolymer electrolytes based on poly(ethylene oxide) and methacrylic sulfonamide blocks for lithium metal batteries, J. Power Sources 364 (2017) 191–199. https://doi.org/10.1016/j.jpowsour.2017.08.023.

[10] G. Lingua, V.Y. Shevtsov, P.S. Vlasov, L. Puchot, C. Gerbaldi, A.S. Shaplov, A New (Trifluoromethane)Sulfonylimide Single-Ion Conductor with PEG Spacer for All-Solid-State Lithium-Based Batteries, ACS Mater. Lett. 6 (2024) 5429–5437. https://doi.org/10.1021/acsmaterialslett.4c01647.

[11] L. Porcarelli, P.S. Vlasov, D.O. Ponkratov, E.I. Lozinskaya, D.Y. Antonov, J.R. Nair, C. Gerbaldi, D. Mecerreyes, A.S. Shaplov, Design of ionic liquid like monomers towards easy-accessible single-ion conducting polymer electrolytes, Eur. Polym. J. 107 (2018) 218–228. https://doi.org/10.1016/j.eurpolymj.2018.08.014.

[12] T. Ikeda, Anionic Glycidyl Triazolyl Polymers: Oppositely Charged Analogs of Imidazolium-Based Cationic Glycidyl Triazolyl Polymers, Macromolecules 56 (2023) 9229–9236. https://doi.org/10.1021/acs.macromol.3c01501.

[13] K. Matsumoto, T. Endo, Preparation and properties of ionic-liquid-containing poly(ethylene glycol)-based networked polymer films having lithium salt structures, J. Polym. Sci. A Polym. Chem. 49 (2011) 3582–3587. https://doi.org/10.1002/pola.24795.

[14] S. Li, A.I. Mohamed, V. Pande, H. Wang, J. Cuthbert, X. Pan, H. He, Z. Wang, V. Viswanathan, J.F. Whitacre, K. Matyjaszewski, Single-Ion Homopolymer Electrolytes with High Transference Number Prepared by Click Chemistry and Photoinduced Metal-Free Atom-Transfer Radical Polymerization, ACS Energy Lett. 3 (2018) 20–27. https://doi.org/10.1021/acsenergylett.7b00999.

[15] M. Taghavikish, S. Subianto, N.K. Dutta, N.R. Choudhury, Facile Fabrication of Polymerizable Ionic Liquid Based-Gel Beads via Thiol-ene Chemistry, ACS Appl. Mater. Interfaces 7 (2015) 17298–17306. https://doi.org/10.1021/acsami.5b04405.

[16] J. Hu, W. Wang, H. Peng, M. Guo, Y. Feng, Z. Xue, Y. Ye, X. Xie, Flexible Organic-Inorganic Hybrid Solid Electrolytes Formed via Thiol-Acrylate Photopolymerization, Macromolecules 50 (2017) 1970–1980. https://doi.org/10.1021/acs.macromol.7b00035.

[17] C.E. Hoyle, A.B. Lowe, C.N. Bowman, Thiol-click chemistry: A multifaceted toolbox for small molecule and polymer synthesis, Chem. Soc. Rev. 39 (2010) 1355–1387. https://doi.org/10.1039/b901979k.

[18] C. Xuan, S. Gao, Y. Wang, Q. You, X. Liu, J. Liu, R. Xu, K. Yang, S. Cheng, Z. Liu, Q. Guo, In-situ generation of high performance thiol-conjugated solid polymer electrolytes via reliable thiol-acrylate click chemistry, J. Power Sources 456 (2020). https://doi.org/10.1016/j.jpowsour.2020.228024.

[19] M.J. Kade, D.J. Burke, C.J. Hawker, The power of thiol-ene chemistry, J. Polym. Sci. A Polym. Chem. 48 (2010) 743–750. https://doi.org/10.1002/pola.23824.

[20] J. Suk, Y.H. Lee, D.Y. Kim, D.W. Kim, S.Y. Cho, J.M. Kim, Y. Kang, Semi-interpenetrating solid polymer electrolyte based on thiol-ene cross-linker for all-solid-state lithium batteries, J. Power Sources 334 (2016) 154–161. https://doi.org/10.1016/j.jpowsour.2016.10.008.

[21] R. Xu, B. Xiao, C. Xuan, S. Gao, J. Chai, S. Liu, Y. Chen, Y. Zheng, X. Cheng, Q. Guo, Z. Liu, Facile and Powerful in Situ Polymerization Strategy for Sulfur-Based All-Solid Polymer Electrolytes in Lithium Batteries, ACS Appl. Mater. Interfaces 13 (2021) 34274–34281. https://doi.org/10.1021/acsami.1c07805.

[22] J.M. Sarapas, G.N. Tew, Poly(ether-thioethers) by Thiol-Ene Click and Their Oxidized Analogues as Lithium Polymer Electrolytes, Macromolecules 49 (2016) 1154–1162. https://doi.org/10.1021/acs.macromol.5b02513.

[23] A. Chiappone, C. Gerbaldi, I. Roppolo, N. Garino, R. Bongiovanni, Degradable photopolymerized thiol-based solid polymer electrolytes towards greener Li-ion batteries, Polymer (Guildf). 75 (2015) 64–72. https://doi.org/10.1016/j.polymer.2015.08.019.

[24] H.T. Ho, M. Rollet, T.N.T. Phan, D. Gigmes, "Michael addition" reaction onto vinyl sulfonyl(trifluoromethylsulfonyl)imide: An easy access to sulfonyl(trifluoromethylsulfonyl)imide-based monomers and polymers, Eur. Polym. J. 107 (2018) 74–81. https://doi.org/10.1016/j.eurpolymj.2018.07.042.

[25] V.Y. Shevtsov, B.F. Soares, D.R. Nosov, I.M. Marrucho, A.S. Shaplov, Ionic Liquids with Asymmetric Thioether-TFSI Anions: Thermal Properties and Gas Separation, Journal of Ionic Liquids (2025) 100186. https://doi.org/10.1016/j.jil.2025.100186.

[26] C.E. Hoyle, C.N. Bowman, Thiol-ene click chemistry, Angew. Chem. Int. Ed. 49 (2010) 1540–1573. https://doi.org/10.1002/anie.200903924.

[27] R. Matsuno, K. Takami, K. Ishihara, Simple synthesis of a library of zwitterionic surfactants via michael-type addition of methacrylate and alkane thiol compounds, Langmuir 26 (2010) 13028–13032. https://doi.org/10.1021/la1015466.

[28] R. Matsuno, Y. Kokubo, S. Kumagai, S. Takamatsu, K. Hashimoto, A. Takahara, Molecular Design and Characterization of Ionic Monomers with Varying Ion Pair Interaction Energies, Macromolecules 53 (2020) 1629–1637. https://doi.org/10.1021/acs.macromol.9b02731.

Concluding Remarks

The transition toward sustainable energy systems represents one of the most pressing scientific and technological challenges of the twenty-first century. In this context, the development of advanced electrochemical energy storage devices plays a central role in enabling the large-scale integration of renewable energy sources and the electrification of transportation. Among the various technologies currently available, lithium-based batteries have emerged as the most mature and widely adopted solution, owing to their high energy density, long cycle life, and continuously improving performance.

In such scenario, this Ph.D. work addressed a central challenge in the development of all-solid-state lithium metal batteries, namely how to combine ionic transport, interfacial stability, electrochemical robustness, and scalable processing within polymer-based electrolytes. Starting from conventional PEO-based systems, the three years' work described in the Thesis progressively explored three complementary design directions: optimization of the polymer matrix and processing route, molecular engineering of lithium salts, and the development of single-ion conducting polymer electrolytes. Taken together, these investigations define a coherent pathway from established PEO chemistry toward more advanced and application-oriented electrolyte platforms for safer and higher-performance solid-state Li-metal batteries.

A first major outcome of the thesis was the demonstration that solvent-free processing can be effectively combined with polymer blending to improve the performance of PEO-based solid polymer electrolytes. The blending of PEO with polycarbonates, developed through melt extrusion, enabled the preparation of homogeneous and scalable electrolytes with reduced crystallinity and improved ion transport. Within this framework, the PEO400k/PEC 1:1 formulation emerged as the best compromise in the initial stage, showing enhanced conductivity and electrochemical stability compared with neat PEO. This platform was then further strengthened through UV-induced crosslinking, which did not alter the solvent-free

character of the process but significantly improved the chemical and interfacial stability of the electrolyte, preventing polymer matrix dissolution and enabling stable lithium plating/stripping over extended cycling. On this already optimized basis, the introduction of succinonitrile as a solid plasticizer provided the next decisive step: by combining crosslinking, composition tuning, and SN plasticization, the optimized PEO/PEC 7:3 system extended stable operation to 40 °C and enabled practical cycling with both LFP and high-voltage NMC cathodes. In this way, the thesis established a clear progression from formulation design to interfacial stabilization, and even to moderate-temperature and higher-voltage operation within a truly solvent-free polymer-electrolyte platform.

Another important contribution concerned the role of the lithium salt as an active design parameter rather than a fixed component of the electrolyte. Moving beyond the benchmark LiTFSI, the thesis demonstrated that targeted anion engineering can effectively modify the behavior of PEO-based electrolytes. In particular, the newly developed asymmetric thioether-TFSI lithium salts combined lower melting points with reduced aluminum corrosion and improved compatibility with lithium metal, while preserving suitable electrochemical stability. These results show that salt design can be used not only to improve conductivity through matrix plasticization, but also to tailor interphases and current-collector passivation, thereby addressing some of the most persistent limitations of conventional PEO/LiTFSI systems. In the broader context of solid-state lithium batteries, this is especially relevant because it highlights that electrolyte optimization cannot rely on polymer design alone: the conducting salt must be considered equally powerful in controlling bulk and interfacial properties.

The final, key and more forward-looking part of the thesis focused on developing single-ion conducting polymer electrolytes. Here, the work moved from improving conventional salt-in-polymer formulations to addressing a more fundamental limitation of polymer electrolytes, namely concentration polarization arising from anion mobility. Through the design of new ionic liquid-like monomers bearing thioether-containing flexible spacers, and their straightforward synthesis via thiol–ene click chemistry, a new family of SICPs was developed with markedly improved transport and electrochemical features. Among them, Li coPIL1.3 proved especially significant, combining a lithium-ion transference number of 0.96, anodic stability above 5.0 V vs. Li^+/Li, stable lithium plating/stripping for more than 1400

h, and promising cycling in truly solid-state Li‖$LiFePO_4$ cells with 92% capacity retention. These findings are important not only because they validate the designed material itself, but because they demonstrate that the long-standing trade-off of SICPs between high selectivity and insufficient conductivity can be mitigated through rational monomer design and synthetically accessible chemistry.

Overall, the results collected in this thesis show that no single modification is sufficient, by itself, to overcome the complexity of solid-state lithium metal batteries. Rather, meaningful progress emerges from the combination of several coordinated advances: dry and scalable processing, structural control of the polymer host, stabilization of the electrode/electrolyte interface, rational salt design, and ultimately the transition toward single-ion conducting polymer systems. From this perspective, the thesis does not simply present a series of separate electrolyte formulations, but outlines a clear, integrated materials-design strategy that starts from practical PEO-based systems and progressively expands toward more sophisticated and higher-performing architectures. Its main impact on the solid-state battery community lies in showing that polymer electrolytes can be engineered through modular and scalable approaches to address both technological requirements and more fundamental transport limitations.

Looking ahead, the materials developed in this work offer several promising directions for future research. The solvent-free PEO/polycarbonate platform appears particularly attractive for scale-up and for further validation in larger-format cells, especially under practical areal loadings and thinner-electrolyte configurations. The new lithium salts open the way to broader exploration of lower-melting, less corrosive, and potentially lower-fluorine conducting salts. Finally, the single-ion conductors developed here provide a strong basis for the next generation of polymer electrolytes aimed at combining high lithium selectivity with durable cycling and high-voltage compatibility. In this sense, the thesis contributes not only to the advancement of specific materials and production process thereof in the perspective of an effective transition towards market deployment, but also to the broader understanding of how polymer chemistry, salt chemistry, and process engineering can converge toward safer, more sustainable, and more competitive all-solid-state lithium metal batteries.

Appendix

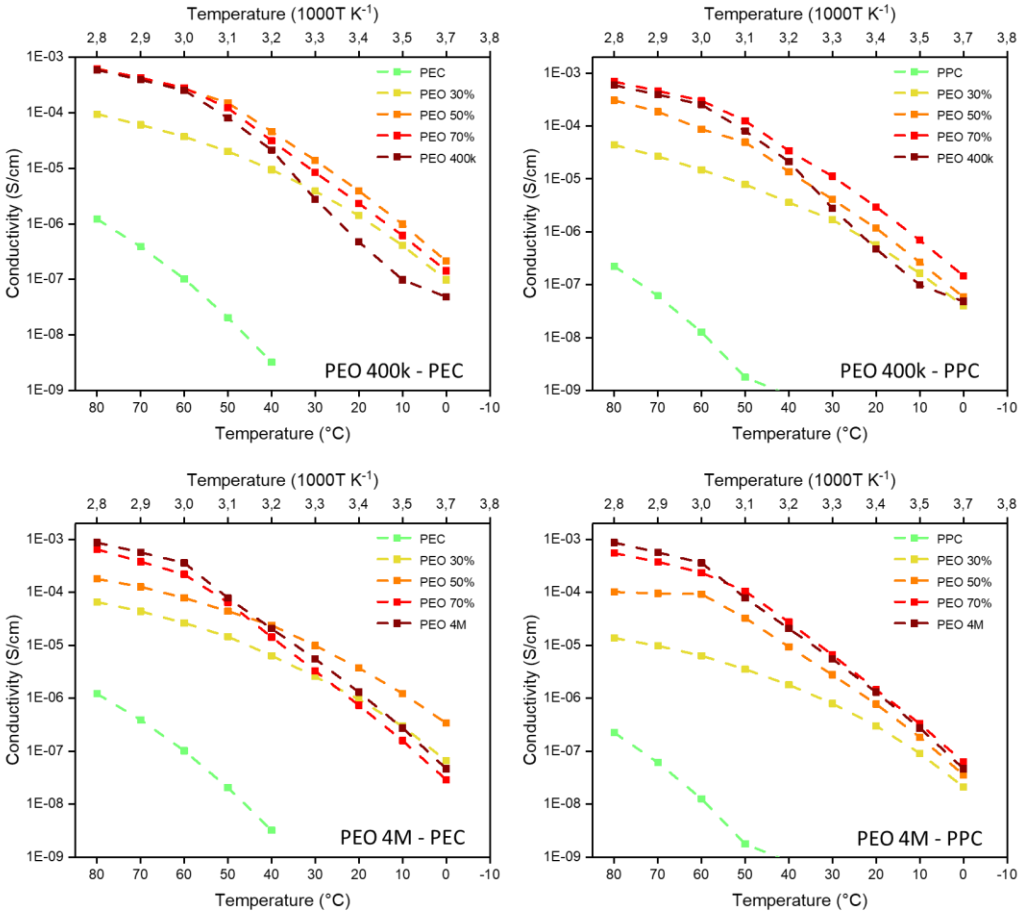

Figure A1. Arrhenius plots of ionic conductivity versus temperature determined by EIS in the range of 0 − 80 °C for blended SPEs.

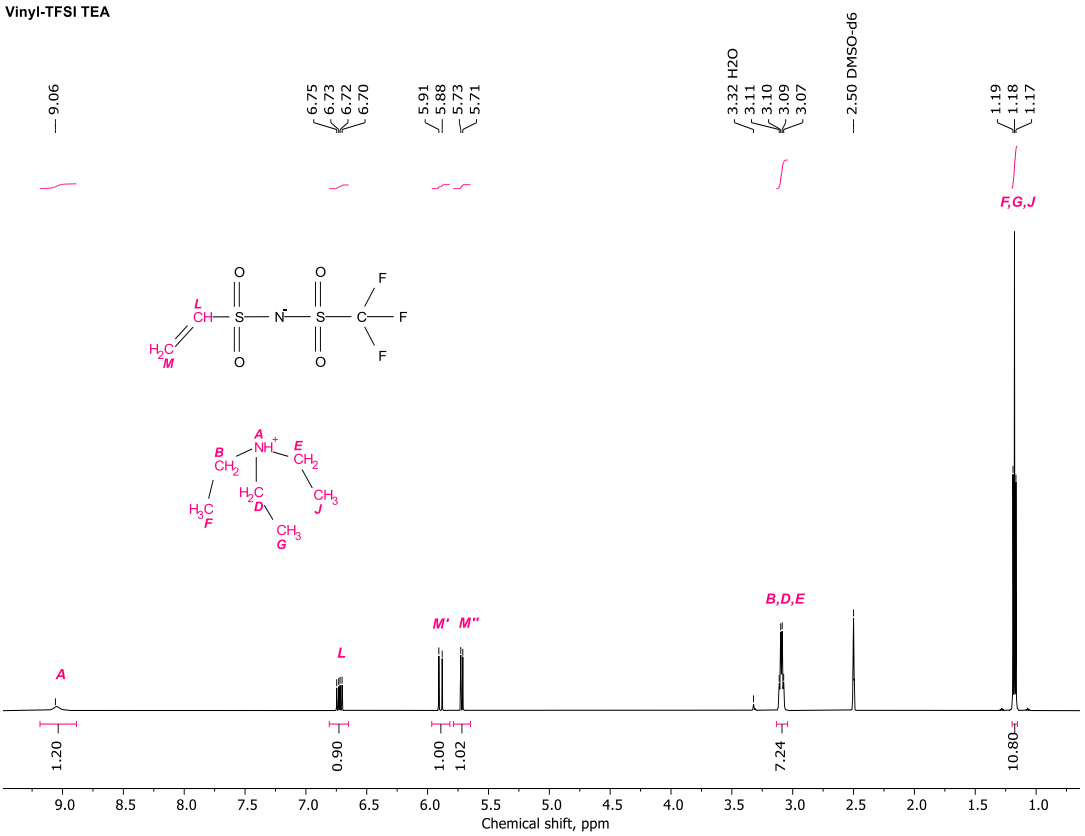

Figure A2. ^{1}H NMR spectrum of **Vinyl-TFSI TEA** (DMSO-d$_6$, 25.0 °C).

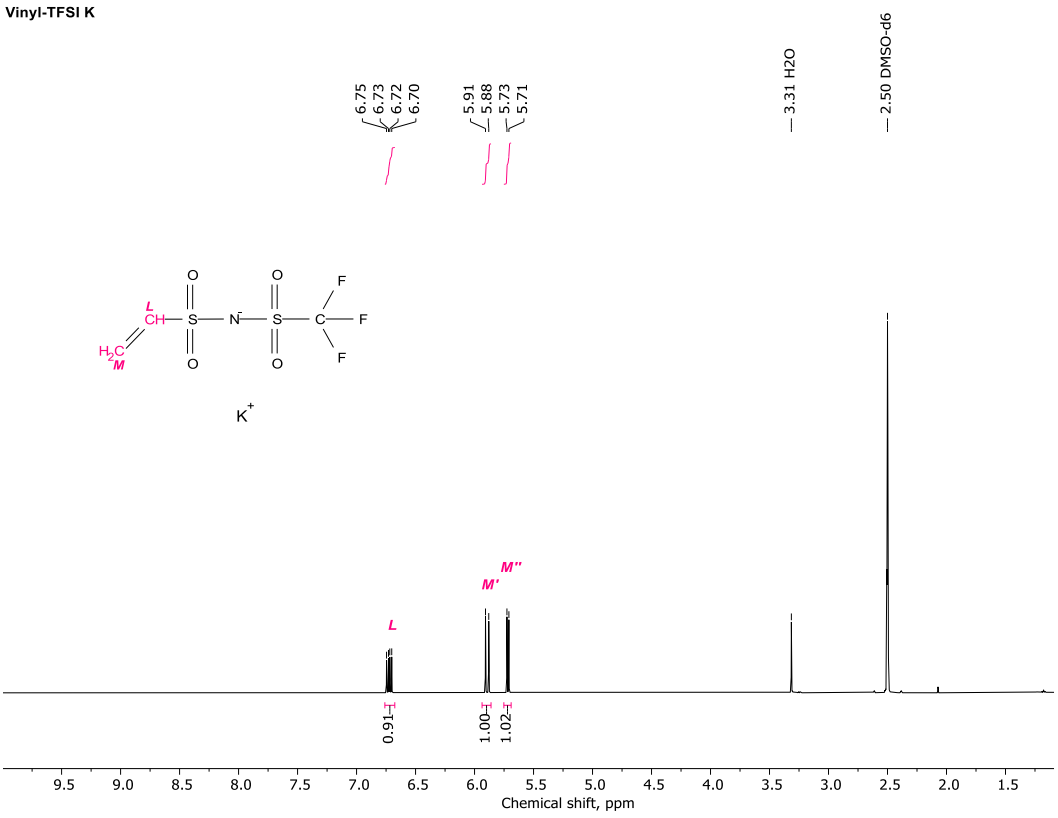

Figure A3. ^{1}H NMR spectrum of **Vinyl-TFSI K** (DMSO-d$_6$, 25.0 °C).

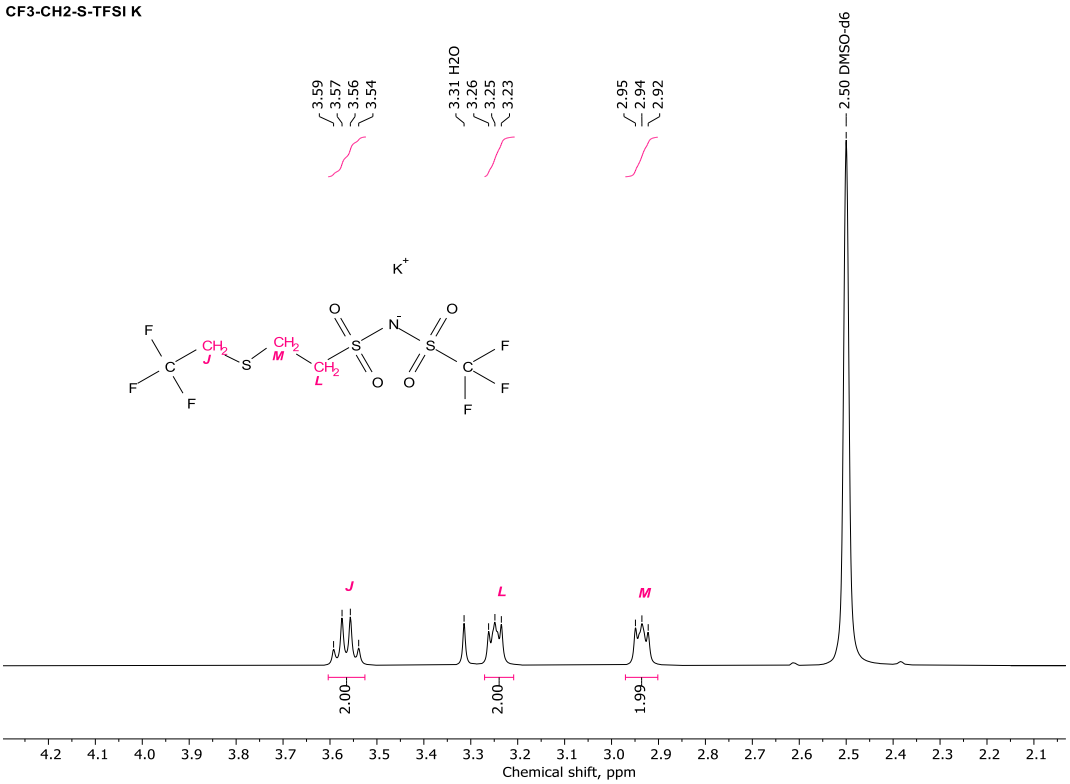

Figure A4. ^{1}H NMR spectrum of **CF_3-CH_2-S-TFSI K** (DMSO-d_6, 25.0 °C).

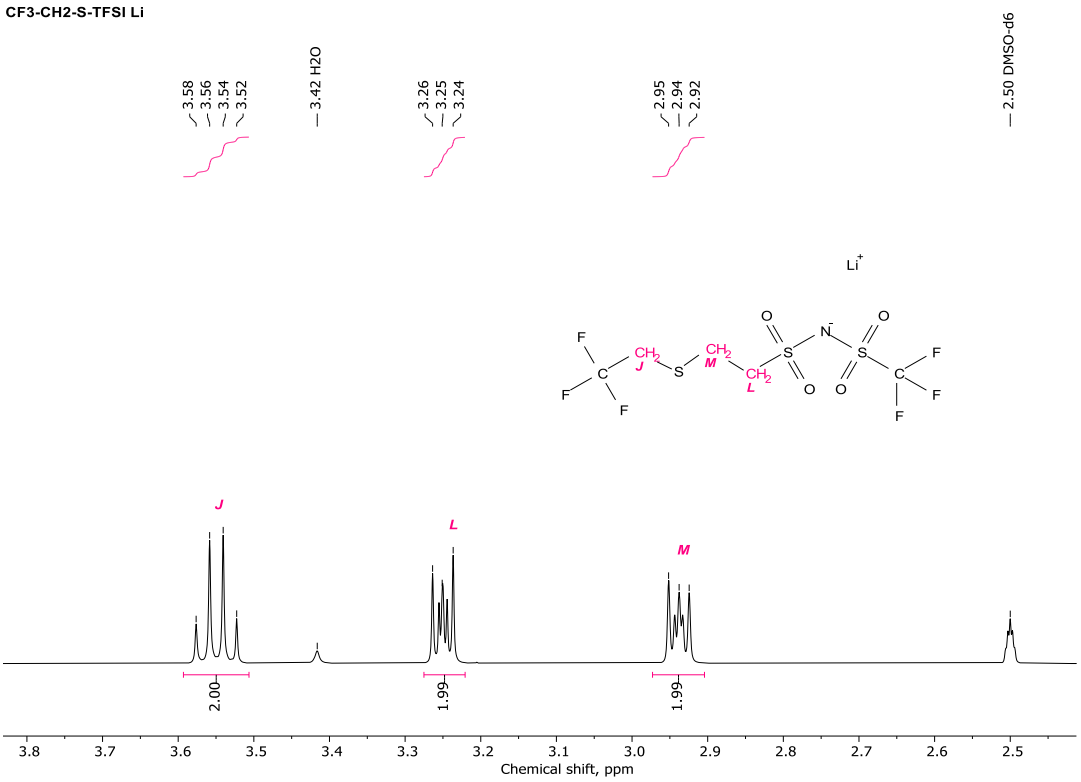

Figure A5. ^{1}H NMR spectrum of **Li TFT-TFSI** (DMSO-d_6, 25.0 °C).

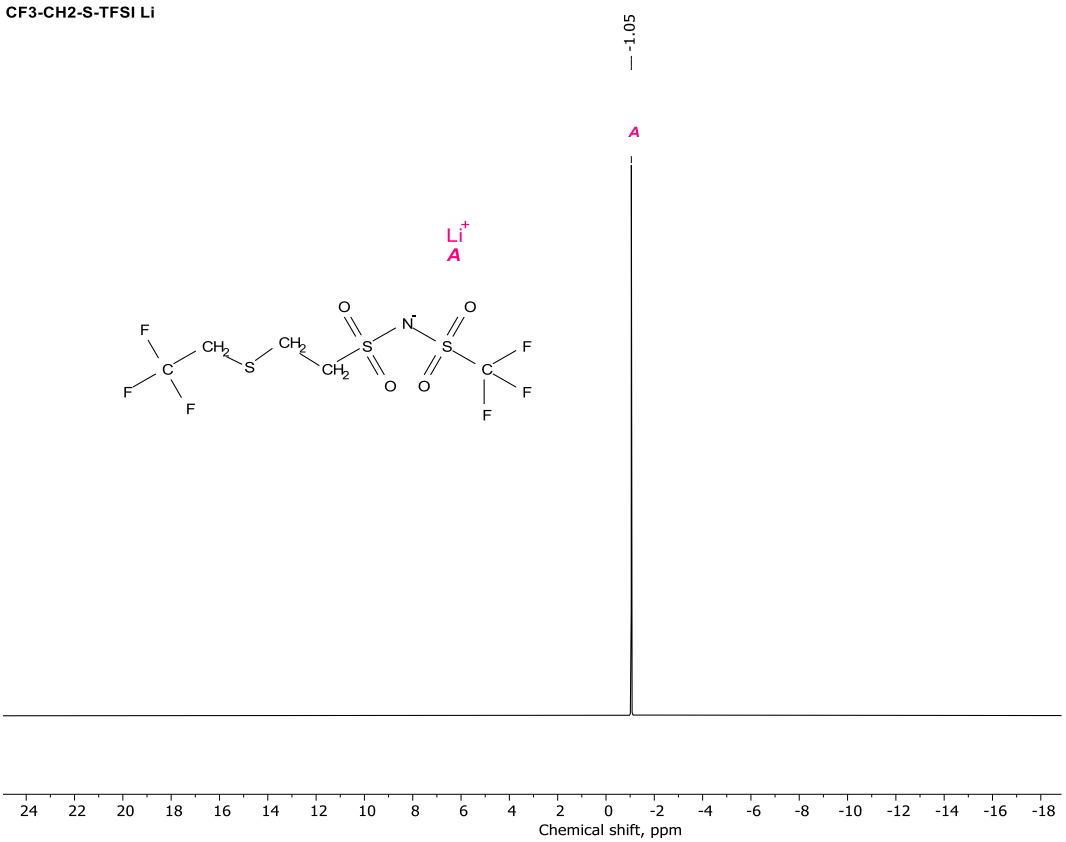

Figure A6. ^{7}Li NMR spectrum of **Li TFT-TFSI** (DMSO-d$_6$, 25.0 °C).

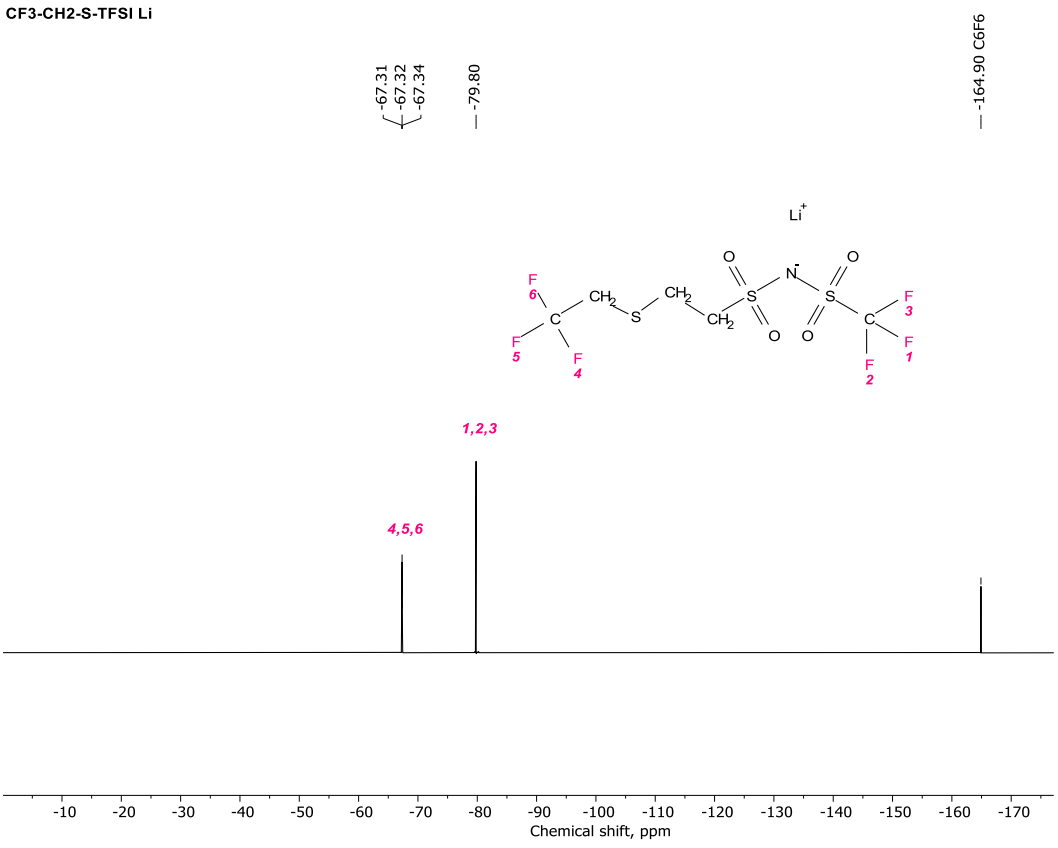

Figure A7. ^{19}F NMR spectrum of **Li TFT-TFSI** (DMSO-d$_6$, 25.0 °C).

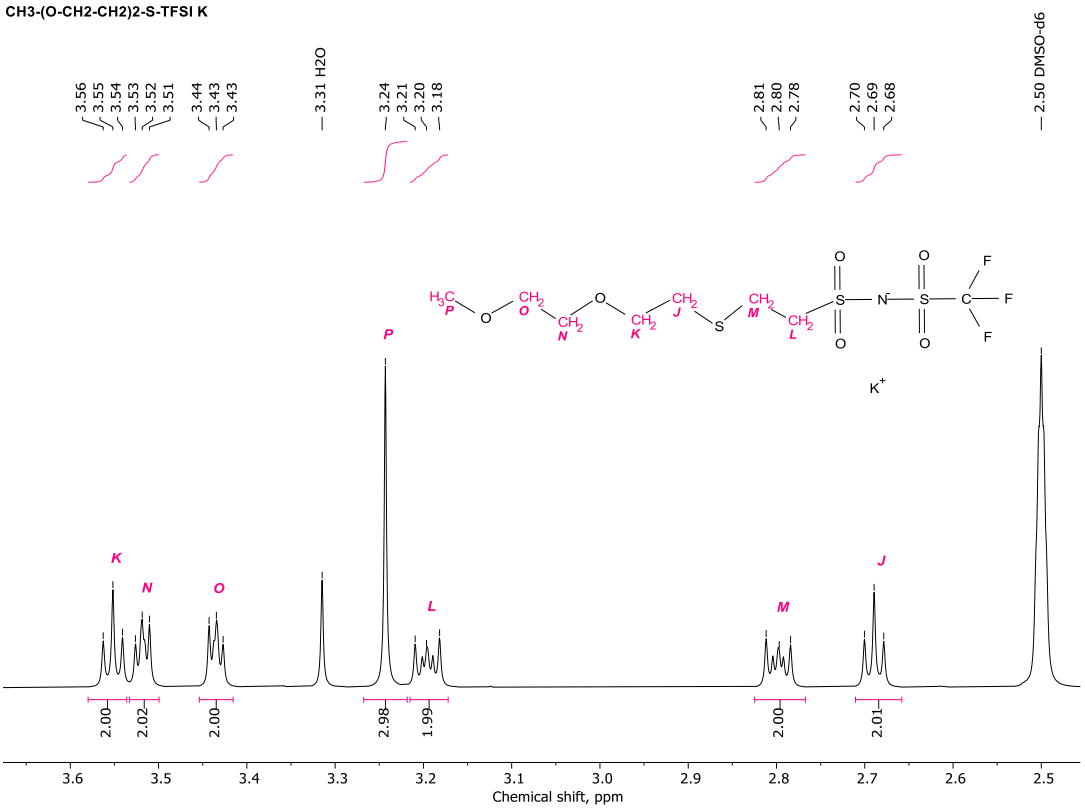

Figure A8. ^{1}H NMR spectrum of **CH_3-(O-CH_2-CH_2)$_2$-S-TFSI K** (DMSO-d_6, 25.0 °C).

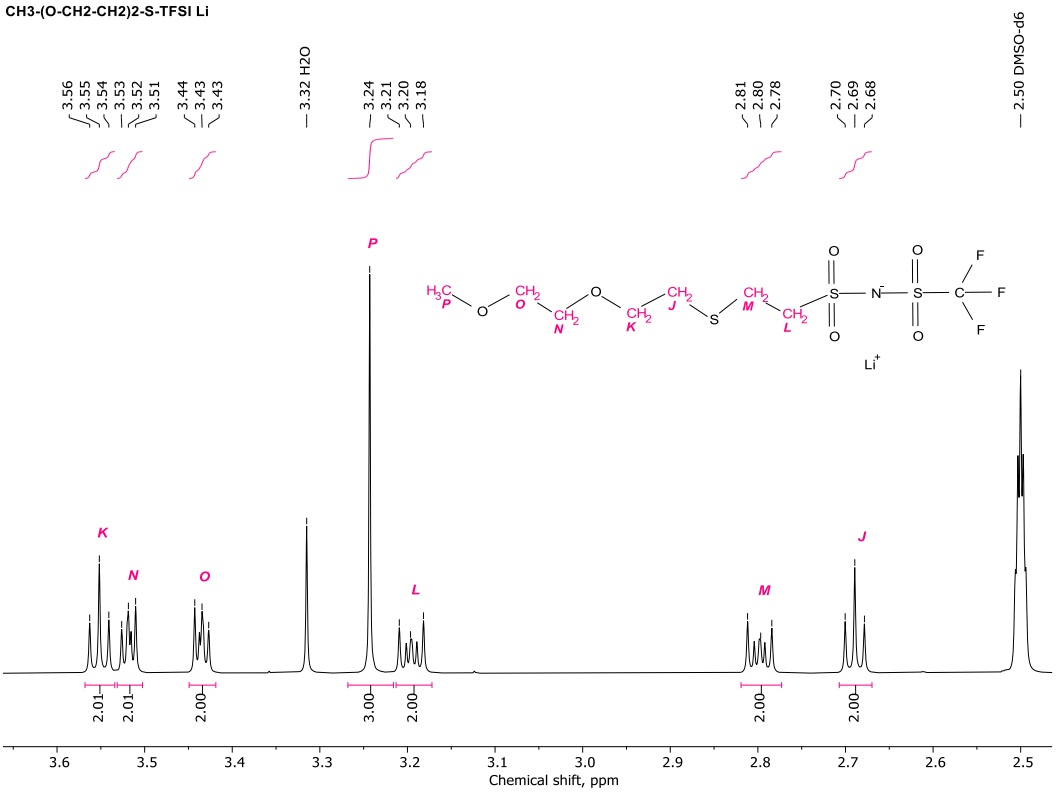

Figure A9. ^{1}H NMR spectrum of **Li MET-TFSI** (DMSO-d_6, 25.0 °C).

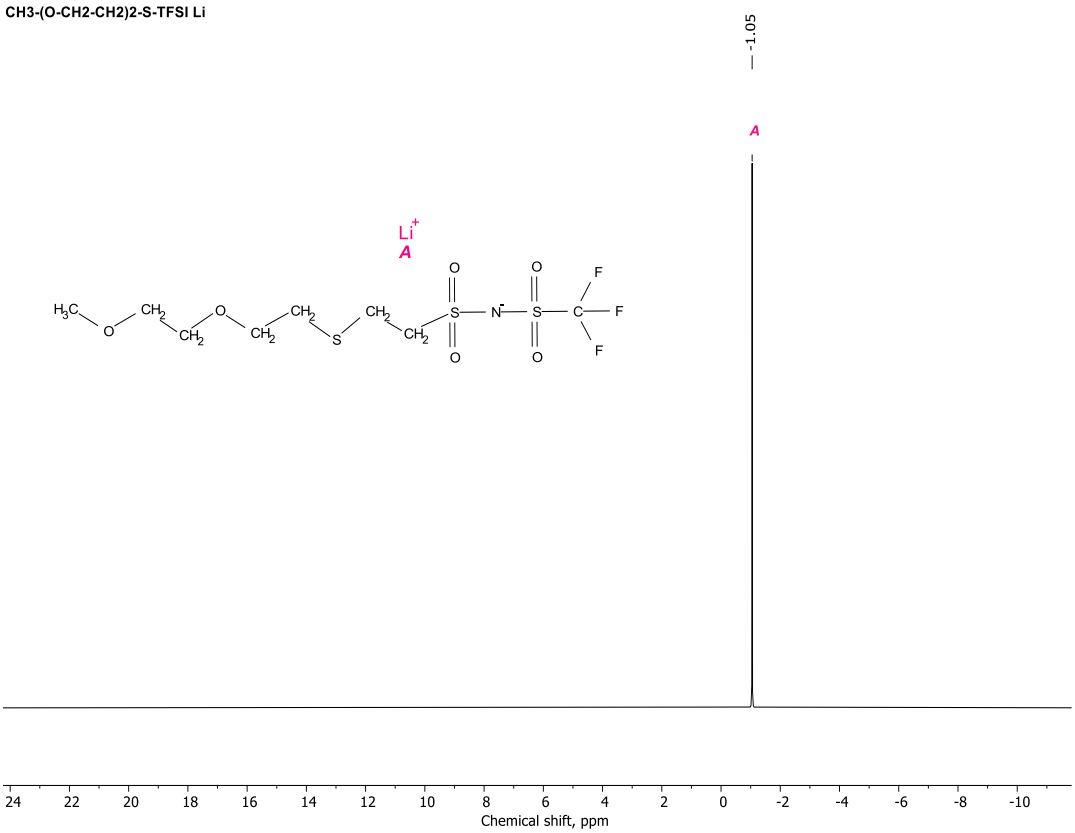

Figure A10. ^{7}Li NMR spectrum of **Li MET-TFSI** (DMSO-d$_6$, 25.0 °C).

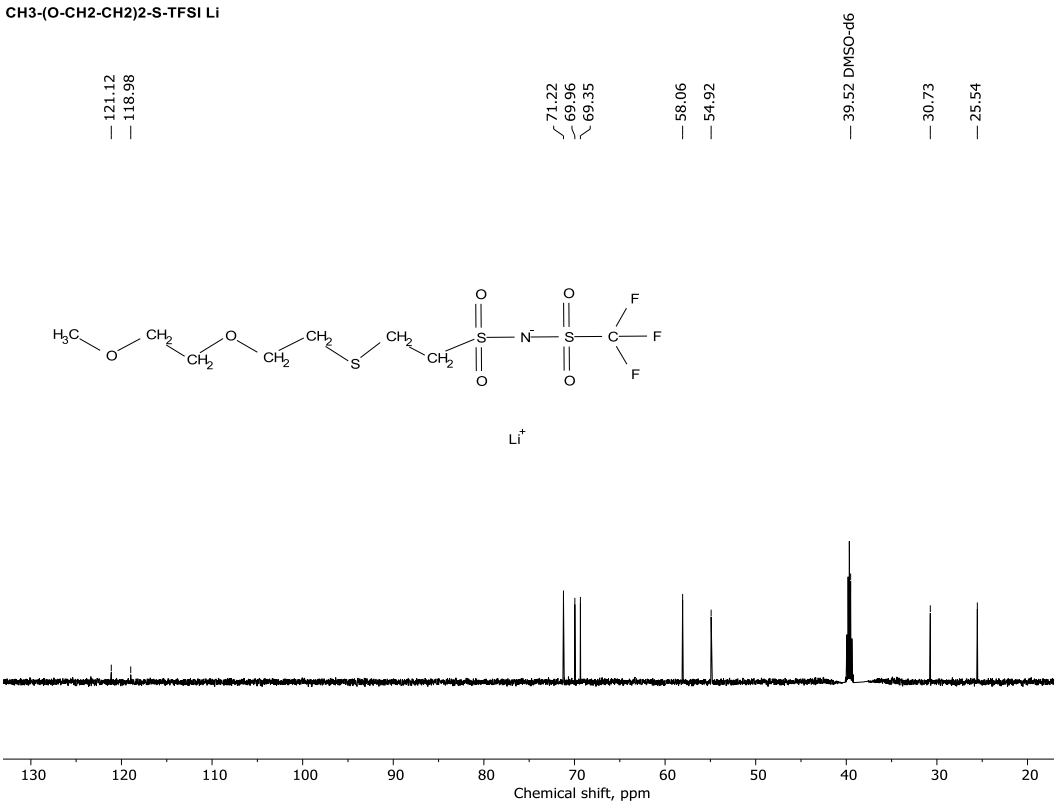

Figure A11. ^{13}C NMR spectrum of **Li MET-TFSI** (DMSO-d$_6$, 25.0 °C).

Figure A12. ^{19}F NMR spectrum of **Li MET-TFSI** (DMSO-d$_6$, 25.0 °C).

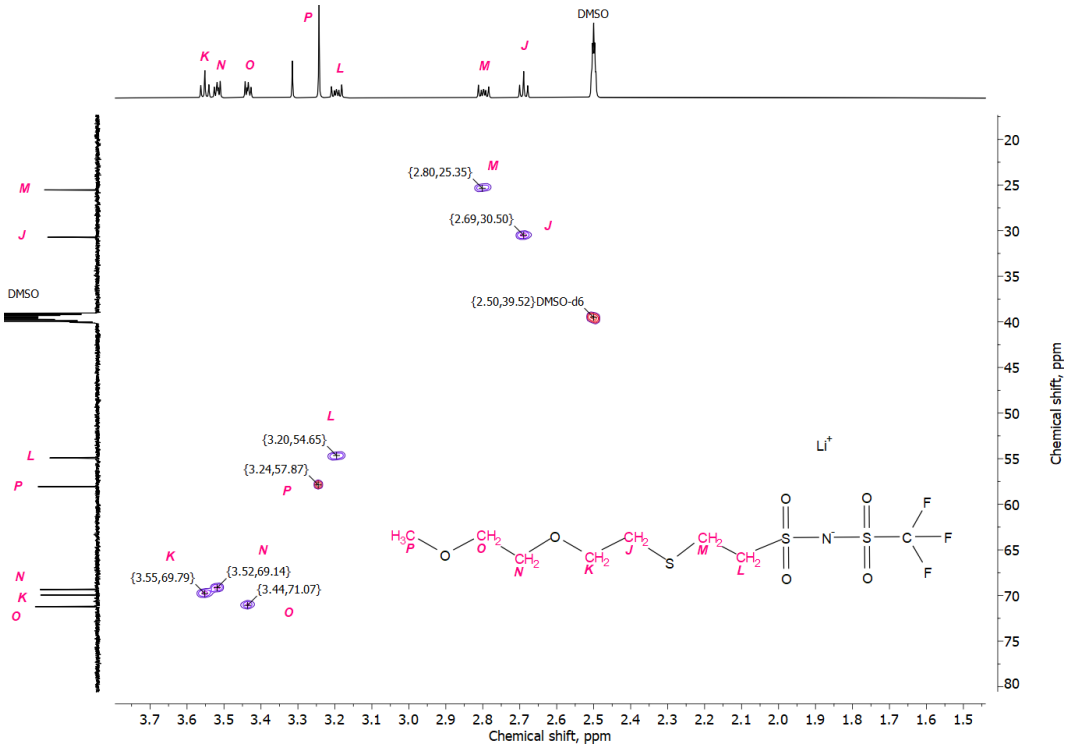

Figure A13. 2D HSQC spectrum of **Li MET-TFSI** (DMSO-d$_6$, 25.0 °C).

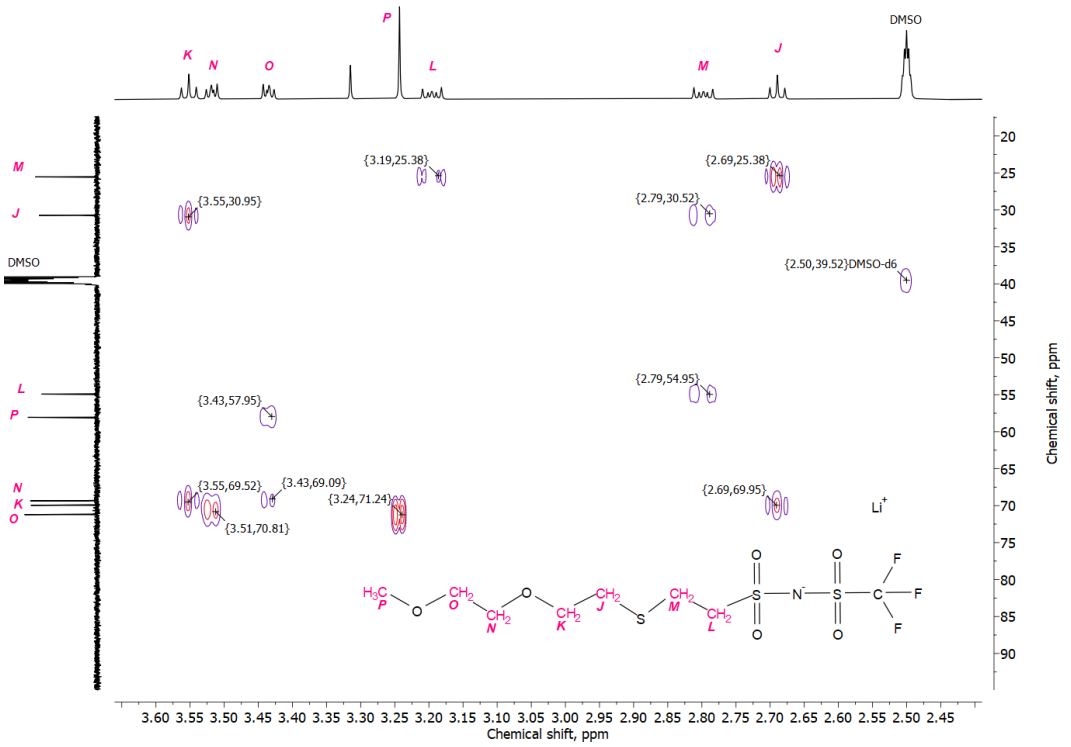

Figure A14. 2D HMBC Spectrum of **Li MET-TFSI** (DMSO-d_6, 25.0 °C).

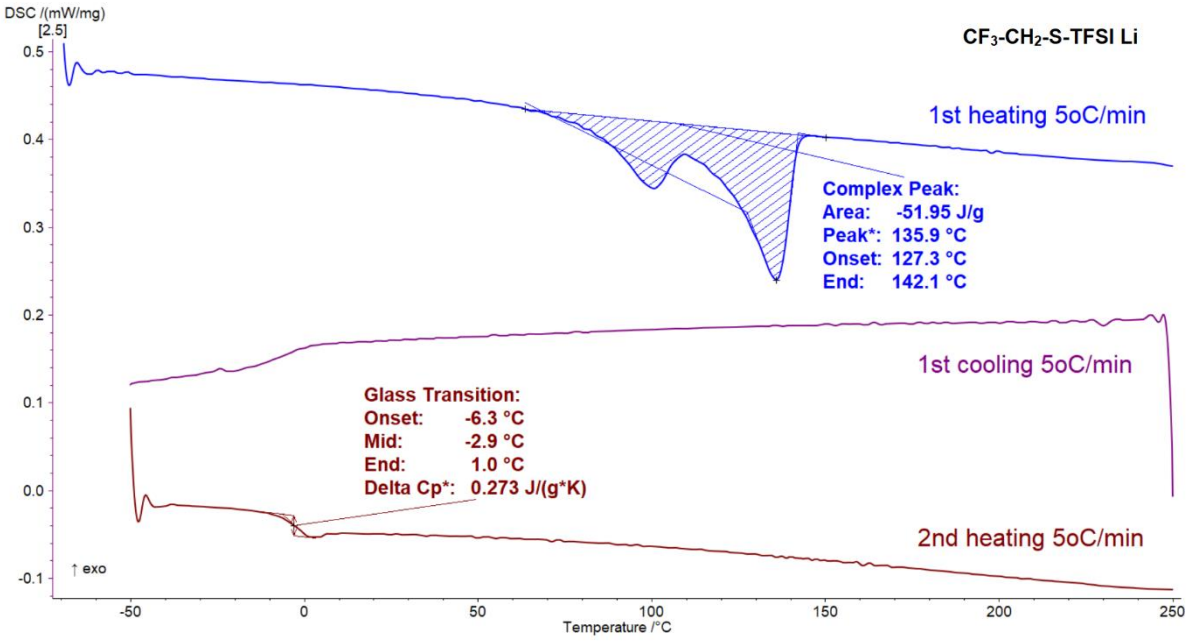

Figure A15. DSC curves of **Li TFT-TFSI.**

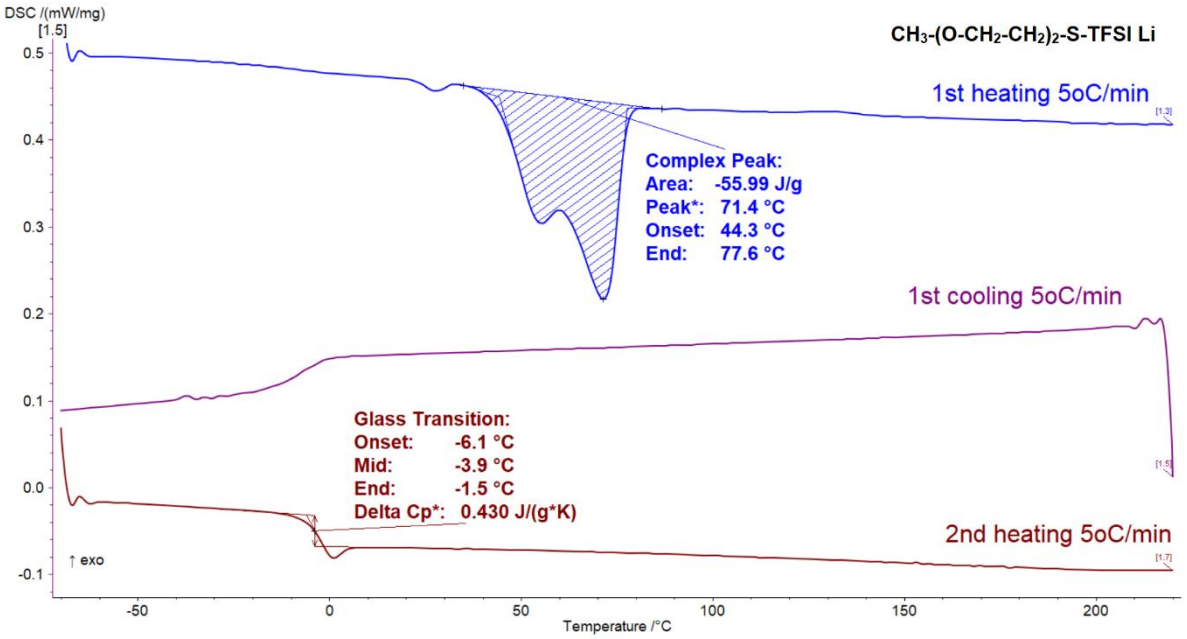

Figure A16. DSC curves of **Li MET-TFSI.**

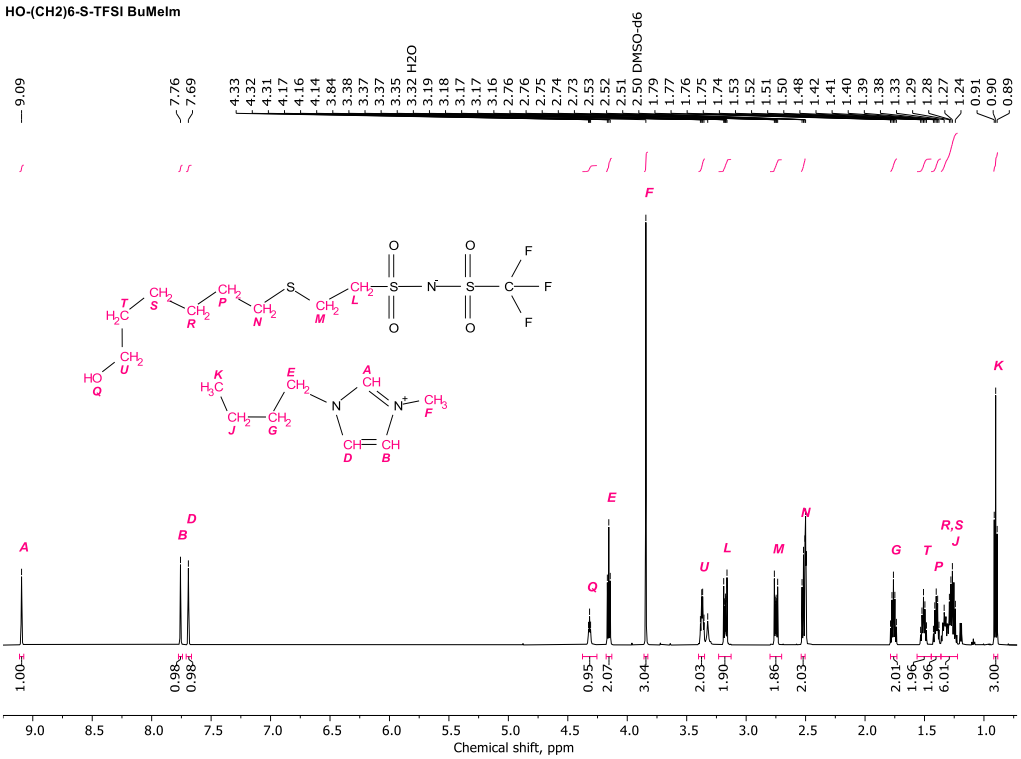

Figure A17. ^{1}H NMR Spectrum of **BMIM HO-$(CH_2)_6$-S-TFSI** in DMSO-d6 at 25°C.

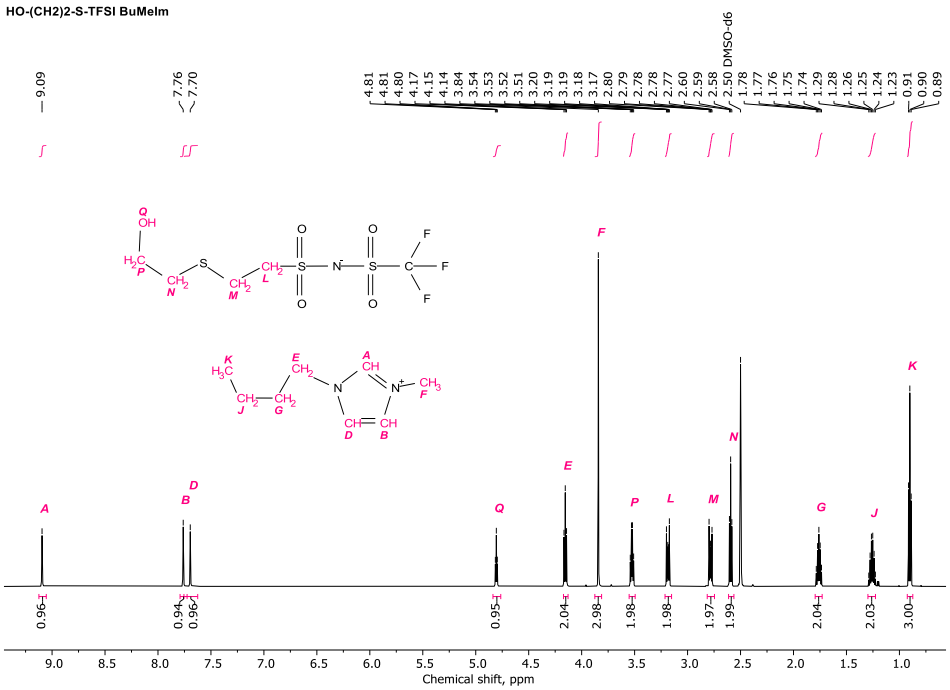

Figure A18. ^{1}H NMR Spectrum of **BMIM HO-$(CH_2)_2$-S-TFSI** in DMSO-d6 at 25°C.

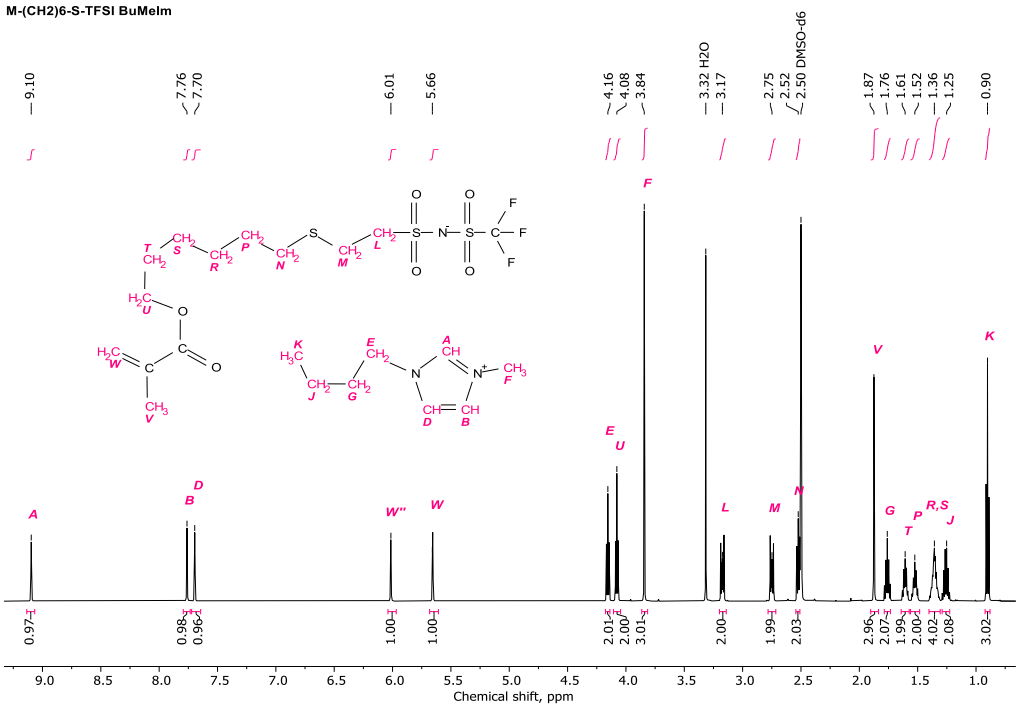

Figure A19. ^{1}H NMR Spectrum of **BMIM ILM1** in DMSO-d6 at 25°C.

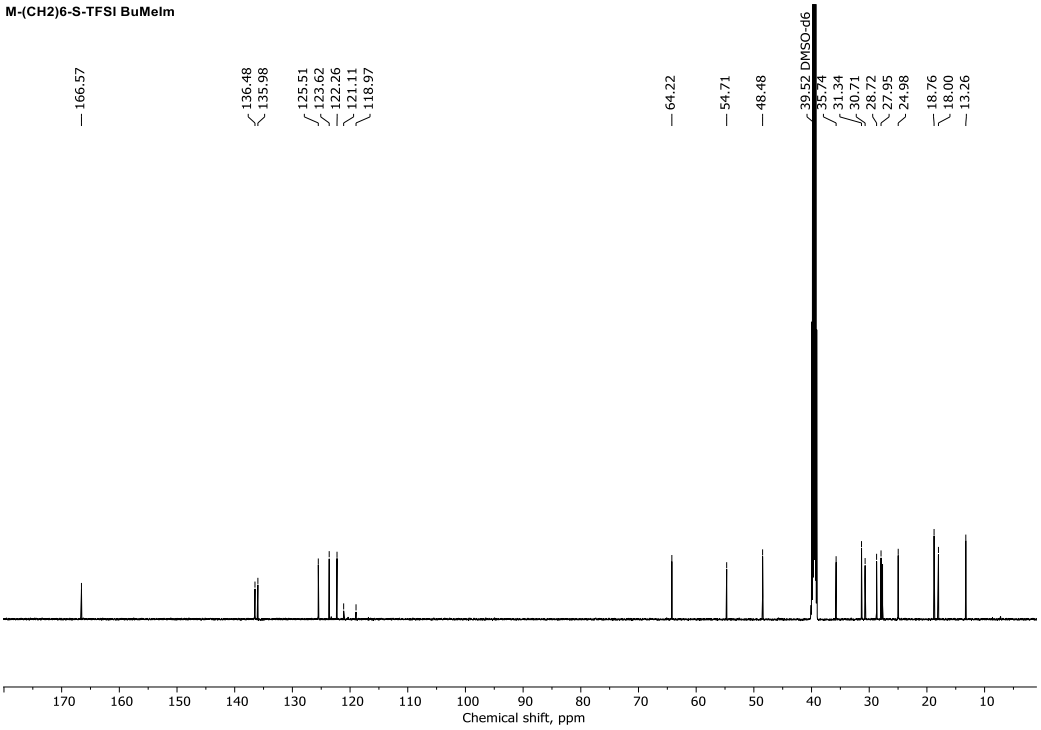

Figure A20. ^{13}C NMR Spectrum of **BMIM ILM1** in DMSO-d6 at 25°C.

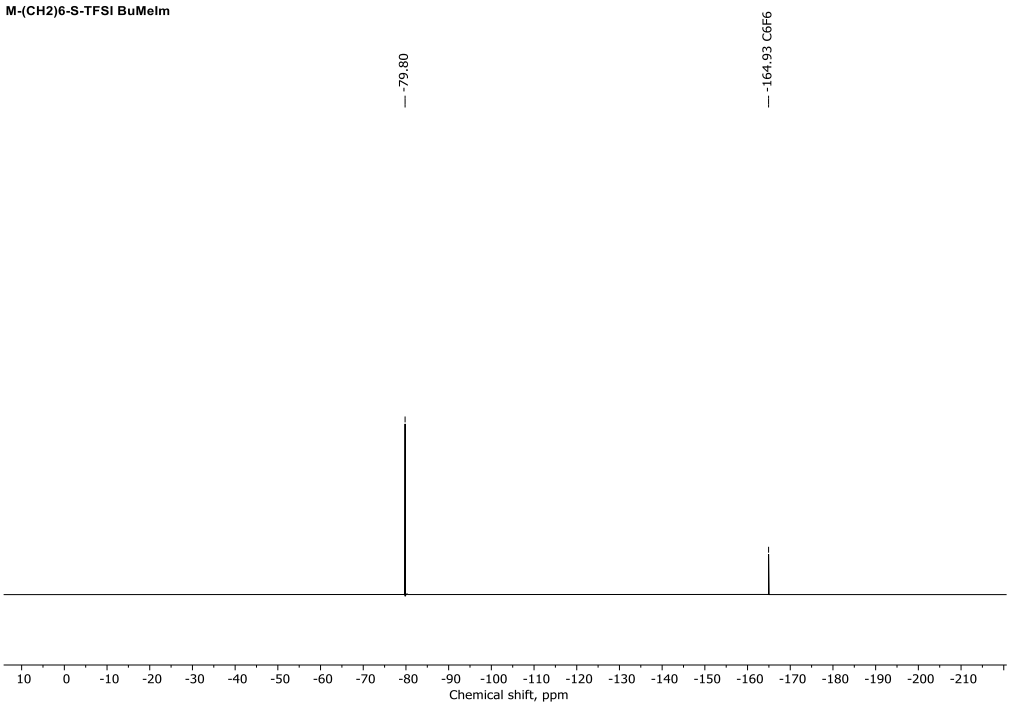

Figure A21. ^{19}F NMR Spectrum of **BMIM ILM1** in DMSO-d6 at 25°C.

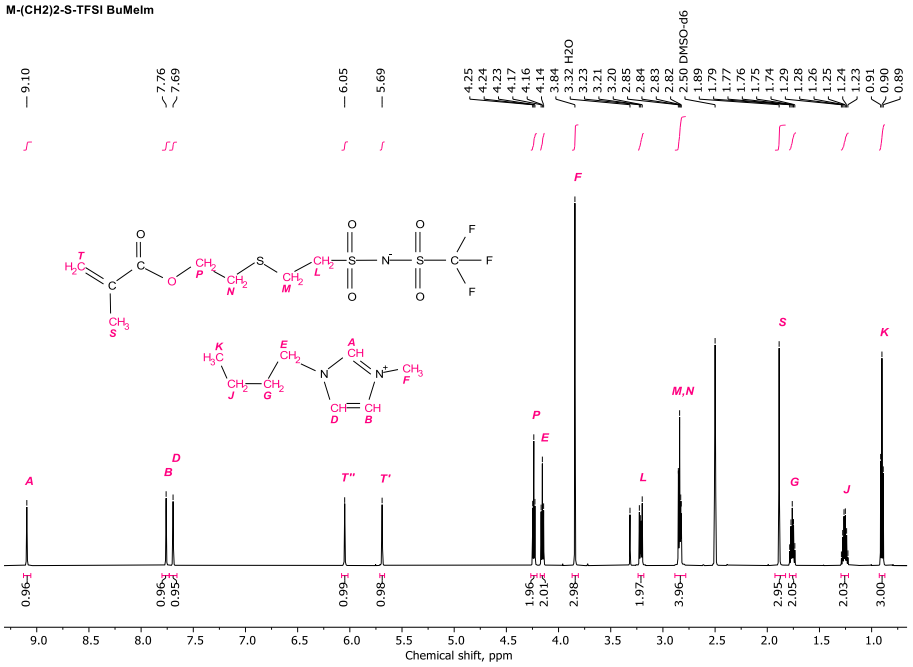

Figure A22. ^{1}H NMR Spectrum of **BMIM ILM2** in DMSO-d6 at 25°C.

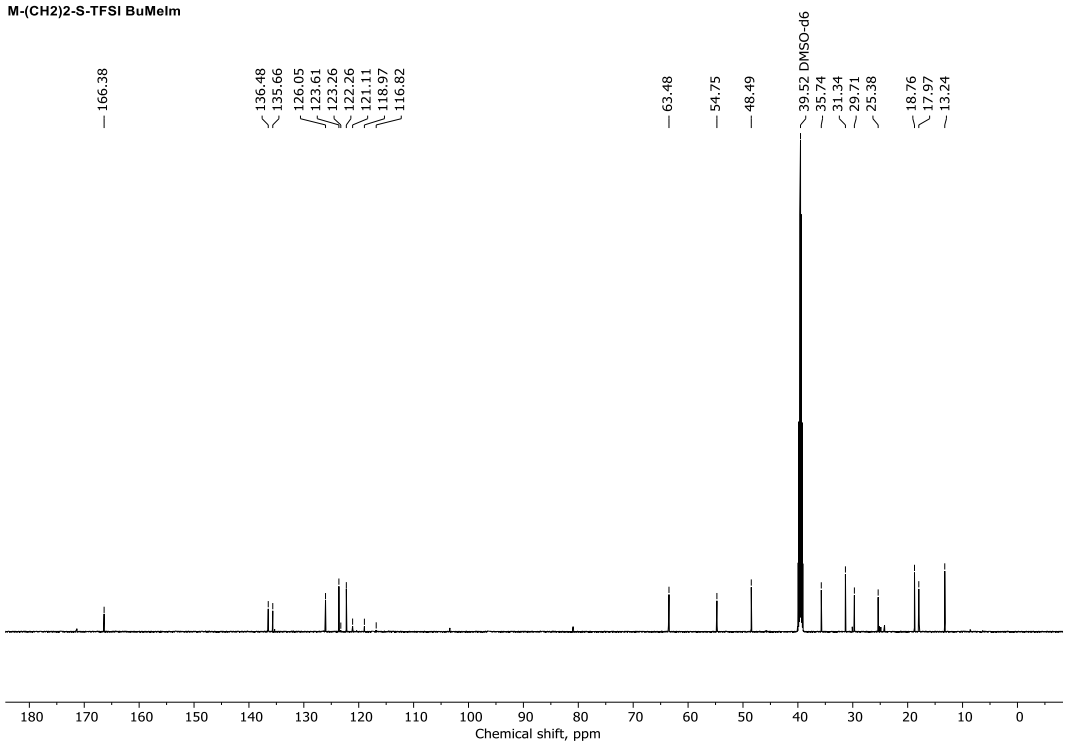

Figure A23. ^{13}C NMR Spectrum of **BMIM ILM2** in DMSO-d6 at 25°C.

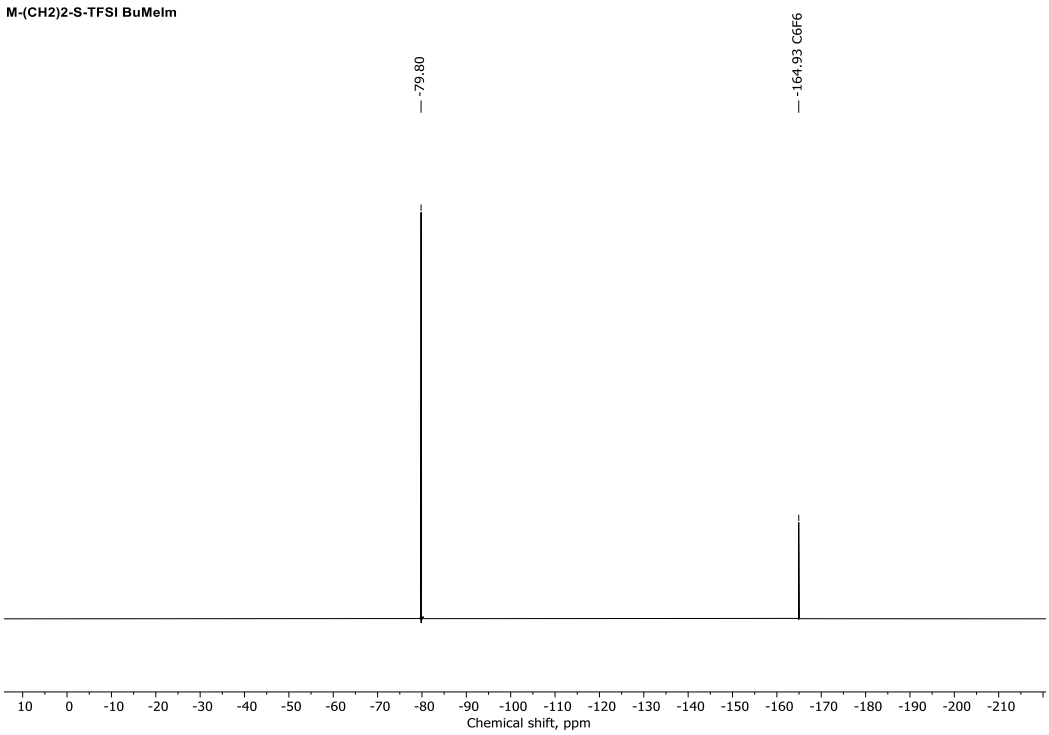

Figure A24. ^{19}F NMR Spectrum of **BMIM ILM2** in DMSO-d6 at 25°C.

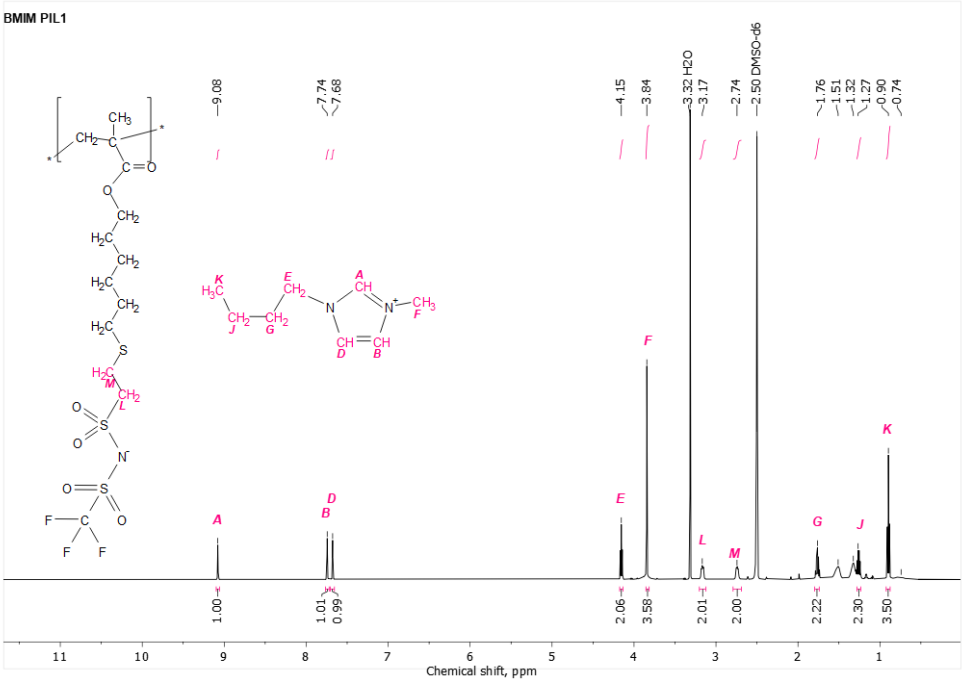

Figure A25. ^{1}H NMR Spectrum of **BMIM PIL1** in DMSO-d6 at 25°C.

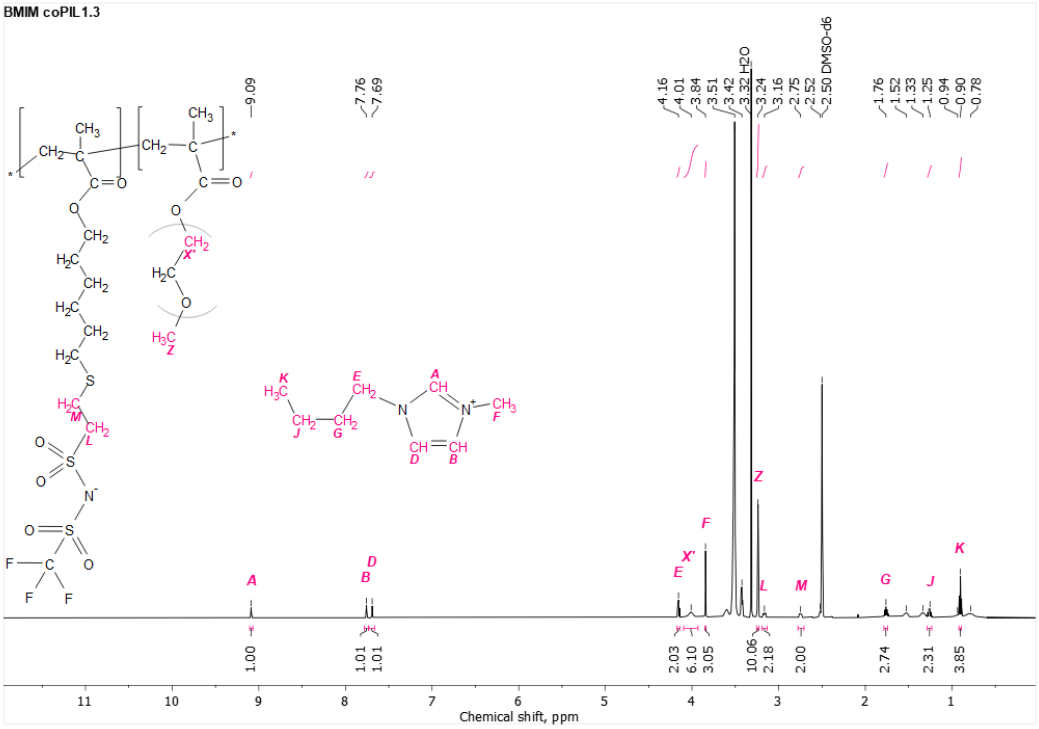

Figure A26. ^{1}H NMR Spectrum of **BMIM coPIL1.3** in DMSO-d6 at 25°C.

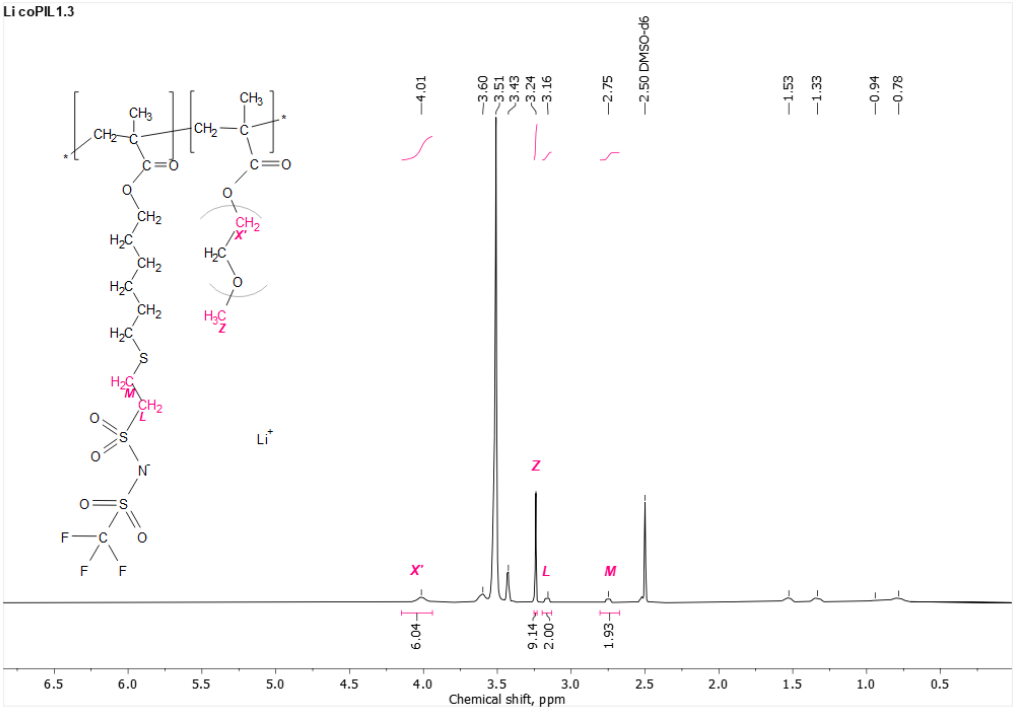

Figure A27. ^{1}H NMR Spectrum of **Li coPIL1.3** in DMSO-d6 at 25°C.

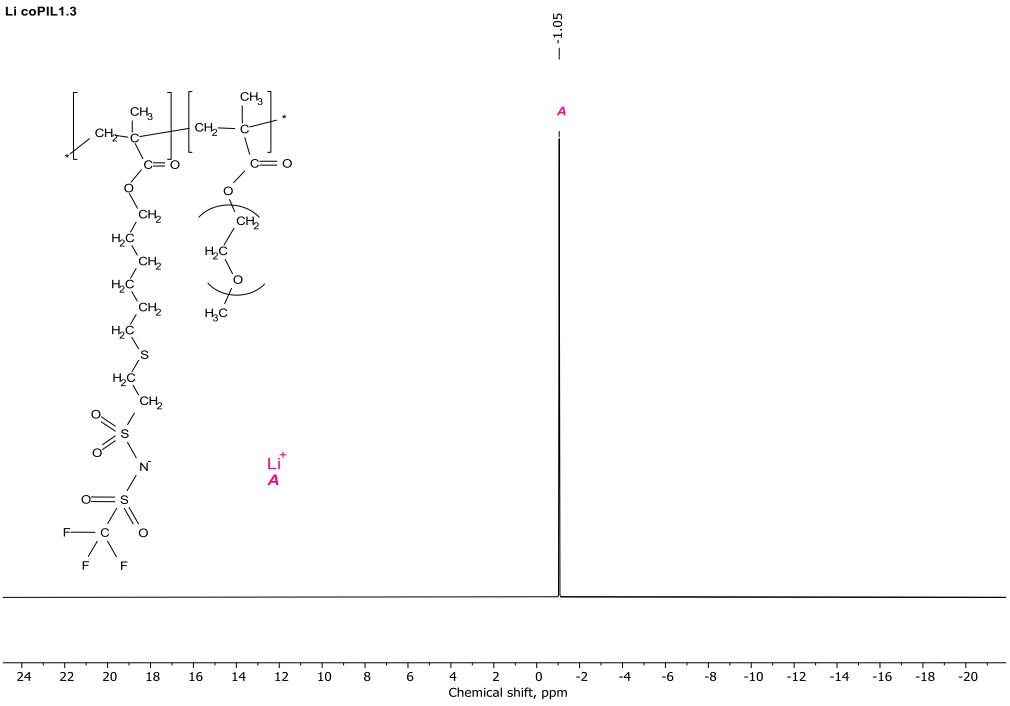

Figure A28. ^{7}Li NMR Spectrum of **Li coPIL1.3** in DMSO-d6 at 25°C.

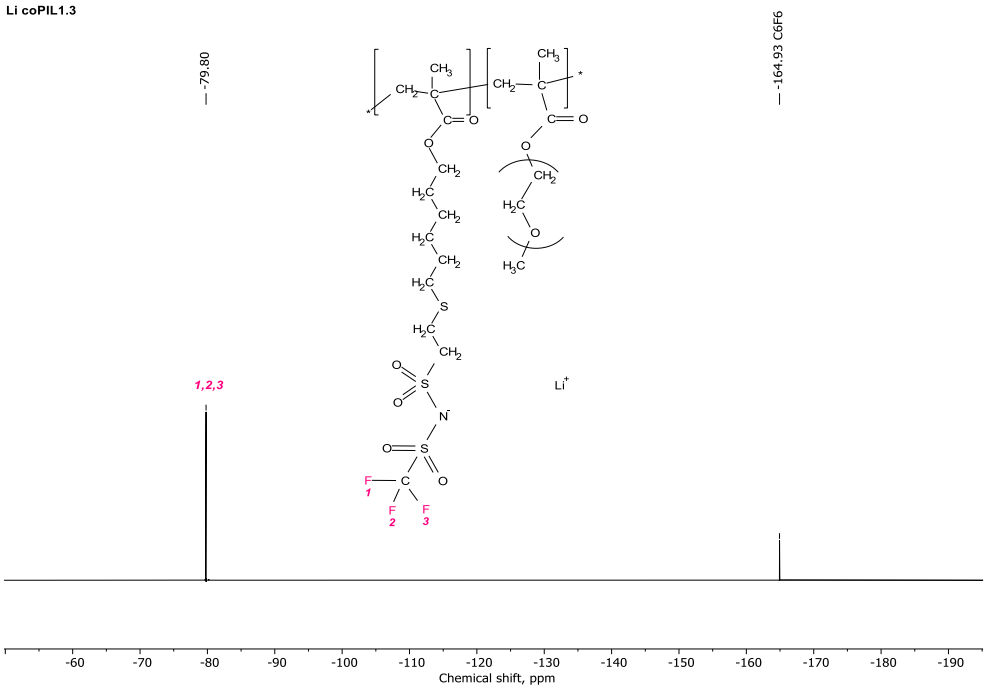

Figure A29. ^{19}F NMR Spectrum of **Li coPIL1.3** in DMSO-d6 at 25°C

.

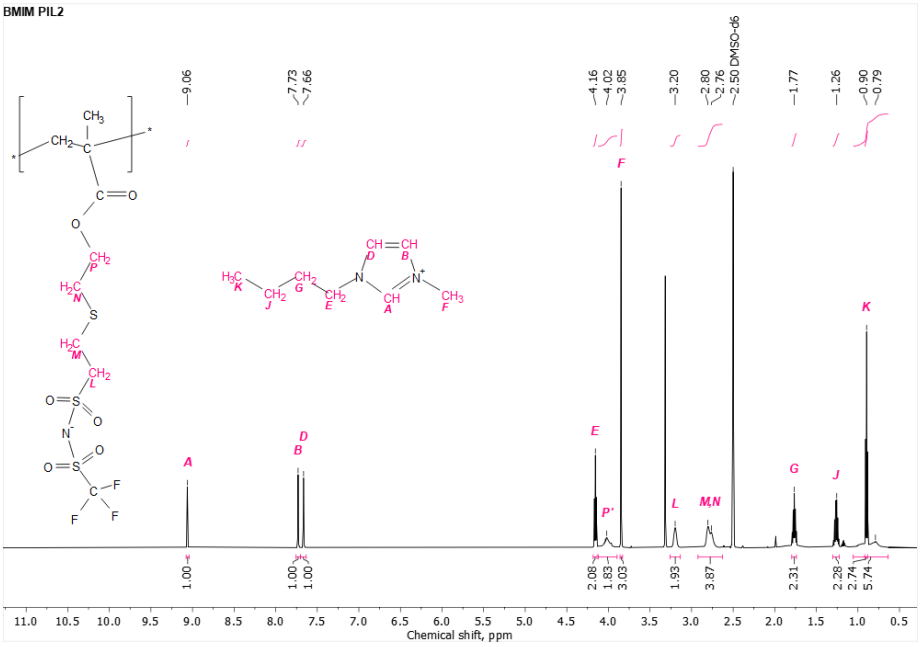

Figure A30. ^{1}H NMR Spectrum of **BMIM PIL2** in DMSO-d6 at 25°C.

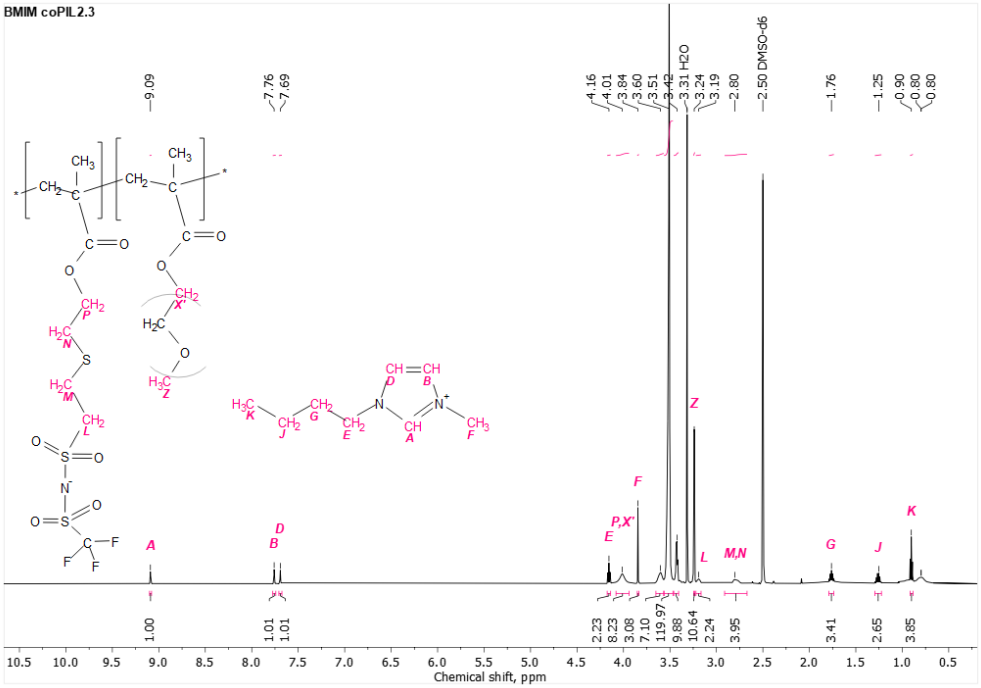

Figure A31. ^{1}H NMR Spectrum of **BMIM coPIL2.3** in DMSO-d6 at 25°C.

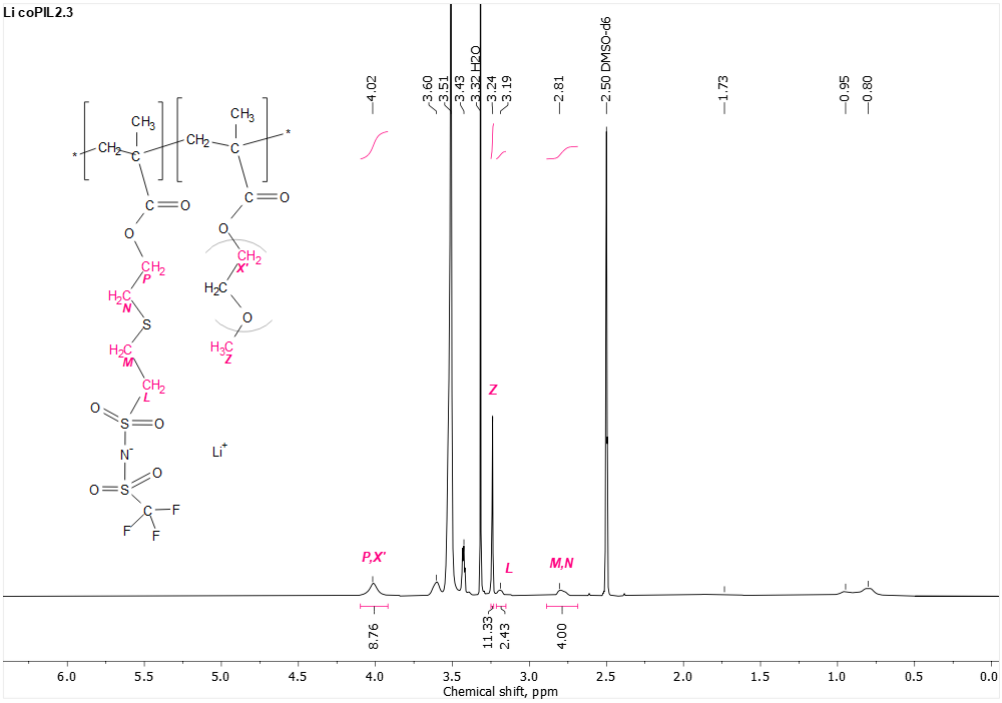

Figure A32. ^{1}H NMR Spectrum of **Li coPIL2.3** in DMSO-d6 at 25°C

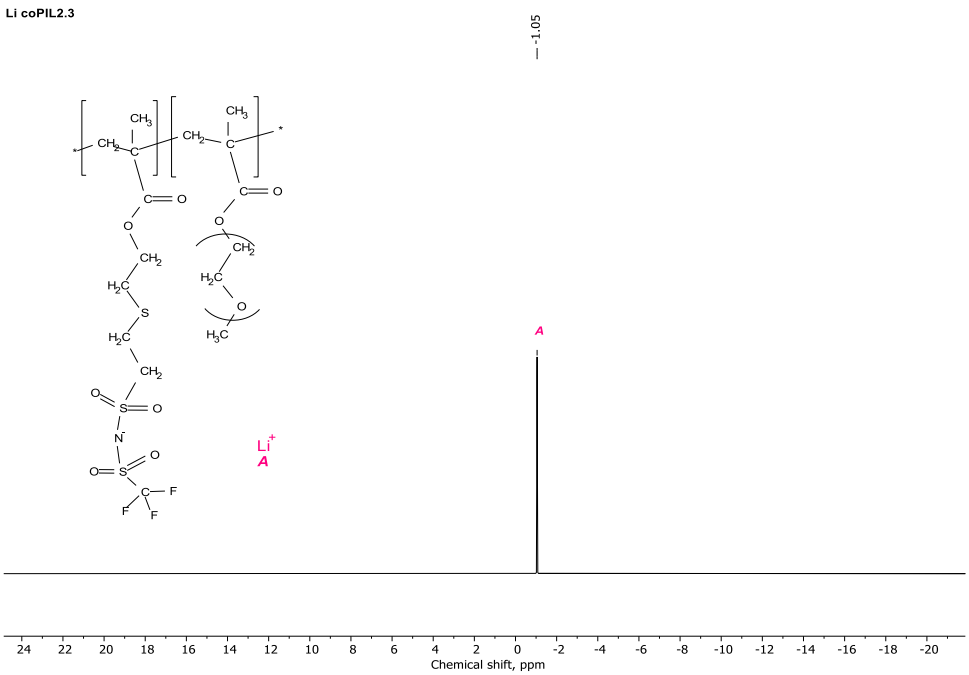

Figure A33. ^{7}Li NMR Spectrum of **Li coPIL2.3** in DMSO-d6 at 25°C.

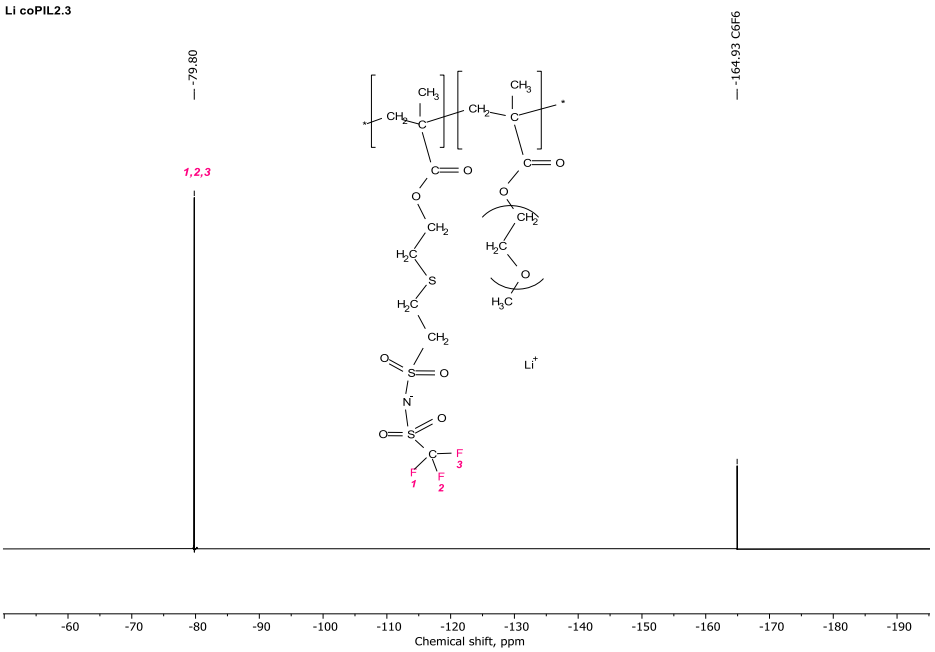

Figure A34. ^{19}F NMR Spectrum of **Li coPIL1.3** in DMSO-d6 at 25°C.

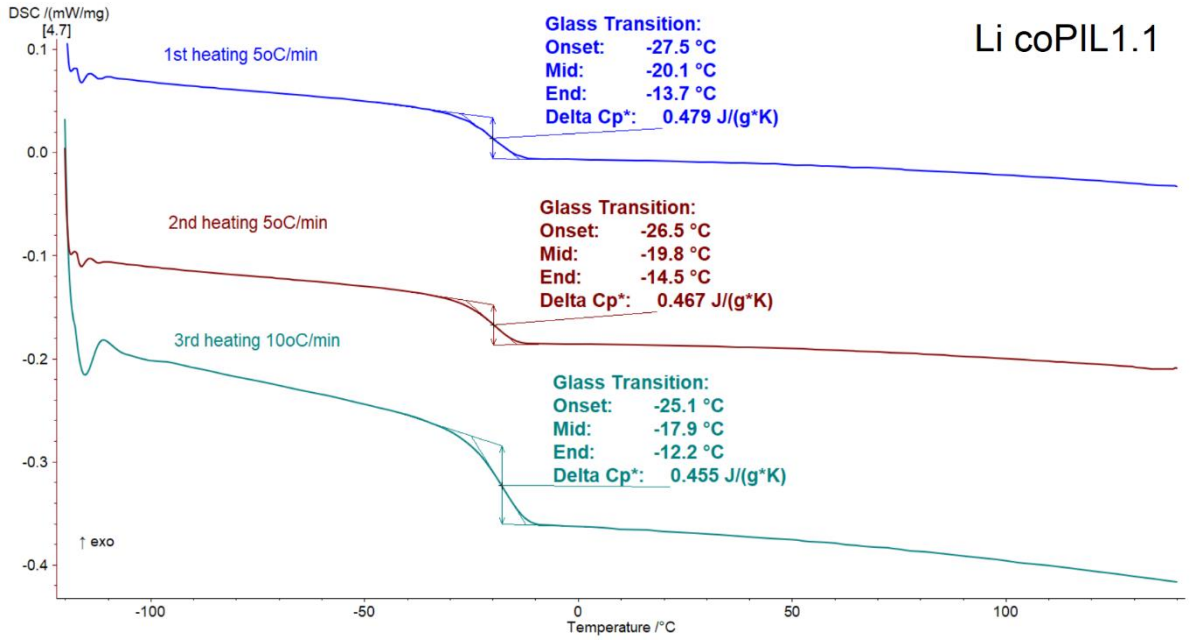

Figure A35. DSC traces of Li coPIL1.1.

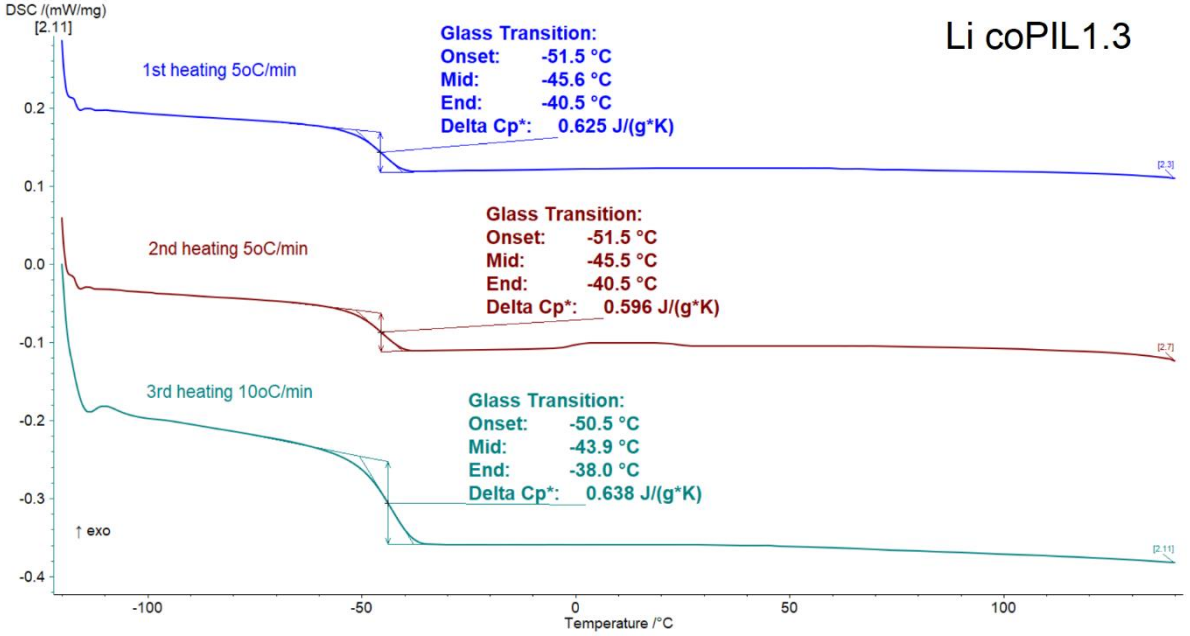

Figure A36. DSC traces of Li coPIL1.3.

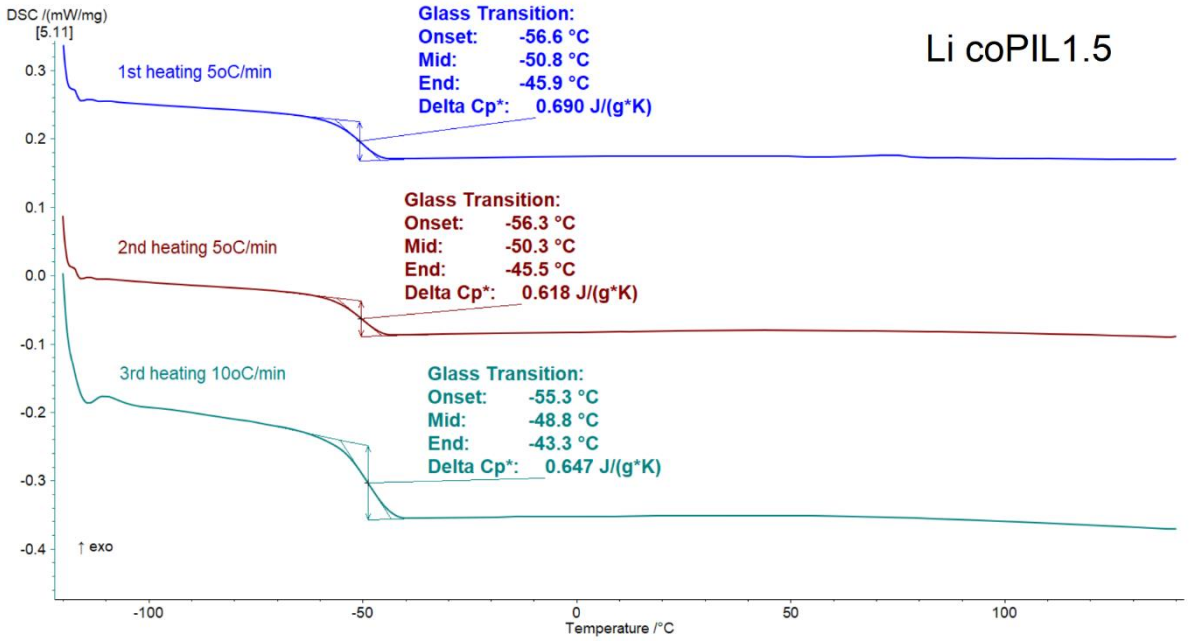

Figure A37. DSC traces of Li coPIL1.5.

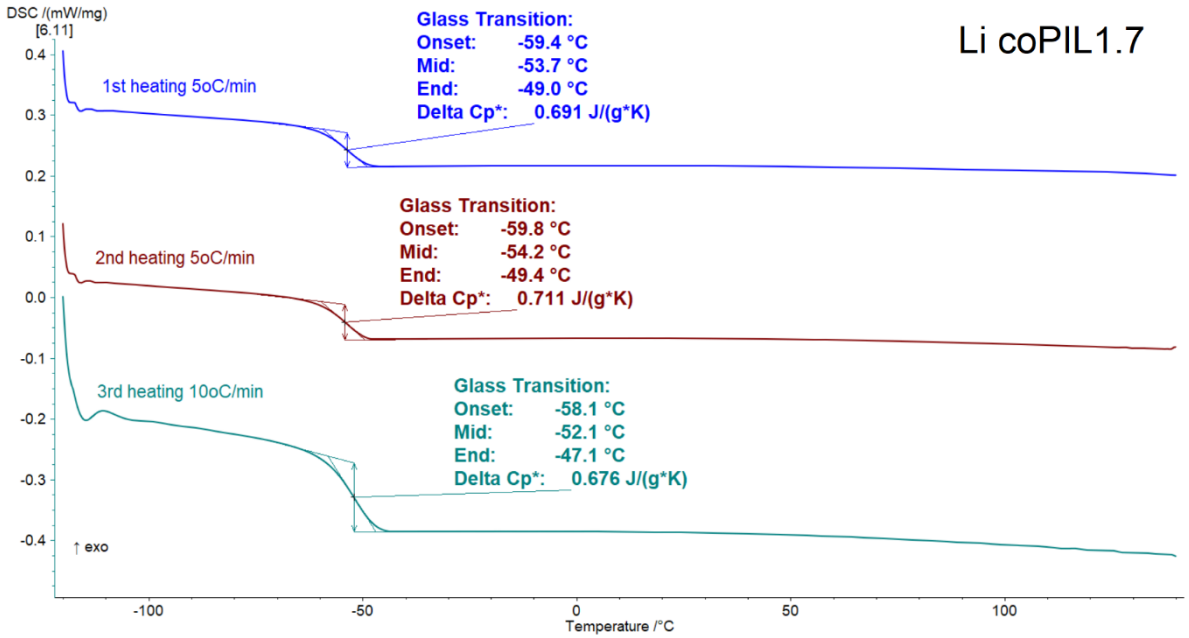

Figure A38. DSC traces of Li coPIL1.7.

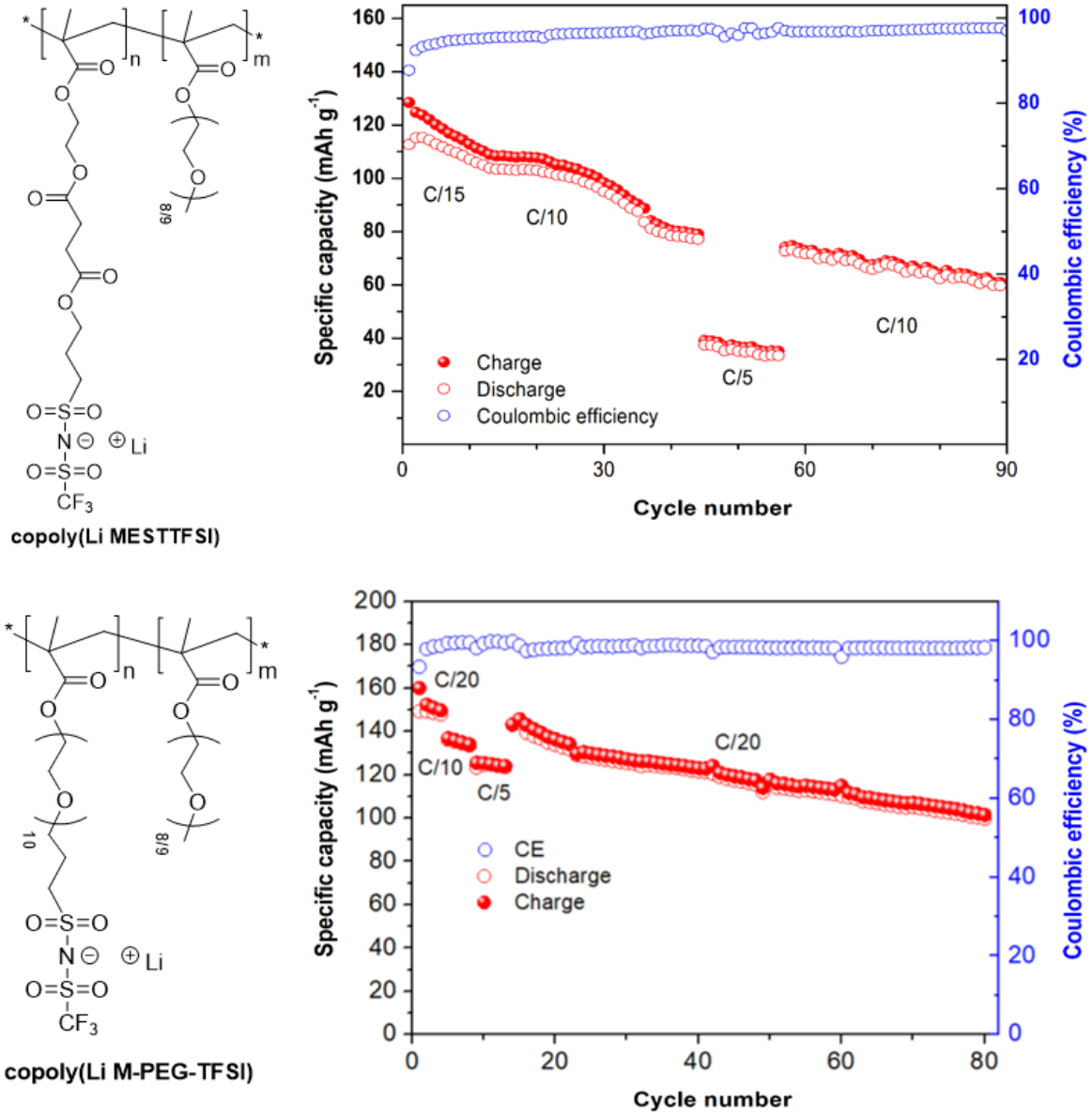

Figure A39. Specific capacity versus cycle number profile of Li/copoly(LiMESTTFSI)/LFP cell (top) and Li/copoly(LiM-PEG-TFSI)/LFP cell (bottom) at different charge/discharge rates at 70 °C. Provided for comparison.